Effects of passive porous walls on the first Mack mode instability of hypersonic boundary layers over a sharp cone

by

Vipin George Michael

A thesis submitted to
The University of Birmingham
for the degree of
Doctor of Philosophy

School of Mathematics
The University of Birmingham
October 2012

Abstract

Passive porous coatings have been proposed in literature as a means of delaying transition to turbulence in hypersonic boundary layers. The nonlinear stability of hypersonic viscous flow over a sharp slender cone with passive porous walls is investigated in this study. Hypersonic flows are unstable to viscous and inviscid disturbances, and following Mack (1984) these have been called the first and second Mack modes. A weakly nonlinear analysis of the instability of the flow to axisymmetric and non-axisymmetric viscous (first Mack mode) disturbances is performed here. The attached shock and effect of curvature are taken into account. Asymptotic methods are used at large Reynolds number and large Mach number to examine the viscous modes of instability, which may be described by a triple-deck structure. Various porous wall models have been incorporated into the stability analysis. The eigenrelations governing the linear stability of the problem are derived. Neutral and spatial instability results show the presence of multiple unstable modes and the destabilising effect of the porous wall models on them. The weakly nonlinear stability analysis carried out allows an equation for the amplitude of disturbances to be derived. The stabilising or destabilising effect of nonlinearity is found to depend on the cone radius. It is shown that porous walls significantly influences the effect of nonlinearity. They allow nonlinear effects to destabilise linearly unstable lower frequency modes and stabilise linearly unstable higher frequency modes.

Dedication

I am eternally grateful to the Divine Mercy of God and His presence in my life. He has always shown me the light at the end of the tunnel in my darkest of times. I thank my Heavenly Mother who has continually prayed for me. I thank Padre Pio, all the saints and angels including my own guardian angel who have continually interceded for me in my difficult moments.

I thank Ammachi for praying for me and laying the foundation for where I am today. I thank all the souls (including my forefathers) who have prayed for me. I sincerely thank Mummy for instilling in me the importance of higher education. I am eternally grateful for every small and big sacrifice she has made and for each and every encouraging word she has spoken to me during my uncertainties. I sincerely thank Papa for showing me the importance of faith in God and how hard work can lead to gratification of the soul. He has always strived to financially provide for me and paved the path for me to have a good education. I want to thank Mithun for all the times we have shared growing up. I thank Pareappachan, Tate uncle, Annie aunty and Babu uncle for being my guardians and everyone else who has taken care of me during my school days. I would like to thank Nupur and her family who have been a continual source of motivation and inspiration for me to achieve my potential and fulfill my dreams. She has truly been my better half and a rock during all the testing times we have gone through these past few years.

I would like to thank all my teachers right from my school days through to university.

Last but not the least I want to thank the rest of my family and friends especially my 'gang' from AUS.

This thesis is dedicated to all of the above and to all those in the pursuit of knowledge.

Acknowledgements

I would like to sincerely thank my supervisor Dr. Sharon Stephen, whose constant encouragement, insight and guidance was instrumental in the successful completion of this thesis. I would also like to thank my colleagues with whom I have had the privilege of sharing an office for their camaraderie, support and encouragement. I would like to acknowledge the help and support received from the teaching and administrative staff of the School of Mathematics. Last but definitely not the least, I would also like to acknowledge the financial contribution of the School of Mathematics towards my maintenance and the Air Force Office of Scientific Research and Material Command, U.S. Air Force, who have partially sponsored this research under grant number FA8655-08-1-3044.

Contents

Chapter 1

Introduction

The state of the boundary-layer flow over a flying surface has an enormous impact on the viscous drag (or skin friction) experienced by a body. This is because the boundary layer can undergo a transition from a smooth, low drag, laminar state to a chaotic, higher drag turbulent state as it evolves over a flying surface. The transition process is still not completely understood and has been an intense area of research for the past several decades. A sound knowledge of this process is essential in devising methods to delay the location along the flying surface at which the flow becomes turbulent. Transition to turbulence becomes even more important at hypersonic speeds as a turbulent boundary layer contributes significantly to aerodynamic heating of the body.

Laminar to turbulent transition of the boundary layer therefore has important implications on the design and performance of a hypersonic flight vehicle (Malik *et al.* 1990). For example, early transition can increase the surface heat transfer by a factor of $3-8$ which translates to higher cost and weight of thermal protection systems incorporated in the vehicle (Schneider *et al.* 1999, 2004). Existing hypersonic vehicle designs fall under either blunt configurations, moderate blunt lifting type configurations or air-breathing types. The latter has relatively sharp leading edges and can achieve high lift-to-drag ratios. Premature transition in such vehicles may become critical as it reduces propulsion

efficiency, increases viscous drag (being up to 30% of total drag), as well as degrading aerodynamic control surfaces and reaction control systems of the vehicle (Kimmel 2003).

Extensive experimental, numerical and theoretical studies have been carried out to understand the instability mechanisms that arise in hypersonic flows over sharp slender bodies. As a result of these studies, it is now widely accepted that transition to turbulence in hypersonic flows over smooth bodies and with low levels of free-stream turbulence is associated with amplification of the first and/or second Mack modes. The first Mack mode is the high speed counterpart of Tollmien-Schlichting waves, so a viscous instability, with modes located close to the boundary. The second Mack mode is an inviscid instability driven by a region of supersonic mean flow relative to the disturbance phase velocity. The second-mode instability occurs when the Mach number becomes high (> 4 on insulated surfaces), and has growth rates that exceed that of the first mode. Experimental findings (Fedorov *et al.* 2003a,b and Stetson *et al.* 1982, 1993) reveal that the first-mode instability occurs in a lower frequency band, $50 - 100$kHz, while the second mode occurs around $70 - 150$kHz and higher in hypersonic boundary layers over a cone. Spectral data obtained from various stations along the cone surface show that the first-mode fluctuations increase their amplitude without any special selectivity in the frequency of the disturbances which are amplified, while the second mode fluctuations are highly 'tuned' to the boundary-layer thickness, resulting in considerable selectivity in the disturbance frequencies which are most amplified (Stetson & Kimmel 1992). This tuning effect causes the second-mode disturbance peaks to shift to lower frequencies as the boundary layer grows. The experiments also confirm the dominance of the second mode in the disturbance spectra. Thus the second mode is believed to be responsible for transition to turbulence on hypersonic slender bodies, as it is the dominant instability.

This finding initiated several recent theoretical, experimental and numerical investigations into concepts that can damp this instability and thereby achieve an increased

laminar run over the flying surface. This has led to development of the concept of 'ultrasonically absorptive coatings' (UACs), which will be discussed in detail in this chapter. However, compressible boundary layers are also susceptible to the lower frequency first-mode disturbances, and there has been very little investigation into the effects that these coatings may have on this type of instability. This forms the motivation behind the present investigation.

1.1 Stability of compressible boundary layers

A compressible boundary layer is susceptible to two types of travelling-wave instability modes. These are called Mack's first and second modes as they were first identified by Mack (reviewed in Mack 1984) in compressible boundary layers. Recently different terminologies have been introduced by Fedorov & Tumin (2010) with regards to the receptivity study of Fedorov & Khokhlov (2001). Their analysis reveals that in a leading-edge region, two discrete modes that are synchronized with acoustic waves of the continuous spectrum exist. According to this terminology, a discrete mode is a fast (F) or slow (S) mode if it is synchronized with the fast or slow acoustic wave of the continuous spectrum respectively, in the limit of small Reynolds number. Depending on the flow parameters, both mode S and mode F can be unstable or only mode S is unstable having two maxima of the growth rate. The low-frequency (long-wavelength) maximum of the S mode is associated with Mack's first mode, whereas the high-frequency (short-wavelength) maximum is associated with Mack's second mode (Fedorov & Tumin 2010.) Cowley & Hall (1990) examined the linear stability properties of both the first and second mode for the hypersonic flow over a wedge. The first mode is a viscous instability which is governed by a triple-deck type structure. The details of this analysis for a general hypersonic boundary layer were first given by Smith (1989), who derived the scalings that need to be adopted in such analyses. In addition to these viscous modes, a compressible boundary layer is susceptible to inviscid

disturbances. Two classes of inviscid modes have been identified. One type consists of a family of disturbances called the 'acoustic modes', whilst the second kind comprises a single 'vorticity mode'. At large values of Mach number, the vorticity mode is faster growing than the acoustic modes. Concurrent with Cowley & Hall (1990), Smith & Brown (1990) also investigated both forms of the inviscid modes and showed that a near-linking of the neutral modes occur with increasing Mach number. They also found that the stability of these inviscid modes is critically dependent on the choice of temperature-viscosity law. This is because these disturbances are concentrated in a temperature adjustment layer located within the main boundary layer (middle deck) whose precise form is dependent on the viscosity law adopted. This contrasts with viscous disturbances which are concentrated near the wall (lower deck), and the choice of viscosity law only affects the bounds on the parameters present in the problem.

Although at large Mach numbers the inviscid modes have larger growth rates than the viscous modes, the latter may become important in certain situations such as 'low free-stream disturbance' wind tunnels or instabilities in the presence of porosity or micro-roughness. Furthermore, Cowley & Hall (1990) have shown that the presence of a shock significantly affects the viscous modes, but has a negligible effect on the acoustic modes unless the distance of the shock from the surface is of the order of the boundary layer thickness. Their significant finding was that the presence of the shock gives rise to an infinite number of unstable modes as it allows both incoming and outgoing waves in the boundary layer. The influence of an attached shock on the growth rates of Tollmien-Schlichting waves was also demonstrated by Chang *et al.* (1990). Numerical studies by Stilla (1994), Leung & Emmanuel (1995), and Stuckert & Reed (1994) also conclude that the effect of the shock must be taken into account.

The additional effects of curvature on the viscous instability was investigated by Seddougui & Bassom (1997) who considered the linear stability of hypersonic flow over a

cone. Their results conclude that in the presence of an attached shock, the effect of curvature is significant. Multiple unstable modes are possible, and modes which exist in the absence of a shock are now totally destroyed. In contrast to the planar case, the influence of the shock is always present and the spatial growth rates decrease as the shock moves away from the cone. The stability analysis of Duck & Hall (1989, 1999) for supersonic flow over axisymmetric bodies show that neutral curves bear no resemblance to those in the absence of curvature. Significant differences between hypersonic planar and conical boundary layers were also elucidated by the experiments of Stetson *et al.* (1991) and Wendt *et al.* (1995).

Several experimental studies have been conducted on conical models at hypersonic speeds (Stetson *et al.* 1983, Lachowicz *et al.* 1996, Bountin *et al.* 2000, Kimmel *et al.* 1996, Germain & Hornung 1997, Schneider 2004). These experiments confirm the results of linear stability theory, namely existence of multiple unstable regions, and the dominance of higher frequency second mode instability. In addition to the first and second mode disturbances identified by linear stability theory, subsequent stability experiments (reviewed in Stetson 1988) observed disturbance growth at higher frequencies, which were identified to be higher harmonics of the second mode disturbances. These were not observed until significant second mode growth had occurred. Stetson (1988) and Kimmel & Kendall (1991) attribute these findings to nonlinear wave propagation. These early experimental studies are reviewed in Stetson & Kimmel (1992). Nonlinear interactions involving the second mode were observed by Kimmel & Kendall (1991), Chokani (1999) and Shiplyuk *et al.* (2003). These investigations were conducted using bispectral analysis which involves statistical analysis of the disturbance spectrum at various downstream locations. Kimmel & Kendall (1991) and Chokani (1999) observed that harmonic resonance was the dominant nonlinear interaction, while Shiplyuk *et al.* (2003) observed that subharmonic resonance was the primary nonlinear interaction. Kimmel & Kendall (1991) and

Chokani (1999) measured naturally occuring disturbances while Shiplyuk *et al.* (2003) made measurements using artificial excitation of controlled disturbances. Subharmonic or parametric resonance had previously also been observed in the weakly nonlinear region of supersonic boundary layers by the investigations of Kosinov *et al.* (1994) on controlled disturbances. Investigations by Chokani (2005) on natural disturbances in a 'quiet' wind tunnel identified sum and difference interactions of the second Mack mode. These interactions led to the generation of the first and second harmonic of the second Mack mode. Further investigations following Shiplyuk *et al.* (2003) have been reported in Bountin *et al.* (2008) and Maslov *et al.* (2010). They observed nonlinear interaction of second mode waves with disturbances whose frequencies lie in the first-mode frequency range. They found that the second-mode subharmonic frequency belongs to the range of frequencies corresponding to the first-mode. These subharmonic interactions can be considered a secondary instability as it involves the interaction between a primary 2-D second-mode wave with a secondary 3-D first-mode wave.

These studies help us gain a better understanding of the role played by frequency interactions in the transition process. Further insight can be obtained from studies performing direct numerical simulations (DNS) of the complete Navier-Stokes equations. The spatial DNS study of Bestek & Eissler (1996) at Mach 4.8 was able to confirm the existence of multiple Mack modes. The presence of two further types of secondary instabilities namely, oblique breakdown and fundamental (K-type) breakdown were observed by the simulations of Husmeier & Fasel (2007). These studies matched the experimental conditions of Stetson & Kimmell (1992). The simulations of Laible & Fasel (2011) and Koevary *et al.* (2010) provide further proof of the relevance of these two transition scenarios in hypersonic boundary layers. Fundamental breakdown, first observed by Klebanoff (1962) in incompressible boundary layers, is characterised by the interaction of a 2-D finite-amplitude primary wave with a pair of symmetric small-amplitude oblique waves

at the same frequency (Koevary *et al.* 2010). Oblique breakdown, first observed by the simulations of Thumm *et al.* (1990) in a Mach 1.6 flow, is characterised by the interaction of a pair of oblique waves at the same frequency with identical but opposite spanwise wavenumbers. The initial stage of this process may be described by a wave-vortex triad consisting of the oblique waves and a streamwise vortex (Chang & Malik 1994). Evidence of the oblique transition scenario in hypersonic boundary layers were also provided by the simulations of Pruett & Chang (1995) corresponding to the experiments of Stetson *et al.* (1983). The state of the art in DNS studies on hypersonic boundary layer stability and transition is given in Wang & Zhong (2012). Much of the current knowledge of the physical mechanisms of hypersonic boundary layer stability and transition including transition control strategies is reviewed in Fedorov (2011)

Despite these studies, the physical mechanism of nonlinear breakdown of laminar hypersonic boundary layers is still not completely understood. There is still no consensus on the dominant mechanisms for the breakdown in high-speed flows. The second Mack mode is however thought to be dominant in these nonlinear processes and much scientific attention has been devoted to efforts that can damp this instability.

1.2 Laminar flow control

Laminar flow control deals with techniques based on linear stability analysis to extend the laminar region over the flying surface for the purposes of drag and surface heating reduction. Broadly such techniques may be classified as being passive, active or reactive. Passive techniques include concepts such as surface coatings, and shaping of the aerodynamic surface to induce favourable pressure gradients. They achieve their objective without the need for introducing any disturbances into the flow. Active flow control refer to techniques such as boundary layer suction and wall cooling. They utilize an open-loop control scheme to achieve their objective. Reactive techniques on the other hand rely on

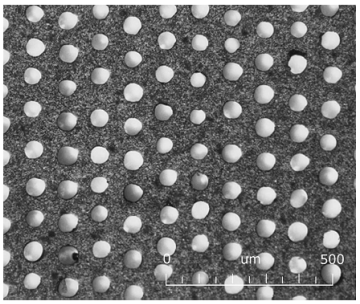

(a)

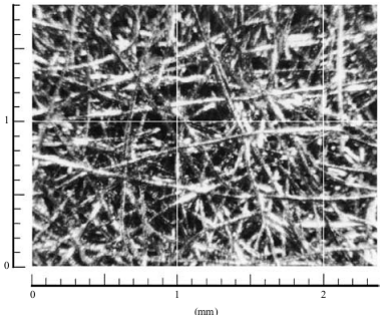

(b)

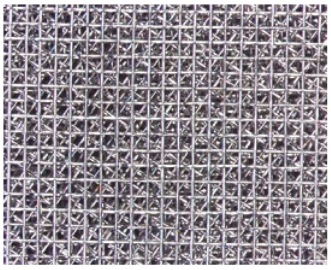

(c)

Figure 1.1: Magnified images depicting three different types of ultrasonically absorptive coatings. Shown are (a) stainless-steel perforated sheet, (b) felt-metal (stainless-steel fibres sintered on a sheet), (c) ten layers of stainless-steel wire mesh.

closed-loop control schemes and introduce disturbances that are counter-phase to the instability. Wall vibrations, periodic blowing/suction, and alternating heating and cooling fall under this category (Fedorov *et al.* 2001). Active control schemes have received the most widespread attention over the past fifty years and several concepts have been investigated in experiments for subsonic and supersonic flow conditions. In hypersonic flow conditions, active and reactive techniques have not found favour owing to technological complexities and harsh flight environments. Simple passive flow control techniques offer the best solution in this case. Linear stability analysis of Malmuth *et al.* (1998) and proof of concept experiments by Rasheed (2001) propose such a scheme using acoustically absorbing surfaces that damp the second mode instability. Some examples of porous coatings that have been experimentally investigated are shown in figure 1.1.

1.2.1 Passive porous walls for laminar flow control

Malmuth *et al.* (1998) proposed that a passive ultrasonically absorptive coating (UAC) may suppress the relatively high frequency fluctuations of the dominant second mode in hypersonic flow, while not tripping the boundary layer due to roughness effects. Thus the boundary layer could be stabilized by a passive disturbance energy extraction mechanism. This hypothesis was examined using a linear inviscid stability analysis. Using the WKB method, the authors formulated the boundary condition on an ultrasonically absorptive wall for second and higher modes. Subsequently Fedorov & Malmuth (2001) analysed the UAC effect using viscous linear stability theory and found that viscosity weakly affects the stabilization mechanism. They consider an UAC of regular microstructure, namely a relatively thin coating with cylindrical blind micro-holes and demonstrated a significant decrease in the second mode growth rates. The UAC concept was investigated experimentally by Rasheed *et al.* (2001) in a Mach 5 shock tunnel using a 5-deg half-angle sharp cone. The experimental results qualitatively confirmed the theoretical predictions

of Federov *et al.* (2001). To provide quantitative information, a series of stability experiments (Federov *et al.* 2003a,b) was conducted in a Mach 6 shock tunnel using a 7-deg half-angle sharp cone. Non-parallel stability analyses for 2-D and 3-D disturbances showed that the porous coating stabilizes the second mode and weakly destabilizes the first mode. Hot-wire measurements of artificially excited wave packets associated with the second mode provided good quantitative agreement with the theoretical predictions. Further experimental measurements of natural and artificially excited disturbances in the presence of UAC were reported in Maslov (2003) and support the stabilization effect on the second mode instability. Maslov (2003) also report on parametric calculations that investigate the effect of various factors such as wall cooling, gas rarefaction, and porous layer characteristics on the UAC performance. Numerical investigations of Wang & Zhong (2009, 2010, 2011a,b) for Mach 6 flow over a flat plate also showed that different types of porous coatings destabilized mode S in Mack's first mode region concurrent with second-mode stabilization. This finding was also observed by the two-dimensional DNS of Egorov *et al.* (2008).

Nonlinear aspects of hypersonic flow over porous coatings on a sharp cone are reported in Chokani *et al.* (2005) and Bountin *et al.* (2010) who investigated the nonlinear interaction of artificially excited second-mode disturbances using bispectral analysis. On a solid surface, disturbance amplitude spectra revealed that the second mode was dominant. The amplitude of the second mode also increased downstream and was always larger than the amplitude of the first mode at a given station. On the porous surface, the amplitude of the second mode was much smaller at all stations and showed only a small change in its amplitude in the downstream direction. However, in contrast to the solid surface, at a particular location on the porous surface, the amplitude of the first mode was larger than that of the second mode. This effect was more evident at the most upstream station. Bispectral measurements show that subharmonic and harmonic reso-

nance of the second mode are observed on the solid surface and are significantly modified on the porous surface. Harmonic resonance which is dominant on the solid surface was completely absent on the porous surface. Subharmonic resonance of the second mode increases in the downstream direction on solid surfaces, but was observed to be weak and to persist further downstream on the porous surface. These studies also observed subharmonic resonance of the first mode on porous surfaces that was not present on the solid surface. Chokani *et al.* (2005) state that this nonlinear interaction is too weak to adversely affect the performance of porous walls. Chokani *et al.* (2005) only considered measurements from the maximum mass-flow fluctuation location in the boundary layer while Bountin *et al.* (2010) took measurements throughout the entire thickness of the boundary layer. As the porous wall weakens resonant interactions in the maximum fluctuation layer, nonlinear interactions above and below the layer start to play a major role (Maslov *et al.* 2010). Nonlinear interaction between vortex (first-mode) waves and filling of the low-frequency vortex-mode spectrum in the presence of porous walls have also been found by the theoretical analysis of Gaponov & Terekhova (2009). They used a nonlinear interaction model in three-wave resonance systems for compressible flat-plate boundary layers. Gaponov *et al.* (2010) investigated experimentally and theoretically, the influence of porous coatings on the stability and transition of a supersonic (Mach 2) boundary layer over a flat plate. They found that the use of a porous coating destabilizes the disturbances in supersonic boundary layers (oblique first-mode type) and accelerates boundary-layer transition. Transition of a Mach 6 boundary layer over a flat plate with porous coating was also investigated by three-dimensional temporal DNS of De Tullio & Sandham (2010). Their calculations revealed that an oblique first-mode wave is the most amplified mode in the presence of the porous surface. This wave is slightly destabilized by the porous coating. With the oblique first mode excited, the flow becomes turbulent due to nonlinear interactions without the need for secondary instabilities (as is the case

over solid surfaces).

From these experimental and numerical investigations it is clear that the first Mack mode instability is affected by the presence of porous coatings. This instability can become destabilised by porous coatings and further research is warranted to ascertain whether they play a role in premature breakdown of the laminar flow.

1.2.2 Porous wall models and formulation

The first theoretical investigation of the linear stability of hypersonic flows to include the effects of an absorptive porous coating was reported in Fedorov & Malmuth (1996). They included the effects of the porous coating by introducing the wall boundary condition $v(0) = Ap(0)$, where v is the wall normal velocity perturbation, p is the pressure perturbation and A is a complex absorption coefficient. Their first investigation involved an inviscid stability analysis of flow over a flat plate following Mack (1975), whereby a compressible Rayleigh equation may be solved to obtain solutions for the pressure fluctuations. From this solution, an expression for the absorption coefficient A was obtained as a function of a reflection coefficient (defined as the ratio of reflected to incident wave on the surface). Numerical results for temporal stability indicated that decreasing the reflection coefficient (increasing absorption) tends to decrease the growth rate of the most unstable mode. Following Mack (1984), a viscous spatial stability analysis was also performed utilizing the same boundary condition. Results obtained showed the trend of strong stabilization of spatial growth rate at second mode frequency with increasing absorption. These analyses using a generic absorption coefficient successfully demonstrated that ultrasonic absorption could in principle damp second mode disturbances. It did not address the issue of how a specific surface could be constructed to perform this task, and how to obtain a boundary condition representative of a surface with specific microstructure. Theoretical work to develop appropriate boundary conditions was first done by Gaponov.

He studied the effects of porosity in subsonic (Gaponov 1971, 1975) and low supersonic flows (Gaponov 1977). In his studies, the transition process is dominated by the unstable growth of viscous Tollmien-Schlichting waves that correspond to first mode disturbances in hypersonic flows. The propagation of disturbances within the porous wall is independent of the type of disturbances, and following the analysis of Gaponov (1971, 1975, 1977), Federov & Malmuth (1996) developed a model appropriate for UACs. Fedorov & Malmuth (1996) utilized the theory of sound wave propagation in thin, long tubes. This problem is directly analogous to the problem of electrical transmission of current and voltage over long, lossy transmission lines, which have been studied extensively. In this case, the acoustic (or electric) field within the tube (transmission line) can be completely characterized by a propagation constant (Λ) and a characteristic impedance (Z_o). From the electrical analogy, these two parameters can in turn be expressed in terms of a series impedance (Z) and a shunt admittance (Y) per unit length of tube through the relations $Z_0 = \sqrt{\frac{Z}{Y}}$ and $\Lambda = \sqrt{ZY}$. Expressions for Z and Y may be derived from the flow physics of the problem. From the electrical analogy, input impedance Z_i, which is a ratio of the voltage to the current at the input of the transmission line, may be taken as analogous to the ratio of pressure to the average vertical velocity at the entrance of the pore. Thus it may be shown that $Z_i = \frac{p(0)}{v(0)} = -Z_o \coth(\Lambda h)$, where h is the non-dimensionalised depth of the pore. The absorption coefficient for a single pore may now be taken as being the reciprocal of the input impedance. This result is extended to the overall porous surface by averaging the vertical velocity over the surface area using the porosity n defined as $n = \frac{\text{Vol. of Pores}}{\text{Total Vol.}} = \frac{\pi r^2}{s^2}$, where r and s are the non-dimensionalised pore radius and pore spacing. Thus $A = \frac{n}{Z_i}$. A similar analysis following the work of Stinson & Champoux (1992) was also performed by Fedorov & Malmuth (1996) to develop the thermal admittance for use in a thermal boundary condition. They have however found that thermal perturbations had very little effect on the spatial growth rates and may be neglected.

A different approach to the electrical analogy is described in Attenborough (1982), Stinson (1991) and Stinson & Champoux (1992). They propose the use of a 'complex dynamic density', $\rho(\omega)$ and 'complex dynamic compressibility', $C(\omega)$, where ω is the angular frequency of disturbance propagation within the pore. The complex density is derived based on the linearized momentum equation for the propagation of a plane acoustic wave. It represents the effective increased density of the medium due to inertial and viscous effects. The complex compressibility is obtained from the solution of the continuity equation. The expressions for the characteristic impedance and the propagation constant now becomes $Z_0 = \sqrt{\rho C}$ and $\Lambda = \mathrm{i}\omega\sqrt{\frac{\rho}{C}}$. Such an approach allows a rational extension of these ideas to tubes of arbitrary cross-sections and allows the consideration of more general porous microstructures. The formulation of the porous wall model using this approach was reported by Kozlov *et al.* (2005) and will be adopted in this study.

The work described thus far has been based on the classical solutions of Navier-Stokes equations which describe acoustic waves travelling inside a long circular tube. Such results have been obtained under the assumption that the gas inside the pores is a continuum. However this assumption is not always valid. Rarefaction effects become important in flows within porous materials which have ultra-fine pores or operate at low ambient pressures such that the molecular mean free path λ_m becomes comparable to the characteristic length scale of the flow. Such cases may be modelled using the concept of slip-flows, in which the gas is treated as a continuum except in thin Knudsen layers on the wall. Molecular processes inside the Knudsen layer can affect the boundary condition. On a macroscopic level, rarefaction effects lead to slipping and temperature jumps on the interface boundary (Maslov 2003). For typical wind tunnel experimental conditions involving UACs, the Knudsen number $Kn = \lambda_m/r \sim 0.1$. Kozlov *et al.* (2005) analysed the problem of propagation of sound in isolated long pores of arbitrary cross-section, accounting for the rarefaction effects. Their analytical solutions for flat slits and pores of

circular or rectangular cross-sections have been utilized in this study to model the effect of various types of porous coatings. They consider each pore as an infinitely long tube of characteristic cross-sectional length scale L_p filled with gas of low density. Beyond the Knudsen layer and far from the tube ends, the disturbance generated by an infinitesimal oscillatory pressure gradient is governed by linearized momentum and energy equations. In these equations Λ is the dimensionless parameter, whose modulus characterizes the ratio of the characteristic length to the viscous and thermal boundary layer thickness on the tube walls. This quantity may be expressed as $\Lambda = \sqrt{\mathrm{i}\omega\rho_w L_p^2/\mu_w}$, where ρ_w, μ_w and ω are the density, viscosity and frequency respectively of the gas flow inside each pore. These equations may be solved for the amplitudes of gas particle velocity along the tube and temperature disturbance subject to a slip flow boundary condition characterised by a quantity B. This quantity B, is a function of the Knudsen number and depends on the laws governing the interaction between gas molecules and a solid surface. The solutions can then be expressed as a function $F(B, \Lambda)$. The acoustic properties of an isolated pore (dynamic density and dynamic compressibility) can be obtained by averaging of the gas particle velocity and temperature respectively over the pore cross-sectional area. Finally this allows us to obtain expressions for the characteristic impedance and propagation constants as mentioned previously and thus obtain an expression for the porous layer admittance. This approach can be used for porous walls that can be modelled as isolated long pores with well defined cross-sectional area. Unfortunately, there is no rigorous theory to predict these characteristics for porous materials of random microstructure. Since the majority of thermal protection systems used in hypersonic flight vehicles have have random microstructure, Fedorov *et. al* (2003b) investigated the use of fibrous absorbent material (felt metal) consisting of a network of stainless steel fibres. Allard & Champoux (1992) derived semi-empirical relations for the dynamic density and compressibility of such materials. These relations were used by Fedorov *et. al* (2003) to derive the admittance

for a random microstructure porous layer model.

1.3 Concluding remarks

In this chapter a brief survey of the literature concerning stability of hypersonic boundary layers and the use of passive porous coatings to damp the dominant instability modes in such flows has been presented. A background into the formulation of a theoretical model to describe these porous coatings was also given. The focus of this thesis is on utilising such porous models and performing a theoretical investigation into the linear and weakly nonlinear stability of hypersonic flows over a sharp cone.

In Chapter 2 the basic flow problem and porous wall models are described. The problem considered is the hypersonic flow over a sharp slender cone. The set of equations governing such flows are the compressible Navier-Stokes equations and energy equation in a spherical coordinate system. The basic flow is considered to be steady and axisymmetric. The problem is considered in the limit of large Reynolds number and Mach number. The incoming flow stream is parallel to the cone generatrix. A shock wave attached to the nose of the cone is present. At large Reynolds numbers, the viscous nature of the flow is only felt in a thin boundary layer close to the cone surface. Away from this boundary layer, inviscid Euler equations can be used to describe the flow between the cone surface and the shock. The flow must satisfy jump conditions at the shock. These jump conditions ensure that mass, momentum and energy are conserved across the shock. Close to the cone surface we consider the boundary layer problem. The flow here is coupled to the porous coating through a wall boundary condition. Various porous wall models are used to model the different types of porous coatings. The boundary layer equations bring back viscous effects into the problem. In the limit of large Reynolds number an interaction between the inviscid flow and the boundary layer occurs which may be described by dividing the boundary layer into three regions, collectively called the “triple-deck”. Asymptotic

solutions to the governing boundary layer equations can be sought in each region. The theoretical framework for the subsequent stability analysis is setup in Chapter 2. The stability problem is described in Chapter 3. In Chapter 4 the results of the linear and weakly nonlinear analysis is presented. A discussion of these results with reference to published experimental and numerical results is given in Chapter 5. Finally in Chapter 6, the conclusions of this study and possible avenues for further research are given.

Chapter 2

Formulation

The aim of the present investigation is to examine the stability of hypersonic flow over a cone with porous walls where the attached shock and curvature are taken into account. Porous wall models are described in Section 2.3. In Section 2.1, the inviscid flow over the cone is described. The shock is a discontinuity that occurs in the normal velocity of the flow. The conditions satisfied at the shock by a disturbance to this basic flow are described in Section 2.2. The weakly nonlinear stability of the basic flow is then investigated using the triple-deck formulation in Section 2.4.

2.1 Base Flow

The derivation of the basic flow follows Seddougui & Bassom (1997) and is described here. The flow of a compressible, viscous gas over a sharp cone with porous boundary, of semi-angle θ_c is considered at hypersonic speeds, with magnitude U_0 parallel to its axis. The attached shock makes an angle θ_s with the cone. The situation is illustrated in figure 2.1. The main dimensional quantities are depicted in figure 2.2. Spherical polar coordinates (x, θ, ϕ) are used to describe the flow. Here ϕ denotes the azimuthal angle. The radial distance x has been non-dimensionalised with respect to L^*, the distance from the tip of the cone to the location under consideration. Away from the surface of the cone,

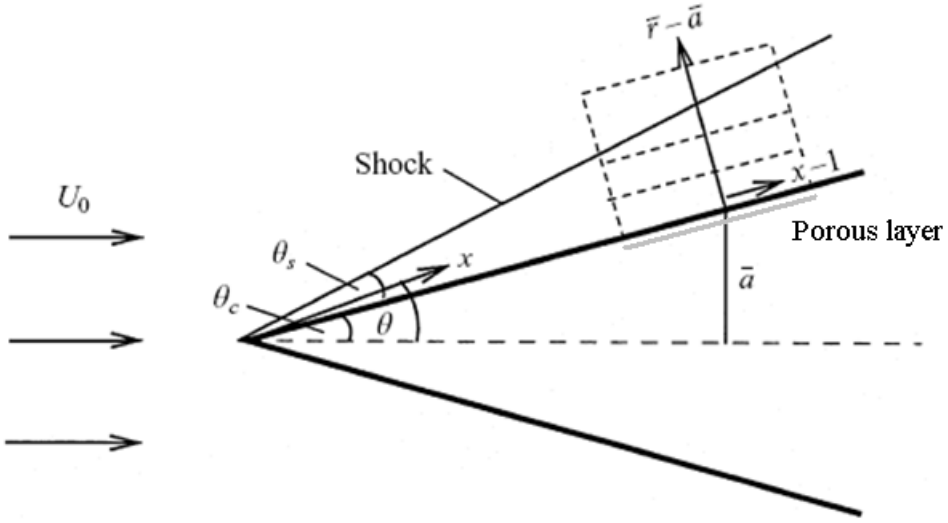

Figure 2.1: Geometry of the cone and the attached shock.

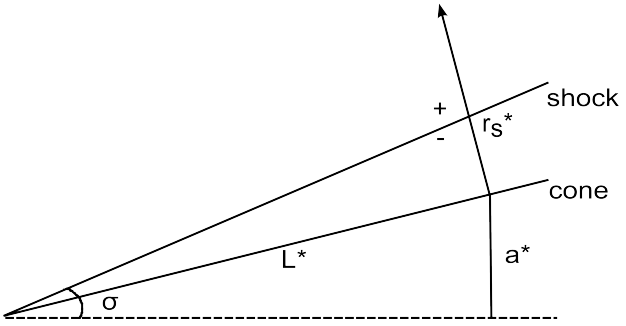

Figure 2.2: Geometry depicting main dimensional quantities.

viscous effects are neglected and the fluid velocities $(\overline{u}, \overline{v}, \overline{w})$, pressure $(\overline{p})$ and density $(\overline{\rho})$ satisfy the compressible continuity, Euler and energy equations.

$$\begin{aligned}
&\frac{\partial \overline{\rho}}{\partial t} + \frac{1}{x^2 \sin\theta}\left[\frac{\partial}{\partial x}\left(x^2 \sin\theta \overline{\rho}\,\overline{u}\right) + \frac{\partial}{\partial \theta}\left(x \sin\theta \overline{\rho}\,\overline{v}\right) + \frac{\partial}{\partial \phi}\left(x \overline{\rho}\,\overline{w}\right)\right] = 0,\\
&\overline{\rho}\frac{D\overline{u}}{Dt} - \frac{\overline{\rho}\,\overline{v}^2}{x} - \frac{\overline{\rho}\,\overline{w}^2}{x} = -\frac{\partial \overline{p}}{\partial x},\\
&\overline{\rho}\frac{D\overline{v}}{Dt} + \frac{\overline{\rho}\,\overline{u}\,\overline{v}}{x} - \frac{\overline{\rho}\,\overline{w}^2 \cos\theta}{x \sin\theta} = -\frac{1}{x}\frac{\partial \overline{p}}{\partial \theta},\\
&\overline{\rho}\frac{D\overline{w}}{Dt} + \frac{\overline{\rho}\,\overline{u}\,\overline{w}}{x} - \frac{\overline{\rho}\,\overline{v}\,\overline{w}\cos\theta}{x \sin\theta} = -\frac{1}{x \sin\theta}\frac{\partial \overline{p}}{\partial \phi},\\
&\overline{\rho}\gamma\frac{D}{Dt}\left(\frac{\overline{p}}{\overline{\rho}}\right) = (\gamma - 1)\frac{D\overline{p}}{Dt},
\end{aligned} \tag{2.1.1}$$

where

$$\frac{D}{Dt} \equiv \frac{\partial}{\partial t} + \overline{u}\frac{\partial}{\partial x} + \frac{\overline{v}}{x}\frac{\partial}{\partial \theta} + \frac{\overline{w}}{x \sin\theta}\frac{\partial}{\partial \phi},$$

and $\gamma = \frac{c_p}{c_v}$ is the ratio of specific heats of the gas. We consider the steady, non-dimensional version of these equations. The velocities are non-dimensionalised with respect to U_-, the magnitude of fluid velocity just behind the shock. The time, pressure and density are non-dimensionalised with respect to L^*/U_-, $\rho_- U_-^2$, and ρ_-, respectively, with ρ_- being the density behind the shock. Finally the temperature is non-dimensionalised with respect to T_-, the temperature just behind the shock. We define $\varepsilon \equiv \frac{\rho_+}{\rho_-}$ to be the ratio of gas densities just ahead of the shock and just behind it and take it to be sufficiently small to obtain a steady constant density solution. Such types of solutions were first obtained by Hayes & Probstein (1966). The assumption of constant density is exact in the case of hypersonic flow over a wedge, and is a suitable approximation for cases where pressure changes in the flow field are small as can be expected for flow over a slender cone. This assumption implies that the shock layer is thin, the density and viscosity are constant in the region between the shock and the surface of the cone and that the shock inclination

angle $\sigma = \theta_c + \theta_s$ is a constant (i.e., oblique shock).

Since the flow behind a straight shock is isentropic, the flow in the region between the shock and cone is irrotational. Thus for an axisymmetric conical flow the velocity potential Φ satisfies Laplace's equation in spherical coordinates. The general axisymmetric solution of Laplace's equation may be obtained using the method of separation of variables in terms of Legendre polynomials. Following Seddougui & Bassom (1997) we can write

$$\Phi = x\frac{U_0}{U_-}\left[AP_1(z) + BQ_1(z)\right], \tag{2.1.2a}$$

where P_1 and Q_1 are the Legendre functions

$$P_1(z) = z,$$
$$Q_1(z) = \frac{z}{2}\ln\left(\frac{1+z}{z}\right) - 1.$$

Here $z \equiv \cos\theta$ and $(\overline{u}, \overline{v}) = (\partial\Phi/\partial x, (1/x)\partial\Phi/\partial\theta)$. A and B are constants that can be determined from the conditions at the shock whose location is defined by $z_s = \cos\sigma$. By considering conservation principles at an oblique shock we can show that the radial component of velocity is constant across the shock and given by $\frac{U_0}{U_-}z_s$ and that the polar component of velocity is normal to the shock and satisfies $v_+ = v_-/\varepsilon = -z\frac{U_0}{U_-}\left(1 - z_s^2\right)^{1/2}$. These conditions can be used to calculate A and B. Thus the basic flow solutions valid

in the region between the shock and the cone surface may be given as

$$\overline{u} = \frac{U_0}{U_-}\left(AP_1(z) + BQ_1(z)\right), \tag{2.1.2b}$$

$$\overline{v} = -\frac{U_0}{U_-}\left(1 - z_s^2\right)^{1/2}\left(A + B\left(Q_0(z) + \frac{z}{1-z^2}\right)\right), \tag{2.1.2c}$$

$$\left(\frac{U_0}{U_-}\right)^2 \overline{p} = \frac{1}{2\gamma}\varepsilon(1+\varepsilon)(1-z_s^2) - \left[ABQ_0(z) + \frac{B^2}{2}\left(Q_0^2(z) + \frac{1}{1-z^2}\right) + \frac{A^2}{2} - \frac{\varepsilon}{2}(1-z^2) - \frac{z_s^2}{2}\right], \tag{2.1.2d}$$

where $Q_0(z) = \frac{1}{2}\ln\left(\frac{1+z}{1-z}\right)$. Using conservation principles at the shock and the perfect gas relations, Hayes & Probstein (2004) show that the density ratio may be written as

$$\varepsilon = \left(\frac{\gamma-1}{\gamma+1}\right)\left(1 + \frac{2}{(\gamma-1)M_+^2\sin^2\sigma}\right), \tag{2.1.2e}$$

where M_+ is the Mach number just ahead of the shock. Expressions for the remaining flow quantities (pressure, velocity, Mach number) behind the shock are given in Seddougui & Bassom (1997) in terms of the density ratio and shock inclination angle. We mention a few important results here.

$$\tan\theta_s = \varepsilon\tan\sigma, \tag{2.1.2f}$$

$$M_-^2 = \frac{M_+^2\cos^2\sigma(1+\varepsilon^2\tan^2\sigma)^{1/2}}{1 + \frac{1}{2}(\gamma-1)(1-\varepsilon^2)M_+^2\sin^2\sigma}, \tag{2.1.2g}$$

$$M_+^2 = \frac{M_-^2}{\cos^2\sigma(1+\varepsilon^2\tan^2\sigma) - \frac{1}{2}(\gamma-1)(1-\varepsilon^2)M_-^2\sin^2\sigma}. \tag{2.1.2h}$$

The foregoing calculations allows us to completely describe the basic flow in the region between the shock and the cone provided the location of the shock is known a priori. A significant feature of this solution is that the velocities are not uniform in this region, in contrast to the case for flow over a wedge. A typical streamline for flow past a cone

undergoes an outward deflection when it crosses the shock. It then undergoes further gradual deflection until it asymptotes to the cone body. Thus the total deflection of the flow through the shock is equal to the cone angle θ_c. This situation is depicted in figure 2.3. The problem that remains is to determine the location of the shock. In the case of flow

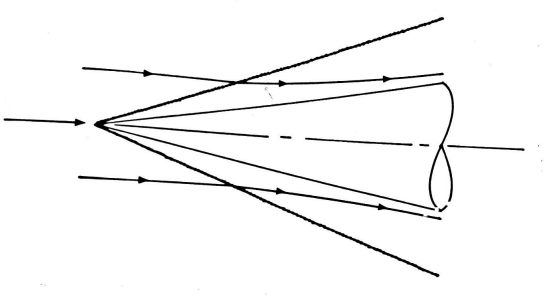

Figure 2.3: Typical streamline for compressible flow past a cone. (Taken from Rasmussen 1994.)

over a wedge (oblique shock) this can be obtained from geometrical considerations. For the problem of flow over a cone we turn to Rasmussen (1994) who considers the "exact" solution of the problem of supersonic flow over a cone as given by the Taylor-Maccoll equation (Taylor & Maccoll 1933). This is an ordinary differential equation whose solution is called exact because it can be made once and then tabulated, even though it must be done numerically (Rasmussen 1994). Rasmussen (1994) then obtains an approximate analytical solution of this equation in the hypersonic flow regime. From this solution an explicit similarity expression for σ as a function of θ_c, $M_+ = M_\infty$ and γ can be found. For an axisymmetric conical flow recall that all flow variables are functions of the polar angle θ only. By considering the axisymmetric form of (2.1.1) Rasmussen (1994) shows that these equations may be reduced to form a single second-order ordinary differential

equation for $\overline{u}(\theta)$

$$\left(1-\frac{\overline{v}^2}{\check{a}^2}\right)\frac{d^2\overline{u}}{d\theta^2}+\cot\theta\frac{d\overline{u}}{d\theta}+\left(2-\frac{\overline{v}^2}{\check{a}^2}\right)\overline{u}=0. \tag{2.1.3a}$$

To obtain this equation we use $\overline{v}=d\overline{u}/d\theta$ which is obtained from requiring that the vorticity $\Omega=\frac{1}{x}\left(\overline{v}-\frac{d\overline{u}}{d\theta}\right)=0$ and $\check{a}^2$, is the square of the local speed of sound and may be expressed in terms of $\overline{u}$. Following Rasmussen (1994) we can seek an approximate analytical solution to (2.1.3a). This approach is equivalent to that followed by Hayes & Probstein who also solved the axisymmetric form of (2.1.1) for the velocity potential. We turn to the continuity equation in (2.1.1) and carrying out the x derivatives for a steady axisymmetric conical flow we can obtain

$$\frac{d\overline{v}}{d\theta}+\cot\theta\overline{v}+2\overline{u}+\frac{\overline{v}}{\overline{\rho}}\frac{d\overline{\rho}}{d\theta}=0. \tag{2.1.3b}$$

We now set $\overline{v}\frac{d\overline{\rho}}{d\theta}=0$ in the above equation. This is correct on the cone surface where the polar component of velocity $\overline{v}=0$. Away from the surface this can be interpreted as $\frac{d\rho}{d\theta}$ being small. We now are in effect making the constant density assumption for this flow. (2.1.3b) thus becomes

$$\frac{d\overline{u}^2}{d^2\theta}+\cot\theta\frac{d\overline{u}}{d\theta}+2\overline{u}=0. \tag{2.1.3c}$$

We can also note that the same equation may be obtained from (2.1.3a) by setting $\overline{v}^2/\check{a}^2=0$, as a linear approximation of the exact governing equation. Since $\overline{u}=\cos\theta$ satisfies (2.1.3c) we can obtain the solution using the reduction of order method by seeking a solution of the form $\overline{u}(\theta)=\check{U}(\theta)\cos\theta$. Thus the solution that satisfies the boundary

conditions at the shock may be obtained as

$$\frac{\overline{u}(\theta)}{U_0} = \cos\theta - (1-\varepsilon)\cos\sigma\sin^2\sigma\left[\frac{\cos\theta}{\cos\sigma} - 1 + \cos\theta\ln\left(\frac{\tan(\sigma/2)}{\tan(\theta/2)}\right)\right], \tag{2.1.3d}$$

$$\frac{\overline{v}(\theta)}{U_0} = -\sin\theta + (1-\varepsilon)\cos\beta\sin^2\beta\left[\frac{\sin\theta}{\cos\beta} + \cot\theta + \sin\theta\ln\left(\frac{\tan(\beta/2)}{\tan(\theta/2)}\right)\right]. \tag{2.1.3e}$$

For hypersonic flow over slender bodies we can define a similarity parameter $K_\sigma = M_\infty\sigma$, such that in the limits $\sigma \to 0$, $\theta_c \to 0$, and $M_\infty \to \infty$, K_σ remains finite. This is called the "hypersonic small-disturbance approximation". On the cone surface $\overline{v}(\theta_c) = 0$. Keeping only terms of order θ in (2.1.3e) we get

$$-\theta_c\left[1 - (1-\varepsilon)\frac{\sigma^2}{\theta_c^2}\right] = 0. \tag{2.1.3f}$$

By using (2.1.2e) in the above equation we can obtain the following result

$$\frac{\sigma}{\theta_c} = \sqrt{\frac{\gamma+1}{2} + \frac{1}{K_c^2}}, \tag{2.1.3g}$$

where $K_c \sim M_\infty\theta_c$. Note that since $K_c \sim O(1)$, we get $\theta_s \sim \theta_c$. Thus, we are now able to prescribe the shock angle for a given cone angle and free-stream Mach number. Good agreement between this approximate theory and the exact weak-shock solution for cones is shown in Rasmussen (1994).

The basic flow solutions (2.1.2b) are not valid close to the surface of the cone, so we introduce a boundary layer in this region. We define the Reynolds number as $Re = \frac{\rho_- U_- L^*}{\mu_-}$ and take it to be large. Since we are consider flow over a slender cone we take θ_c to be small. This implies that θ_s will be also be small. The flow here satisfies the compressible continuity, Navier-Stokes and energy equations in terms of non-dimensional coordinates $(x, \overline{r}, \phi)$ and Mach number M, just behind the shock. x and ϕ are as defined previously and $L^*\overline{r}$ is the normal direction to the cone surface where $\overline{r} = \overline{a}$ on the cone generatrix.

The corresponding non-dimensional flow velocities, pressure, temperature and density are (u, v, w), p, T, and ρ, respectively. Thus, neglecting terms of $O(\theta_c)$, the equations satisfied by these quantities are

$$
\begin{aligned}
\frac{\partial \rho}{\partial t} + \frac{\partial}{\partial x}(\rho u) + \frac{1}{\overline{r}}\frac{\partial}{\partial \overline{r}}(\overline{r}\rho v) + \frac{1}{\overline{r}}\frac{\partial}{\partial \phi}(\rho w) &= 0, \\
\rho\frac{Du}{Dt} =& -\frac{\partial p}{\partial x} + \frac{1}{Re}\left\{\frac{\partial}{\partial x}\left[2\mu\frac{\partial u}{\partial x} + \left(\mu' - \frac{2\mu}{3}\right)\nabla\cdot\mathbf{u}\right]\right. \\
&\left. + \frac{1}{\overline{r}}\frac{\partial}{\partial \overline{r}}\left[\mu\overline{r}\left(\frac{\partial v}{\partial x} + \frac{\partial u}{\partial \overline{r}}\right)\right] + \frac{1}{\overline{r}}\frac{\partial}{\partial \phi}\left[\mu\left(\frac{1}{\overline{r}}\frac{\partial u}{\partial \phi} + \frac{\partial w}{\partial x}\right)\right]\right\}, \\
\rho\left(\frac{Dv}{Dt} - \frac{w^2}{\overline{r}}\right) =& -\frac{\partial p}{\partial \overline{r}} + \frac{1}{Re}\left\{\frac{\partial}{\partial \overline{r}}\left[2\mu\frac{\partial v}{\partial \overline{r}} + \left(\mu' - \frac{2\mu}{3}\right)\nabla\cdot\mathbf{u}\right]\right. \\
&+ \frac{1}{\overline{r}}\frac{\partial}{\partial \phi}\left[\mu\left(\frac{1}{\overline{r}}\frac{\partial v}{\partial \phi} + \frac{\partial w}{\partial \overline{r}} - \frac{w}{\overline{r}}\right)\right] \\
&\left. + \frac{\partial}{\partial x}\left[\mu\left(\frac{\partial v}{\partial x} + \frac{\partial u}{\partial \overline{r}}\right)\right] + \frac{2\mu}{\overline{r}}\left(\frac{\partial v}{\partial \overline{r}} - \frac{1}{\overline{r}}\frac{\partial w}{\partial \phi} - \frac{v}{\overline{r}}\right)\right\}, \qquad (2.1.4) \\
\rho\left(\frac{Dw}{Dt} + \frac{vw}{\overline{r}}\right) =& -\frac{1}{\overline{r}}\frac{\partial p}{\partial \phi} + \frac{1}{Re}\left\{\frac{1}{\overline{r}}\frac{\partial}{\partial \phi}\left[\frac{2\mu}{\overline{r}}\frac{\partial w}{\partial \phi} + \left(\mu' - \frac{2\mu}{3}\right)\nabla\cdot\mathbf{u}\right]\right. \\
&+ \frac{\partial}{\partial \overline{r}}\left[\mu\left(\frac{1}{\overline{r}}\frac{\partial v}{\partial \phi} + \frac{\partial w}{\partial \overline{r}} - \frac{w}{\overline{r}}\right)\right] \\
&\left. + \frac{\partial}{\partial x}\left[\mu\left(\frac{\partial w}{\partial x} + \frac{1}{\overline{r}}\frac{\partial u}{\partial \phi}\right)\right] + \frac{2\mu}{\overline{r}}\left(\frac{\partial w}{\partial \overline{r}} + \frac{1}{\overline{r}}\frac{\partial v}{\partial \phi} - \frac{w}{\overline{r}}\right)\right\}, \\
\rho\frac{DT}{Dt} =& (\gamma-1)M^2\frac{Dp}{Dt} + \frac{1}{PrRe}\left[\frac{\partial}{\partial x}\left(\mu\frac{\partial T}{\partial x}\right) + \frac{1}{\overline{r}}\frac{\partial}{\partial \overline{r}}\left(\overline{r}\mu\frac{\partial T}{\partial \overline{r}}\right)\right. \\
&\left. + \frac{1}{\overline{r}^2}\frac{\partial}{\partial \phi}\left(\mu\frac{\partial T}{\partial \phi}\right)\right] + \frac{(\gamma-1)M^2}{Re}\Phi_T.
\end{aligned}
$$

Here Pr is the Prandtl number, the viscosities μ and μ' have been non-dimensionalised

with respect to μ_- and

$$\frac{D}{Dt} \equiv \frac{\partial}{\partial t} + u\frac{\partial}{\partial x} + v\frac{\partial}{\partial \overline{r}} + \frac{w}{\overline{r}}\frac{\partial}{\partial \phi},$$

$$\nabla \cdot \mathbf{u} \equiv \frac{\partial u}{\partial x} + \frac{1}{\overline{r}}\frac{\partial}{\partial \overline{r}}(\overline{r}v) + \frac{1}{\overline{r}}\frac{\partial w}{\partial \phi},$$

$$\Phi_T \equiv 2\mu\left[\left(\frac{\partial u}{\partial x}\right)^2 + \left(\frac{\partial v}{\partial \overline{r}}\right)^2 + \left(\frac{1}{\overline{r}}\frac{\partial w}{\partial \phi} + \frac{v}{\overline{r}}\right)^2 + \frac{1}{2}\left\{\left(\frac{\partial u}{\partial \phi} + \frac{\partial w}{\partial x}\right)^2 + \left(\frac{\partial u}{\partial \overline{r}} + \frac{\partial v}{\partial x}\right)^2 + \left(\frac{1}{\overline{r}}\frac{\partial v}{\partial \phi} + \frac{\partial w}{\partial \overline{r}} - \frac{w}{\overline{r}}\right)^2\right\}\right] + \left(\mu' - \frac{2\mu}{3}\right)(\nabla \cdot \mathbf{u})^2 .$$

The non-dimensional temperature and viscosity on the cone surface is denoted by T_w and μ_w. The boundary conditions are imposed at the cone surface where the flow is coupled to the porous layer and at the shock where jump conditions need to be satisfied. Following Seddougui & Bassom (1997) the only restriction imposed on the temperature boundary condition is $T_w >> 1$, which is violated only for situations involving strong cooling on the cone wall. Usually the wall temperature is taken to be $T_w = T_b T_r$, where T_r is the adiabatic wall temperature given by $T_r = 1 + \sqrt{Pr}\frac{\gamma-1}{2}M^2$. Thus unless the constant T_b is very small, T_w will be of $O((\gamma-1)M^2)$ for both adiabatic walls ($T_b = 1$) or isothermal walls. The analysis is unaffected by the particular choice of temperature-viscosity law. The choice only affects bounds placed on various parameters of the problem (see Section 2.4). Sutherland's viscosity law ($\mu_w \sim (1+\overline{C})T_w^{1/2}$) is used henceforth.

2.2 Shock conditions

The conditions to be satisfied at the shock by a disturbance to the basic flow must be now considered. They are derived in detail by Seddougui (1994). The main ideas are summarised here. We consider a shock at $\theta = f(\overline{r}, \phi, t)$ and write $\overline{\theta} = f(\overline{r}, \phi, t) - \theta$. Under this transformation the governing flow equations may be transformed into jump conditions at the shock. The basic flow solution (2.1.2b) satisfies the jump conditions at

$\overline{\theta} = 0$. We assume there is a small disturbance just beneath the shock such that we can write for example $p = P + \tilde{p}$, where P represents the known form of basic flow just beneath the shock. The disturbance cannot propagate through the shock so just above the shock we can write for example $p = \overline{P}$, where $\overline{P}$ represents the basic flow just above the shock. The shock will be perturbed from $\theta = \sigma$ and so we write $f = \sigma + \tilde{f}$. We restrict ourselves to the linearised shock conditions which are obtained by substituting the disturbance equations into the jump equations and neglecting non-linear terms. Seddougui (1994) showed that although the basic flow is not uniform in the regions above and below the shock, the jump conditions may be evaluated at the undisturbed shock location $\theta = \sigma$ instead of $\theta = \sigma + \tilde{f}$.

The scales chosen in this problem are appropriate for acoustic (pressure) waves. As shown by Cowley & Hall (1990) whenever an acoustic wave is incident on a shock, entropy and vorticity waves are generated in addition to a reflected/transmitted acoustic wave. The entropy/vorticity waves propagate in the direction of the mean flow with wavelengths shorter than the acoustic wavelength. In our analysis we focus on the form of these waves just below the shock and write all perturbations proportional to $\exp[\mathrm{i}(\alpha\overline{r} + \nu(\theta - \sigma) + n\phi - \Omega t)]$, where α and n are wavenumbers of the disturbance in the radial and azimuthal directions, Ω is the frequency of the disturbance and ν, n are integers. We let the disturbance be a linear combination of acoustic, vorticity and entropy waves and denote the pressure amplitudes of the incident and reflected acoustic waves by p_1 and p_2 and their respective θ-wavenumbers by ν_1 and ν_2. Substitution of this form of disturbance into the jump conditions at $\theta = \sigma$ will yield an expression involving p_1 and p_2. The limiting process appropriate to the scalings chosen yield, to leading order, the required condition to be satisfied at the shock as $p_1 + p_2 = 0$.

2.3 Porous wall models

We will present results corresponding to porous surfaces used in previous experimental investigations (Fedorov *et al.* 2003, Maslov 2003, Lukashevich *et al.* 2010). In all cases the porous layer admittance $\overline{A_y}$ can be expressed in the form

$$\overline{A_y} = -(\phi_0/Z_0)\tanh(\Lambda h), \tag{2.3.1}$$

where ϕ_0 is the porosity and h is the thickness of the porous layer. The porous layer parameters are non-dimensionalised with respect to the boundary-layer displacement thickness δ^*. Z_0 and Λ are the characteristic impedance and propagation constant of an isolated pore, respectively. Fedorov *et al.* (2006) give the following expressions for the porous layer characteristics:

$$Z_0 = \frac{\sqrt{\rho_D/C_D}}{M\sqrt{T_w}} \quad \text{and} \quad \Lambda = \frac{\mathrm{i}\omega M}{\sqrt{T_w}}\sqrt{\rho_D C_D}, \tag{2.3.2}$$

where ω is the frequency of disturbance propagation in the pore. These are functions of the complex dynamic density ρ_D and complex dynamic compressibility C_D. The precise definitions of these quantities depends on the structure of the porous wall and are given below for the cases investigated here. The wall boundary condition, in all cases, is then given by

$$v = \overline{A_y}\,(p - p_-)\,, \tag{2.3.3}$$

where $p_- = \gamma^{-1}M^{-2}$.

2.3.1 Regular microstructure

Following Fedorov *et al.* (2001, 2006) we consider the porous layer on the cone surface to be a sheet of thickness h^* perforated with cylindrical blind holes of radius r_p^* and equal

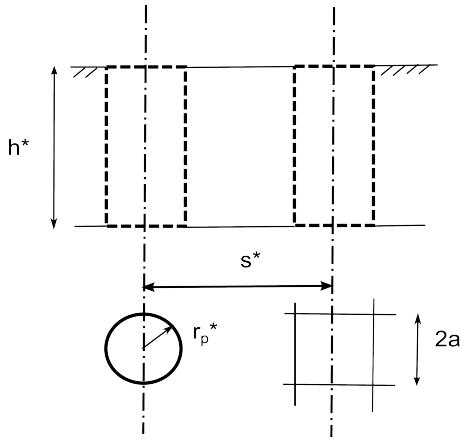

Figure 2.4: Schematic of a typical regular microstructure model. Cylindrical pores of thickness h^*, spaced s^* apart may either have a circular cross-section (2.3.4) or a square cross-section (2.3.6).

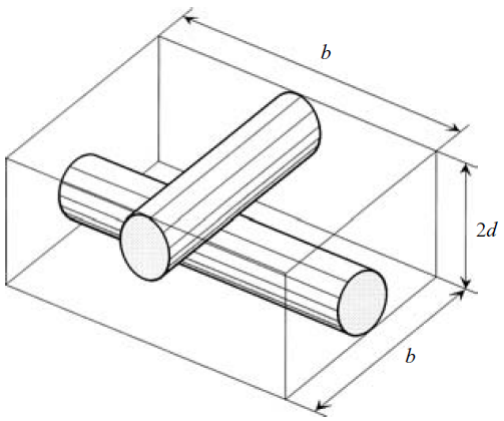

Figure 2.5: Schematic of the elementary cell of the random microstructure model (2.3.9), taken from Fedorov *et al.* 2003b. Here d is the diameter of an individual fibre and b is the width of a typical cell. These quantities can be used to obtain a typical pore radius $r_p = 4d/(1 + \pi/4b)$ and porosity $\phi_0 = 1 - \pi d/4b$ (Fedorov *et al.* 2003b).

spacing $s^* = r_p^*\sqrt{\pi/\phi_0}$ (see figure 2.4). This model takes into account gas rarefaction effects. We have

$$\left.\begin{aligned} &\rho_D = \frac{1}{1-F(B_\nu,\zeta)}, \quad C_D = 1+(\gamma-1)F(B_E,\zeta\sqrt{Pr}), \\ &F(B_\nu,\zeta) = \frac{G(\zeta)}{1-0.5B_\nu\zeta^2G(\zeta)}, \quad F(B_E,\zeta\sqrt{Pr}) = \frac{G(\zeta\sqrt{Pr})}{1-0.5B_E(\zeta\sqrt{Pr})^2G(\zeta\sqrt{Pr})}, \end{aligned}\right\} \tag{2.3.4}$$

where

$$B_\nu = (2\alpha_\nu^{-1}-1)Kn, \quad B_E = [2\gamma(2\alpha_E^{-1}-1)/((\gamma+1)Pr)]Kn, \quad G(\zeta) = \frac{2J_1(\zeta)}{\zeta J_0(\zeta)}, \tag{2.3.5}$$

with $\zeta = r_p\sqrt{\mathrm{i}\omega\rho_w R/\mu_w}$. Here $J_{0,1}$ are Bessel functions of the first kind, α_ν and α_E are molecular accommodation coefficients, Kn is the Knudsen number and R is the Reynolds number based on the boundary-layer displacement thickness of the gas flow.

2.3.2 Mesh microstructure

Following Lukashevich *et al.* (2010) we consider the porous coating on the cone surface to comprise of several layers of stainless steel wire mesh as shown in figure 1.1c. A similar model to the one described in Section 2.3.1 for a regular microstructure is employed. Following Kozlov *et al.* (2005) we have different expressions for the complex dynamic density and compressibility. Hence we can obtain the following expressions for the porous layer characteristics for a square mesh microstructure:

$$\left.\begin{aligned} &\rho_D = 1/(1-F(\zeta)), \qquad C_D = 1+(\gamma-1)F(\widetilde{\zeta}), \\ &F(\zeta) = 1+\zeta^2\sum_{m=0}^{\infty}\left[\frac{2}{\gamma_m^2\beta_m^2}\Big(1-\frac{\tanh(\beta_m)}{\beta_m}\Big)\right], \\ &F(\widetilde{\zeta}) = 1+\widetilde{\zeta}^2\sum_{m=0}^{\infty}\left[\frac{2}{\gamma_m^2\widetilde{\beta_m}^2}\Big(1-\frac{\tanh(\widetilde{\beta_m})}{\widetilde{\beta_m}}\Big)\right], \end{aligned}\right\} \tag{2.3.6}$$

where

$$\gamma_m = \pi\left(m + \frac{1}{2}\right), \qquad \beta_m = \sqrt{\gamma_m^2 - \zeta^2}, \qquad \widetilde{\beta_m} = \sqrt{\gamma_m^2 - \widetilde{\zeta}^2}, \tag{2.3.7}$$

$$\zeta = \sqrt{\frac{\mathrm{i}\omega\rho_w\widetilde{a}^2}{\mu_w}R}, \quad \text{and} \quad \widetilde{\zeta} = \sqrt{Pr}\zeta, \tag{2.3.8}$$

with $\widetilde{a}$ being the half-pore width (see figure 2.4). Following Lukashevich *et al.* (2010) gas rarefaction effects are neglected in this model.

2.3.3 Random microstructure

Following Fedorov *et al.* (2003) we consider the porous layer on the cone surface to have a random microstructure. Physically this type of coating represents felt metals that comprise of a random network of cylindrical fibres. A similar model to the one used for the regular microstructure is employed by modelling the microstructure based on elementary cells as shown in figure 2.5. We have different expressions for the complex dynamic density and compressibility. Fedorov *et al.* (2003b) give the following expressions for the porous layer characteristics for flow over a felt metal microstructure:

$$\left.\begin{aligned} &\rho_D = a_\infty\Big(1 + \frac{g(\lambda_1)}{\lambda_1}\Big), \quad C_D = \gamma - \frac{\gamma - 1}{1 + \frac{g(\lambda_2)}{\lambda_2}}, \\ &g(\lambda_i) = \sqrt{1 + \frac{4a_\infty\mu_w^*\lambda_i}{\sigma^*\phi_0 r_p^{*2}}}, \quad \lambda_1 = \frac{\mathrm{i}a_\infty\rho_w^*\omega^*}{\phi_0\sigma^*}, \quad \lambda_2 = 4Pr\lambda_1, \end{aligned}\right\} \tag{2.3.9}$$

with

$$r_p^* = \frac{\pi d^*}{(1-\phi_0)(2-\phi_0)}. \tag{2.3.10}$$

Here μ_w^*, ρ_w^*, and ω^* are dimensional wall viscosity, wall density and frequency, respectively. d^* is the fibre diameter and σ^* is the flow resistivity whose value is chosen to fit the experimental data for flow over the felt metal. The tortuosity a_∞ is taken to be unity. Following Fedorov *et al.* (2003) gas rarefaction effects are neglected.

2.3.4 Porous layer parameters and flow conditions

We now consider the variation of the magnitude of the porous layer admittance $\overline{A_y}$ on two main parameters: characteristic pore-size L_p and porosity ϕ_0. In figure 2.6a we see the variation of $|\overline{A_y}|$ with L_p for the regular microstructure model (2.3.4) and mesh microstructure model (2.3.6). Here L_p represents either the pore radius r_p^* or half-pore width $\tilde{a}^*$, the porosity ϕ_0 is fixed and the pores are assumed to be infinitely long ($h^* >> r_p^*$). We can see that an increase in pore-size leads to a corresponding increase in the magnitude of the porous wall admittance for both models. Figure 2.6b shows the corresponding results for the random microstructure model (2.3.9). Here L_p represents the typical pore radius r_p^* (c.f. figure 2.5). We see that the variation of the porous wall admittance with pore-size is small. By comparing figures 2.6a and 2.6b we see that for a given pore-size and porosity the random microstructure model has the highest magnitude of admittance, followed by the regular model and then the mesh model. In figure 2.7 we show the variation of $|\overline{A_y}|$ with porosity ϕ_0 for a fixed pore-size. We see that an increase in porosity leads to a corresponding increase in the magnitude of the porous wall admittance for all three models. Again we note that for a given porosity and pore-size the random microstructure model has the highest magnitude of admittance followed by the regular model and then the mesh model.

In order for the results of the asymptotic analysis carried out to be relevant to published experimental studies the porous layer parameters and parameters for flow of a perfect gas were chosen to correspond to the linear stability calculations and experiments of Maslov (2003) and Fedorov *et al.* (2006). This will also enable a comparison of the first mode results obtained here with the second mode results of these authors.

$$M_- = 5.3, \quad T_-^* = 56.4K, \quad Pr = 0.708,$$

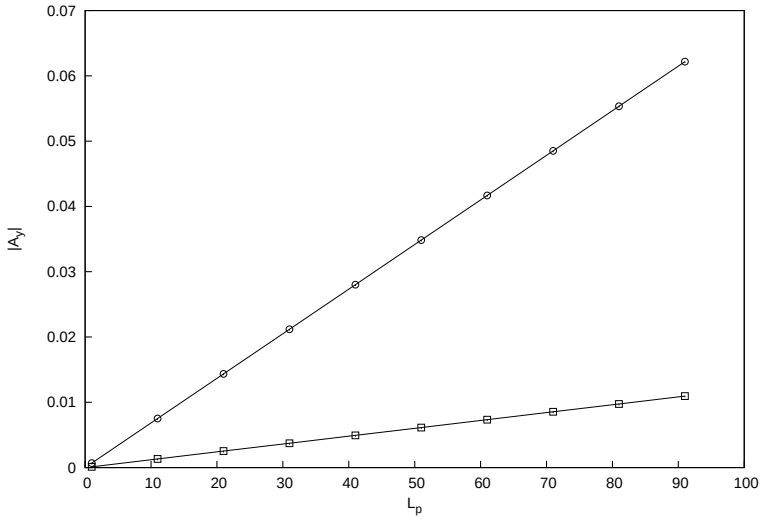

(a)

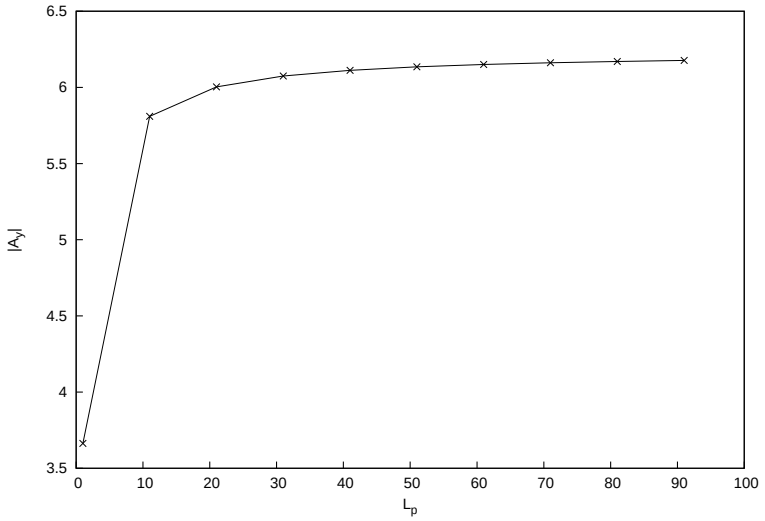

(b)

Figure 2.6: Variation of the magnitude of the porous layer admittance $\overline{A_y}$ with characteristic pore-size $L_p(\mu\text{m})$ and fixed porosity $\phi_0 = 0.5$. We show results for (a) the regular microstructure model (2.3.4, $\circ$), mesh microstructure model (2.3.6, $\square$) and (b) the random microstructure model (2.3.9).

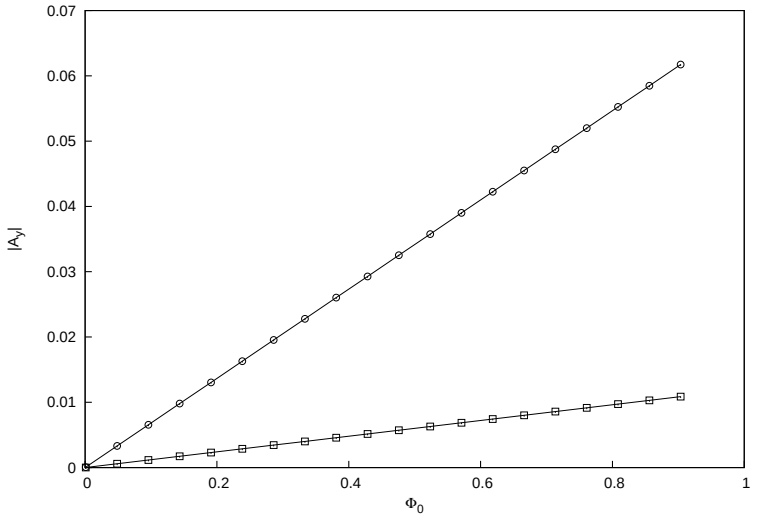

(a)

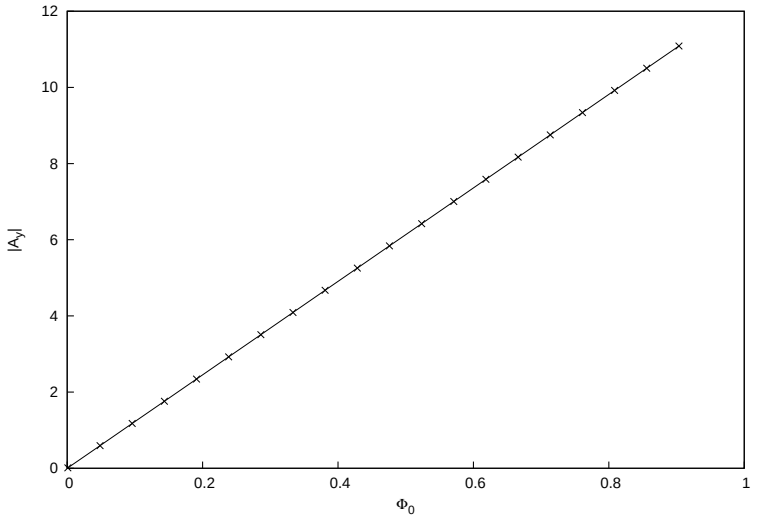

(b)

Figure 2.7: Variation of the magnitude of the porous layer admittance $\overline{A_y}$ with porosity ϕ_0 for a fixed pore-size $L_p = 50\mu$m. We show results for (a) the regular microstructure model (2.3.4, $\circ$), mesh microstructure model (2.3.6, $\square$) and (b) the random microstructure model (2.3.9).

$$Re_1 = 15.2 \times 10^6, \quad Re = Re_1 L^*, \quad R = \sqrt{Re},$$

$$T_w = T_{ad}, \quad T_{ad} = 1 + \sqrt{Pr}\frac{\gamma - 1}{2} M_-^2,$$

$$\rho_w = \frac{1}{T_w}, \quad \mu_w(T_w) = \frac{1+S}{T_w + S} T_w^{3/2}, \quad S = \frac{110}{T_-^*}.$$

Here Re_1 is the unit Reynolds number taken to hold just behind the shock and the boundary-layer displacement thickness is approximated using the Blasius length scale $\delta^* = \sqrt{L^*/Re_1}$. For the stability computations, the regular porous model parameters are chosen as $r_p^* = 28.5\mu m$, $\phi_0 = 0.2$ and $h >> r_p$ based on Maslov (2003) and Federov *et al.* (2001). The last relation implies that $\Lambda h \to \infty$, and so our admittance equation may be simplified to $\overline{A_y} = -\phi_0/Z_0$. This simplification was also made in Fedorov *et al.* (2001). The porosity of the random microstructure (felt metal) is taken to be 0.75 and the fibre diameter is 30μm following Federov *et al.* (2003b). The porosity of the mesh microstructure model is taken to be 0.8, and width of each pore section is taken to be 100μm following Lukashevich *et al.* (2010). The results using these two models will be compared with the regular microstructure model having a porosity of 0.2 and pore radius of 30μm as regular porous models with higher porosity or pore-size have not been investigated in experiments.

2.4 Triple-deck structure

The stability of the basic flow to Tollmien-Schlichting (first-mode) waves for $Re >> 1$ and $M >> 1$ is governed by a triple-deck structure. This formulation was used by Cowley & Hall (1990) for flow over a wedge and by Duck & Hall (1989, 1990) for flow over cylindrical bodies. It is assumed that the triple-deck structure lies in a weak interaction region. Here weak interaction is defined by the parameter $\chi = M_\infty^3 Re^{-1/2} << 1$ (Brown *et al.* 1991 and Stewartson 1964). For experiments conducted in a Mach 6 wind tunnel, typical unit Reynolds numbers are $Re_1 \sim 15 \times 10^6$. For a typical test length of 0.5m, this

gives $\chi \approx 0.08 << 1$. This result implies that our point of interest is far enough from the nose of the cone to ensure that viscous-inviscid interaction between the boundary layer and inviscid flow is small (Stewartson 1964). It was shown by Smith (1989) that an asymptotic description of Tollmien-Schlichting waves can be obtained for wave directions sufficiently oblique to lie outside the local wave-Mach-cone direction ($\tan\theta > \sqrt{M_\infty^2 - 1}$), where M_∞ is the free-stream Mach number. In the limit of large Mach number, following Smith (1989) Cowley & Hall (1990) gives the frequencies and the x and ϕ direction wavelengths of the most rapidly growing waves as $Re^{1/4}\mu_w^{-1/4}T_w^{-3/4}M^{-1/2}$, $Re^{-3/8}\mu_w^{3/8}T_w^{9/8}M^{3/4}$, and $Re^{-3/8}\mu_w^{3/8}T_w^{9/8}M^{-1/4}$, respectively. Henceforth we take $M_- = M$ for convenience. These fix the first-mode disturbances as short-scale fast disturbances. To adopt the classical triple-deck formulation, we argue that at large Reynolds numbers, the normal direction variation of our disturbances exhibit three main regions: lower deck which is the viscous sublayer, the main deck which is the main boundary layer and the upper deck containing potential flow. We can study how the growth rates of the oblique first-mode disturbances are modified by the presence of the shock as the shock lies in the upper deck. For a fixed free-stream Mach number and cone angle, the shock angle is shown to be $\theta_s \approx \theta_c$. This makes the thickness of the upper deck (where the shock is located) comparable with the radius of the cone allowing us to capture the effects of the shock. We now follow Cowley & Hall (1990) to formulate the appropriate asymptotic scalings. The conventional lower, middle and upper scales are

$$Re^{-5/8}\mu_w^{5/8}T_w^{7/8}M^{1/4}, \tag{2.4.1a}$$

$$Re^{-1/2}\mu_w^{1/2}T_w^{1/2}, \tag{2.4.1b}$$

$$Re^{-3/8}\mu_w^{3/8}T_w^{9/8}M^{-1/4}. \tag{2.4.1c}$$

respectively. This is illustrated in figure 2.8. As stated, the first-mode disturbance

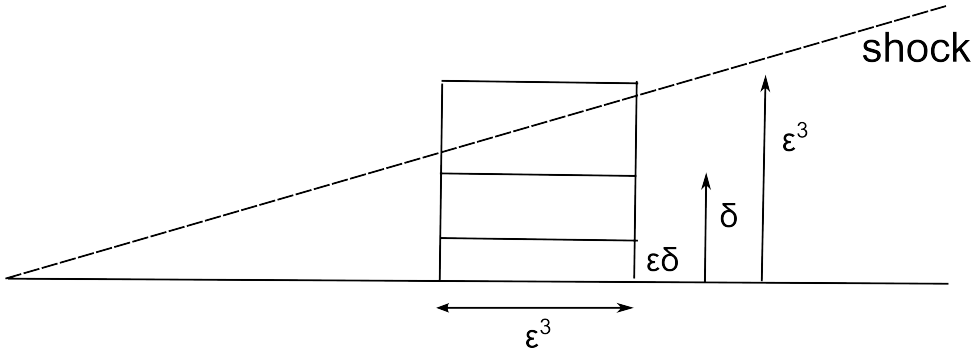

Figure 2.8: Schematic showing the lower, middle and upper decks in relation to the shock. Here $\varepsilon = Re^{-1/8}$, and $\delta = Re^{-1/2}$.

wavelength (l) in the x-direction along the cone is of order

$$Re^{-3/8}\mu_w^{3/8}T_w^{9/8}M^{3/4}. \tag{2.4.2}$$

Since the shock lies in the upper deck, from (2.1.2f) and (2.4.1c), and using θ_s is small we see that

$$\theta_s \sim \varepsilon \tan\sigma \sim Re^{-3/8}\mu_w^{3/8}T_w^{9/8}M^{-1/4}, \tag{2.4.3}$$

which from (2.4.2) implies that $l \sim M\varepsilon\tan\sigma$. To neglect non-parallel effects we want the wavelength l to be much less than the distance from the apex of the cone, $L^* = O(1)$. Assuming $\sigma << 1$, we require

$$M\varepsilon\sigma << 1. \tag{2.4.4}$$

From (2.1.2e) we can see that

$$\varepsilon = O\left(\frac{1}{M_+^2\sigma^2}\right). \tag{2.4.5}$$

From (2.1.2g) and (2.1.2h) we see that $M_+ \sim M_-$, so (2.4.4) becomes

$$\sigma M >> 1. \tag{2.4.6}$$

However for $M_+^2 > 0$ in (2.1.2h) we require (neglecting $O(\varepsilon^2)$ terms) that

$$(\gamma - 1)(M\sigma)^2 < 2. \tag{2.4.7}$$

Hence in order to consider the effect of the shock on the instability waves without effects of non-parallelism we must make the assumption

$$(\gamma - 1) << 1, \tag{2.4.8}$$

called the "Newtonian assumption". In order to fix a scaling we use (2.4.7) to assume that

$$(\gamma - 1)(M\sigma)^2 \sim 1. \tag{2.4.9}$$

Using $T_w \sim (\gamma - 1)M^2 >> 1$, Sutherlands viscosity law ($\mu_w \sim T_w^{1/2}$) along with (2.4.5), the shock interaction condition (2.4.3) becomes

$$M \sim \sigma^{13/14} Re^{3/14}. \tag{2.4.10}$$

The restriction (2.4.6) implies

$$\sigma >> Re^{-1/9}, \quad \text{i.e.} \quad M >> Re^{1/9}. \tag{2.4.11}$$

Pressure disturbances that develop in the lower deck generate a velocity perturbation normal to the cone (and shock) in the upper deck. In order that the linearised shock condition remains applicable we require the undisturbed velocity normal to the shock (from the outer flow solution) to be larger than this generated velocity perturbation. From Cowley & Hall (1990) the pressure perturbation is of order $Re^{-1/4}\mu_w^{1/4}T_w^{-1/4}M^{-3/2}$ and from the inviscid equations we can see that this generates a normal velocity perturbation of order $Re^{-1/4}\mu_w^{1/4}T_w^{-1/4}M^{-1/2}$ in the upper deck. From geometric considerations we can show that the velocity normal to the shock is $-\varepsilon U_0 \sin\sigma$. Thus we require

$$\varepsilon\sigma >> Re^{-1/4}\mu_w^{1/4}T_w^{-1/4}M^{-1/2}, \tag{2.4.12}$$

or by using (2.4.5)

$$\sigma^4 M^6 << Re\mu_w^{-1}T_w. \tag{2.4.13}$$

Expressing μ_w and T_w in terms of M and using (2.4.10) in the above we can formulate the following restrictions on the Mach number and shock angle

$$Re^{1/9} << M << Re^{7/37}, \qquad Re^{-1/9} << \sigma << Re^{-1/37}. \tag{2.4.14}$$

The lower bounds are obtained from (2.4.11).

Typical wind tunnel experiments are conducted on 0.5m long 7° half-angle cone models at a free stream Mach number $M_\infty \approx 6$ and unit Reynolds numbers $Re_1 \approx 15\times10^6$. Using (2.4.14) this requires that the shock angle σ be bounded as $9.85° < \sigma < 37.5°$ and the lower bound on the Mach number behind the shock to be $M \sim 5.8$. Using (2.1.3g) we can calculate the experimental shock angle to be $\sigma = 12.3°$ which lies within the range of validity of the asymptotic analysis. From Section 2.3.4 we see that the typical Mach

number behind the shock $M_- = 5.3$ is reasonably close to the lower bound required for the asymptotic analysis to be valid ($M \sim 5.8$). The lower bound is attained when the non-parallel assumption is violated.

Following Seddougui & Bassom (1997) we now restrict our attention to a location along the cone surface where the non-dimensional radius $\overline{a} \sim Re^{-3/8} M^{-1/4} \mu_w^{3/8} T_w^{9/8}$. This fixes the size of the cone half-angle θ_c since $\sin(\theta_c) = \overline{a} L^*$. This restriction also ensures that the boundary layer thickness, $O(Re^{-1/2} L^*)$, is small compared to the cone radius allowing the subsequent analysis to capture the effects of curvature on the stability problem. It is convenient to scale out parameters such as T_w and μ_w as shown by Cowley & Hall (1990) to simplify the analysis. We consider $\lambda(x) = \lambda_1 + \ldots$ such that $\lambda_1 = \widehat{\lambda} x^{-1/2}$ is the leading order neutral value of the boundary-layer skin-friction. $\widehat{\lambda}$ is taken to be equal to the neutral Blasius solution value. This will make our problem valid for a weakly nonlinear analysis. If we were to only consider the linear problem, then λ is a constant and can also be scaled out of the problem as in Cowley & Hall (1990) and Seddougui & Bassom (1997). Thus, the following scales are introduced

$$\begin{aligned} x &= 1 + Re^{-3/8} \mu_w^{3/8} T_w^{9/8} M^{3/4} X, \\ \overline{a} &= Re^{-3/8} \mu_w^{3/8} T_w^{9/8} M^{-1/4} a, \\ t &= Re^{-1/4} \mu_w^{1/4} T_w^{3/4} M^{1/2} \tau. \end{aligned} \tag{2.4.15}$$

These scales are fixed throughout the triple-deck structure.

2.4.1 Lower deck

The lower deck is the region in which viscous effects are important. The non-linearity of the problem appears here. The scalings here take the form

$$\begin{aligned}
\overline{r} - \overline{a} &= Re^{-5/8}\mu_w^{5/8}T_w^{7/8}M^{1/4}Y, \\
u &\sim Re^{-1/8}\mu_w^{1/8}T_w^{3/8}M^{1/4}U, \\
v &\sim Re^{-3/8}\mu_w^{3/8}T_w^{1/8}M^{-1/4}V, \\
w &\sim Re^{-1/8}\mu_w^{1/8}T_w^{3/8}M^{-3/4}W, \\
\overline{A_y} &\sim Re^{-1/8}\mu_w^{1/8}T_w^{3/8}M^{5/4}A_y, \\
p &\sim \gamma^{-1}M^{-2} + Re^{-1/4}\mu_w^{1/4}T_w^{-1/4}M^{-3/2}P, \\
T &\sim T_w, \\
\rho &\sim T_w^{-1}.
\end{aligned} \tag{2.4.16}$$

Substituting these expressions into the non-dimensional continuity and Navier-Stokes equations give to leading order

$$\begin{aligned}
U_X + V_Y + \frac{1}{a}W_\phi &= 0, \\
U_\tau + UU_X + VU_Y + \frac{W}{a}U_\phi &= U_{YY}, \\
W_\tau + UW_X + VW_Y + \frac{W}{a}W_\phi &= -\frac{1}{a}P_\phi + W_{YY}.
\end{aligned} \tag{2.4.17a}$$

In the hypersonic limit ($M \to \infty$) the term P_X does not appear at leading order. The porous wall boundary condition is to be satisfied on the surface of the cone. In addition, the solution here must match with the main deck in the limit $Y \to \infty$. Thus the necessary

boundary conditions to be satisfied are

$$\begin{aligned} U = W = 0 \quad \text{and} \quad V = A_y P \quad \text{on} \quad Y = 0, \\ U \to \lambda(Y + A(X, \phi, \tau)), \quad W \to D/Y \quad \text{as} \quad Y \to \infty. \end{aligned} \tag{2.4.17b}$$

Here A is a displacement function whose evolution will be obtained from the non-linear stability analysis and D satisfies the equation $D_X = -P_\phi/a$.

2.4.2 Middle deck

The middle deck has the same thickness as the undisturbed boundary layer. Since $T_w >> 1$ for $M >> 1$, there exists a thin transition region in which T is quickly reduced to its free stream value of unity. Thus the middle deck consists of three regions (i) a high temperature boundary layer region of thickness $O(Re^{-1/2}M^{-3/2})$ where $T \sim O(M^2)$, (ii) a thin region of $O(Re^{-1/2})$ thickness where $T \sim O(1)$ and (iii) a small transition region between the two. Similar solutions occur in all three regions, and we focus on region (i) where the basic temperature is large and find the scalings here to be

$$\begin{aligned} \overline{r} - \overline{a} &= Re^{-1/2}\mu_w^{1/2}T_w^{1/2}y, \\ u &\sim \overline{U}_0(y) + Re^{-1/8}\mu_w^{1/8}T_w^{3/8}M^{1/4}A\overline{U}_{0y}, \\ v &\sim Re^{-1/4}\mu_w^{1/4}T_w^{-1/4}M^{-1/2}A_X\overline{U_0}, \\ w &\sim Re^{-1/4}\mu_w^{1/4}T_w^{-1/4}M^{-1/2}D\overline{U_0\,R_0}, \\ p &\sim Re^{-1/4}\mu_w^{1/4}T_w^{-1/4}M^{-3/2}P, \\ \rho &\sim \overline{R}_0(y) + Re^{-1/8}\mu_w^{1/8}T_w^{3/8}M^{1/4}A\overline{R}_{0y}. \end{aligned} \tag{2.4.18}$$

Here $\overline{U_0}$ and $\overline{R_0}$ are the non-dimensional velocity and density respectively of the unperturbed boundary layer flow. These may be obtained from solutions of the boundary layer equations satisfying the conditions $\overline{U_0}(y) \to 1/(1 + \varepsilon^2 \tan\sigma^2)^{1/2}$, $\overline{R_0}(y) \to 1$ as $y \to \infty$

and $\overline{U_0}(0) = 0$, $\overline{R_0}(0) = 1/T_w$.

2.4.3 Upper deck

In the upper deck the basic flow quantities go to their values just below the shock. It is here that the curvature effects are important. The flow in the upper deck can be scaled as pressure-acoustic waves.

$$\begin{aligned}
\overline{r} &= Re^{-3/8}\mu_w^{3/8}T_w^{9/8}M^{-1/4}r,\\
u &\sim 1 + Re^{-1/4}\mu_w^{1/4}T_w^{-1/4}M^{-3/2}\tilde{u},\\
v &\sim Re^{-1/4}\mu_w^{1/4}T_w^{-1/4}M^{-1/2}\tilde{v},\\
w &\sim Re^{-1/4}\mu_w^{1/4}T_w^{-1/4}M^{-1/2}\tilde{w},\\
p &\sim Re^{-1/4}\mu_w^{1/4}T_w^{-1/4}M^{-3/2}\tilde{p},\\
\rho &\sim 1 + Re^{-1/4}\mu_w^{1/4}T_w^{-1/4}M^{-1/2}\tilde{\rho}.
\end{aligned} \tag{2.4.19a}$$

Substituting the above into the governing inviscid equations then give us

$$\begin{aligned}
&\tilde{\rho}_X + \tilde{v}_r + \frac{\tilde{v}}{r} + \frac{1}{r}\tilde{w}_\phi = 0,\\
&\tilde{u}_X + \tilde{p}_X = 0,\\
&\tilde{v}_X + \tilde{p}_r = 0,\\
&\tilde{w}_X + \frac{1}{r}\tilde{p}_\phi = 0,\\
&\tilde{p}_X + \tilde{\rho}_r = 0.
\end{aligned} \tag{2.4.19b}$$

These equations then reduce to

$$\frac{\partial^2\tilde{p}}{\partial r^2} + \frac{1}{r}\frac{\partial\tilde{p}}{\partial r} + \frac{1}{r^2}\frac{\partial^2\tilde{p}}{\partial\phi^2} - \frac{\partial^2\tilde{p}}{\partial X^2} = 0. \tag{2.4.19c}$$

The boundary conditions to be satisfied are obtained by matching the solution with the

main deck as $r \to a$, and by applying the necessary constraint at the location of the shock ($r = r_s$). The matching condition yields

$$\tilde{p_r} = A_{XX} \quad \text{and} \quad \tilde{p} = P \quad \text{at} \quad r = a. \tag{2.4.19d}$$

By considering linear waves beneath the shock (Section 2.2), Seddougui (1994) shows the required shock condition to be

$$\tilde{p} = 0 \quad \text{at} \quad r = r_s. \tag{2.4.19e}$$

In the absence of a shock, this condition will occur in the limit $r_s \to \infty$.

2.4.4 Axisymmetric problem

Before proceeding to the stability problem we discuss the solution for axisymmetric disturbances. Here the disturbances lose their ϕ co-ordinate dependence. This situation is considered separately as now the Mach number can be completely scaled out of the stability problem (Duck & Hall 1989). In the lower deck equations (2.4.17a), to leading order, the pressure gradient term P_X is not neglected. This ensures that a pressure term is retained in the lower deck problem. The porous layer admittance now scales as

$$\overline{A_y} = Re^{-1/8}\mu_w^{1/8}T_w^{3/8}(M^2-1)^{3/8}A_y,$$

while the pressure perturbation scales as $(M^2-1)^{-1/4}$ instead of $M^{-3/2}$. This necessitates changes in the factors of M for u and ρ in the upper deck equations (2.4.19c). The analysis follows that for non-axisymmetric disturbances with M replaced by appropriate powers of (M^2-1) throughout. The analysis of the axisymmetric problem is given in Section 3.4.

Chapter 3

Stability Problem

We proceed with analyzing the stability of the system of equations described in Chapter 2. We adopt the method of Smith (1979a) who implemented a weakly nonlinear analysis of an incompressible Blasius boundary layer to Tollmien-Schlichting waves. We set up the nonlinear stability problem, from which the linear stability problem can be recovered. The objective of the analysis is to monitor the streamwise development of the Tollmien-Schlichting type (first-mode) disturbances. We consider disturbances proportional to

$$E = \exp[\mathrm{i}(\alpha X + n\phi - \Omega\tau)], \tag{3.0.1}$$

where α is the streamwise wavenumber, Ω is the frequency and n is the azimuthal wavenumber which is an integer $\geqslant 0$. The subsequent analysis is strictly valid for $n > 0$, with the special case of axisymmetric disturbances ($n = 0$) described in Section 3.4. In this thesis, the focus is on the spatial evolution of small amplitude disturbances. Disturbances that are spatially stable will have real values for the streamwise wavenumber α. Such disturbances are said to be "neutrally stable". These solutions of the governing equations with real values for α and Ω for a particular choice of local cone radius a are called neutral points. Existence of multiple neutral points will be demonstrated in Section

4.1.1. Away from the linear neutral point, solutions for the streamwise wavenumber α will be complex and disturbances can either grow or decay depending on the sign of its imaginary part α_i (Section 4.1.2). As spatially unstable disturbances ($\alpha_i < 0$) evolve further away from a linear neutral point, nonlinear effects come into play. In this study we perform a weakly nonlinear stability analysis. The key assumptions of the weakly nonlinear theory is that we remain close to the linear neutral point such that the growth rate is small. This implies that leading order dispersion relations can determined by the linear analysis and nonlinear effects are included at higher order.

So we consider a weakly nonlinear disturbance that is allowed to develop in the vicinity of a linear neutral point (real α, Ω with fixed n). If the relative amplitude of the disturbance in the lower deck is $O(h)$, with $h << 1$, then the scaled amplitude A of the mode will evolve on an $O(h^2)$ lengthscale. A lower bound on the possible size of h is obtained from Hall & Smith (1984) who demonstrated that to neglect non-parallel effects we must have

$$O(Re^{-3/32}M^{3/16}T_w^{21/64}) << h << 1.$$

If the lower bound of this inequality is attained, then the lengthscale $(x-1)$ over which the disturbance amplitude modulates, $O(Re^{-3/8}h^{-2})$, becomes identical to the lengthscale over which non-parallelism of the basic flow occurs, $O(h^2)$. Due to our non-dimensionalization we take the linear stability of the flow to occur at $x = 1$ and consider a perturbation at the point

$$x = 1 + h^2 x_2. \tag{3.0.2a}$$

Since the skin friction is a function of x, it will also be slightly perturbed from its neutral

value as

$$\lambda = \lambda_1 + h^2\lambda_2, \tag{3.0.2b}$$

where $\lambda_2 = x_2\frac{d\lambda}{dx}|_{x=1}$. We fix the azimuthal wavenumber n and allow the frequency to vary as

$$\Omega = \Omega_1 + h^2\Omega_2, \tag{3.0.2c}$$

where Ω_1 is the neutral value of the frequency obtained from the linear stability problem (Section 3.1). To account for the slow streamwise modulation of the amplitude we now introduce a new streamwise coordinate as

$$\tilde{X} = h^2 X. \tag{3.0.2d}$$

By the method of multiple scales we know that $\frac{\partial}{\partial X} \rightarrow \frac{\partial}{\partial X} + h^2\frac{\partial}{\partial \tilde{X}}$. We now seek solutions to our system of equations (2.4.17a) (lower deck) and (2.4.19c) (upper deck). The perturbations imply that for $h << 1$ we seek solutions of the form

$$\begin{aligned} U &= \lambda_1(1 + h^2\lambda_2)Y + hU_1 + h^2U_2 + h^3U_3 + O(h^4), \\ (V, W, P, A, \tilde{p}) &= \sum_{j=1}^{3} h^j(V_j, W_j, P_j, A_j, \tilde{p_j}) + O(h^4). \end{aligned} \tag{3.0.3}$$

Substitution of (3.0.3) into (2.4.17a, 2.4.19c) leads to a hierarchy of problems in increasing orders of h. At $O(h)$ we get

$$U_{1X} + V_{1Y} + \frac{1}{a}W_{1\phi} = 0, \tag{3.0.4a}$$

$$U_{1\tau} + YU_{1X} + V_1 = U_{1YY}, \tag{3.0.4b}$$

$$W_{1\tau} + YW_{1X} = -\frac{1}{a}P_{1\phi} + W_{1YY}, \tag{3.0.4c}$$

$$\tilde{p}_{1rr} + \frac{1}{r}\tilde{p}_{1r} + \frac{1}{r^2}\tilde{p}_{1\phi\phi} - \tilde{p}_{1XX} = 0. \tag{3.0.4d}$$

At $O(h)$ the boundary conditions (2.4.17b, 2.4.19d, 2.4.19e) become

$$Y = 0: \qquad U_1, W_1 = 0, \quad V_1 = A_y P_1, \tag{3.0.5a}$$

$$Y = \infty: \qquad U_1 \to \lambda_1 A_1, \quad W_1 \to D_1/Y, \tag{3.0.5b}$$

$$r = r_s: \qquad \tilde{p}_1 = 0, \tag{3.0.5c}$$

$$r = a: \qquad \tilde{p}_1 = P_1, \quad \tilde{p}_{1r} = A_{1XX}. \tag{3.0.5d}$$

At $O(h^2)$ we get

$$U_{2X} + V_{2Y} + \frac{1}{a}W_{2\phi} = 0, \tag{3.0.6a}$$

$$U_{2\tau} + YU_{2X} + U_1U_{1X} + V_1U_{1Y} + V_2 + \frac{1}{a}W_1U_{1\phi} = U_{2YY}, \tag{3.0.6b}$$

$$W_{2\tau} + YW_{2X} + V_1W_{1Y} + \frac{1}{a}W_1W_{1\phi} + U_1W_{1X} = -\frac{1}{a}P_{2\phi} + W_{2YY}, \tag{3.0.6c}$$

$$\tilde{p}_{2rr} + \frac{1}{r}\tilde{p}_{2r} + \frac{1}{r^2}\tilde{p}_{2\phi\phi} - \tilde{p}_{2XX} = 0. \tag{3.0.6d}$$

At $O(h^2)$ the boundary conditions (2.4.17b, 2.4.19d, 2.4.19e) become

$$Y = 0: \qquad U_2, W_2 = 0, \quad V_2 = A_y P_2, \tag{3.0.7a}$$

$$Y = \infty: \qquad U_2 \to \lambda_1 A_2, \quad W_2 \to D_2/Y, \tag{3.0.7b}$$

$$r = r_s: \qquad \tilde{p}_2 = 0, \tag{3.0.7c}$$

$$r = a: \qquad \tilde{p}_2 = P_2, \quad \tilde{p}_{2r} = A_{2XX}. \tag{3.0.7d}$$

At $O(h^3)$ we get

$$U_{3X} + V_{3Y} + \frac{1}{a}W_{3\phi} = -U_{1\tilde{X}}, \tag{3.0.8a}$$

$$U_{3\tau} + Y(U_{3X} + U_{1\tilde{X}}) + U_1U_{2X} + U_{1X}(\lambda_2 Y + U_2) + V_1(\lambda_2 + U_{2Y}) + V_2U_{1Y} + V_3 + \frac{1}{a}W_1U_{2\phi} + \frac{1}{a}W_2U_{1\phi} = U_{3YY}, \tag{3.0.8b}$$

$$W_{3\tau} + Y(W_{3X} + W_{1\tilde{X}}) + U_1W_{2X} + W_{1X}(\lambda_2 Y + U_2) + V_1W_{2Y} + V_3 + \frac{1}{a}W_2W_{1\phi} + \frac{1}{a}W_1W_{2\phi} + V_2W_{1Y} = -\frac{1}{a}P_{3\phi} + W_{3YY}, \tag{3.0.8c}$$

$$\tilde{p}_{3rr} + \frac{1}{r}\tilde{p}_{3r} + \frac{1}{r^2}\tilde{p}_{3\phi\phi} - \tilde{p}_{3XX} - 2\tilde{p}_{1X\tilde{X}} = 0. \tag{3.0.8d}$$

At $O(h^3)$ the boundary conditions (2.4.17b, 2.4.19d, 2.4.19e) become

$$Y = 0: \qquad U_3, W_3 = 0, \quad V_3 = A_y P_3, \tag{3.0.8e}$$

$$Y = \infty: \qquad U_3 \to \lambda_1(A_3 + \lambda_2 A_1), \quad W_3 \to D_3/Y, \tag{3.0.8f}$$

$$r = r_s: \qquad \tilde{p}_3 = 0, \tag{3.0.8g}$$

$$r = a: \qquad \tilde{p}_3 = P_3, \quad \tilde{p}_{3r} = A_{3XX} + 2A_{1XX}. \tag{3.0.8h}$$

We now address our problem at each order of h in turn.

3.1 First-order problem

The linear stability problem is described by the equations at $O(h)$. The analysis follows that of Seddougui & Bassom (1997). They obtained the eigenrelations that govern the linear stability of the flow for the solid wall case. This analysis is extended in a straightforward manner for the porous wall case by incorporating the porous wall boundary condition. We seek solutions to (3.0.4) of the form

$$(U_1, V_1, W_1) = (U_{11}(\tilde{X}, Y), V_{11}(\tilde{X}, Y), W_{11}(\tilde{X}, Y))E + (c.c.), \tag{3.1.1a}$$

$$(P_1, A_1) = (P_{11}(\tilde{X}), A_{11}(\tilde{X}))E + (c.c.), \tag{3.1.1b}$$

$$\tilde{p}_1 = \tilde{p}_{11}(\tilde{X}, r)E + (c.c.). \tag{3.1.1c}$$

where E is given by (3.0.1) and $(c.c.)$ represents the complex conjugate of the form $A_{11}^c E^{-1}$, with A_{11}^c the complex conjugate of A_{11}. Substitution of (3.1.1c) in (3.0.4d) gives

$$\frac{d^2\tilde{p}_{11}}{dr^2} + \frac{1}{r}\frac{d\tilde{p}_{11}}{dr} + \left(\alpha^2 - n^2/r^2\right)\tilde{p}_{11} = 0, \tag{3.1.2}$$

the solution of which is $\tilde{p}_{11} = C_1 I_n(\mathrm{i}\alpha r) + C_2 K_n(\mathrm{i}\alpha r)$, where I_n and K_n are modified Bessel functions of order n. Applying (3.0.5c) and the second condition from (3.0.5d) gives

$$\tilde{p}_{11} = -\mathrm{i}\alpha A_{11}\frac{I_n(\mathrm{i}\alpha r_s)K_n(\mathrm{i}\alpha r) - I_n(\mathrm{i}\alpha r)K_n(\mathrm{i}\alpha r_s)}{I_n'(\mathrm{i}\alpha a)K_n(\mathrm{i}\alpha r_s) - I_n(\mathrm{i}\alpha r_s)K_n'(\mathrm{i}\alpha a)}. \tag{3.1.3}$$

Substitution of (3.1.1a) and (3.1.1b) in (3.0.4a) to (3.0.4c) and making the transformation

$$\xi = \Delta^{1/3}Y + \xi_0,$$

where $\xi_0 = -\mathrm{i}\Omega\Delta^{-2/3}, (\Delta = \mathrm{i}\alpha)$ gives

$$\Delta U_{11} + \Delta^{1/3}V_{11\xi} + (\Delta n/\alpha a)W_{11} = 0, \tag{3.1.4a}$$

$$(-\mathrm{i}\Omega + \Delta Y)U_{11} + V_{11} = \Delta^{2/3}U_{11\xi\xi}, \tag{3.1.4b}$$

$$(-\mathrm{i}\Omega + \Delta Y)W_{11} = (-\Delta n/\alpha a)P_{11} + \Delta^{2/3}W_{11\xi\xi}. \tag{3.1.4c}$$

Performing $\frac{d}{d\xi}$(3.1.4b) + $\frac{d}{d\xi}$(3.1.4c) $\times$ $(n/\alpha)-$ (3.1.4a) simplifies our system of lower deck equations to the following single equation

$$(-\mathrm{i}\Omega + \Delta Y)\Delta^{1/3}(U_{11} + (n/\alpha a)W_{11})_\xi = \Delta(U_{11} + (n/\alpha a)W_{11})_{\xi\xi\xi}.$$

This may be rewritten as

$$(U_{11} + (n/\alpha a)W_{11})_{\xi\xi\xi} - \xi(U_{11} + (n/\alpha a)W_{11})_{\xi} = 0$$

which we can immediately recognize as Airy's equation. The solution we require is the one which is bounded as $Y \to \infty$. Thus we have

$$(U_{11} + (n/\alpha a)W_{11})_{\xi} = B_1 \mathrm{Ai}(\xi), \tag{3.1.5a}$$

$$U_{11} + (n/\alpha a)W_{11} = B_1 \int_{\xi_0}^{\xi} \mathrm{Ai}(s)ds. \tag{3.1.5b}$$

Here B_1 is an unknown complex constant. Using solution (3.1.5) and applying the boundary condition (3.0.5a) (when $Y \to 0$) to (3.1.4b) and (3.1.4c) we can determine

$$B_1 = \frac{\Delta^{-2/3}}{\mathrm{Ai}'(\xi_0)} P_{11}\left(A_y + \frac{\Delta n^2}{\alpha^2 a^2}\right). \tag{3.1.6a}$$

Applying the condition (3.0.5b) (when $Y \to \infty$) gives us

$$A_{11} = B_1 \int_{\xi_0}^{\infty} \mathrm{Ai}(s)ds, \tag{3.1.6b}$$

which is a result of importance in the subsequent nonlinear analysis relating B_1 to the amplitude A_{11}. Finally using our solution for B_1 and applying the first boundary condition in (3.0.5d) (when $r = a$) gives us a dispersion relation that relates the wavenumbers with the frequency. Thus the required equation that governs the linear stability of our flow to infinitesimal first mode disturbances is

$$\frac{\mathrm{Ai}'(\xi_0)}{\int_{\xi_0}^{\infty} \mathrm{Ai}(\xi)d\xi} = (\mathrm{i}\alpha)^{1/3}\left[A_y + \frac{\mathrm{i}n^2}{\alpha a^2}\right]\frac{I_n(\mathrm{i}\alpha r_s)K_n(\mathrm{i}\alpha a) - I_n(\mathrm{i}\alpha a)K_n(\mathrm{i}\alpha r_s)}{I_n(\mathrm{i}\alpha r_s)K_n'(\mathrm{i}\alpha a) - I_n'(\mathrm{i}\alpha a)K_n(\mathrm{i}\alpha r_s)}. \tag{3.1.7}$$

This eigenrelation (3.1.7) is valid for non-axisymmetric disturbance modes. The corresponding relation for axisymmetric disturbances is given in Section 3.4. The solid wall case is recovered by simply setting $A_y = 0$ in (3.1.7). Solutions to this equation that have real α and Ω are said to be "neutrally stable" solutions i.e., they do not grow in space or time. These solutions can be represented as curves in the (α, a) parameter space and (Ω, a) parameter space. The presence of the shock allows multiple neutral modes. Spatially varying solutions lie on either side of the neutral curves, and the sign of α_{i}, the imaginary part of the streamwise wavenumber α, determines whether the flow is stable or unstable in these regions. Solutions for these complex wavenumbers govern the spatial stability of the flow and by comparing results between the solid and porous wall cases (Section 4.1) we can determine the effect of the porous wall on the linear stability of the flow.

3.2 Second-order problem

We now proceed to the nonlinear stability of the problem and begin with the equations at $O(h^2)$ (3.0.6). We seek solutions here in the form of

$$\begin{aligned}(U_2, V_2, W_2) &= (U_{22}(\tilde{X}, Y), V_{22}(\tilde{X}, Y), W_{22}(\tilde{X}, Y))E^2 \\ &\quad + (U_{20}(\tilde{X}, Y), V_{20}(\tilde{X}, Y), W_{20}(\tilde{X}, Y)) + (c.c.), \\ (P_2, A_2) &= (P_{22}(\tilde{X}), A_{22}(\tilde{X}))E^2 + (P_{20}(\tilde{X}), A_{20}(\tilde{X})) + (c.c.), \\ \tilde{p}_2 &= \tilde{p}_{22}(\tilde{X}, r)E^2 + \tilde{p}_{20}(\tilde{X}) + (c.c.),\end{aligned} \tag{3.2.1}$$

where E is given by (3.0.1) and $(c.c.)$ represents the complex conjugate of the form $A_{22}^{c}E^{-2}$. We can now proceed to substitute (3.2.1) into (3.0.6) and (3.0.7). We begin by looking

at the upper deck problem (3.0.6d). We then obtain

$$\left(\frac{d^2\tilde{p}_{22}}{dr^2}+\frac{1}{r}\frac{d\tilde{p}_{22}}{dr}-\left[(2\mathrm{i}\alpha)^2+\frac{(2n)^2}{r^2}\right]\tilde{p}_{22}\right)E^2+\frac{d^2\tilde{p}_{20}}{dr^2}+\frac{1}{r}\frac{d\tilde{p}_{20}}{dr}=0, \tag{3.2.2a}$$

the solutions to which are

$$\tilde{p}_{22}=C_{21}I_{2n}(2\mathrm{i}\alpha r)+C_{22}K_{2n}(2\mathrm{i}\alpha r), \tag{3.2.2b}$$

$$\tilde{p}_{20}=\overline{C_{20}}+\overline{C_{21}}\ln(r). \tag{3.2.2c}$$

3.2.1 Second-order terms

We now turn to the lower deck equations (3.0.6a), (3.0.6b) and (3.0.6c) and collect terms that are proportional to E^2 to yield

$$\begin{aligned}
2\Delta U_{22}+V_{22Y}+\frac{1}{a}2\Delta W_{22}&=0,\\
-2\mathrm{i}\Omega U_{22}+\Delta U_{11}^2+Y(2\Delta U_{22})+V_{11}U_{11Y}+V_{22}+\frac{in}{\alpha}U_{11}W_{11}&=U_{22YY},\\
-2\mathrm{i}\Omega W_{22}+Y(2\Delta W_{22})+V_{11}W_{11Y}+\frac{in}{\alpha}W_{11}^2+\Delta U_{11}W_{11}&=-\frac{2in}{a}P_{22}+W_{22YY}.
\end{aligned} \tag{3.2.3}$$

Applying the transformation in ξ to (3.2.3) we obtain

$$2\Delta U_{22}+V_{22\xi}\Delta^{1/3}+2\frac{\Delta n}{\alpha a}W_{22}=0, \tag{3.2.4a}$$

$$2(\Delta Y-\mathrm{i}\Omega)U_{22}+\Delta U_{11}^2+V_{11}U_{11\xi}\Delta^{1/3}+V_{22}+\frac{\Delta n}{\alpha a}W_{11}U_{11}=\Delta^{2/3}U_{22\xi\xi}, \tag{3.2.4b}$$

$$2(\Delta Y-\mathrm{i}\Omega)W_{22}+V_{11}W_{11\xi}\Delta^{1/3}+\frac{\Delta n}{\alpha a}W_{11}^2+\Delta W_{11}U_{11}=-2\frac{\Delta n}{\alpha a}P_{22}+\Delta^{2/3}W_{22\xi\xi}. \tag{3.2.4c}$$

We can now proceed to eliminate the second-order pressure and velocity terms. Recall that first-order terms are now known from our analysis in Section 3.1. We first take

$\frac{d}{d\xi}$ (3.2.4b) to obtain

$$2(\Delta Y - \mathrm{i}\Omega)U_{22\xi}\Delta^{1/3} + 2\Delta^{4/3}U_{11}U_{11\xi} + 2U_{22}\Delta + \Delta^{2/3}(V_{11}U_{11\xi\xi} + V_{11\xi}U_{11\xi}) + \Delta^{1/3}V_{22\xi} + \frac{\Delta n}{\alpha a}(W_{11}U_{11\xi} + W_{11\xi}U_{11})\Delta^{1/3} = \Delta U_{22\xi\xi\xi}, \tag{3.2.5a}$$

and subtracting from it (3.2.4a) we get

$$2(\Delta Y - \mathrm{i}\Omega)U_{22\xi}\Delta^{1/3} + 2\Delta^{4/3}U_{11}U_{11\xi} + \Delta^{2/3}(V_{11}U_{11\xi\xi} + V_{11\xi}U_{11\xi}) + \frac{\Delta n}{\alpha a}(W_{11}U_{11\xi} + W_{11\xi}U_{11})\Delta^{1/3} - 2\frac{\Delta n}{\alpha a}W_{22} = \Delta U_{22\xi\xi\xi}. \tag{3.2.5b}$$

Now we take $(n/\alpha a)\frac{d}{d\xi}$ (3.2.4c) to obtain

$$2(\Delta Y - \mathrm{i}\Omega)\frac{n}{\alpha a}W_{22\xi} + 2\frac{\Delta n}{\alpha a}W_{22} + \Delta^{2/3}\frac{\Delta n}{\alpha a}(V_{11}W_{11\xi\xi} + W_{11\xi}V_{11\xi}) + 2\Delta^{4/3}\left(\frac{\Delta n}{\alpha a}\right)^2 W_{11}W_{11\xi} + \Delta^{4/3}\frac{\Delta n}{\alpha a}(W_{11}U_{11\xi} + W_{11\xi}U_{11}) = \frac{\Delta n}{\alpha a}W_{22\xi\xi\xi}, \tag{3.2.5c}$$

and add it to (3.2.5b), use $(\Delta Y - \mathrm{i}\Omega)\Delta^{1/3} = \Delta\xi$ along with some rearranging of terms to obtain a single equation

$$\left(U_{22\xi\xi\xi} + \frac{\Delta n}{\alpha a}W_{22\xi\xi\xi}\right) - 2\xi\left(U_{22\xi} + \frac{\Delta n}{\alpha a}W_{22\xi}\right) = 2\Delta^{1/3}\left(U_{11}U_{11\xi} + \left(\frac{\Delta n}{\alpha a}\right)^2 W_{11}W_{11\xi}\right) + \Delta^{1/3}\left\{V_{11}\left(U_{11\xi\xi} + \frac{n}{\alpha a}W_{11\xi\xi}\right) + V_{11\xi}\left(U_{11\xi} + \frac{n}{\alpha a}W_{11\xi}\right)\right\} + 2\Delta^{1/3}\left(\frac{\Delta n}{\alpha a}W_{11}U_{11\xi} + \frac{\Delta n}{\alpha a}W_{11\xi}U_{11}\right). \tag{3.2.5d}$$

Since

$$\frac{d}{dY}\left(U_{11} + \frac{\Delta n}{\alpha a}W_{11}\right)^2 = 2\Delta^{1/3}\left(U_{11}U_{11\xi} + \left(\frac{\Delta n}{\alpha a}\right)^2 W_{11}W_{11\xi} + \frac{\Delta n}{\alpha a}W_{11}U_{11\xi} + \frac{\Delta n}{\alpha a}W_{11\xi}U_{11}\right),$$

we can simplify (3.2.5d) to finally obtain

$$\left(U_{22\xi\xi\xi} + \frac{\Delta n}{\alpha a} W_{22\xi\xi\xi}\right) - 2\xi \left(U_{22\xi} + \frac{\Delta n}{\alpha a} W_{22\xi}\right) = \Delta^{1/3} F_{11\xi}^2 + \Delta^{-1/3} \left\{V_{11} F_{11\xi\xi} + V_{11\xi} F_{11\xi}\right\}. \tag{3.2.5e}$$

Here we define

$$F_{11} \;=\; U_{11} + \frac{\Delta n}{\alpha a} W_{11},$$

and from (3.1.5a) and (3.1.5b) we know that

$$F_{11} = B_1 \int_{\xi_0}^{\xi} \mathrm{Ai}(s) ds,$$

$$F_{11\xi} = B_1 \mathrm{Ai}(\xi) \quad \text{and}$$

$$F_{11\xi\xi} = B_1 \mathrm{Ai}'(\xi).$$

What remains to be found is an expression for the first-order vertical velocity term. From the first-order continuity equation (3.1.4a) we can see that

$$\Delta^{1/3} V_{11\xi} = -\Delta F_{11} = -\Delta B_1 \int_{\xi_0}^{\xi} \mathrm{Ai}(s) ds.$$

Integrating we obtain

$$V_{11} = V_{11}(\xi_0) - B_1 \Delta^{2/3} \int_{\xi_0}^{\xi} \int_{\xi_0}^{\xi_2} \mathrm{Ai}(\xi_1) d\xi_1 d\xi_2. \tag{3.2.6a}$$

For the solid wall problem $V_{11}(\xi_0) = 0$. In this problem we know that $V_{11}(\xi_0) = A_y P_{11}$.

So the RHS of (3.2.5e) becomes

$$\Delta^{1/3}B_1^2\left[\mathrm{Ai}(\xi)\int_{\xi_0}^{\xi}\mathrm{Ai}(s)ds-\mathrm{Ai}'(\xi)\int_{\xi_0}^{\xi}\int_{\xi_0}^{\xi_2}\mathrm{Ai}(\xi_1)d\xi_1 d\xi_2+A_y\left(\frac{\mathrm{Ai}'(\xi_0)}{A_y+\frac{\Delta n^2}{\alpha^2a^2}}\right)\mathrm{Ai}'(\xi)\right], \tag{3.2.6b}$$

where we have eliminated P_{11} using (3.1.6a). If we use the identity

$$-\int_{\xi_0}^{\xi}\int_{\xi_0}^{\xi_2}\mathrm{Ai}(\xi_1)d\xi_1 d\xi_2=\mathrm{Ai}'(\xi)-\mathrm{Ai}'(\xi_0)-\xi\int_{\xi_0}^{\xi}\mathrm{Ai}(\xi_1)d\xi_1, \tag{3.2.6c}$$

(which can be shown by using integration by parts) we can rewrite (3.2.6b) as

$$\Delta^{1/3}B_1^2\left[\mathrm{Ai}(\xi)\int_{\xi_0}^{\xi}\mathrm{Ai}(s)ds+[\mathrm{Ai}'(\xi)]^2-\mathrm{Ai}'(\xi)\mathrm{Ai}'(\xi_0)[1-A_y\mathbb{P}_1]-\xi\mathrm{Ai}(\xi)\int_{\xi_0}^{\xi}\mathrm{Ai}(\xi_1)d\xi_1\right]. \tag{3.2.6d}$$

Here we define $\mathbb{P}_1=(A_y+\frac{\Delta n^2}{\alpha^2a^2})^{-1}$ for simplicity. Finally we define $F_{22}=\left(U_{22}+\frac{n}{\alpha a}W_{22}\right)$ and obtain the following equation that describes the nonlinear second-order lower-deck problem

$$\begin{aligned}F_{22\xi\xi\xi}-2\xi F_{22\xi}=\Delta^{1/3}B_1^2\Bigg[&\mathrm{Ai}(\xi)\int_{\xi_0}^{\xi}\mathrm{Ai}(s)ds+[\mathrm{Ai}'(\xi)]^2-\mathrm{Ai}'(\xi)\mathrm{Ai}'(\xi_0)[1-A_y\mathbb{P}_1]\\&-\xi\mathrm{Ai}(\xi)\int_{\xi_0}^{\xi}\mathrm{Ai}(\xi_1)d\xi_1\Bigg].\end{aligned} \tag{3.2.7}$$

The solution to (3.2.7) may be obtained as the superposition of the homogeneous solution and particular integral. If we define a new variable $\widehat{\xi}=2^{1/3}\xi$ then the homogeneous solution may be easily obtained as $B_2\mathrm{Ai}(\widehat{\xi})$, where B_2 is a complex constant. The appropriate form of the particular integral was given by Smith (1979a) allowing modifications for the

porous wall boundary condition. Thus the complete solution to (3.2.7) is

$$F_{22\xi} = B_2 \mathrm{Ai}(\widehat{\xi}) + \Delta^{1/3} B_1^2 \left[F_p(\xi) + \mathrm{Ai}'(\widehat{\xi}) \int_{\xi_0}^{\xi} \mathrm{Ai}(\xi_1) d\xi_1 \right], \tag{3.2.8a}$$

where

$$F_p(\xi) = \mathrm{Ai}(\widehat{\xi}) \int_{\widehat{\xi_0}}^{\widehat{\xi}} \frac{dq}{\mathrm{Ai}^2(q)} \int_{\infty}^{q_1} \mathrm{Ai}(q_2) R(q_2) dq_2, \tag{3.2.8b}$$

$$R(\widehat{\xi}) = -2^{-2/3} \Big[2\mathrm{Ai}(\xi)\mathrm{Ai}''(\xi) + (1 - A_y \mathbb{P}_1)\mathrm{Ai}'(\xi_0)\mathrm{Ai}'(\xi) \Big]. \tag{3.2.8c}$$

We note here that by setting $A_y = 0$ in the expressions for $F_p(\xi)$ and $R(\widehat{\xi})$, we obtain the expressions of Smith (1979a). We can integrate (3.2.8a) once to obtain the solution to the second-order lower-deck problem as

$$F_{22} = B_1^2 \int_{\xi_0}^{\xi} H(t) + B_2 \int_{\xi_0}^{\xi} \mathrm{Ai}(2^{1/3} t) dt, \tag{3.2.8d}$$

where

$$H(\xi) = \Delta^{1/3} \left(F_p(\xi) + \mathrm{Ai}'(\xi) \left(\int_{\xi_0}^{\xi} \mathrm{Ai}(s) ds \right) \right) = \Delta^{1/3} \overline{H}. \tag{3.2.8e}$$

Here we also state an useful result obtained by differentiating (3.2.8e) and evaluating it at $\xi = \xi_0$:

$$\Big[\frac{d\overline{H}}{d\xi} \Big]_{\xi=\xi_0} = \frac{2^{1/3}}{\mathrm{Ai}(\widehat{\xi_0})} \int_{\infty}^{\widehat{\xi_0}} \mathrm{Ai}(q_2) R(q_2) dq_2 + \mathrm{Ai}'(\xi_0)\mathrm{Ai}(\xi_0). \tag{3.2.8f}$$

3.2.2 Mean flow terms

We return to our $O(h^2)$ equations (3.0.6) and recall that the substitution of (3.2.1) leads to mean flow terms such as A_{20}. So we now proceed to collect all terms at $O(E^0)$

to obtain

$$V_{20Y} = 0, \tag{3.2.9a}$$

$$P_{20Y} = 0, \tag{3.2.9b}$$

$$V_{11}U^c_{11Y} + V^c_{11}U_{11Y} + V_{20} + \frac{in}{\alpha}(U_{11}W^c_{11} - W_{11}U^c_{11}) = U_{20YY}, \tag{3.2.9c}$$

$$V_{11}W^c_{11Y} + V^c_{11}W_{11Y} + \Delta U^c_{11}W_{11} - \Delta U_{11}W^c_{11} = W_{20YY}. \tag{3.2.9d}$$

We add (3.2.9c) to $(n/\alpha a)$(3.2.9d) to obtain

$$V_{20} - \left(U_{20YY} + \frac{n}{\alpha a}W_{20YY}\right) = -V_{11}\left(U_{11Y} + \frac{n}{\alpha a}W_{11Y}\right)^c - \{c.c.\}. \tag{3.2.10a}$$

Integrating (3.2.9a) we see that V_{20} =constant= $V_{20}(Y = 0) = A_y P_{20}$, the value on the wall. For the solid case $V_{20} = 0$. So returning to (3.2.10a) and making the transformation in ξ we obtain

$$U_{20\xi\xi} + \frac{n}{\alpha a}W_{20\xi\xi} = \Delta^{-2/3}\left[A_y P_{20} + V_{11}\Delta^{c1/3}\left[U_{11\xi} + \frac{n}{\alpha a}W_{11\xi}\right]^c + \{c.c.\}\right]. \tag{3.2.10b}$$

Using (3.2.6a) and the conjugate of (3.1.5a) and defining a new function

$$\begin{aligned} f^*(\xi) =& \Delta^{2/3}B_1 B_1^c\left[\left(A_y\mathbb{P}_1\mathrm{Ai}(\xi_0) - \int_{\xi_0}^{\xi}\int_{\xi_0}^{\xi_2}\mathrm{Ai}(\xi_1)d\xi_1 d\xi_2\right) + A_y P_{20}\right](\Delta^c)^{1/3}\,\mathrm{Ai}^c(\xi) \\ &+ \{c.c.\}, \end{aligned} \tag{3.2.10c}$$

we can write (3.2.10b) tidily as

$$U_{20\xi\xi} + \frac{n}{\alpha a}W_{20\xi\xi} = \Delta^{-2/3}f^*(\xi). \tag{3.2.11a}$$

Integrating (3.2.11a) twice we can then obtain the mean flow solution as

$$F_{20} = U_{20} + \frac{n}{\alpha a} W_{20} = \Delta^{-2/3} \int_{\xi_0}^{\xi} \int_{\infty}^{\xi_2} f^*(\xi_1) d\xi_1 d\xi_2. \tag{3.2.11b}$$

3.2.3 Second-order problem solution

We have now obtained solutions to the lower-deck problem at $O(E^2)$ and $O(E^0)$. To obtain a complete solution to the second-order problem we need to match these solutions with those obtained from the upper-deck problem. This procedure is similar to the linear analysis of Section 3.1 the end result of which was the eigenrelation (3.1.7). A similar procedure is carried out here, at the end of which, we will obtain a relationship between B_1 and B_2, the complex constants at each order. So we turn to the upper deck solutions. We begin with (3.2.2b), the solution at $O(E^2)$. The appropriate boundary conditions to be satisfied are

$$\tilde{p}_{22}(r_s) = 0, \quad \tilde{p}_{22}(a) = P_{22}, \quad \tilde{p}_{22r}(a) = -4\alpha^2 A_{22}.$$

We can then obtain the particular solution for the upper deck pressure term $\tilde{p}_{22}$ as

$$\begin{aligned} \tilde{p}_{22}(r) &= -2\mathrm{i}\alpha A_{22} \frac{I_{2n}(2\mathrm{i}\alpha r_s) K_{2n}(2\mathrm{i}\alpha r) - I_{2n}(2\mathrm{i}\alpha r) K_{2n}(2\mathrm{i}\alpha r_s)}{I'_{2n}(2\mathrm{i}\alpha a) K_{2n}(2\mathrm{i}\alpha r_s) - I_{2n}(2\mathrm{i}\alpha r_s) K'_{2n}(2\mathrm{i}\alpha a)} \\ &= -2\mathrm{i}\alpha A_{22} G_2(r). \end{aligned} \tag{3.2.12}$$

We now turn to the $O(E^0)$ upper deck problem and see that P_{20} remains arbitrary as matching to the upper deck solution (3.2.2c) gives $\tilde{p}_{20}(a) = \overline{C_{21}} \ln(a/r_s) = P_{20}$. So without loss of generality we can set $P_{20} = 0$ for the remainder of the analysis. This also implies that $V_{20} = 0$. Thus the porous wall does not influence the mean flow perturbations.

We now return to (3.0.6) and apply the boundary condition at $Y = 0$ ($\xi = \xi_0$) to

(3.0.6b) and (3.0.6c) and combining them gives,

$$F_{22Y} = P_{22}\Big[A_y + 2\frac{\Delta n^2}{\alpha a^2}\Big] + A_y P_{11} F_{11Y}. \tag{3.2.13a}$$

By transforming variables to ξ and using (3.1.5a) we obtain

$$P_{22}\Big[A_y + 2\frac{\mathrm{i}n^2}{\alpha a^2}\Big] + \Delta^{1/3} B_1 \mathrm{Ai}(\xi_0) A_y P_{11} = \Delta^{2/3} F_{22\xi\xi}. \tag{3.2.13b}$$

Now we apply the boundary condition as $\xi \to \infty$. We see that $F_{22}|_{\xi\to\infty} = A_{22}$. Thus by $\int_\xi^\infty$(3.2.8a) we get

$$\begin{aligned} A_{22} &= B_2 2^{-1/3} \int_{\widehat{\xi_0}}^{\infty} \mathrm{Ai}(\xi_1) d\xi_1 + \Delta^{1/3} B_1^2 \left[\int_{\xi_0}^{\infty} F_p(\xi) + \int_{\xi_0}^{\infty} \mathrm{Ai}'(\xi_2) \int_{\xi_0}^{\xi_2} \mathrm{Ai}(\xi_1) d\xi_1 d\xi_2 \right] \\ &= B_2 2^{-1/3} \int_{\widehat{\xi_0}}^{\infty} \mathrm{Ai}(\xi_1) d\xi_1 + B_1^2 \int_{\xi_0}^{\infty} H(\xi) d\xi, \end{aligned} \tag{3.2.13c}$$

by using (3.2.8e). Now $\frac{d}{d\xi}$(3.2.8a)$|_{\xi=\xi_0}$ and using (3.2.8f) leads to

$$F_{22\xi\xi}(\xi_0) = 2^{1/3} B_2 \mathrm{Ai}'(\widehat{\xi_0}) + \Delta^{1/3} B_1^2 \left[\frac{dH}{d\xi}\right]_{\xi=\xi_0}. \tag{3.2.13d}$$

We know that $P_{22} = -2\mathrm{i}\alpha A_{22} G_2$ and substituting in (3.2.13c) we can express the second order pressure term as

$$P_{22} = -2\mathrm{i}\alpha G_2 \left[B_{22}^{-1/3} \int_{\widehat{\xi_0}}^{\infty} \mathrm{Ai}(\xi_1) d\xi_1 + B_1^2 \int_{\xi_0}^{\infty} H(\xi) d\xi \right].$$

Using this result and (3.2.13d) in (3.2.13b) gives

$$\left[\left(A_y + \frac{2\mathrm{i}n^2}{\alpha a^2} \right) \left\{ -2\mathrm{i}\alpha G_2 \left[B_2 2^{-1/3} \int_{\widehat{\xi_0}}^{\infty} \mathrm{Ai}(\xi_1) d\xi_1 + B_1^2 \Delta^{1/3} \int_{\xi_0}^{\infty} H(\xi) d\xi \right] \right\} \right.$$

$$+\Delta^{1/3}B_1\mathrm{Ai}(\xi_0)A_y\left(-\Delta A_{11}G_1\right)\Bigg] = \left[2^{1/3}B_2\mathrm{Ai}'(\widehat{\xi_0}) + \Delta^{1/3}B_1^2\frac{dH}{d\xi}(\xi_0)\right]\Delta^{2/3} \quad (3.2.14a)$$

Here we have redefined (3.1.3) as $p_{11} = -\Delta A_{11}G_1(a)$. We can simplify (3.2.14a) and make use of (3.1.6b) to obtain

$$\begin{aligned}
&B_2\left\{2^{5/3}\frac{\mathrm{i}n^2}{\alpha a^2}(\mathrm{i}\alpha)^{1/3}G_2\int_{\widehat{\xi_0}}^{\infty}\mathrm{Ai}(\xi_1)d\xi_1 + 2^{1/3}\mathrm{Ai}'(\widehat{\xi_0})\right\}\\
&+B_2\left\{2^{2/3}(\mathrm{i}\alpha)^{1/3}G_2\int_{\widehat{\xi_0}}^{\infty}\mathrm{Ai}(\xi_1)d\xi_1\right\}A_y = -B_1^2\left\{(\mathrm{i}\alpha)^{1/3}\frac{d\overline{H}}{d\xi}(\xi_0)+\right.\\
&\left.\frac{4\mathrm{i}n^2}{\alpha a^2}G_2(\mathrm{i}\alpha)^{2/3}\int_{\xi_0}^{\infty}\overline{H}(\xi)d\xi\right\}-\\
&B_1^2\left\{2G_2(\mathrm{i}\alpha)^{2/3}\int_{\xi_0}^{\infty}H(\xi)d\xi + G_1(\mathrm{i}\alpha)^{2/3}\mathrm{Ai}(\xi_0)\int_{\xi_0}^{\infty}\mathrm{Ai}(s)ds\right\}Ay
\end{aligned} \quad (3.2.14b)$$

In terms of predefined constants (see Appendix A) we can write the above as

$$\begin{aligned}
&B_2\left\{2\frac{\mathrm{i}n^2}{\alpha^{2/3}a^2}G_2T_{13} - T_{14}\right\} + B_2\left\{\alpha^{1/3}G_2T_{13}\right\}A_y\\
&= -B_1^2\alpha^{1/3}\left\{T_7 + 2\frac{\mathrm{i}n^2}{\alpha^{2/3}a^2}G_2T_{12} + \left[\alpha^{1/3}G_2T_{12} + T_2\frac{G_1}{2}\right]A_y\right\}.
\end{aligned} \quad (3.2.14c)$$

The equation (3.2.14c) relates B_2 to B_1^2. This completes our analysis of the second order nonlinear stability problem.

3.3 Third-order problem

We now turn to our third and final system of equations (3.0.4c) and boundary conditions (3.0.5c) at $O(h^3)$. The analysis at this order will reveal an evolution equation for the unknown amplitude function $A_{11}(\tilde{X})$. The coefficients of the terms in this equation will be complex and they will be evaluated numerically. This in turn will allow us to determine the stabilizing or destabilizing effects of nonlinearity on the flow. We proceed

by seeking solutions of the form

$$A_3 = A_{31}E + A_{32}E^2 + A_{33}E^3 + A^c_{31}E^{-1} + A^c_{32}E^{-2} + A^c_{33}E^{-3} + A_{30}, \tag{3.3.1}$$

with similar expansions for U_3, V_3, W_3, P_3 and $\tilde{p}_3$. Here E is given by (3.0.1).

3.3.1 Lower-deck problem

We begin with the lower-deck equations and substitute our solutions of the form (3.3.1) in (3.0.8a), (3.0.8b) and (3.0.8c). We then collect all terms of $O(E)$. This gives us the following system of equations that describe the lower deck problem.

$$\Delta U_{31} + V_{3Y} + \frac{\mathrm{i}n}{a}W_{31} = -\frac{\partial U_{11}}{\partial \tilde{X}}, \tag{3.3.2a}$$

$$\begin{aligned}
&- \mathrm{i}\Omega_2 U_{11} + U_{31}(\Delta Y - \mathrm{i}\Omega_1) + Y(U_{11\tilde{X}} + \Delta\lambda_2 U_{11}) + \Delta(U^c_{11}U_{22} + U_{11}U_{20}) + \lambda_2 V_{11} \\
&+ V_{22}U^c_{11Y} + V^c_{11}U_{22Y} + V_{11}U_{20Y} + V_{20}U_{11Y} + V_{31} \\
&+ \frac{\mathrm{i}n}{a}\left[2U_{22}W^c_{11} - W_{22}U^c_{11} + W_{20}U_{11}\right] = U_{31YY},
\end{aligned} \tag{3.3.2b}$$

$$\begin{aligned}
&- \mathrm{i}\Omega_2 W_{11} + (-\mathrm{i}\Omega_1 + \Delta Y)W_{31} + Y(W_{11\tilde{X}} + \Delta\lambda_2 W_{11}) + \Delta(2U^c_{11}W_{22} + W_{11}U_{20} - W^c_{11}U_{22}) \\
&+ V_{11}W_{20Y} + V^c_{11}W_{22Y} + V_{20}W_{11Y} + V_{22}W^c_{11Y} \\
&+ \frac{\mathrm{i}n}{a}\left[W^c_{11}W_{22} + W_{20}W_{11}\right] = -\frac{\mathrm{i}n}{a}P_{31} + W_{31YY}.
\end{aligned} \tag{3.3.2c}$$

We will now eliminate the unknown pressure and velocity terms and reduce the system to a single equation in the usual manner. First we take $\frac{\partial}{\partial Y}$(3.3.2c) to get

$$\begin{aligned}
&(-\mathrm{i}\Omega_1 + \Delta Y)W_{31Y} + \Delta W_{31} - \mathrm{i}\Omega_2 W_{11Y} + Y\left[\frac{\partial}{\partial Y}\left(\frac{\partial W_{11}}{\partial \tilde{X}}\right) + \Delta\lambda_2 W_{11Y}\right] \\
&+ \left(\frac{\partial W_{11}}{\partial \tilde{X}} + \Delta\lambda_2 W_{11}\right) + \Delta\left[2U^c_{11}W_{22Y} + 2U^c_{11Y}W_{22} - W^c_{11Y}U_{22} - W^c_{11}U_{22Y} + W_{11Y}U_{20}\right. \\
&\left.+ W_{11}U_{20Y}\right] + V_{11Y}W_{20Y} + V_{11}W_{20YY} + V_{20}W_{11YY} + V^c_{11Y}W_{22Y} + V^c_{11}W_{22YY} + V_{22Y}W^c_{11Y} +
\end{aligned}$$

$$V_{22}W^c_{11YY} + \frac{\mathrm{i}n}{a}\left[W^c_{11}W_{22Y} + W^c_{11Y}W_{22} + W_{20Y}W_{11} + W_{20}W_{11Y}\right] = W_{31YYY}. \tag{3.3.2d}$$

Then we take $\frac{\partial}{\partial Y}$(3.3.2b) and eliminate V_{31Y} using (3.3.2a) to get

$$\begin{aligned}
&(-\mathrm{i}\Omega_1 + \Delta Y)U_{31Y} - \mathrm{i}\Omega_2 W_{11Y} + Y\left[\frac{\partial}{\partial Y}\left(\frac{\partial U_{11}}{\partial \tilde{X}}\right) + \Delta\lambda_2 U_{11Y}\right] + \Delta\lambda_2 U_{11} \\
&+ \Delta\left[U^c_{11Y}U_{22} + U^c_{11}U_{22Y} + U_{11Y}U_{20} + U_{11}U_{20Y}\right] + \lambda_2 V_{11Y} \\
&+ V_{22Y}U^c_{11Y} + V_{22}U^c_{11YY} + V_{11Y}U_{20Y} + V_{11}U_{20YY} + V^c_{11Y}U_{22Y} + V^c_{11}U_{22YY} + V_{20}U_{11YY} \\
&- \frac{\mathrm{i}n}{a}\left[2U_{22Y}W^c_{11Y} + 2U_{22}W^c_{11Y} - W_{22Y}U^c_{11} - W_{22}U^c_{11Y} + W_{20Y}U_{11} + W_{20}U_{11Y}\right] = U_{31YYY}.
\end{aligned} \tag{3.3.2e}$$

Now performing $\frac{n}{\alpha a}$(3.3.2d)+(3.3.2e) and rearranging terms we get

$$\begin{aligned}
&-\mathrm{i}\Omega_2\frac{\partial}{\partial Y}F_{11} - \frac{\partial U_{11}}{\partial \tilde{X}} + \lambda_2\frac{\partial}{\partial Y}V_{11} + \frac{\partial}{\partial Y}\left(\Delta\lambda_2 Y F_{11}\right) + \frac{\partial}{\partial Y}\left(Y\frac{\partial F_{11}}{\partial \tilde{X}}\right) + \Delta\frac{\partial}{\partial Y}\left(F^c_{11}F_{22}\right) \\
&+ \Delta\frac{\partial}{\partial Y}(F_{20}F_{11}) + \frac{\partial}{\partial Y}\left(V_{11}F_{20Y} + V^c_{11}F_{22Y} + V_{22}F^c_{11Y} + V_{20}F_{11Y}\right) \\
&= \left(U_{31YYY} + \frac{n}{\alpha a}W_{31YYY}\right) - \mathrm{i}(\alpha Y - \Omega)\left(U_{31Y} + \frac{n}{\alpha a}W_{31Y}\right),
\end{aligned} \tag{3.3.2f}$$

where F_{11} and F_{22} have been defined previously. To obtain (3.3.2f) we had the term $\frac{\partial U_{11}}{\partial \tilde{X}}$ added and subtracted from the RHS. We now make the transformation in ξ and define $F_{31} = \alpha U_{31} + \frac{n}{a}W_{31}$. This allows us to express our third-order lower-deck problem as

$$\frac{\partial F^3_{31}}{\partial^3 \xi} - \xi\frac{\partial F_{31}}{\partial \xi} = \mathrm{i}\frac{\partial U_{11}}{\partial \tilde{X}} - \Delta^{-2/3}\frac{\partial G}{\partial \xi} - \Omega_2 F_{11\xi}\Delta^{1/3}, \tag{3.3.3a}$$

where we define a new function $G(\xi)$ as

$$G(\xi) = -\alpha\Bigg\{\lambda_2 V_{11} + \Delta F^c_{11}F_{22} + \Delta F_{20}F_{11} + \Delta^{2/3}\lambda_2\big(\xi - \xi_0\big)F_{11} + \Delta^{-1/3}\big(\xi - \xi_0\big)F_{11\tilde{X}}$$

$$+\Delta^{1/3}V_{11}F_{20\xi} + \Delta^{1/3}V_{11}^{c}F_{22\xi} + [\Delta^{1/3}]^{c}V_{22}F_{22\xi}^{c}\Big\}. \tag{3.3.3b}$$

The boundary conditions that need to be satisfied by (3.3.3a) may be obtained from (3.0.8e) and (3.0.8f) as

$$F_{31}(\xi_0) = 0, \qquad V_{31} = A_y P_{31}, \tag{3.3.3c}$$

$$F_{31}(\xi \to \infty) \to \lambda_1(A_{31} + \lambda_2 A_{11}). \tag{3.3.3d}$$

Thus (3.3.3a) along with (3.3.3c) and (3.3.3d) define the third-order lower-deck problem. We can observe that the homogeneous form of this problem is also satisfied by the linear solution (3.1.5). Thus we need a compatibility condition that must hold to ensure the validity of the inhomogeneous solution. This is obtained from the adjoint system of the problem as demonstrated by Hall & Smith (1982).

3.3.2 Upper-deck problem

We now turn to the upper-deck problem at $O(h^3)$, (3.0.8d) to obtain a solution of the upper deck pressure $\tilde{p}_{31}$. We substitute (3.3.1) into (3.0.8d) and (3.0.8g), (3.0.8h) and collect terms proportional to E. This gives us an inhomogeneous equation and corresponding boundary conditions as follows:

$$\tilde{p}_{31rr} + \frac{1}{r}\tilde{p}_{31r} - \left(\frac{n^2}{r^2} - \alpha^2\right)\tilde{p}_{31} = 2\alpha^2 A_{11\tilde{X}} G_1(r), \tag{3.3.4a}$$

$$\tilde{p}_{31}(r_s) = 0, \tag{3.3.4b}$$

$$\tilde{p}_{31}(a) = P_{31}, \tag{3.3.4c}$$

$$\left.\frac{\partial \tilde{p}_{31}}{\partial r}\right|_{r=a} = \mathrm{i}\alpha\frac{dA_{11}}{d\tilde{X}} - \alpha^2 A_{31}. \tag{3.3.4d}$$

Here we have used the definition $\tilde{p}_{11} = -\mathrm{i}\alpha A_{11}(\tilde{X})G_1(r)$. We now define

$$G_1(r) = b_n K_n(\mathrm{i}\alpha r) + c_n I_n(\mathrm{i}\alpha r),$$

where b_n and c_n are defined as

$$b_n = \frac{I_n(\mathrm{i}\alpha r_s)}{I_n'(\mathrm{i}\alpha a)K_n(\mathrm{i}\alpha r_s) - I_n(\mathrm{i}\alpha r_s)K_n'(\mathrm{i}\alpha a)} \tag{3.3.5}$$

$$c_n = \frac{-K_n(\mathrm{i}\alpha r_s)}{I_n'(\mathrm{i}\alpha a)K_n(\mathrm{i}\alpha r_s) - I_n(\mathrm{i}\alpha r_s)K_n'(\mathrm{i}\alpha a)}. \tag{3.3.6}$$

We can now write the solution of (3.3.4a) as the superposition of a complementary function and particular integral. We can immediately see that the complimentary function may be given as

$$\tilde{p}_{31} = F_1 K_n(\mathrm{i}\alpha r) + F_2 I_n(\mathrm{i}\alpha r). \tag{3.3.7a}$$

We choose the particular integral to be of the form

$$\tilde{p}_{31} = D_1(r)K_n(\mathrm{i}\alpha r) + D_2(r)I_n(\mathrm{i}\alpha r), \tag{3.3.7b}$$

subject to

$$D_1'(r)K_n(\mathrm{i}\alpha r) + D_2'(r)I_n(\mathrm{i}\alpha r) = 0. \tag{3.3.7c}$$

Substituting into (3.3.4a) gives

$$\mathrm{i}\alpha\left[D_1'K_n'(\mathrm{i}\alpha r) + D_2'I_n'(\mathrm{i}\alpha r)\right] = 2\alpha^2 A_{11\tilde{X}}\left[b_n K_n(\mathrm{i}\alpha r) + c_n I_n(\mathrm{i}\alpha r)\right]. \tag{3.3.7d}$$

We can then simplify to obtain

$$\begin{aligned} D_1'(r) &= -\mathrm{i}I_n(\mathrm{i}\alpha r)\left[\frac{2\alpha A_{11\tilde{X}}\{b_nK_n(\mathrm{i}\alpha r)+c_nI_n(\mathrm{i}\alpha r)\}}{I_n(\mathrm{i}\alpha r)K_n'(\mathrm{i}\alpha r)-K_n(\mathrm{i}\alpha r)I_n'(\mathrm{i}\alpha r)}\right], \\ D_2'(r) &= \mathrm{i}K_n(\mathrm{i}\alpha r)\left[\frac{2\alpha A_{11\tilde{X}}\{b_nK_n(\mathrm{i}\alpha r)+c_nI_n(\mathrm{i}\alpha r)\}}{I_n(\mathrm{i}\alpha r)K_n'(\mathrm{i}\alpha r)-K_n(\mathrm{i}\alpha r)I_n'(\mathrm{i}\alpha r)}\right]. \end{aligned} \tag{3.3.7e}$$

Integrating and choosing $D_1(r_s) = D_2(r_s) = 0$ gives

$$\begin{aligned} D_1(r) &= -\mathrm{i}\int_{r_s}^{r} I_n(\mathrm{i}\alpha q)\left[\frac{2\alpha A_{11\tilde{X}}\{b_nK_n(\mathrm{i}\alpha q)+c_nI_n(\mathrm{i}\alpha q)\}}{I_n(\mathrm{i}\alpha q)K_n'(\mathrm{i}\alpha q)-K_n(\mathrm{i}\alpha q)I_n'(\mathrm{i}\alpha q)}\right]dq, \\ D_2(r) &= \mathrm{i}\int_{r_s}^{r} K_n(\mathrm{i}\alpha q)\left[\frac{2\alpha A_{11\tilde{X}}\{b_nK_n(\mathrm{i}\alpha q)+c_nI_n(\mathrm{i}\alpha q)\}}{I_n(\mathrm{i}\alpha q)K_n'(\mathrm{i}\alpha q)-K_n(\mathrm{i}\alpha q)I_n'(\mathrm{i}\alpha q)}\right]dq. \end{aligned} \tag{3.3.7f}$$

Recall that we have cast the solution of (3.3.4a) in the form

$$\tilde{p}_{31}(r) = F_1K_n(\mathrm{i}\alpha r) + F_2I_n(\mathrm{i}\alpha r) + D_1(r)K_n(\mathrm{i}\alpha r) + D_2(r)I_n(\mathrm{i}\alpha r), \tag{3.3.8a}$$

subject to (3.3.4b), (3.3.4c) and (3.3.4d). We can solve for F_1 and F_2 using (3.3.4b) and (3.3.4c). We get

$$F_1 = -b_n\left[A_{11\tilde{X}} + \mathrm{i}\alpha A_{31} - D_1(a)K_n'(\mathrm{i}\alpha a) - D_2(a)I_n'(\mathrm{i}\alpha a)\right], \tag{3.3.8b}$$

$$F_2 = -c_n\left[A_{11\tilde{X}} + \mathrm{i}\alpha A_{31} - D_1(a)K_n'(\mathrm{i}\alpha a) - D_2(a)I_n'(\mathrm{i}\alpha a)\right]. \tag{3.3.8c}$$

Finally using (3.3.4d) we get

$$P_{31} = \left[F_1 + D_1(a)\right]K_n(\mathrm{i}\alpha a) + \left[F_2 + D_2(a)\right]I_n(\mathrm{i}\alpha a). \tag{3.3.8d}$$

$D_1(a)$ and $D_2(a)$ remains to be evaluated. It can be shown that the Wronskian $W[I_n(\mathrm{i}\alpha r), K_n(\mathrm{i}\alpha r)] = I_n(\mathrm{i}\alpha r)K_n'(\mathrm{i}\alpha r) - K_n(\mathrm{i}\alpha r)I_n'(\mathrm{i}\alpha r) = -1/\mathrm{i}\alpha r$. Thus we can write

$$D_1(a) = 2\mathrm{i}\alpha A_{11\tilde{X}}[b_n d_n + c_n e_n], \tag{3.3.9a}$$

$$D_2(a) = -2\mathrm{i}\alpha A_{11\tilde{X}}[b_n f_n + c_n d_n]. \tag{3.3.9b}$$

Here we define the following integrals

$$\begin{aligned} d_n &= \int_a^{r_s} \frac{I_n(\mathrm{i}\alpha r)K_n(\mathrm{i}\alpha r)}{W[I_n(\mathrm{i}\alpha r), K_n(\mathrm{i}\alpha r)]} dr, \\ e_n &= \int_a^{r_s} \frac{I_n^2(\mathrm{i}\alpha r)}{W[I_n(\mathrm{i}\alpha r), K_n(\mathrm{i}\alpha r)]} dr, \\ f_n &= \int_a^{r_s} \frac{K_n^2(\mathrm{i}\alpha r)}{W[I_n(\mathrm{i}\alpha r), K_n(\mathrm{i}\alpha r)]} dr. \end{aligned} \tag{3.3.9c}$$

We will now proceed to evaluate these integrals using certain properties of the Bessel functions (Abramovitz & Stegun 1972). If we take $t = \alpha r$, then it can be shown that $I_n(\mathrm{i}t) = e^{1/2n\pi\mathrm{i}} J_n(t)$ and $K_n(\mathrm{i}t) = -\frac{\pi\mathrm{i}}{2} e^{-1/2n\pi\mathrm{i}}[J_n(t) - \mathrm{i}Y_n(t)]$. Thus using this result and the Wronskian we get

$$\begin{aligned} d_n &= -\int_a^{r_s} (\mathrm{i}\alpha r) I_n(\mathrm{i}\alpha r) K_n(\mathrm{i}\alpha r) dr \\ &= -\frac{\pi}{2\alpha} \int_{\alpha a}^{\alpha r_s} [t J_n^2(t) - \mathrm{i}t J_n(t) Y_n(t)] dt, \\ e_n &= -\int_a^{r_s} \mathrm{i}\alpha r I_n^2(\mathrm{i}\alpha r) dr \\ &= -\frac{\mathrm{i}e^{n\pi\mathrm{i}}}{\alpha} \int_{\alpha a}^{\alpha r_s} t J_n^2(t) dt, \\ f_n &= -\int_a^{r_s} \mathrm{i}\alpha r K_n^2(\mathrm{i}\alpha r) dr \\ &= \frac{\mathrm{i}\pi^2}{4\alpha} e^{-n\pi\mathrm{i}} \int_a^{r_s} t[J_n(t) - \mathrm{i}Y_n(t)]^2 dt \\ &= \frac{\mathrm{i}\pi^2}{4\alpha} e^{-n\pi\mathrm{i}} \int_a^{r_s} [t J_n^2(t) - t Y_n^2(t) - 2\mathrm{i}t J_n(t) Y_n(t)] dt. \end{aligned}$$

If we now use the result $J_{-n}(t)J_n(t) = (-1)^n J_n^2(t)$ and $Y_{-n}(t)Y_n(t) = (-1)^n Y_n^2(t)$ we can define three integrals

$$\begin{aligned}
\overline{I}_1 &= \int_a^{r_s} tJ_n^2(t)dt = (-1)^n \int_a^{r_s} tJ_{-n}(t)J_n(t)dt, \\
\overline{I}_2 &= \int_a^{r_s} tY_n^2(t)dt = (-1)^n \int_a^{r_s} tY_{-n}(t)Y_n(t)dt, \\
\overline{I}_3 &= \int_a^{r_s} tJ_n(t)Y_n(t)dt = (-1)^n \int_a^{r_s} tJ_{-n}(t)Y_n(t)dt,
\end{aligned}$$

so that

$$\begin{aligned}
d_n &= -\frac{\pi}{2\alpha}(\overline{I}_1 - \mathrm{i}I_3), \\
e_n &= -\frac{\mathrm{i}}{\alpha} e^{n\pi\mathrm{i}} \overline{I}_1, \\
f_n &= \frac{\mathrm{i}\pi^2}{a\alpha} e^{-n\pi\mathrm{i}} (\overline{I}_1 - \overline{I}_2 - 2\mathrm{i}\overline{I_3}).
\end{aligned}$$

We now evaluate these integrals using the following results

$$\begin{aligned}
\int^z t^{\mu+\nu+1} J_\mu J_\nu dt &= \frac{z^{\mu+\nu+2}}{2(\mu+\nu+1)} [J_\mu J_\nu + J_{\mu+1} J_{\nu+1}], \\
\int^z t^{\mu+\nu+1} Y_\mu Y_\nu dt &= \frac{z^{\mu+\nu+2}}{2(\mu+\nu+1)} [Y_\mu Y_\nu + Y_{\mu+1} Y_{\nu+1}], \\
\int^z t^{\mu+\nu+1} J_\mu Y_\nu dt &= \frac{z^{\mu+\nu+1}}{2(\mu+\nu+1)} [J_\mu Y_\nu + J_{\mu+1} Y_{\nu+1}],
\end{aligned}$$

by setting $\nu = n$ and $\mu = -n$. Thus we obtain

$$\begin{aligned}
\overline{I}_1 &= \frac{\alpha^2 r_s^2}{2} \left[J_n^2(\alpha r_s) - J_{n-1}(\alpha r_s) J_{n+1}(\alpha r_s) \right] \\
&\quad - \frac{\alpha^2 a^2}{2} \left[J_n^2(\alpha a) - J_{n-1}(\alpha a) J_{n+1}(\alpha a) \right], \\
\overline{I}_2 &= \frac{\alpha^2 r_s^2}{2} \left[Y_n^2(\alpha r_s) - Y_{n-1}(\alpha r_s) Y_{n+1}(\alpha r_s) \right] \\
&\quad - \frac{\alpha^2 a^2}{2} \left[Y_n^2(\alpha a) - Y_{n-1}(\alpha a) Y_{n+1}(\alpha a) \right],
\end{aligned}$$

$$\overline{I}_3 = \frac{\alpha^2 r_s^2}{2}\left[J_n(\alpha r_s)Y_n(\alpha r_s) - J_{n-1}(\alpha r_s)Y_{n+1}(\alpha r_s)\right] - \frac{\alpha^2 a^2}{2}\left[J_n(\alpha a)Y_n(\alpha a) - J_{n-1}(\alpha a)Y_{n+1}(\alpha a)\right].$$

We can now revert back to modified Bessel functions I_n and K_n by making the appropriate substitutions in the above expressions to obtain our required constants as

$$d_n = -\frac{\mathrm{i}\alpha r_s^2}{2}[I_n(\mathrm{i}\alpha r_s)K_n(\mathrm{i}\alpha r_s) + I_{n-1}(\mathrm{i}\alpha r_s)K_{n+1}(\mathrm{i}\alpha r_s)] + \frac{\mathrm{i}\alpha a^2}{2}[I_n(\mathrm{i}\alpha a)K_n(\mathrm{i}\alpha a) + I_{n-1}(\mathrm{i}\alpha a)K_{n+1}(\mathrm{i}\alpha a)], \tag{3.3.9d}$$

$$e_n = -\frac{\mathrm{i}\alpha r_s^2}{2}[I_n^2(\mathrm{i}\alpha r_s) - I_{n-1}(\mathrm{i}\alpha r_s)I_{n+1}(\mathrm{i}\alpha r_s)] + \frac{\mathrm{i}\alpha a^2}{2}[I_n^2(\mathrm{i}\alpha a) - I_{n-1}(\mathrm{i}\alpha a)I_{n+1}(\mathrm{i}\alpha a)], \tag{3.3.9e}$$

$$f_n = -\frac{\mathrm{i}\alpha r_s^2}{2}[K_n^2(\mathrm{i}\alpha r_s) - K_{n-1}(\mathrm{i}\alpha r_s)K_{n+1}(\mathrm{i}\alpha r_s)] + \frac{\mathrm{i}\alpha a^2}{2}[K_n^2(\mathrm{i}\alpha a) - K_{n-1}(\mathrm{i}\alpha a)K_{n+1}(\mathrm{i}\alpha a)]. \tag{3.3.9f}$$

This completes our evaluation of $D_1(a)$ and $D_2(a)$. We have thus completed the solution of the third-order upper-deck problem.

3.3.3 Adjoint problem

We are now at the stage where we can complete the solution of the third order problem to obtain the required amplitude equation. Recall that (3.3.3a) is an inhomogeneous differential equation whose homogeneous solution is also a solution of the linear (first-order) problem. The nonlinear forcing terms on the RHS of (3.3.3a) also contain terms involving the linear solution. We thus need to establish a "solvability condition". The approach is to consider the adjoint of the equation (3.3.3a). The adjoint function satisfies the homogeneous problem and is orthogonal to the nonlinear forcing terms over the domain. We then multiply our equation with its adjoint and integrate over the domain of

our problem. This establishes the solvability condition from which an evolution equation for the perturbation amplitude is obtained. Following the methodology of Hall & Smith (1982) we define a vector $\mathbf{W}$ as

$$\mathbf{W} = \begin{pmatrix} F_{31} \\ F_{31\xi} \\ F_{31\xi\xi} \end{pmatrix}$$

so that the third order inhomogeneous problem is given by

$$\frac{\partial \mathbf{W}}{\partial \xi} - \mathbf{D}\mathbf{W} = \begin{pmatrix} 0 \\ 0 \\ \mathrm{i}\frac{\partial U_{11}}{\partial \tilde{X}} - \Delta^{-2/3}\frac{\partial G}{\partial \xi} - \Omega_2 \Delta^{1/3} F_{11\xi} \end{pmatrix} \tag{3.3.10a}$$

where the matrix $\mathbf{D}$ is

$$\mathbf{D} = \begin{pmatrix} 0 & 1 & 0 \\ 0 & 0 & 1 \\ 0 & \xi & 0 \end{pmatrix}$$

Notice that the homogeneous form of the problem is $\frac{\partial \mathbf{W}}{\partial \xi} - \mathbf{D}\mathbf{W} = 0$ whose solution is the eigenrelation from Section 3.1. Now define a system

$$\frac{\partial}{\partial \xi}\begin{pmatrix} P \\ Q \\ R \end{pmatrix} + \mathbf{D}^T \begin{pmatrix} P \\ Q \\ R \end{pmatrix} = 0, \tag{3.3.10b}$$

where

$$R(\infty) = 0, \qquad Q(\xi_0) = 0, \quad \text{and} \quad P(\infty) = \frac{\mathrm{Ai}'(\xi_0)}{\int_{\xi_0}^{\infty} \mathrm{Ai}(\xi) d\xi} R(\xi_0).$$

We now need to obtain the vector $(P, Q, R)^T$ which we then multiply (3.3.10a) by and integrate over the domain $[\xi_0, \infty]$. However we can notice from (3.3.10a) that it is the third row of the matrix equation that corresponds to (3.3.3a) so in effect we only need to obtain $R(\xi)$ and use it to multiply (3.3.3a). Proceeding to analyse the system (3.3.10a) we see that

$$\begin{aligned}
&\frac{\partial}{\partial \xi} \begin{pmatrix} P \\ Q \\ R \end{pmatrix} + \begin{pmatrix} 0 \\ P + \xi R \\ Q \end{pmatrix} = 0, \\
&\implies \frac{\partial P}{\partial \xi} = 0, \quad \frac{\partial Q}{\partial \xi} + P + \xi R = 0, \quad \frac{\partial R}{\partial \xi} + Q = 0, \\
&\implies \frac{\partial^2 R}{\partial \xi^2} - \xi R = P = \text{constant},
\end{aligned}$$

a homogeneous solution of which is simply $\mathrm{Ai}(\xi)$. Consider now a function $L(\xi)$ such that

$$\frac{\partial^2 L}{\partial \xi^2} - \xi L = 1. \tag{3.3.10c}$$

A particular integral of this equation is $bL(\xi)$, where b is a constant. Following Hall & Smith (1982) we can then write the solution as

$$R = \mathrm{Ai}(\xi) + bL(\xi). \tag{3.3.10d}$$

Since $Q(\xi_0) = 0$ we can get $R'(\xi_0) = 0$ and thus $b = -\frac{\mathrm{Ai}'(\xi_0)}{L'(\xi_0)}$. We now need to seek a solution to (3.3.10c). Using the method of reduction of order we let $L(\xi) = u(\xi)\mathrm{Ai}(\xi)$.

We can then show that

$$u(\xi) = \int_{\xi_0}^{\xi} \frac{ds}{\mathrm{Ai}^2(s)} \int_{\infty}^{s} \mathrm{Ai}(q)dq,$$

so

$$L(\xi) = \mathrm{Ai}(\xi) \int_{\xi_0}^{\xi} \frac{ds}{\mathrm{Ai}^2(s)} \int_{\infty}^{s} \mathrm{Ai}(q)dq. \tag{3.3.10e}$$

We now multiply both sides of (3.3.3a) by (3.3.10d) and integrate over $[\xi_0, \infty]$. Thus

$$\begin{aligned} &\int_{\xi_0}^{\infty} \big[\mathrm{Ai}(\xi) + bL(\xi)\big]\big[F_{31\xi\xi\xi} - \xi F_{31\xi}\big]d\xi = \\ &\int_{\xi_0}^{\infty} \big[\mathrm{Ai}(\xi) + bL(\xi)\big] \left[\mathrm{i}\frac{\partial U_{11}}{\partial \tilde{X}} - \Delta^{-2/3}\frac{\partial G}{\partial \xi} - \Omega_2 \Delta^{1/3} F_{11\xi}\right] d\xi. \end{aligned} \tag{3.3.10f}$$

We have now obtained the orthogonality condition, which we can manipulate to derive our required amplitude equation.

3.3.4 Amplitude equation

We will begin with the LHS of (3.3.10f). We know that $R(\infty) = 0$, $R'(\xi_0) = 0$ and $L(\xi_0) = 0$. Integrating by parts and using these results we get

$$-\mathrm{Ai}(\xi_0)F_{31\xi\xi}(\xi_0) - \Big[R'(\xi)F_{31\xi}\Big]_{\xi_0}^{\infty} + \int_{\xi_0}^{\infty} F_{31\xi}R''(\xi)d\xi = \int_{\xi_0}^{\infty} F_{31\xi}[\xi R(\xi)]d\xi.$$

Using $\mathrm{Ai}''(\xi) = \xi \mathrm{Ai}(\xi)$, along with $F_{31\xi}(\infty) = 0$, and $R'(\xi_0) = 0$ we can simplify the above expression to get

$$-\mathrm{Ai}(\xi_0)F_{31\xi\xi}(\xi_0) + \int_{\xi_0}^{\infty} F_{31\xi}[bL''(\xi) - \xi bL(\xi)]d\xi,$$

and using (3.3.10c) we get

$$-\mathrm{Ai}(\xi_0)F_{31\xi\xi}(\xi_0) + b\int_{\xi_0}^{\infty} F_{31\xi}d\xi.$$

Now if we use the conditions on F_{31} from (3.3.3c) and (3.3.3d) we will get

$$\mathrm{LHS}(3.3.10\mathrm{f}) = -\mathrm{Ai}(\xi_0)F_{31\xi\xi}(\xi_0) + b\left[A_{31} + \lambda_2 A_{11}\right], \tag{3.3.11a}$$

where we now need to find $F_{31\xi\xi}$ at $\xi = \xi_0$. To do this we turn to our momentum equations and take $\alpha(3.3.2\mathrm{b}) + n/a(3.3.2\mathrm{c})$ with $Y = 0$. Transforming variables to ξ and evaluating all terms involving our first-order and second-order solutions at ξ_0, we get

$$\begin{aligned}\left[\alpha U_{31\xi\xi} + \frac{n}{a}\alpha W_{31\xi\xi}\right]_{\xi=\xi_0} &= \Delta^{-2/3}\left\{\frac{\mathrm{i}n^2}{a^2}P_{31} + \alpha V_{31} + \alpha\lambda_2 V_{11}\right\}_{\xi=\xi_0} \\ &\quad + \alpha\Delta^{-1/3}\left\{V_{22}F^c_{11\xi} + V^c_{11}F_{22\xi} + V_{11}F_{20\xi}\right\}_{\xi=\xi_0},\end{aligned} \tag{3.3.11b}$$

where we have $F_{11}(\xi_0) = B_1\mathrm{Ai}(\xi_0)$, $F_{20}(\xi_0) = \Delta^{-2/3}\int_{\infty}^{\xi_0} f^*(\xi)d\xi$ and $F_{22}(\xi_0) = B_2\mathrm{Ai}(\widehat{\xi_0})$. We also use $V_{ii} = A_y P_{ii}$, where $P_{11} = -\Delta A_{11}G_1(a)$ and $P_{22} = -2\Delta A_{22}G_2(a)$. Thus we can write (3.3.11a) as

$$\begin{aligned}&-\mathrm{Ai}(\xi_0)\left[\Delta^{-2/3}\left\{\left(\alpha A_y + \frac{\mathrm{i}n^2}{a^2}\right)P_{31} + \alpha\lambda_2 A_y P_{11}\right\}\right. \\ &\left.+\,\alpha\Delta^{-1/3}\left\{B_1^c\mathrm{Ai}(\xi_0)^c A_y P_{22} + (A_y P_{11})^c\, B_2\mathrm{Ai}(\widehat{\xi_0}) + \Delta^{-2/3}A_y P_{11}\int_{\infty}^{\xi_0} f^*(s)ds\right\}\right] \\ &+\, b\alpha\left[A_{31} + \lambda_2 A_{11}\right].\end{aligned} \tag{3.3.11c}$$

If we differentiate (3.3.10e) we can express the constant b as

$$b = \frac{\mathrm{Ai}'(\xi_0)\mathrm{Ai}(\xi_0)}{\int_{\xi_0}^{\infty}\mathrm{Ai}(s)ds}. \tag{3.3.12}$$

The objective now is to express all terms in our adjoint problem in terms of the amplitude functions. We begin with A_{31}. By looking at the RHS of (3.3.10f) we can see that it contains no A_{31} terms. We turn to LHS of (3.3.10f) and see that A_{31} appears both explicitly and from the P_{31} term. By looking at (3.3.8b) and (3.3.8c), we see that the expressions for F_1 and F_2 contain terms with A_{31}. Thus writing out explicitly all coefficients of A_{31} in the LHS of (3.3.10f) we see that

$$-\mathrm{Ai}(\xi_0)\overbrace{\Delta^{1/3}\mathbb{P}_1^{-1}\Big[b_nK_n(\mathrm{i}\alpha a)+c_nI_n(\mathrm{i}\alpha a)\Big]}^{\star}+\frac{\mathrm{Ai}'(\xi_0)\mathrm{Ai}(\xi_0)}{\int_{\xi_0}^{\infty}\mathrm{Ai}(s)ds}, \tag{3.3.13}$$

where from (3.1.7), the linear dispersion relation, we can see that term $\star = \frac{\mathrm{Ai}'(\xi_0)}{\int_{\xi_0}^{\infty}\mathrm{Ai}(s)ds}$. Thus we see that all terms that are coefficients of A_{31} cancel. We have thus eliminated A_{31} terms.

We now turn our attention to terms that contain A_{11} and A_{22}. We can express A_{22} in terms of A_{11} using the results from our second-order analysis since we may write $B_1 = A_{11}/\kappa$, where $\kappa = \int_{\xi_0}^{\infty}\mathrm{Ai}(s)ds$. Thus (3.2.14c) may be written as

$$B_2 = -\frac{A_{11}^2}{\kappa^2}\alpha^{1/3}(B_5B_6), \tag{3.3.14a}$$

where B_5 and B_6 are

$$B_5^{-1} = \left\{2\frac{\mathrm{i}n^2}{\alpha^{2/3}a^2}G_2T_{13} - T_{14} + \left\{\alpha^{1/3}G_2T_{13}\right\}A_y\right\}, \tag{3.3.14b}$$

$$B_6 = \left\{T_7 + 2\frac{\mathrm{i}n^2}{\alpha^{2/3}a^2}G_2T_{12} + \left[\alpha^{1/3}G_2T_{12} + T_2\frac{G_1}{2}\right]A_y\right\}. \tag{3.3.14c}$$

This allows us to write (3.2.13c) as

$$A_{22} = -\frac{A_{11}^2}{\kappa^2}\left[2^{-1/3}\left(\int_{\widehat{\xi_0}}^{\infty}\mathrm{Ai}(s)ds\right)B_5B_6 + \Delta^{1/3}\int_{\xi_0}^{\infty}\overline{H}(s)ds\right] \tag{3.3.14d}$$

and (3.2.10c) as

$$\int_{\infty}^{\xi_0} f^*(\xi)d\xi = \Delta|A_{11}|^2|M_1|^2\left[\int_{\infty}^{\xi_0} f^{**}(\xi)d\xi\right],$$

where

$$f^{**}(\xi) = \mathrm{i}^{1/3}\mathrm{Ai}^c(\xi)\left\{\mathbb{P}_1 A_y \mathrm{Ai}(\xi_0) + \left[\mathrm{Ai}'(\xi) - \mathrm{Ai}'(\xi_0) - \xi\int_{\xi_0}^{\xi}\mathrm{Ai}(t)dt\right]\right\} + \{c.c.\}. \tag{3.3.14e}$$

We now turn back to (3.3.11c) describing the LHS of (3.3.10f).

We define $\mathbb{P}_2 = \left(A_y + \frac{2\Delta n^2}{(\alpha a)^2}\right)^{-1}$ and rename G_1 and G_2 as g_n and g_{2n} respectively. The pressure term P_{31} contains terms proportional to $A_{11\tilde{X}}$. P_{31} is defined by (3.3.4a) where F_1, F_2 are defined by (3.3.8b) and (3.3.8c) and $D_1(a)$, $D_2(a)$ are defined by (3.3.9a) and (3.3.9b) respectively. We will make use of the linear eigenrelation (3.1.7) to express g_n in terms of Airy functions where possible. We will also use predefined constants, L_{ij}, and T_{ij} listed in Appendix A to write the equations in a compact manner. Since we can write $A_{11}A_{11}^c = |A_{11}|^2$, we will find that some terms from $F_{31\xi\xi}(\xi_0)$ are proportional to $A_{11}|A_{11}|^2$, while the remaining terms are proportional to $\lambda_2 A_{11}$. Thus

$$\begin{aligned}\text{LHS terms multiplying } \frac{\partial A_{11}}{\partial \tilde{X}} = \\ &\mathrm{i}\mathrm{Ai}(\xi_0)\mathrm{Ai}'(\xi_0)\kappa^{-1} - 2(\mathrm{i}\alpha)^{1/3}\mathrm{Ai}(\xi_0)\alpha\mathbb{P}_1^{-1}\times \\ &\Bigg[(b_n f_n + c_n d_n)\left\{K_n(\mathrm{i}\alpha a) - \frac{\mathrm{Ai}'(\xi_0)}{\kappa}(\mathrm{i}\alpha)^{-1/3}\mathbb{P}_1 K_n'(\mathrm{i}\alpha a)\right\} \\ &- (b_n d_n + c_n e_n)\left\{I_n(\mathrm{i}\alpha a) - \frac{\mathrm{Ai}'(\xi_0)}{\kappa}(\mathrm{i}\alpha)^{-1/3}\mathbb{P}_1 I_n'(\mathrm{i}\alpha a)\right\}\Bigg] \\ &= -\mathrm{i}^{4/3}T_3\kappa^{-1} - 2(\mathrm{i}\alpha)^{1/3}\mathrm{Ai}(\xi_0)\alpha\mathbb{P}_1^{-1}\times\end{aligned}$$

$$\left[(b_n f_n + c_n d_n)\left\{K_n(\mathrm{i}\alpha a) - \frac{\mathrm{Ai}'(\xi_0)}{\kappa}(\mathrm{i}\alpha)^{-1/3}\mathbb{P}_1 K_n'(\mathrm{i}\alpha a)\right\}\right.$$
$$\left. - (b_n d_n + c_n e_n)\left\{I_n(\mathrm{i}\alpha a) - \frac{\mathrm{Ai}'(\xi_0)}{\kappa}(\mathrm{i}\alpha)^{-1/3}\mathbb{P}_1 I_n'(\mathrm{i}\alpha a)\right\}\right]. \tag{3.3.15a}$$

$$\text{LHS terms multiplying } \lambda_2 A_{11} = \alpha\Big[\mathrm{Ai}'(\xi_0)\mathrm{Ai}(\xi_0)\kappa^{-1} + A_y\left(\mathrm{Ai}(\xi_0)g_n\Delta^{1/3}\right)\Big]$$
$$= \alpha\left\{-\mathrm{i}^{1/3}T_3\kappa^{-1} - \mathrm{i}^{1/3}T_3\kappa^{-1}A_y\right\}. \tag{3.3.15b}$$

$$\text{LHS terms multiplying } A_{11}|A_{11}|^2 = -\alpha\mathrm{Ai}(\xi_0)(\mathrm{i}\alpha)^{-1/3}\left[V_{22}F_{11\xi} + V_{11}^c F_{22\xi} + V_{11}F_{20\xi}\right]_{\xi=\xi_0}. \tag{3.3.15c}$$

We do not need to consider the last set of terms as we will show later that similar terms arise on the RHS of the equation that allows us to cancel them. In the solid case these set of LHS terms would be zero.

We have now completed the consideration of the LHS of our adjoint problem. We can now consider

$$\text{RHS(3.3.10f)} = \int_{\xi_0}^{\infty}\left[\mathrm{Ai}(\xi) + bL(\xi)\right]\left\{\mathrm{i}U_{11\tilde{X}} - \Delta^{-2/3}G_\xi - \Omega_2\Delta^{1/3}F_{11\xi}\right\}d\xi. \tag{3.3.16a}$$

We will begin by expressing $\frac{\partial U_{11}}{\partial \tilde{X}}$ in terms of A_{11}. From the lower-deck equation (3.1.4c) we can write

$$W_{11\xi\xi} - \xi W_{11} = \Delta^{-2/3}\frac{\mathrm{i}n}{a}P_{11}.$$

Since P_{11} is not a function of ξ, the above is just an inhomogeneous Airy's equation with

a constant in RHS. Thus the solution may be written as

$$W_{11} = \Delta^{-2/3}\frac{\mathrm{i}n}{a}P_{11}L(\xi) = \frac{\mathrm{i}n}{a}\frac{\mathrm{Ai}'(\xi_0)}{\kappa}\mathbb{P}_1 A_{11}L(\xi).$$

Going back to the first-order problem we know that

$$F_{11} = B\int_{\xi_0}^{\xi}\mathrm{Ai}(s)ds = A_{11}\kappa^{-1}\int_{\xi_0}^{\xi}\mathrm{Ai}(s)ds, \tag{3.3.16b}$$

using (3.1.6b). So we can now express $\frac{\partial U_{11}}{\partial \tilde{X}}$ as

$$\frac{\partial U_{11}}{\partial \tilde{X}} = \frac{\partial A_{11}}{\partial \tilde{X}}\left\{\kappa^{-1}\left(\int_{\xi_0}^{\xi}\mathrm{Ai}(s)ds\right) - \frac{\mathrm{i}n}{a}\frac{\mathrm{Ai}'(\xi_0)}{\kappa}\mathbb{P}_1 L(\xi)\right\}. \tag{3.3.16c}$$

We will now rename the adjoint function $R(\xi)$ as $K(\xi)$ and write the first term in (3.3.16a) as

$$\begin{aligned}\int_{\xi_0}^{\infty}\left[K(\xi)\{\mathrm{i}U_{11\tilde{X}}\}\right]d\xi =& \frac{\partial A_{11}}{\partial \tilde{X}}\left[\mathrm{i}\kappa^{-1}\int_{\xi_0}^{\infty}K(\xi)\Big(\int_{\xi_0}^{\xi}\mathrm{Ai}(s)ds\Big)d\xi\right.\\ &\left.+\frac{n^2}{\alpha a^2}\frac{\mathrm{Ai}'(\xi_0)}{\kappa}\mathbb{P}_1\int_{\xi_0}^{\infty}K(\xi)L(\xi)d\xi\right].\end{aligned} \tag{3.3.16d}$$

The third term in (3.3.16a) becomes

$$-\int_{\xi_0}^{\infty}K(\xi)\{\Omega_2\Delta^{1/3}A_{11}\mathrm{Ai}(\xi)\kappa^{-1}\}d\xi = -\left(\int_{\xi_0}^{\infty}K(\xi)\mathrm{Ai}(\xi)d\xi\right)\Delta^{1/3}\Omega_2\kappa^{-1}A_{11}. \tag{3.3.16e}$$

Using integration by parts we can show that

$$\int_{\xi_0}^{\infty}K(\xi)\mathrm{Ai}(\xi)d\xi = -\int_{\xi_0}^{\infty}\left[K'(\xi)\left(\int_{\xi_0}^{\xi}\mathrm{Ai}(s)ds\right)d\xi\right].$$

Thus (3.3.16e) becomes

$$\Omega_2 A_{11}\Delta^{1/3}\kappa^{-1}\left(\int_{\xi_0}^{\infty}\left[K'(\xi)\left(\int_{\xi_0}^{\xi}\mathrm{Ai}(s)ds\right)d\xi\right]\right) = (\mathrm{i}\alpha^{1/3})\frac{T_{18}}{\kappa}. \tag{3.3.16f}$$

We now need to consider the expression $\frac{\partial G}{\partial \xi}$ in (3.3.16a). We can see that this expression contains terms multiplying $\lambda_2 A_{11}$, $A_{11\tilde{X}}$ and $A_{11}|A_{11}|^2$. We will begin by considering terms multiplying $\lambda_2 A_{11}$. These terms are

$$-\alpha(\mathrm{i}\alpha)^{-2/3}\int_{\xi_0}^{\infty}K(\xi)\frac{\partial}{\partial\xi}\left[V_{11}+\Delta^{2/3}\big(\xi-\xi_0\big)F_{11}\right]d\xi. \tag{3.3.17a}$$

By using (3.2.6c) and (3.2.6a) and then substituting in the above we will obtain

$$\frac{\alpha}{\kappa}\int_{\xi_0}^{\infty}K(\xi)(\xi-\xi_0)\mathrm{Ai}(\xi)d\xi, \tag{3.3.17b}$$

which using integration by parts may be written as

$$\frac{\alpha}{\kappa}\left\{\left[K(\xi)(\xi-\xi_0)\int_{\xi_0}^{\xi}\mathrm{Ai}(s)ds\right]_{\xi_0}^{\infty}-\int_{\xi_0}^{\infty}\frac{\partial}{\partial\xi}\left[K(\xi)(\xi-\xi_0)\right]\left(\int_{\xi_0}^{\xi}\mathrm{Ai}(s)ds\right)d\xi\right\}. \tag{3.3.17c}$$

The second term in the above may be written as

$$-\frac{\alpha}{\kappa}\int_{\xi_0}^{\xi}\Big((\xi-\xi_0)K'(\xi)+K(\xi)\Big)\left(\int_{\xi_0}^{\xi}\mathrm{Ai}(s)ds\right)d\xi = -\frac{\alpha}{\kappa}\mathrm{i}^{1/3}T_1. \tag{3.3.17d}$$

We need to evaluate the upper limit of the first term in (3.3.17c). By using the definitions of $L(\xi)$ and $K(\xi)$ and noting that for $\xi >> 1$, $L(\xi)\sim -\frac{1}{\xi}$ we can obtain the following result

$$\lim_{\xi\to\infty}\left[K(\xi)(\xi-\xi_0)\int_{\xi_0}^{\xi}\mathrm{Ai}(s)ds\right] = \lim_{\xi\to\infty}\left\{\left[\mathrm{Ai}(\xi)-\frac{\mathrm{Ai}'(\xi_0)L(\xi)}{L'(\xi_0)}\right](\xi-\xi_0)\int_{\xi_0}^{\xi}\mathrm{Ai}(s)ds\right\}$$

$$= \frac{\mathrm{Ai}'(\xi_0)}{L'(\xi_0)} \int_{\xi_0}^{\infty} \mathrm{Ai}(s)ds = -\mathrm{Ai}(\xi_0)\mathrm{Ai}'(\xi_0). \tag{3.3.17e}$$

We may thus write (3.3.17c) as

$$-\frac{\alpha}{\kappa}\mathrm{i}^{1/3}T_1 + \frac{\alpha}{\kappa}\mathrm{i}^{1/3}T_3. \tag{3.3.17f}$$

We will now consider the term in $\frac{\partial G}{\partial \xi}$ multiplying $A_{11\tilde{X}}$. This term is

$$(\mathrm{i}\alpha)^{-1/3}(\xi - \xi_0)F_{11\tilde{X}} = A_{11\tilde{X}}\kappa^{-1}(\mathrm{i}\alpha)^{-1/3}(\xi - \xi_0)\left(\int_{\xi_0}^{\xi} \mathrm{Ai}(s)ds\right).$$

Thus the term proportional to $A_{11\tilde{X}}$ in (3.3.16a) is

$$\begin{aligned} &-\mathrm{i}\kappa^{-1}\int_{\xi_0}^{\infty} K(\xi)\frac{\partial}{\partial \xi}\left[(\xi - \xi_0)\left(\int_{\xi_0}^{\xi}\mathrm{Ai}(s)ds\right)\right]d\xi, \\ &= -\mathrm{i}\kappa^{-1}\int_{\xi_0}^{\infty} K(\xi)\left(\int_{\xi_0}^{\xi}\mathrm{Ai}(s)ds\right)d\xi + \mathrm{i}^{4/3}\kappa^{-1}T_1 - \mathrm{i}^{4/3}T_3. \end{aligned} \tag{3.3.18a}$$

By combining (3.3.16d) and (3.3.18a) we can get

$$\begin{aligned} &\text{RHS terms multiplying } \frac{\partial A_{11}}{\partial \tilde{X}} = \\ &= \mathrm{i}^{4/3}\frac{T_1}{\kappa} - \mathrm{i}^{4/3}\frac{T_3}{\kappa} + \frac{n^2}{\alpha a^2}\frac{\mathrm{Ai}'(\xi_0)}{\kappa}\mathbb{P}_1\int_{\xi_0}^{\infty} K(\xi)L(\xi)d\xi. \end{aligned} \tag{3.3.18b}$$

We will now define a new function $P(\xi)$ that contains all terms proportional to $A_{11}|A_{11}|^2$ in $\frac{\partial G}{\partial \xi}$. We can use integration by parts to write these terms from (3.3.16a) as

$$\begin{aligned} &\alpha\Delta^{-2/3}\int_{\xi_0}^{\infty} K(\xi)\frac{\partial}{\partial \xi}\Big[P(\xi)\Big]d\xi = \alpha\Delta^{-2/3}\left(\Big[P(\xi)K(\xi)\Big]_{\xi_0}^{\infty} - \int_{\xi_0}^{\infty} K'(\xi)P(\xi)d\xi\right) \\ &= -\alpha\Delta^{-2/3}P(\xi_0)\mathrm{Ai}(\xi_0) - \alpha\Delta^{-2/3}\int_{\xi_0}^{\infty} K'(\xi)P(\xi)d\xi. \end{aligned} \tag{3.3.19a}$$

Here

$$P(\xi_0) = \left[\Delta F_{11}^c F_{22} + \Delta F_{20} F_{11} + \Delta^{1/3} V_{11} F_{20\xi} + \Delta^{1/3} V_{11}^c F_{22\xi} + (\Delta^c)^{1/3} V_{22} F_{22\xi}^c\right]_{\xi=\xi_0} \tag{3.3.19b}$$

Since $F_{11}(\xi_0) = 0$ we can see that $-\alpha \mathrm{Ai}(\xi_0)(\mathrm{i}\alpha)^{-1/3}\left[V_{22}F_{11\xi} + V_{11}^c F_{22\xi} + V_{11}F_{20\xi}\right]_{\xi=\xi_0}$ cancels with $-\alpha\Delta^{-2/3}\mathrm{Ai}(\xi_0)P(\xi_0)$. So we are left with the following expression on the RHS to consider:

$$-\alpha\Delta^{-2/3}\int_{\xi_0}^{\infty} K'(\xi)P(\xi)d\xi. \tag{3.3.19c}$$

We need to turn to the definition of $G(\xi)$, (3.3.3b) and examine each of the terms in the expression

$$P(\xi) = \Delta F_{11}^c F_{22} + \Delta F_{20}F_{11} + \Delta^{1/3}V_{11}F_{20\xi} + \Delta^{1/3}V_{11}^c F_{22\xi} + V_{22}\left(\Delta^{1/3}F_{11\xi}\right)^c,$$

one by one. We begin with

$$\Delta F_{11}^c F_{22} = \Delta\left(\frac{A_{11}}{\kappa}\int_{\xi_0}^{\xi}\mathrm{Ai}(s)ds\right)^c\left(B_2\int_{\xi_0}^{\xi}\mathrm{Ai}(2^{1/3}s)ds + \Delta^{1/3}\frac{A_{11}^2}{\kappa^2}\int_{\xi_0}^{\xi}\overline{H}(s)ds\right).$$

Thus

$$-\alpha\left(\mathrm{i}\alpha\right)^{-2/3}\int_{\xi_0}^{\infty}K'(\xi)(\mathrm{i}\alpha)F_{11}^cF_{22}d\xi = \frac{-\alpha\left(\mathrm{i}\alpha\right)^{-2/3}}{\kappa|\kappa|^2}\left[\alpha^{4/3}B_5B_6T_9 - \alpha^{4/3}T_8\right]. \tag{3.3.20a}$$

Next we look at

$$\Delta F_{20}F_{11} = \Delta\left[(\mathrm{i}\alpha)^{-2/3}\int_{\xi_0}^{\xi}\left(\int_{\infty}^{\xi_0}f^{**}(t)dt\right)d\xi\frac{|A_{11}|^2}{|\kappa|^2}\right]\left[\frac{A_{11}}{\kappa}\int_{\xi_0}^{\xi}\mathrm{Ai}(s)ds\right].$$

Thus

$$-\alpha\left(\mathrm{i}\alpha\right)^{-2/3}\int_{\xi_0}^{\infty}K'(\xi)(\mathrm{i}\alpha)F_{20}F_{11}d\xi=\frac{-\alpha\left(\mathrm{i}\alpha\right)^{-2/3}}{\kappa|\kappa|^2}\left(-\alpha^{4/3}T_6\right). \tag{3.3.20b}$$

Next we look at

$$\Delta^{1/3}V_{11}F_{20\xi}=\Delta^{1/3}\left[A_yP_{11}+\frac{A_{11}}{\kappa}\left(\mathrm{Ai}'(\xi)-\mathrm{Ai}'(\xi_0)-\xi\int_{\xi_0}^{\xi}\mathrm{Ai}(s)ds\right)\right]\times$$
$$\frac{A_{11}|^2}{|\kappa|^2}\left[\alpha\int_{\infty}^{\xi}f^{**}(t)dt\right].$$

Thus

$$-\alpha\left(\mathrm{i}\alpha\right)^{-2/3}\int_{\xi_0}^{\infty}K'(\xi)\Delta^{1/3}V_{11}F_{20\xi}=\frac{-\alpha\left(\mathrm{i}\alpha\right)^{-2/3}}{\kappa|\kappa|^2}\left\{\alpha^{4/3}T_{15}+\alpha^2T_{22}\mathbb{P}_1A_y\right\}. \tag{3.3.20c}$$

Next we look at

$$\Delta^{1/3}V_{11}^cF_{22\xi}=-\Delta^{1/3}\left[A_y^cP_{11}^c+\Delta^{2/3c}\frac{A_{11}^c}{\kappa^c}\left(\mathrm{Ai}'(\xi)-\mathrm{Ai}'(\xi_0)-\xi\int_{\xi_0}^{\infty}\mathrm{Ai}(s)ds\right)^c\right]\times$$
$$\frac{A_{11}^2}{\kappa^2}\left[B_5B_6\mathrm{Ai}(\widehat{\xi})+\Delta^{1/3}\overline{H}(\xi)\right].$$

Thus

$$-\alpha\left(\mathrm{i}\alpha\right)^{-2/3}\int_{\xi_0}^{\infty}K'(\xi)\Delta^{1/3}V_{11}^cF_{22\xi}d\xi=$$
$$-\frac{-\alpha\left(\mathrm{i}\alpha\right)^{-2/3}}{\kappa|\kappa|^2}\left\{\alpha^{4/3}T_{16}-\alpha^{4/3}T_{17}B_5B_6+A_y^c\mathbb{P}_1^c\left(\alpha^{4/3}T_{23}-\alpha^{4/3}B_5B_6T_{24}\right)\right\}. \tag{3.3.20d}$$

The remaining term to be examined contains the second-order velocity term V_{22}, for which we have not yet found an explicit expression. This may be obtained from the continuity equation at second order (3.2.4a). Integrating (3.2.4a) and substituting in the second-

order solution (3.2.8a) we obtain the solution

$$V_{22} = A_y P_{22} + |A_{11}|^2 \kappa^{-2} \left[2\alpha^{1/3} \Delta^{2/3} B_5 B_6 \int_{\xi_0}^{\xi} \left(\int_{\xi_0}^{t} \mathrm{Ai}(2^{1/3} s) ds \right) dt - 2\Delta \int_{\xi_0}^{\xi} \left(\int_{\xi_0}^{t} \overline{H}(s) ds \right) dt \right].$$

We can express the term P_{22} in terms of known functions from (3.2.13a). Thus

$$P_{22} = \mathbb{P}_2 \left[-\mathrm{i}^{-2/3} \alpha^{-1/3} B_5 B_6 \mathrm{Ai}' \left(\widehat{\xi}_0 \right) + (\mathrm{i}\alpha)^{-1/3} \overline{H}'(\xi_0) - A_y \left[(\mathrm{i}\alpha) \mathrm{Ai}'(\xi_0) \mathrm{Ai}(\xi_0) \mathbb{P}_1 \right] \right].$$

The term occurring in the RHS is

$$- \alpha \left(\mathrm{i}\alpha \right)^{-2/3} \int_{\xi_0}^{\infty} K'(\xi) \Delta^{1/3c} V_{22} F^c_{11\xi} d\xi = \tag{3.3.20e}$$

$$- \frac{\alpha \left(\mathrm{i}\alpha \right)^{-2/3}}{\kappa |\kappa|^2} \left\{ 2\alpha^{4/3} B_5 B_6 T_{11} - 2\alpha^{4/3} T_{10} \right\} + \tag{3.3.20f}$$

$$- \frac{\mathrm{i}^{-2/3} \left(\alpha \right)^{5/3}}{\kappa |\kappa|^2} A_y \mathbb{P}_2 T_{25} \left[\alpha^{-4/3} T_{14} B_5 B_6 + \alpha^{-4/3} T_7 - A_y \mathbb{P}_1 T_{13} \right]. \tag{3.3.20g}$$

We have now completely expressed the adjoint problem (3.3.10f) as an equation for the amplitude function $A_{11}(\tilde{X})$, which we can express as

$$a_1 \frac{dA_{11}}{d\tilde{X}} = (a_2 \lambda_2 + a_3 \Omega_2) A_{11} + a_4 A_{11} |A_{11}|^2. \tag{3.3.21}$$

What remains is to combine the left- and right-hand terms together to explicitly obtain the four complex constant coefficients in (3.3.21). We begin with a_1 and combine the appropriate terms from (3.3.15) with (3.3.18b) to get

$$a_1 = -\mathrm{i}^{4/3} \frac{T_1}{\kappa} - \frac{n^2}{\alpha a^2} \frac{\mathrm{Ai}'(\xi_0)}{\kappa} \mathbb{P}_1 \int_{\xi_0}^{\infty} K(\xi) L(\xi) d\xi$$

$$- 2(\mathrm{i}\alpha)^{1/3}\mathrm{Ai}(\xi_0)\alpha\mathbb{P}_1^{-1}\Bigg[(b_nf_n + c_nd_n)\left\{K_n(\mathrm{i}\alpha a) - \frac{\mathrm{Ai}'(\xi_0)}{\kappa}(\mathrm{i}\alpha)^{-1/3}\mathbb{P}_1K_n'(\mathrm{i}\alpha a)\right\}$$
$$- (b_nd_n + c_ne_n)\left\{I_n(\mathrm{i}\alpha a) - \frac{\mathrm{Ai}'(\xi_0)}{\kappa}(\mathrm{i}\alpha)^{-1/3}\mathbb{P}_1I_n'(\mathrm{i}\alpha a)\right\}\Bigg]. \tag{3.3.22a}$$

We move on to a_2 and combine the appropriate terms from (3.3.15) with (3.3.17f) to get

$$\begin{aligned} a_2 &= -\alpha\kappa^{-1}\mathrm{i}^{-1/3}T_1 + 2\alpha\kappa^{-1}\mathrm{i}^{-1/3}T_3 + \alpha\kappa^{-1}A_y\mathrm{i}^{1/3}T_3 \\ &= \mathrm{i}^{-2/3}\alpha L_2 + \alpha\kappa^{-1}A_y\mathrm{i}^{1/3}T_3. \end{aligned} \tag{3.3.22b}$$

(3.3.16f) gives us the expression for a_3 as

$$a_3 = (\mathrm{i}\alpha)^{1/3}\kappa^{-1}T_{18}. \tag{3.3.22c}$$

Finally we will look at a_4 which contains terms only from the right-hand side. We rename B_5 and B_6 as L_9 and L_{10}, respectively. Collecting all the terms from (3.3.20) we get

$$\begin{aligned} a_4 = \frac{\mathrm{i}^{-2/3}\alpha^{5/3}}{\kappa|\kappa|^2}\Bigg[&T_8 + T_6 - T_{15} - T_{16} - 2T_{10} - (T_9 - T_{17} + 2T_{11})L_9L_{10} \\ &- A_y\left(\alpha^{2/3}\mathbb{P}_1T_{22} - \mathbb{P}_2T_{25}L_{12}\right) - A_y^c\mathbb{P}_1^c\left(T_{23} - T_{24}L_9L_{10}\right)\Bigg] \\ = \frac{\mathrm{i}^{-2/3}\alpha^{5/3}}{\kappa|\kappa|^2}&\left[L_{11} - A_y\left[\alpha^{2/3}\mathbb{P}_1T_{22} - \mathbb{P}_2T_{25}L_{12}\right] - A_y^c\mathbb{P}_1^cL_{13}\right]. \end{aligned} \tag{3.3.22d}$$

The coefficients a_1-a_4 with $A_y = 0$ can be shown to agree with that of Stephen (2006).

3.4 Axisymmetric problem

From the discussion in Section 2.4.4 it is clear that we must consider the case of axisymmetric disturbances separately. We first seek solutions to the linear stability problem just as in Section 3.1. Since the disturbances are axisymmetric we lose any ϕ dependence

and there is no W component in our equations. For these disturbances the pressure perturbation in the upper deck satisfies (3.1.2) with $n = 0$. The solution in this case is given by

$$\begin{aligned}\tilde{p}_{11}^{0} &= \mathrm{i}\alpha A_{11}\frac{I_0(\mathrm{i}\alpha r_s)K_0(\mathrm{i}\alpha r) - I_0(\mathrm{i}\alpha r)K_0(\mathrm{i}\alpha r_s)}{I_0(\mathrm{i}\alpha r_s)K_0'(\mathrm{i}\alpha a) - I_0'(\mathrm{i}\alpha a)K_0'(\mathrm{i}\alpha r_s)} \\ &= -\mathrm{i}\alpha A_{11}G_1^0(r). \end{aligned} \tag{3.4.1a}$$

Following the same procedures described in Section 3.1 and applying the matching and boundary conditions will eventually give us the corresponding eigenrelation for axisymmetric disturbances as

$$\frac{\mathrm{Ai}'(\xi_0)}{\int_{\xi_0}^{\infty}\mathrm{Ai}(\xi)d\xi} = -(\mathrm{i}\alpha)^{1/3}\left[A_y + \mathrm{i}\alpha\right]\frac{I_0(\mathrm{i}\alpha r_s)K_0(\mathrm{i}\alpha a) - I_0(\mathrm{i}\alpha a)K_0(\mathrm{i}\alpha r_s)}{I_0(\mathrm{i}\alpha r_s)K_1(\mathrm{i}\alpha a) + I_1(\mathrm{i}\alpha a)K_0(\mathrm{i}\alpha r_s)}. \tag{3.4.1b}$$

We note here the difference between the axiymmetric eigenrelation (3.4.1b) and the non-axisymmetric version (3.1.7). Moving to the nonlinear second-order problem, the pressure perturbation equation in the upper deck satisfies (3.2.2a) with $n = 0$. The solution is given by

$$\begin{aligned}\tilde{p}_{22}^{0}(r) &= -2\mathrm{i}\alpha A_{22}\frac{I_0(2\mathrm{i}\alpha r_s)K_0(2\mathrm{i}\alpha r) - I_0(2\mathrm{i}\alpha r)K_0(2\mathrm{i}\alpha r_s)}{I_0'(2\mathrm{i}\alpha a)K_0(2\mathrm{i}\alpha r_s) - I_0(2\mathrm{i}\alpha r_s)K_0'(2\mathrm{i}\alpha a)} \\ &= -2\mathrm{i}\alpha A_{22}G_2^0(r). \end{aligned} \tag{3.4.2a}$$

We can now follow a similar procedure as outlined in Section 3.2.3, to obtain a relationship between B_1 and B_2^2. This is obtained as

$$\begin{aligned}&-2\Delta G_2^0(a)\Big[B_2 2^{-1/3}\int_{\widehat{\xi_0}}^{\infty}\mathrm{Ai}(s)ds\Big]\Big(A_y + 2\Delta\Big) - \Delta^{-2/3}2^{1/3}B_2\mathrm{Ai}'(\widehat{\xi_0}) \\ &\qquad = \Delta^{-1/3}B_1^2\Big(2^{1/3}F_p'(\widehat{\xi_0}) + \mathrm{Ai}'(\xi_0)\mathrm{Ai}(\xi_0)\Big)\end{aligned}$$

$$+ 2\Delta G_2^0(a)\Big(A_y + 2\Delta\Big)B_1^2\left[\Delta^{1/3}\Big[\int_{\widehat{\xi_0}}^{\infty} F_p(\xi)d\xi + \int_{\widehat{\xi_0}}^{\infty} \mathrm{Ai}'(\xi)d\xi \int_{\xi_0}^{\xi_2} \mathrm{Ai}(\xi_1)d\xi_1\Big]\right]$$
$$+ A_y B_1^2 \Delta^{4/3} G_1^0(a)\mathrm{Ai}(\xi_0)\int_{\xi_0}^{\infty} \mathrm{Ai}(s)ds. \tag{3.4.2b}$$

Finally at the third order we will consider solutions for fixed frequency Ω, thus the resulting amplitude equation will be

$$a_{10}\frac{dA_{11}}{d\tilde{X}} = a_{20}\lambda_2 A_{11} + a_{40}A_{11}|A_{11}|^2. \tag{3.4.3}$$

The solution at third order is carried out in a similar fashion to the non-axisymmetric case. The upper deck pressure perturbation is now required to satisfy

$$\tilde{p}^0_{31rr} + \frac{1}{r}\tilde{p}^0_{31r} + \alpha^2\tilde{p}^0_{31} = 2\alpha^2 A_{11\tilde{X}} G_1^0(r). \tag{3.4.4}$$

The solution obtained is similar to (3.3.8d), but with all the terms now functions of modified Bessel functions of zero order. Recall that the axisymmetric lower-deck momentum equation contains the term $-\frac{dP}{dX}$, whose contribution to the third-order problem is $-\mathrm{i}\alpha P_{31} - \frac{\partial P_{11}}{\partial \tilde{X}}$. This modifies the solution of U_{11} in the adjoint problem and makes an additional contribution proportional to $\frac{\partial A_{11}}{\partial \tilde{X}}$. The coefficients in (3.4.3) may be expressed as

$$a_{10} = -\mathrm{i}^{4/3}T_1\kappa^{-1} - 2(\mathrm{i}\alpha)^{1/3}\mathrm{Ai}(\xi_0)\alpha\mathbb{P}_{10}^{-1}\times$$
$$\left[(b_0f_0 + c_0d_0)\left\{K_0(\mathrm{i}\alpha a) - \frac{\mathrm{Ai}'(\xi_0)}{\kappa}(\mathrm{i}\alpha)^{-1/3}\mathbb{P}_{10}K_0'(\mathrm{i}\alpha a)\right\}\right.$$
$$\left. - (b_0d_0 + c_0e_0)\left\{I_0(\mathrm{i}\alpha a) - \frac{\mathrm{Ai}'(\xi_0)}{\kappa}(\mathrm{i}\alpha)^{-1/3}\mathbb{P}_{10}I_0'(\mathrm{i}\alpha a)\right\}\right], \tag{3.4.5a}$$
$$a_{20} = \mathrm{i}^{-2/3}\alpha L_2 + \alpha\kappa^{-1}A_y\mathrm{i}^{1/3}T_3, \tag{3.4.5b}$$

$$a_{40} = \frac{\mathrm{i}^{-2/3}\alpha^{5/3}}{\kappa|\kappa|^2}\left[L_{11}^0 - A_y\left[\alpha^{2/3}\mathbb{P}_{10}T_{22} - \mathbb{P}_{20}T_{25}L_{12}^0\right] - A_y^c\mathbb{P}^c{}_{10}L_{13}^0\right]. \tag{3.4.5c}$$

The coefficients a_{10}-a_{40} with $A_y = 0$ can be shown to agree with that of Stephen (2006) .

3.5 Concluding remarks

The lengthy analysis presented in Chapter 3 allows us to obtain a leading order dispersion relation from a linear analysis, and a weakly nonlinear evolution equation at higher order. The dispersion relations can be solved to obtain both neutrally stable and spatially varying solutions. The evolution equation describes the slow evolution of disturbances away from the linear neutral point. The sign of the coefficients of the equation determines whether nonlinear effects stabilise or destabilise the flow. The evaluations can be done for the case with porous walls and for the case of solid walls by setting $A_y = 0$ where appropriate. In this way the effect of porous walls on the stability of the viscous disturbances can be studied.

Chapter 4

Results

Numerical solutions of the linear non-axisymmetric and axisymmetric eigenrelations (3.1.7) and (3.4.1b) are presented in Section 4.1. Neutral stability of the problem is first examined in Section 4.1.1. Here solutions to eigenrelations (3.1.7) and (3.4.1b) for real values of Ω and α are sought. The spatial stability problem is examined in Section 4.1.2. Here the concern is with spatial evolution of disturbances. Results are presented for solutions of (3.1.7) and (3.4.1b) with Ω real and α complex. In Section 4.2 the effect of varying various parameters of the porous wall models is examined. Finally the results of weakly nonlinear stability problem is presented in Section 4.3. Here the concern is with the numerical evaluation of the coefficients in (3.3.21) and (3.4.3). The numerical results presented in this chapter will be compared with some published experimental and numerical results in Chapter 5.

4.1 Linear stability results

Before proceeding to the numerical solution, a relationship between the angular frequency of disturbances propagating through the pore (ω) and the first-mode disturbance frequency (Ω) (in the lower deck) is obtained. For non-axisymmetric disturbances

$$\omega = \frac{R}{Re}\left[Re^{1/4}\mu_w^{-1/4}T_w^{-3/4}M^{-1/2}\right]\Omega \tag{4.1.1}$$

and for axisymmetric disturbances

$$\omega = \frac{R}{Re}\left[Re^{1/4}\mu_w^{-1/4}T_w^{-3/4}(M^2-1)^{1/4}\right]\Omega. \tag{4.1.2}$$

The relevant flow parameters used in the calculations are given in Section 2.3. The cone angle and Mach number from the experiments will determine the shock angle θ_s and the scaled cone radius a. An approximate value of the shock angle may be obtained using.

$$\sin\sigma = \sin\theta_c\left(\frac{\gamma+1}{2} + \frac{1}{M_\infty^2\sin^2\theta_c}\right)^{1/2}, \tag{4.1.3}$$

where $\sigma = \theta_s + \theta_c$. Once the shock angle has been determined from this equation, the ratio a/r_s may be obtained from geometric arguments. We find for a slender cone of half angle $\theta_c = 7^0$ and $M_\infty = 6$ that

$$\frac{a}{r_s} \approx \frac{\sin\theta_c}{\tan\theta_s + \sin\theta_c} = 0.57, \tag{4.1.4}$$

where we have taken $\cos\theta_c \approx 1$.

4.1.1 Neutral solutions of the eigenrelations

We first consider neutrally stable solutions of the eigenrelations. The presence of shock allows multiple modes of the solution. Neutral solutions for α and Ω are presented against the local cone radius a. For a fixed cone angle, the effect of increasing a is to move further downstream along the cone. Regions of instability lie above the neutral curves. Figure 4.1a presents the neutral solutions to the axisymmetric eigenrelation (3.4.1b) for a solid wall and for the regular microstructure model (2.3.4). There are an infinite number of neutral modes. The presence of multiple modes can be supported by asymptotic approximations of the eigenrelations as shown in Section 5.1. The first four modes of the solution are

depicted here. We do not notice any discernible difference between the α solutions for solid and porous walls with the exception of the first (lowest) mode. Figure 4.1b shows the corresponding Ω solutions. The neutral curves for porous walls are lower than in the solid case. Thus flow over the porous wall will become unstable for slightly lower frequencies than those for the solid wall. This indicates that the porous wall has a destabilising effect on the neutral stability of the flow.

We now turn to neutrally stable solutions of the non-axisymmetric eigenrelation (3.1.7). Figure 4.2 depicts the neutral curves for the first azimuthal mode ($n = 1$). Once again in figure 4.2a we see that the destabilising effect of the porous wall on α solutions is very slight. However the corresponding Ω solutions in figure 4.2b show that the porous wall has a significant destabilising effect. With the exception of the first mode, the curves corresponding to the porous case are significantly lower than that of the solid case. Figure 4.3 shows corresponding neutral solutions for $n = 2$. Here we see there is no discernible change in the behaviour of the solutions of α. For the solid wall case, neutral curves of Ω are slightly lower for $n = 2$ compared to $n = 1$ at small values of a. As a increases the differences become negligible. Similar behaviour is observed for solutions of the porous wall case. By comparing figures 4.1b and 4.2b, we see that the differences between the curves corresponding to the solid and porous wall cases reduce. Similar trends can be observed in figure 4.4 which shows the neutral curves for $n = 3$.

Next we consider neutral solutions using the random microstructure model of (2.3.9). The results using this model are compared with those obtained using the regular microstructure model. The porosity of the felt metal is 0.75 and the fibre diameter is 30μm. For comparison the regular microstructure model is used with a porosity of 0.2 and pore radius of 30μm. In figure 4.5 which shows the axisymmetric neutral modes, we see that neutral curves for the felt metal case are much lower than those for the regular porous model for all modes. This difference reduces for the higher modes in the limit of small

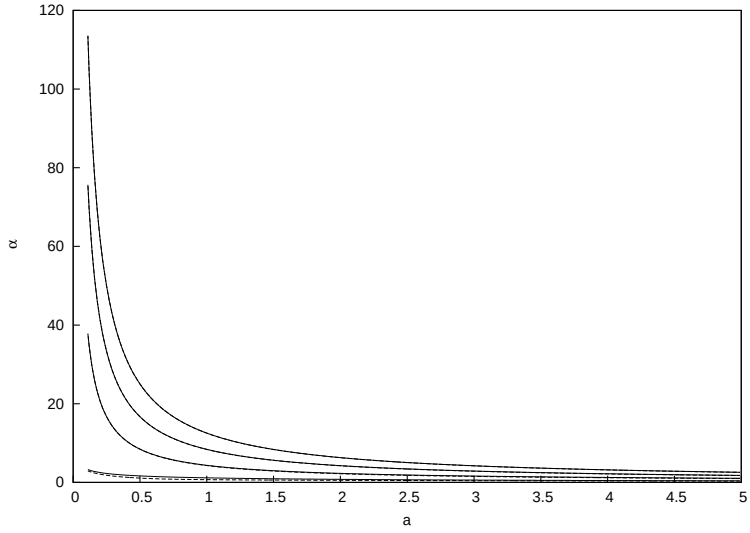

(a)

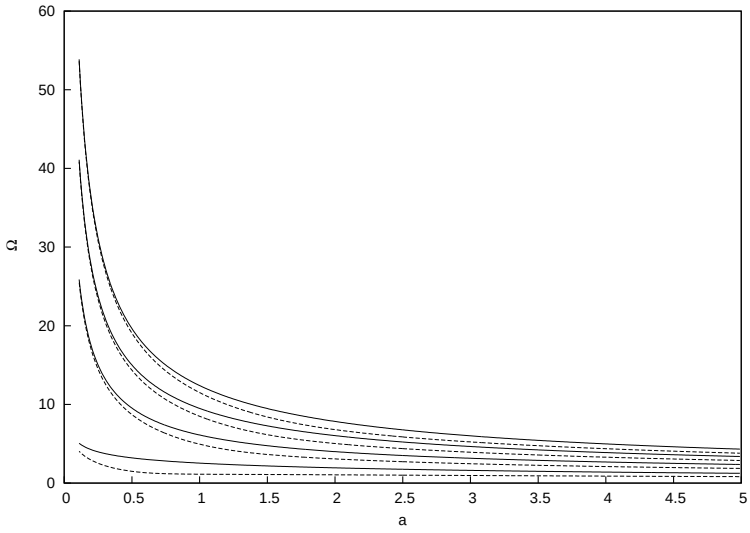

(b)

Figure 4.1: The first four neutral modes of (3.4.1b). Shown is (a) α, (b) Ω against local cone radius a for $a/r_s = 0.57$, $n = 0$: —, solid wall; $- - -$, regular microstructure model (2.3.4).

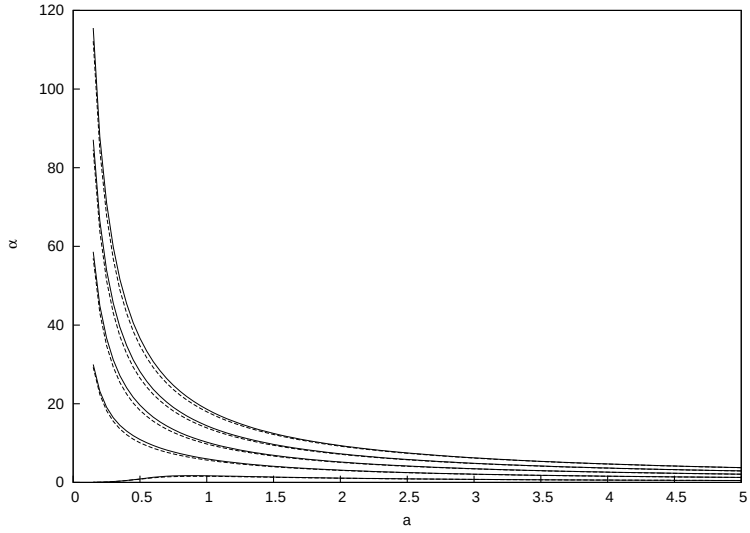

(a)

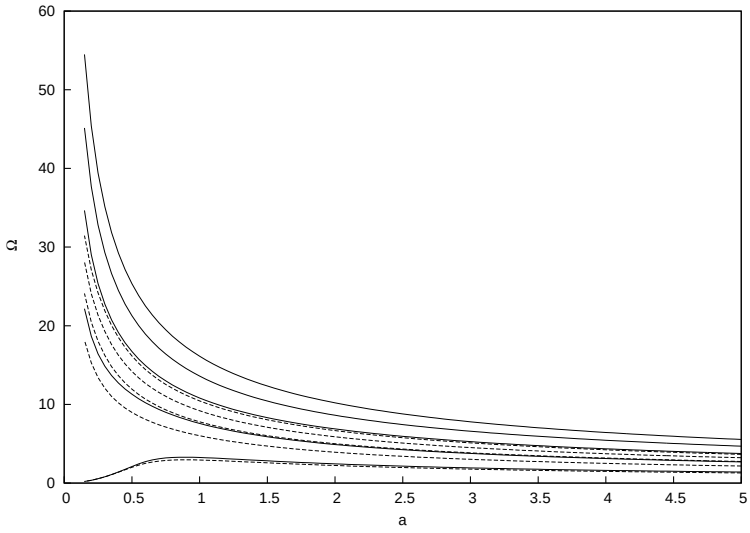

(b)

Figure 4.2: The first five neutral modes of (3.1.7). Shown is (a) α, (b) Ω against local cone radius a for $a/r_s = 0.57$, $n = 1$: —, solid wall; $- - -$, regular microstructure model (2.3.4).

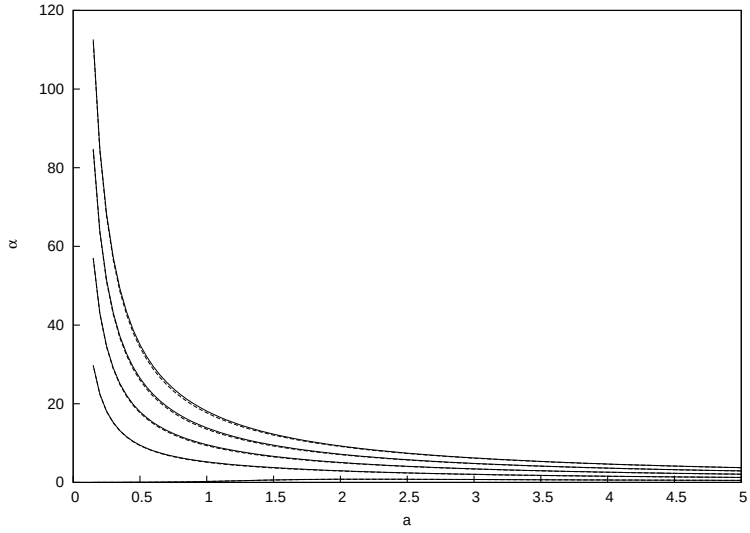

(a)

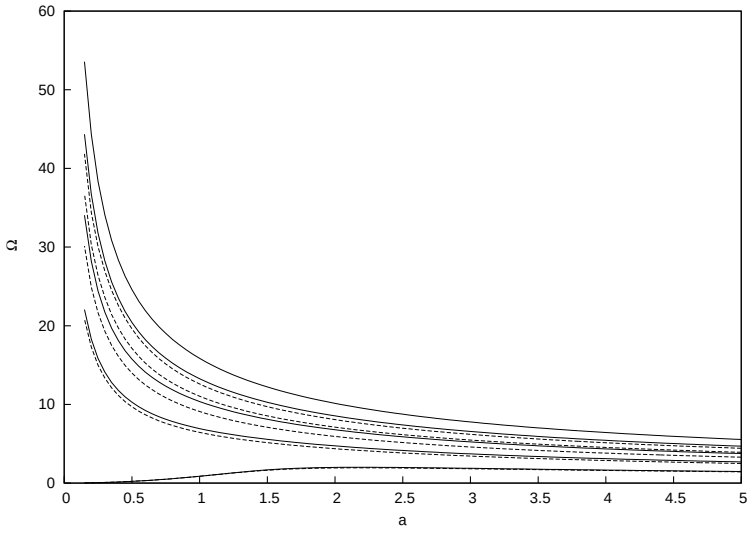

(b)

Figure 4.3: The first five neutral modes of (3.1.7). Shown is (a) α, (b) Ω against local cone radius a for $a/r_s = 0.57$, $n = 2$: —, solid wall; $- - -$, regular microstructure model (2.3.4).

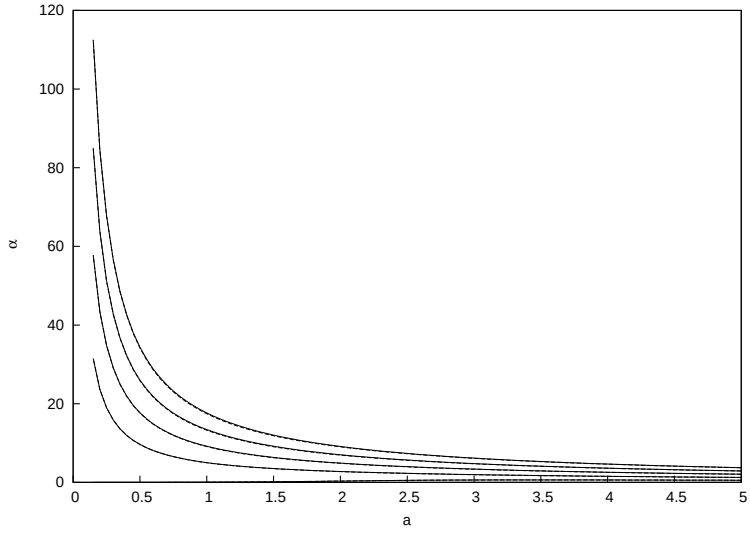

(a)

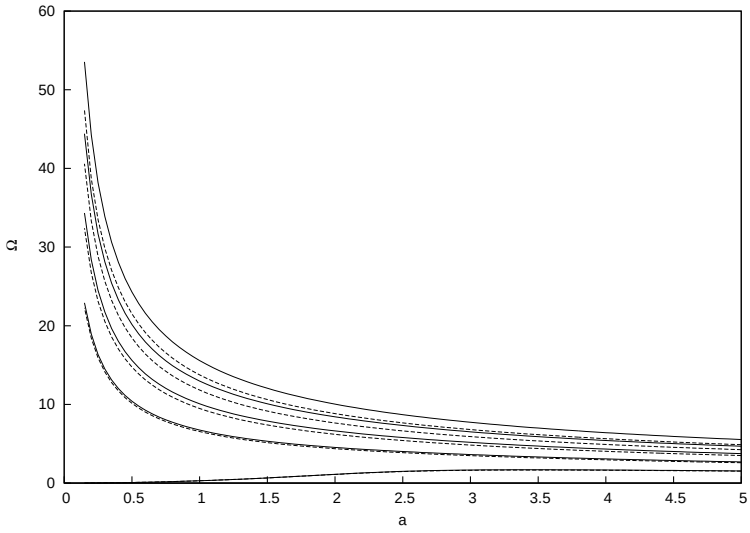

(b)

Figure 4.4: The first five neutral modes of (3.1.7). Shown is (a) α, (b) Ω against local cone radius a for $a/r_s = 0.57$, $n = 3$: —, solid wall; $- - -$, regular microstructure model (2.3.4).

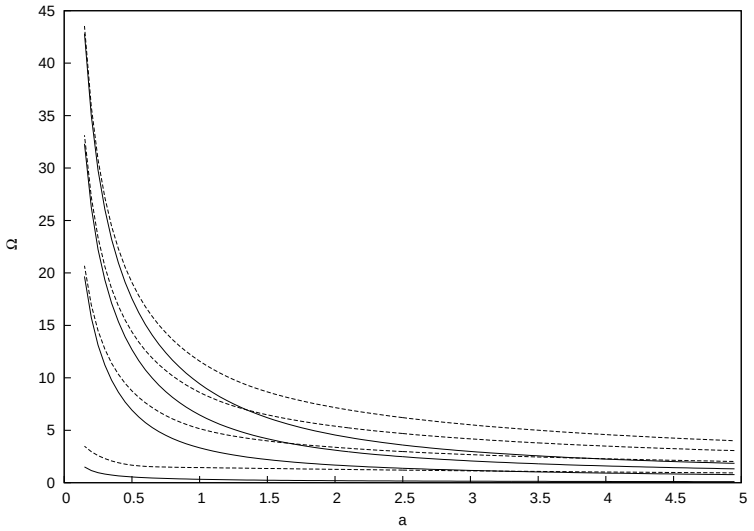

Figure 4.5: The first four neutral modes of (3.4.1b). Shown is Ω against local cone radius a for $a/r_s = 0.57$, $n = 0$: —, random microstructure model (2.3.9); $- - -$, regular microstructure model (2.3.4).

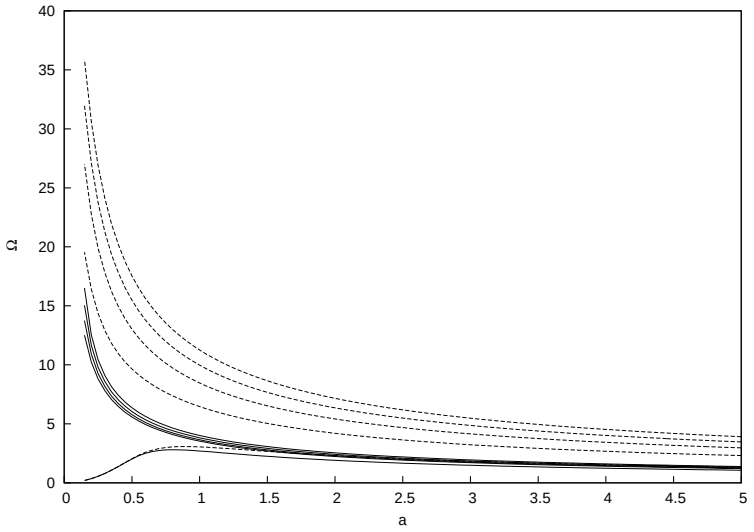

Figure 4.6: The first five neutral modes of (3.1.7) with $n = 1$. Shown is Ω against local cone radius a for $a/r_s = 0.57$: —, random microstructure model (2.3.9); $- - -$, regular microstructure model (2.3.4).

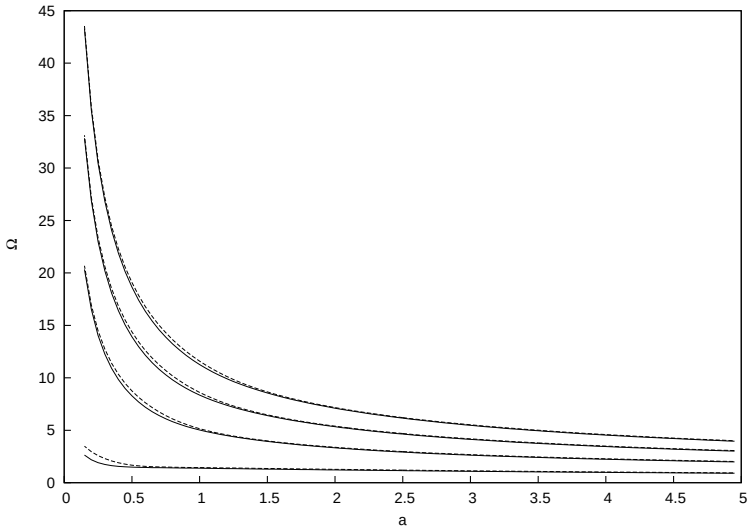

Figure 4.7: The first four neutral modes of (3.4.1b). Shown is Ω against local cone radius a for $a/r_s = 0.57$, $n = 0$: —, mesh microstructure model (2.3.6); $- - -$, regular microstructure model (2.3.4).

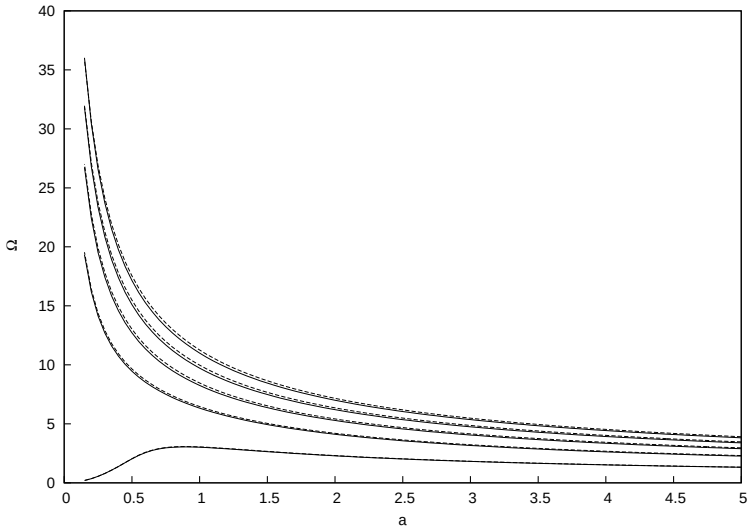

Figure 4.8: The first five neutral modes of (3.1.7) with $n = 1$. Shown is Ω against local cone radius a for $a/r_s = 0.57$: mesh microstructure model (2.3.6); $- - -$, regular microstructure model (2.3.4).

a. In figure 4.6 which shows the non-axisymmetric neutral modes, we see that with the exception of the first mode, neutral values of Ω for the felt metal are significantly lower than the corresponding ones for regular porous model. The felt metal thus significantly destabilises both axisymmetric and non-axisymmetric neutral modes when compared to the regular porous model.

Finally we consider the mesh microstructure model of (2.3.6). The results using this model are compared with those obtained using the regular microstructure model. The porosity of the mesh model is 0.8, and width of each pore section is 100μm. For comparison the regular porous model is used with a porosity of 0.2 and pore diameter of 60μm. In figures 4.7 and 4.8 we see that the higher porosity of the mesh model leads to slightly lower neutral curves.

Although porous coatings using felt metal or stainless steel wire meshes are easier to incorporate into existing thermal protection systems, from these comparisons we can see that they have the potential to excite disturbances across a wider range of frequencies in the first-mode spectrum.

4.1.2 Spatial stability computations

We now examine the spatial evolution of disturbances by seeking solutions of the eigenrelations with Ω real and α complex. If $\alpha = \alpha_r + i\alpha_i$ then $\alpha_i > 0$ denotes stability while $\alpha_i < 0$ is indicative of spatial instability. Figure 4.9 shows the dependence of the spatial growth-rate parameter α_i on the mode frequency Ω for $n = 0$ for a few choices of cone radii a. At each value of a there is a complete family of modes, as observed in the neutral solutions. We can see that for each member of the family there is a cut-off frequency Ω_c such that for $\Omega < \Omega_c$ that particular spatial mode is stable ($\alpha_i > 0$) but it becomes unstable ($\alpha_i < 0$) if $\Omega > \Omega_c$. We can clearly see in figure 4.9 that the porous wall leads to larger unstable growth rates when compared to the solid wall. The

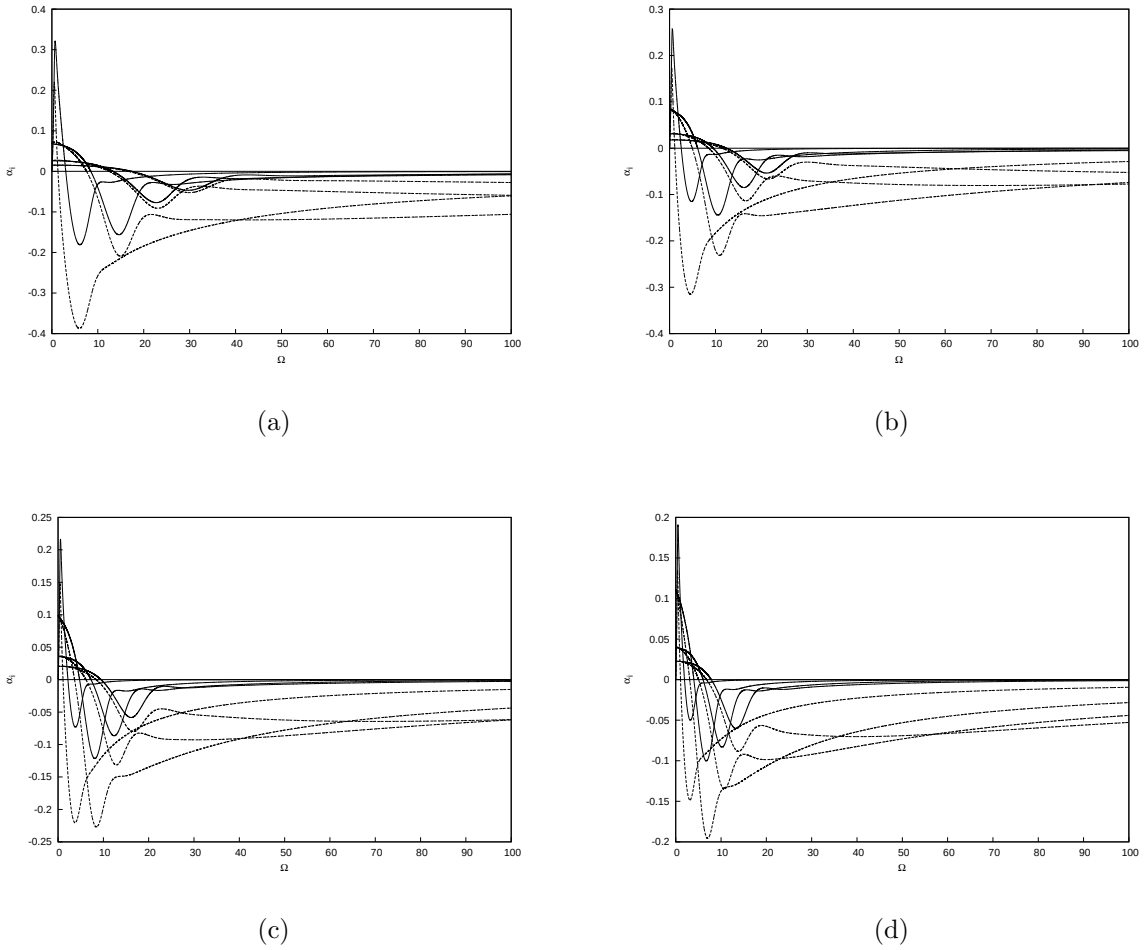

Figure 4.9: Spatial growth rate parameter $\alpha_i(\Omega)$ for non-neutral axisymmetric modes ($n = 0$): —, solid wall; − − −, regular microstructure model (2.3.4). We show the growth rates of the first four modes for (a) $a = 0.6$, (b) $a = 1.0$, (c) $a = 1.5$, (d) $a = 2.0$.

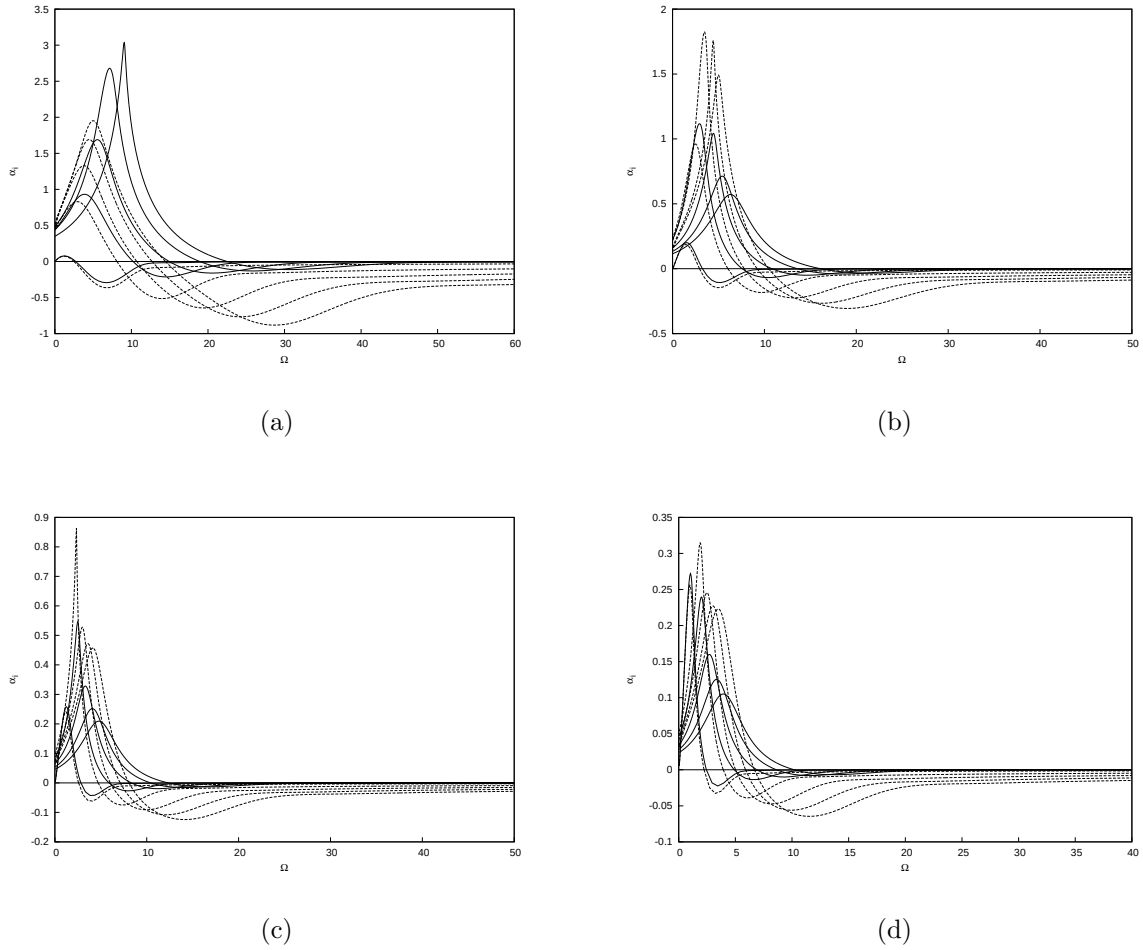

Figure 4.10: Spatial growth rate parameter $\alpha_i(\Omega)$ for non-neutral non-axisymmetric modes with $n = 1$: —, solid wall; $- - -$, regular microstructure model (2.3.4). We show the growth rates of the first five modes for (a) $a = 0.6$, (b) $a = 1.0$, (c) $a = 1.5$, (d) $a = 2.0$.

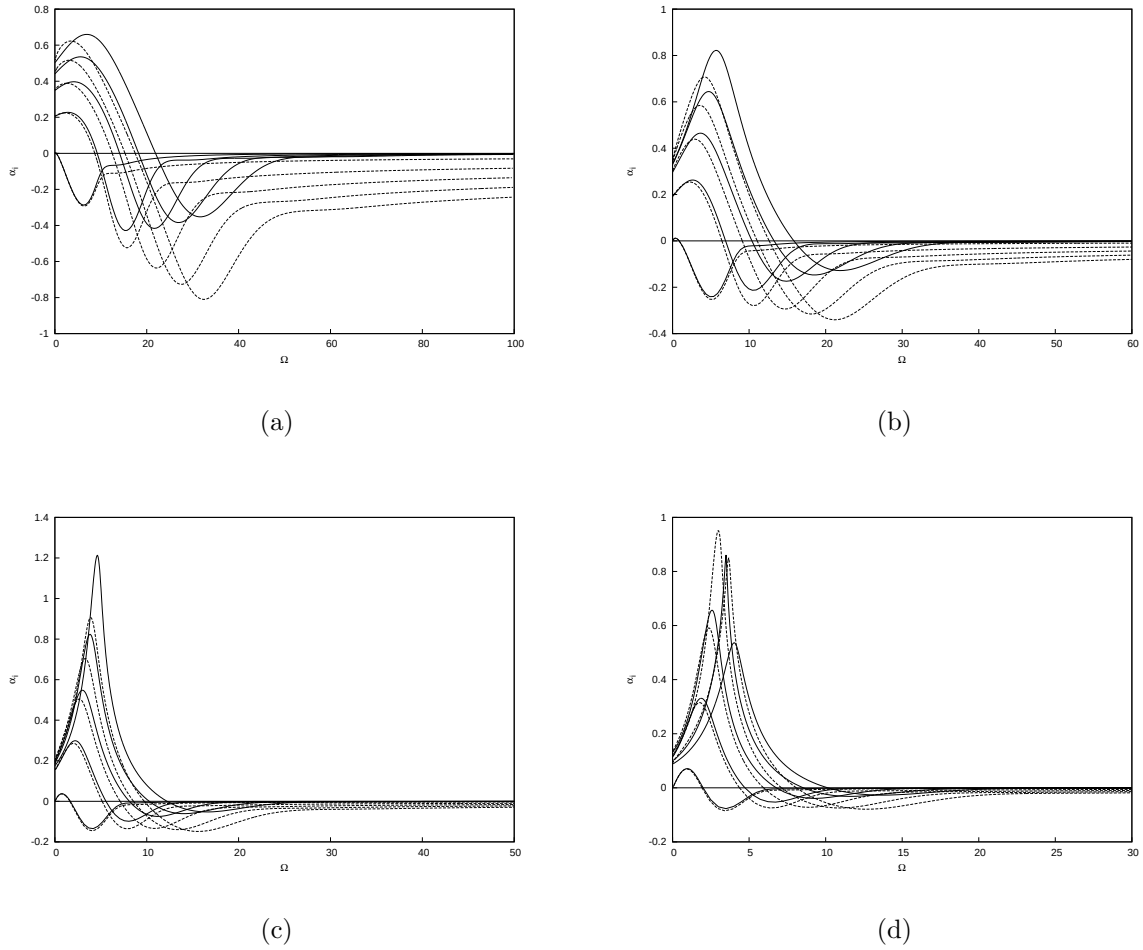

Figure 4.11: Spatial growth rate parameter $\alpha_i(\Omega)$ for non-neutral non-axisymmetric modes with $n = 2$: —, solid wall; $- - -$, regular microstructure model (2.3.4). We show the growth rates of the first five modes for (a) $a = 0.6$, (b) $a = 1.0$, (c) $a = 1.5$, (d) $a = 2.0$.

maximum unstable growth rates occur for disturbances with the same frequency for both solid and porous walls. We notice that for the solid wall the growth rate of all the modes approaches zero at high frequencies. This is not the case for the porous walls as we can see that unstable growth rates persist in the limit of large Ω. As we increase a the index of the most unstable mode (with largest $-\alpha_i$) rises from mode 1 to 2. As we increase a we also notice that the maximum unstable growth rates decrease. These effects occur for both solid and porous walls.

The corresponding growth rates for the first azimuthal mode $n = 1$ are shown in figure 4.10. The destabilizing effect of the porous wall is more significant than the axisymmetric case. We see this from the fact that the maximum unstable growth rates are much larger for the porous wall compared to the solid wall. We again see that as a increases the maximum unstable growth rates decrease. In the solid wall case we see that all unstable disturbances diminish to zero at high frequencies. It is the lowest mode that gives the largest growth rate with the higher modes being effectively damped. Disturbances over the porous wall however do not vanish in the limit of large frequencies, and it is the higher modes that give the largest maximum growth rates. This results in the peak unstable growth rates occurring for disturbances with higher frequencies when compared to the solid wall case. This is in contrast to the axisymmetric case where peak growth rates were concentrated around a narrow low frequency band for both solid and porous walls. Corresponding growth rate curves for $n = 2$ are presented in figure 4.11. The results exhibit the same trends as that observed for $n = 1$.

To gain a better understanding of which azimuthal mode is most dangerous we look at figure 4.12. In this figure we isolate the mode with the maximum growth rate from among the first ten modes for increasing values of a. Since increasing a leads to shifting our point of interest downstream along the cone surface, we plot the maximum growth rate against streamwise distance L^*. The range of L^* is chosen to correspond to a typical

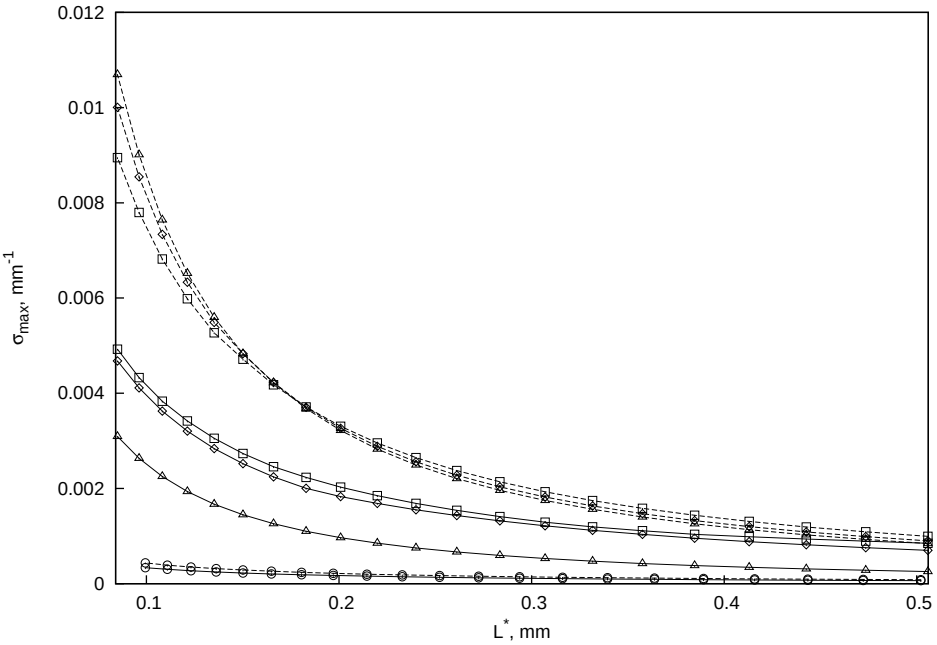

Figure 4.12: Variation of spatial growth rate parameter $\sigma_{\max} = \max(|-\alpha_i(\Omega)|)$ with longitudinal distance L^*: —, solid wall; $- - -$, regular microstructure model (2.3.4). Symbols refer to azimuthal wavenumbers: $\circ$, $n = 0$; $\triangle$, $n = 1$; $\diamond$, $n = 2$; $\square$, $n = 3$.

model length tested in experiments. We return to dimensional variables to account for the difference in scalings for the axisymmetric and non-axisymmetric disturbances. First of all we can see that the axisymmetric disturbances have much lower maximum unstable growth rates compared to the non-axisymmetric disturbances for both solid and porous walls. The extent of destabilisation is thus less significant for the axisymmetric modes. As expected from the spatial stability results presented earlier, maximum unstable growth rates decrease downstream along the cone surface for both solid and porous walls. For the solid wall case, higher azimuthal wavenumbers have the largest growth rates. For the porous wall case which non-axisymmetric azimuthal mode has the largest growth rate depends on the cone radius although overall differences between the non-axisymmetric modes remains small. The destabilising effect of the porous wall dramatically reduces downstream especially for higher azimuthal wavenumbers.

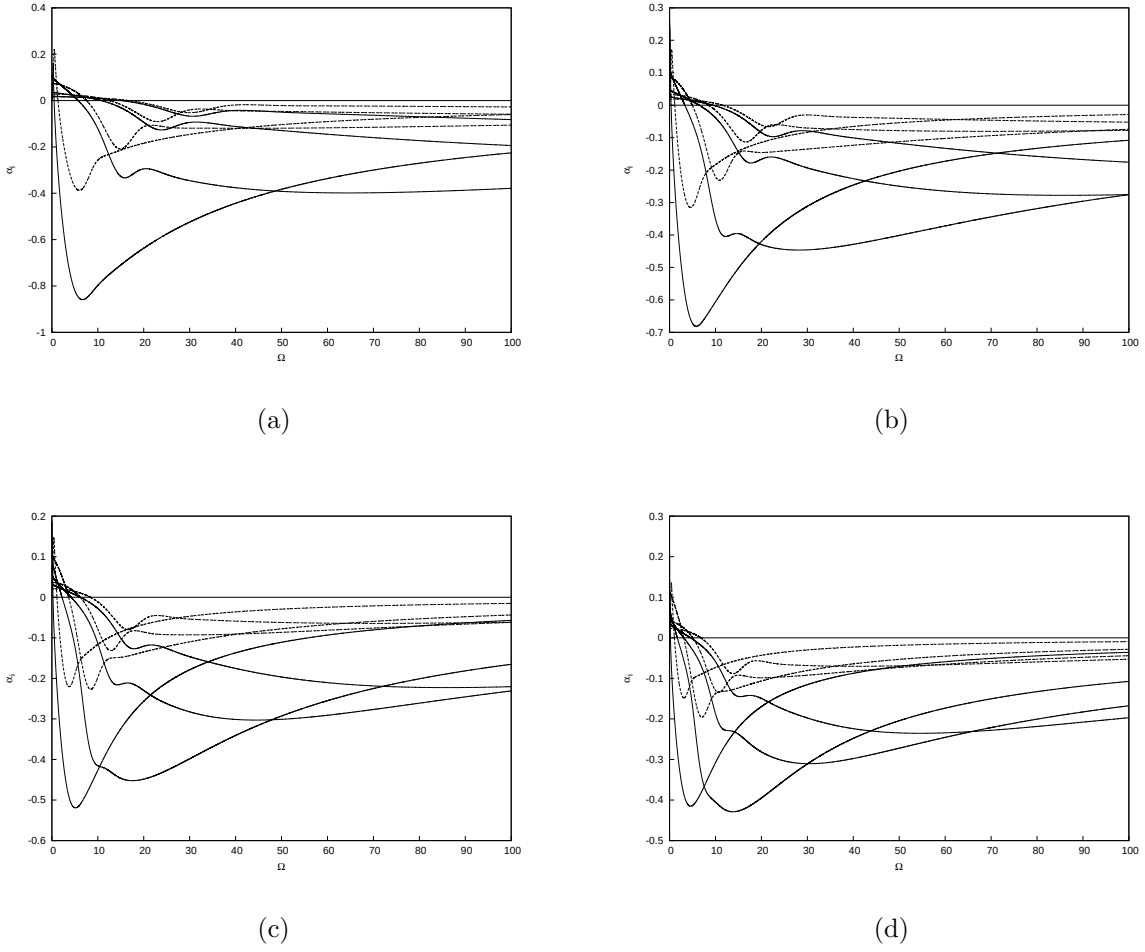

Figure 4.13: Spatial growth rate parameter $\alpha_i(\Omega)$ for non-neutral axisymmetric modes ($n = 0$): —, random microstructure model (2.3.9); − − −, regular microstructure model (2.3.4). We show the growth rates of the first four modes for (a) $a = 0.6$, (b) $a = 1.0$, (c) $a = 1.5$, (d) $a = 2.0$.

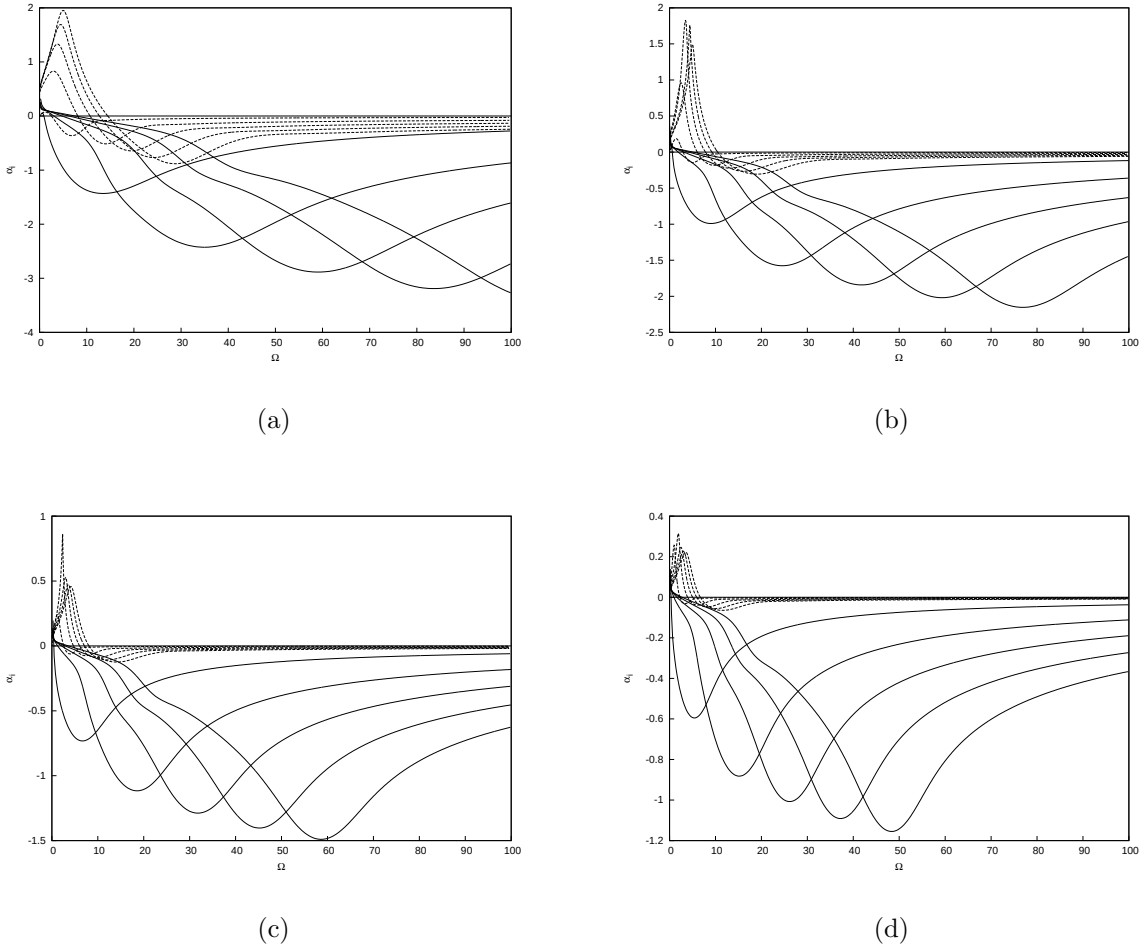

Figure 4.14: Spatial growth rate parameter $\alpha_i(\Omega)$ for non-neutral non-axisymmetric modes with $n = 1$: —, random microstructure model (2.3.9); − − −, regular microstructure model (2.3.4). We show the growth rates of the first five modes for (a) $a = 0.6$, (b) $a = 1.0$, (c) $a = 1.5$, (d) $a = 2.0$.

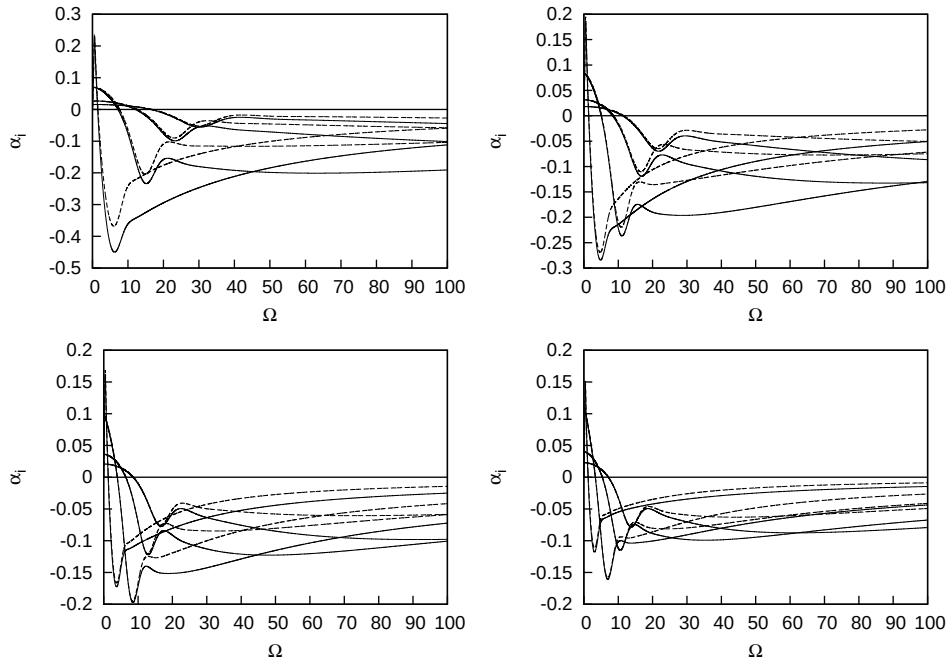

Figure 4.15: Spatial growth rate parameter $\alpha_i(\Omega)$ for non-neutral axisymmetric modes: —, mesh microstructure model (2.3.6); $- - -$, regular microstructure model (2.3.4). We show the growth rates of the first four modes for (a) $a = 0.6$, (b) $a = 1.0$, (c) $a = 1.5$, (d) $a = 2.0$.

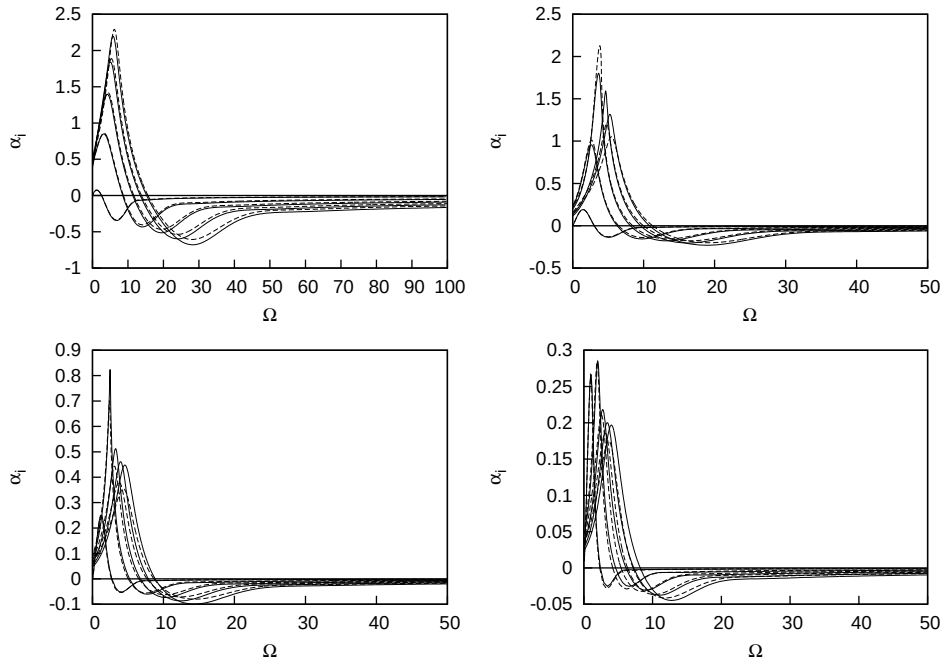

Figure 4.16: Spatial growth rate parameter $\alpha_i(\Omega)$ for non-axisymmetric modes with $n = 1$: —, mesh microstructure model (2.3.6); $- - -$, regular microstructure model (2.3.4). We show the growth rates of the first five modes for (a) $a = 0.6$, (b) $a = 1.0$, (c) $a = 1.5$, (d) $a = 2.0$.

We now consider the spatial stability results using the random microstructure model of (2.3.9). The neutral stability results comparing this model to the regular porous model of (2.3.4) were shown in figures 4.5 and 4.6 for axisymmetric and non-axisymmetric disturbances, respectively. We examine the spatial stability of these disturbances in figure 4.13 for $n = 0$ and in figure 4.14 for $n = 1$. In these figures we see that the felt metal leads to significantly larger maximum unstable growth rates when compared to the regular porous model. For axisymmetric modes the frequency at which the maximum unstable growth rate occurs is preserved while for non-axisymmetric modes, the maximum unstable growth is shifted to significantly higher frequencies which decrease with increasing a. The felt metal coating is thus highly deleterious to the first-mode instability. Similar findings have also been reported experimentally (Shiplyuk 2004), who attribute the greater destabilisation of the first mode to elevated roughness of the felt metal coating.

Next we consider the spatial stability results using the mesh microstructure model of (2.3.6). The neutral stability results comparing this model to the regular porous model of (2.3.4) were shown in figures 4.7 and 4.8 for axisymmetric and non-axisymmetric disturbances respectively. We examine the spatial stability of these disturbances in figure 4.15 for $n = 0$ and in figure 4.16 for $n = 1$. From these figures we see that the higher porosity of the mesh microstructure leads to slightly greater destabilisation of both axisymmetric and non-axisymmetric disturbances when compared to the regular porous model.

4.2 Parametric studies

The results presented in Section 4.1 allow us to conclude that the porous layer has a destabilising effect on both axisymmetric and non-axisymmetric disturbances. All modes generated by the shock are destabilised by the presence of the porous wall. Which mode is the most dangerous depends on the azimuthal wavenumber and cone radius. The porous wall influences the stability of the flow through the wall admittance A_y. Since

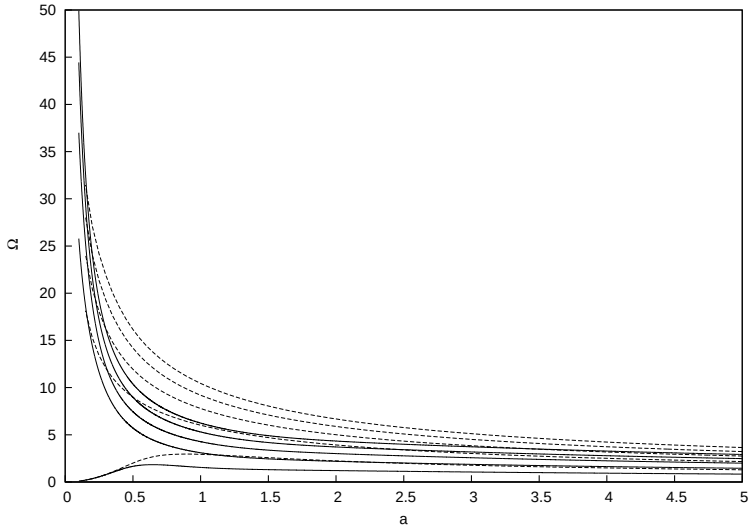

Figure 4.17: The first five neutral modes of (3.1.7) with $n = 1$. Shown is Ω against local cone radius a for $a/r_s = 0.57$ using regular microstructure model (2.3.4): —, $T_w = 0.25T_{ad}$; $- - -$, $T_w = T_{ad}$.

the objective of using porous layers is to stabilise the boundary layer, we can examine the parameters that affect the wall admittance and quantify their effect on the maximum unstable growth rates. We will focus our attention mainly on the regular porous model.

4.2.1 Effect of moderate wall cooling

From Section 2.3 we see that A_y depends on the wall temperature T_w. Recall that in Chapter 2 we argue that the stability analysis is valid for $T_w >> 1$. To study the effects of different wall temperatures we maintain this restriction and vary the wall temperature as $0.25 < T_w/T_{ad} < 1.0$. This corresponds to typical experimental situations and numerical investigations (Fedorov *et al.* 2001, Maslov 2003) where the non-dimensional adiabatic wall temperature is $T_{ad} = 5.5 - 7.0$. We restrict our attention to non-axisymmetric disturbances with $n = 1$. Figure 4.17 shows the effect of wall temperature on the neutral stability. We see that decreasing the wall temperature from $T_w = T_{ad}$ to $T_w = 0.25T_{ad}$

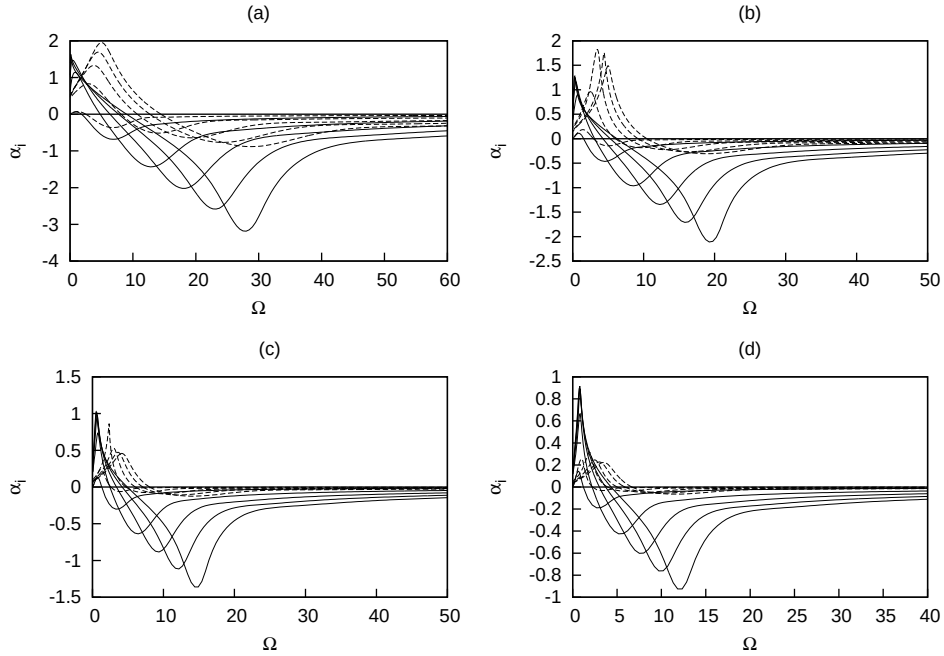

Figure 4.18: Spatial growth rate parameter $\alpha_i(\Omega)$ for non-axisymmetric modes with $n = 1$ using regular microstructure model (2.3.4): —, $T_w = 0.25T_{ad}$; − − −, $T_w = T_{ad}$. We show the growth rates of the first five modes for (a) $a = 0.6$, (b) $a = 1.0$, (c) $a = 1.5$, (d) $a = 2.0$.

leads to a corresponding decrease of the neutral curves for all values of cone radius a. Thus wall cooling has a destabilising effect in the presence of the porous wall. Figure 4.18 shows the corresponding effect of wall cooling on the spatial stability. Concomitant with a decrease in the cut-off frequencies for spatial instability (as may be expected from the neutral results), we see that decreasing the wall temperature from $T_w = T_{ad}$ to $T_w = 0.25T_{ad}$ leads to significantly larger unstable growth rates at all values of a. There is a very slight shift in the peak unstable growth rates to lower frequencies with increasing a. From these two results we can conclude that cooling the wall in the presence of porous coatings significantly destabilises Mack's first mode disturbances and leads to significant amplification of unstable disturbances at all streamwise locations. Further discussion is presented in Section 5.2.3.

4.2.2 Effect of gas rarefaction

As the flow density on the cone wall is relatively small, gas rarefaction effects are important for the flow inside the pores. The regular porous model of (2.3.4) accounts for this effect. Here we examine the influence of gas rarefaction effects within the pore on the stability of the flow. The Knudsen number can be expressed as

$$Kn = \frac{\mu_w M_-}{r_p R}\sqrt{2\pi\gamma T_w}. \tag{4.2.1}$$

Figure 4.19 shows the effect of finite Knudsen number on the neutral modes. We see that gas rarefaction has a destabilising effect on the flow. A similar situation is also revealed in figure 4.20 which shows the effect of finite Knudsen number on the spatial stability of the flow. We see that gas rarefaction leads to larger amplification of unstable disturbances (particularly the higher modes) at a particular frequency.

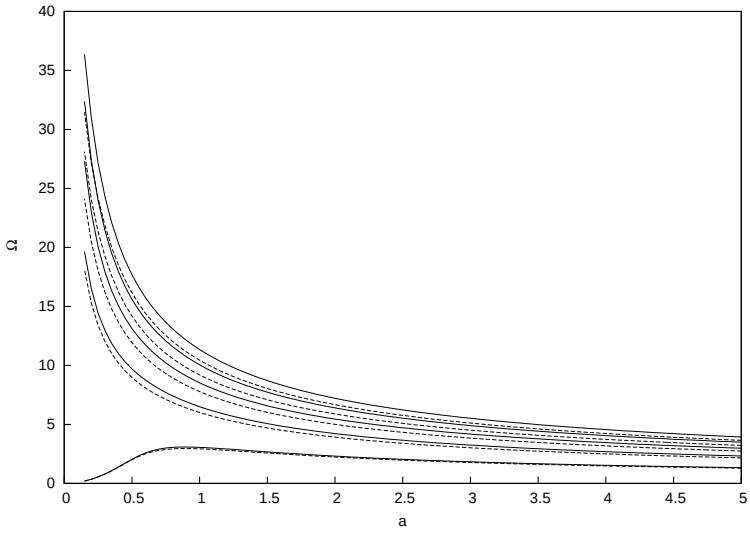

Figure 4.19: The first five neutral modes of (3.1.7) with $n = 1$. Shown is Ω against local cone radius a for $a/r_s = 0.57$: —, $Kn = 0$; − − −, $Kn = 0.494$. Results are shown using the regular porous model (2.3.4).

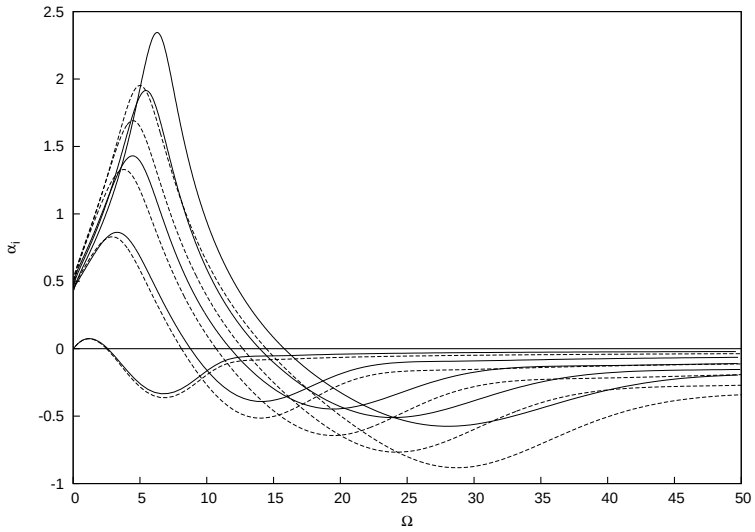

Figure 4.20: Spatial growth rate parameter $\alpha_i(\Omega)|$ for non-axisymmetric mode $n = 1$: —, $Kn = 0$; − − −, $Kn = 0.494$. Results are shown using the regular porous model (2.3.4) at $a = 0.6$.

4.2.3 Effect of porous layer characteristics

The porous layer characteristics are defined by quantities that physically characterise the porous layer i.e., pore radius r_p^*, porosity ϕ_0 and pore depth h^*. Effects of varying pore thickness are also studied by considering the mesh microstructure model of (2.3.6). In this type of porous layer, the overall thickness of the porous wall can be controlled by the number of layers of stainless steel mesh that are laid on top of each other.

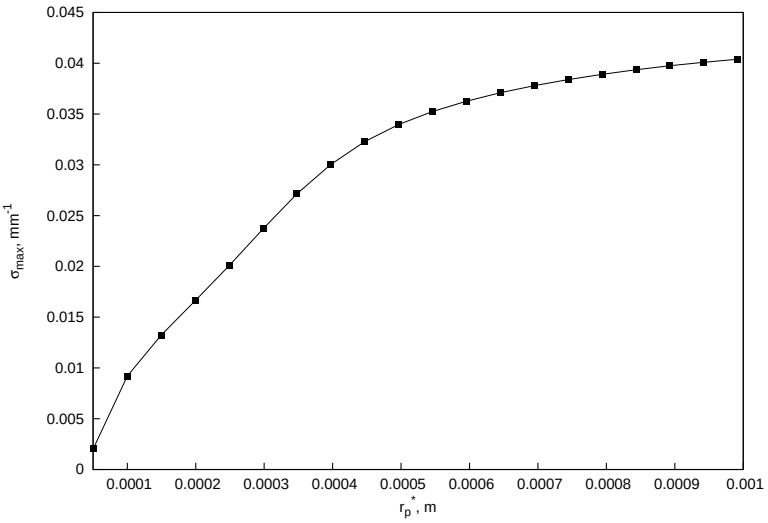

Figure 4.21: Variation of spatial growth rate parameter $\sigma_{\max} = \max(|-\alpha_i(\Omega)|)$ with pore radius r_p^* for non-neutral non-axisymmetric mode $n = 1$. Results are shown using the regular porous model (2.3.4) with $\phi_0 = 0.2$, $\Lambda h >> 1$ at $a = 0.8$.

We begin with the regular porous model and examine the variation of maximum unstable growth rates with increasing pore radius, porosity and pore depth. We again focus on the first non-axisymmetric mode $n = 1$. In figure 4.21 we fix the porosity at $\phi_0 = 0.25$ and vary the pore radius while in figure 4.22 we fix the pore radius at $r_p^* = 30\mu$m and vary the porosity. In figure 4.21 we see that larger pore radii for fixed porosity leads to larger maximum growth rates. Similarly we see from figure 4.22 that increasing porosity

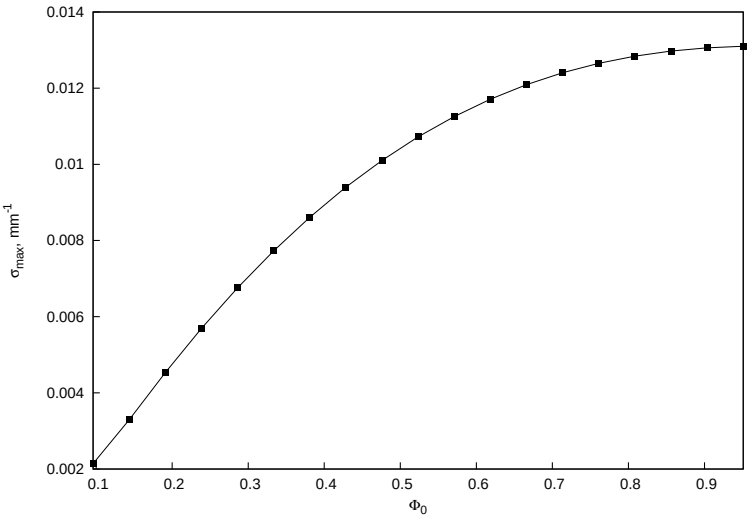

Figure 4.22: Variation of spatial growth rate parameter $\sigma_{\max} = \max(|-\alpha_i(\Omega)|)$ with porosity ϕ_0 for non-neutral non-axisymmetric mode $n = 1$. Results are shown using the regular porous model (2.3.4) with $r_p = 30\mu$m, $\Lambda h >> 1$ at $a = 0.8$.

(by decreasing pore spacing) for fixed sized pores leads to larger maximum growth rates. We have performed these computations in the limit of infinite pore depth ($\Lambda h >> 1$). We now examine the effect of finite pore depth on the maximum unstable growth rates. In figure 4.23a we fix the porosity and pore radius and vary the pore thickness h^*. We see that for very thin porous layers, the maximum growth rate is minimum and does not change with porous layer thickness. For thicker porous layers, the maximum unstable growth rates increase until they level off at very high thickness. Finally in figure 4.23b we examine the effect of increasing the number of stainless steel mesh layers on the maximum unstable growth rates. We see that the maximum growth rate peaks at $h^* = 0.15$mm, and then reduces and levels off for thicker layers. Further discussion is presented in Section 5.2.3.

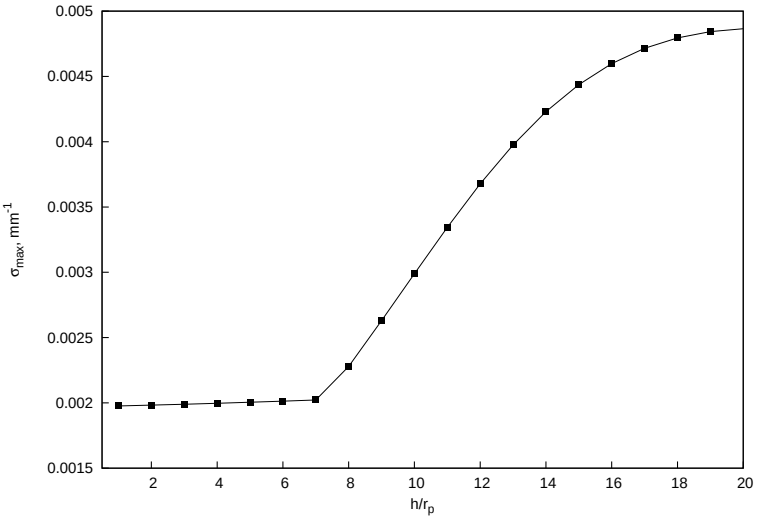

(a)

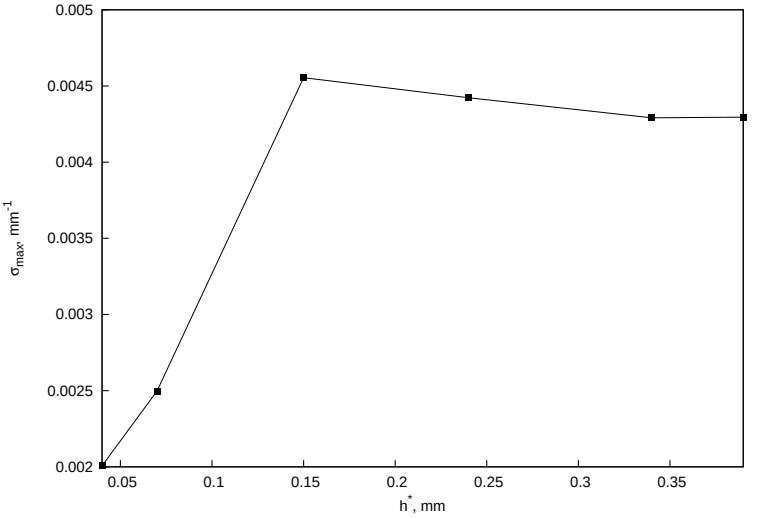

(b)

Figure 4.23: Variation of spatial growth rate parameter $\sigma_{\max} = \max(|-\alpha_i(\Omega)|)$ with pore depth for non-neutral non-axisymmetric mode $n = 1$. Results are shown at $a = 0.8$ using (a) the regular porous model (2.3.4) with $r_p = 30\mu$m, $\phi_0 = 0.2$; (b) mesh microstructure model (2.3.6) with $\widetilde{a} = 50\mu$m, $\phi_0 = 0.8$

4.3 Nonlinear stability results

In this section results obtained from the numerical evaluation of the coefficients in (3.3.21) and (3.4.3) will be presented. Attention will be largely focused on the coefficient of the nonlinear term in these equations ($\mathrm{Re}(a_4/a_1)$ and $\mathrm{Re}(a_{40}/a_{10})$).

4.3.1 Solid wall

We turn to the non-axisymmetric problem and the evolution equation (3.3.21). We can obtain a solution to this equation using separation of variables. Following Stuart (1960) we can determine an explicit expression for the amplitude $|A_{11}|^2$ as

$$|A_{11}|^2 = \frac{2\mathcal{K}e^{\mathcal{K}\tilde{X}}}{\left[\mathcal{K}C_1 - 2\mathrm{Re}\left(\frac{a_4}{a_1}\right)e^{\mathcal{K}\tilde{X}}\right]}, \tag{4.3.1a}$$

where $\mathcal{K} = 2\mathrm{Re}\left(\frac{a_2}{a_1}\lambda_2 + \frac{a_3}{a_1}\Omega_2\right)$ and C_1 is a constant of integration. When $\mathcal{K} > 0$ we have linear instability. Note that λ_2 is negative downstream of the neutral location. If then $\mathrm{Re}\left(\frac{a_4}{a_1}\right) < 0$, nonlinear effects are stabilising and the linearly unstable mode is supercritically stable with an equilibrium amplitude given by

$$|A_{11}| = \sqrt{\frac{\mathrm{Re}\left(\frac{a_2}{a_1}\lambda_2 + \frac{a_3}{a_1}\Omega_2\right)}{-\mathrm{Re}\left(\frac{a_4}{a_1}\right)}}. \tag{4.3.1b}$$

In figure 4.24a we show $\mathrm{Re}(a_2/a_1)$ as a function of a for $n = 1$ corresponding to the first five neutral modes of the non-axisymmetric eigenrelation (3.1.7) for a solid wall. The arrows here and on all the subsequent figures indicate increasing mode number. We can see that this quantity is always negative. The results for $n = 2$ are shown in figure 4.25a. The magnitudes are decreased when compared to $n = 1$. The corresponding values of $\mathrm{Re}(a_3/a_1)$ are shown in figures 4.24b and 4.25b, respectively for $n = 1$ and

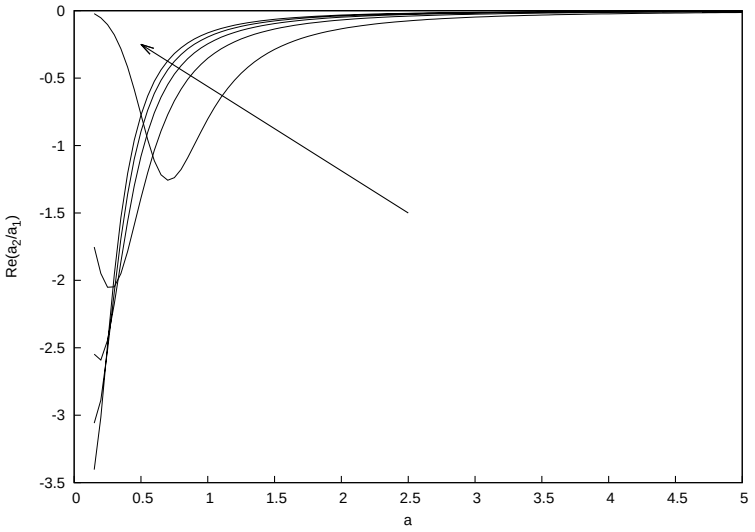

(a)

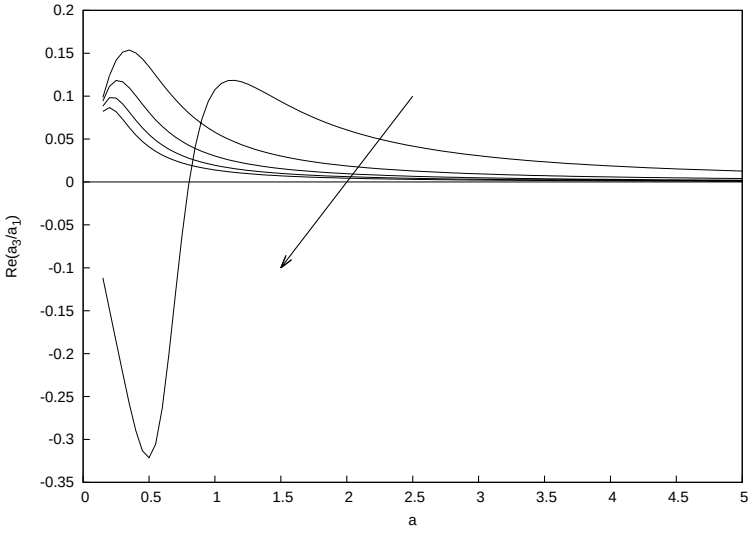

(b)

Figure 4.24: (a) Re(a_2/a_1); (b) Re(a_3/a_1), as a function of local cone radius a for the first five modes. Results are shown for solid wall with $n = 1$ and $a/r_s = 0.57$.

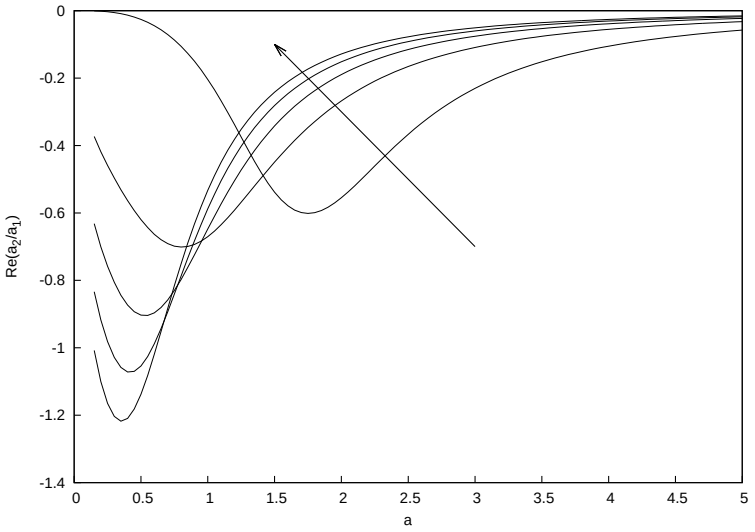

(a)

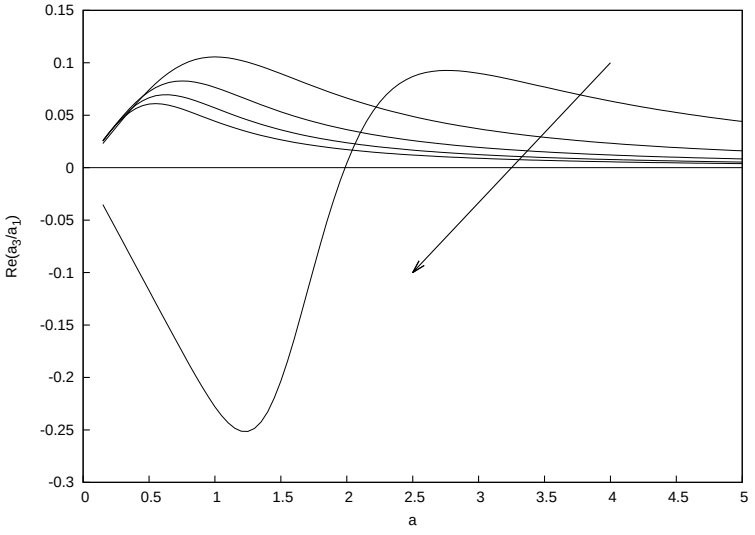

(b)

Figure 4.25: (a) Re(a_2/a_1); (b) Re(a_3/a_1), as a function of local cone radius a for the first five modes. Results are shown for solid wall with $n = 2$ and $a/r_s = 0.57$.

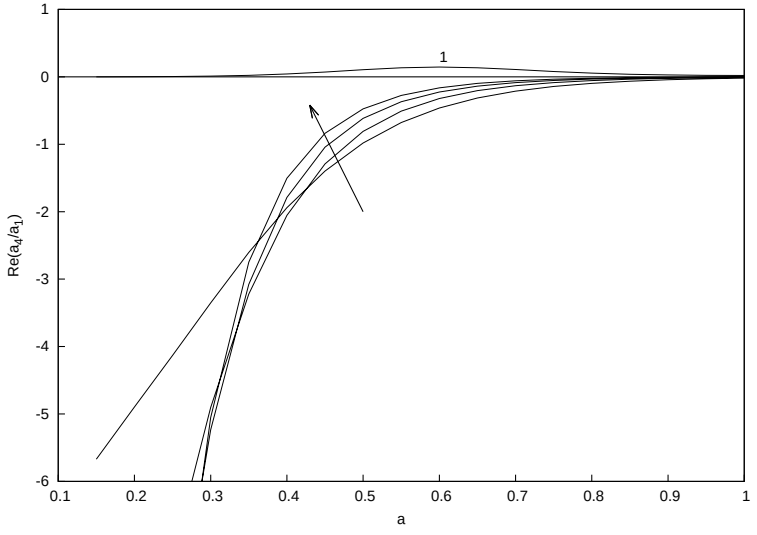

(a)

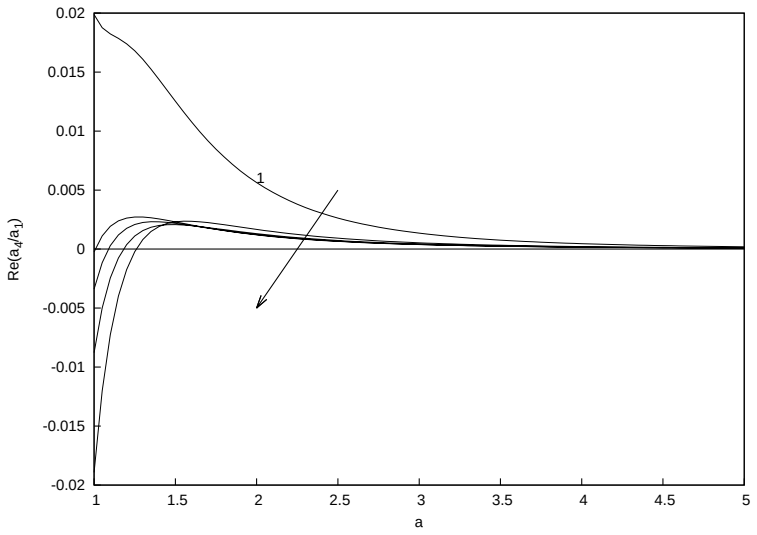

(b)

Figure 4.26: $\mathrm{Re}(a_4/a_1)$ for the first five modes as a function of local cone radius a for (a) $0 \leqslant a \leqslant 1.0$; (b) $1.0 \leqslant a \leqslant 5.0$. Results are shown for a solid wall with $n = 1$ and $a/r_s = 0.57$.

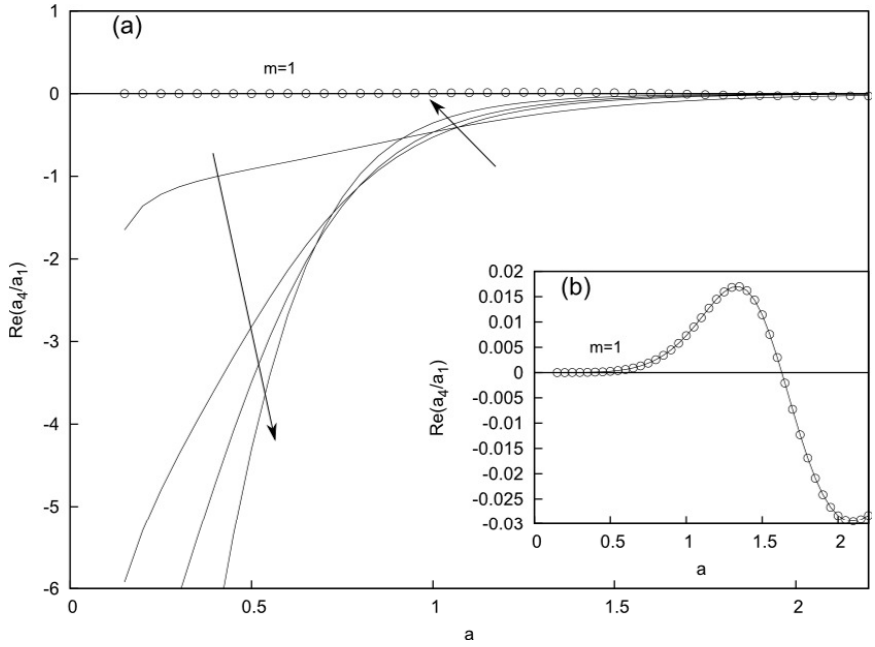

Figure 4.27: (a) $\mathrm{Re}(a_4/a_1)$ for the first five modes as a function of local cone radius a for $0 \leqslant a \leqslant 2.3$. Results are shown for a solid wall with $n = 2$ and $a/r_s = 0.57$; (b) $\mathrm{Re}(a_4/a_1)$ for the first mode as a function of a.

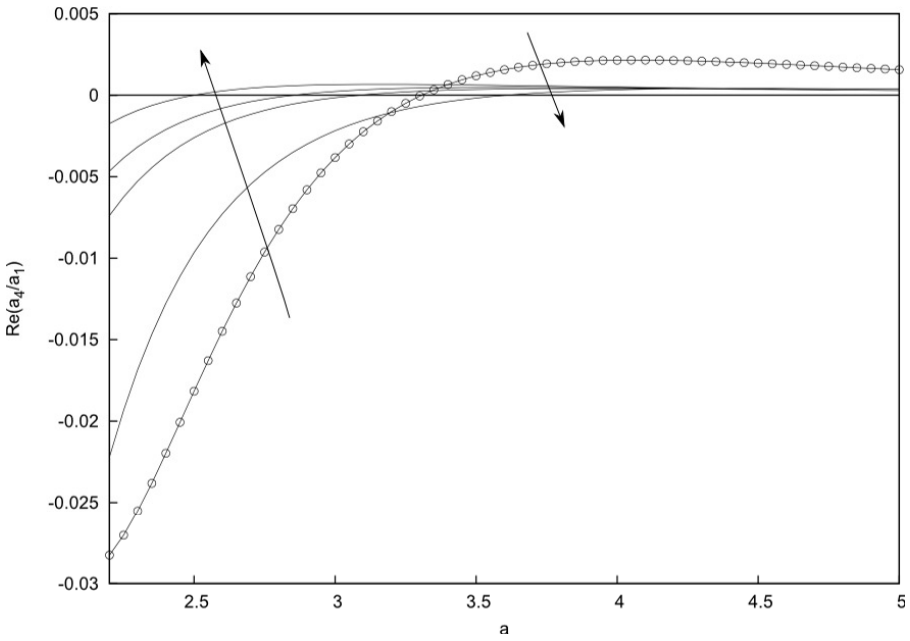

Figure 4.28: $\mathrm{Re}(a_4/a_1)$ for the first five modes as a function of local cone radius a for $2.3 \leqslant a \leqslant 5.0$. Results are shown for a solid wall with $n = 2$ and $a/r_s = 0.57$.

$n = 2$. There is a difference in behaviour of $\mathrm{Re}(a_3/a_1)$ for the first mode for small values of a, corresponding to the anomalous behaviour of the lowest neutral solution (see figure 4.2). The effect of increasing the azimuthal wavenumber is to decrease the magnitude of $\mathrm{Re}(a_3/a_1)$.

We now investigate the effect of nonlinearity on linearly unstable disturbances by considering the sign of $\mathrm{Re}(a_4/a_1)$. In order to see the behaviour of the different modes the values of $\mathrm{Re}(a_4/a_1)$ versus a for $0 < a \leqslant 1$ is shown in figure 4.26a and for $1 \leqslant a \leqslant 5$ is shown in figure 4.26b for $n = 1$. In figures 4.26a and 4.26b we can see that the sign of $\mathrm{Re}(a_4/a_1)$ is always positive for the first mode ($m = 1$). Thus nonlinear effects always destabilise this mode possibly leading to a subcritical instability. The effect of nonlinearity on the remaining four modes depends on the value of a. For $a < 1$, $\mathrm{Re}(a_4/a_1) < 0$ leading to supercritical instability. As the value of a increases, the sign of $\mathrm{Re}(a_4/a_1)$ becomes positive beginning with the higher modes indicating that nonlinear effects now destablise these linearly unstable modes. We also notice an overlapping of modes $m > 1$ for a certain range of a, such that for $a < 0.425$ we see the stabilising effect of nonlinearity increasing with mode number and for $a > 1.5$, we see it decreasing with increasing mode number. In the limit of large a we can see that $\mathrm{Re}(a_4/a_1) \to 0$ for all the modes, with the first mode having the highest amplitude. Recall that for a fixed cone angle the effect of increasing a is to move further along the cone surface. Thus at large streamwise distances we can expect nonlinear disturbance amplitudes to be very small. The corresponding results for $\mathrm{Re}(a_4/a_1)$ with $n = 2$ can be seen in figures 4.27 and 4.28. In figure 4.27a we can see that effect of nonlinearity on modes $m > 1$ for $n = 2$ are similar to that for $n = 1$. Higher azimuthal wavenumber allows the stabilising effect of nonlinearity to persist for larger ranges of a. In figure 4.28 we see that $\mathrm{Re}(a_4/a_1)$ becomes positive for $a > 2.3$ with the higher modes becoming destabilised first. We again notice a region of overlapping of modes $m > 1$ similiar to that seen for $n = 1$. The range of overlap is now wider and shifted

to higher values ($1 < a < 3.3$). The effect of azimuthal wavenumber is more significant on the first mode as can be seen in figure 4.27b. Here we see that the first mode is stabilised by nonlinearity for a narrow range of a ($\mathrm{Re}(a_4/a_1) < 0$ when $1.6 < a < 3.3$). In the limit of large a nonlinear effects on the first mode persist while the effects on the higher modes diminish as $\mathrm{Re}(a_4/a_1) \to 0$ for these modes. The effect of nonlinearity for disturbances with $n = 3$ have also been investigated. The results (see later) indicate that overall trends remain similar to that for $n = 2$. We may thus conclude that nonlinear effects tend to stabilise the higher modes over a wider range of a for higher azimuthal wavenumbers, and the first mode becomes the most destabilised by nonlinearity at large values of a.

We consider the effect of nonlinearity on axisymmetric disturbances next. Axisymmetric disturbances are linearly unstable if $\mathrm{Re}(a_{20}\lambda_2/a_{10}) > 0$. If $\mathrm{Re}(a_{40}/a_{10}) < 0$ for these disturbances then nonlinear effects are stabilising and the linearly unstable modes are supercritically stable with an equilibrium amplitude

$$|A_{11}| = (-\lambda_2)^{1/2} \left(\frac{-\mathrm{Re}(a_{20})}{-\mathrm{Re}(a_{40})} \right)^{1/2}.$$

In figure 4.29a we can see $\mathrm{Re}(a_{20}/a_{10})$ as a function of a. We notice that this quantity is always negative so disturbances are linearly unstable. Figure 4.29b shows $\mathrm{Re}(a_{40}/a_{10})$ versus a corresponding to the first four modes. We see that this quantity is negative for all the modes with the exception of the first mode. For this mode, $\mathrm{Re}(a_{40}/a_{10})$ becomes slightly positive for $a > 2.3$. Thus, we can expect nonlinear effects to stabilise linearly unstable axisymmetric disturbances with the exception of the first mode which is slightly destabilised above a certain value of a.

The results discussed above for $\mathrm{Re}(a_{40}/a_{10})$ and $\mathrm{Re}(a_4/a_1)$ differ from those presented by Stephen (2006). In that paper it was reported that $\mathrm{Re}(a_{40}/a_{10})$ and $\mathrm{Re}(a_4/a_1)$ were always negative, so the nonlinear effects were always stabilising. Our corrected results

have shown the significant result that the nonlinear effects are destabilising for particular ranges of a.

4.3.1.1 Effect of the shock and curvature

Before proceeding to investigate the effect of porous coatings on the nonlinear stability it is useful to consider the stability problem in the absence of a shock. The problem in the absence of shock was first considered by Duck & Hall (1989, 1990). It can be shown that the neutral curves in the absence of shock differ fundamentally from those in the presence of shock as solutions are only possible for a finite range of a (Seddougui & Bassom 1997). If no shock is present, solutions to the upper deck problem, (2.4.19c) at first order are only proportional to $K_n(\mathrm{i}\alpha r)$, allowing only for outgoing waves as $r \to \infty$. Here the shock condition (2.4.19e) is applied at $r_s \to \infty$. This modifies the resulting eigenrelation. The nonlinear stability analysis can be carried out in a straightforward manner for this problem. Figure 4.30 shows $\mathrm{Re}(a_4/a_1)$ as a function of a for $n = 1$ and $n = 2$. It can be seen that the sign of $\mathrm{Re}(a_4/a_1)$ is always negative and two solution branches exist for $0 < a < 0.75$ for $n = 1$ and $0 < a < 1.75$ for $n = 2$. Thus in the absence of shock nonlinear effects are stabilising for all admissible values of a.

We can deduce the significance of curvature on the nonlinear stability by comparing our results for a solid wall to those obtained from the analysis of Seddougui & Bassom (1994) for the weakly nonlinear stability of flow over a wedge. Figure 4.31 shows the variation of the $\mathrm{Re}(a_3)$, the coefficient of the nonlinear term of the amplitude equation in their paper (cf. equation 5.1) with β_1, the leading order scaled spanwise wavenumber. The results are shown for a scaled shock distance $\overline{y}_s = 1.73$ which corresponds to $a/r_s = 0.57$, the condition considered in this study. Corresponding results (cf. figure 5) shown in Seddougui & Bassom (1994) were obtained using incorrect values for two constants in their equation 4.12. Our corrected results shows the significant result that for a small range of $0 < \beta_1 < 0.7$, $\mathrm{Re}(a_3) > 0$. Thus nonlinear effects will be destabilizing for

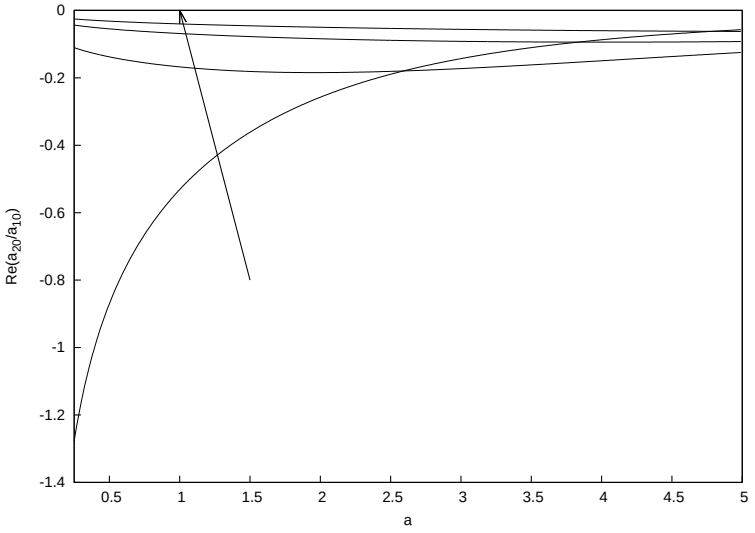

(a)

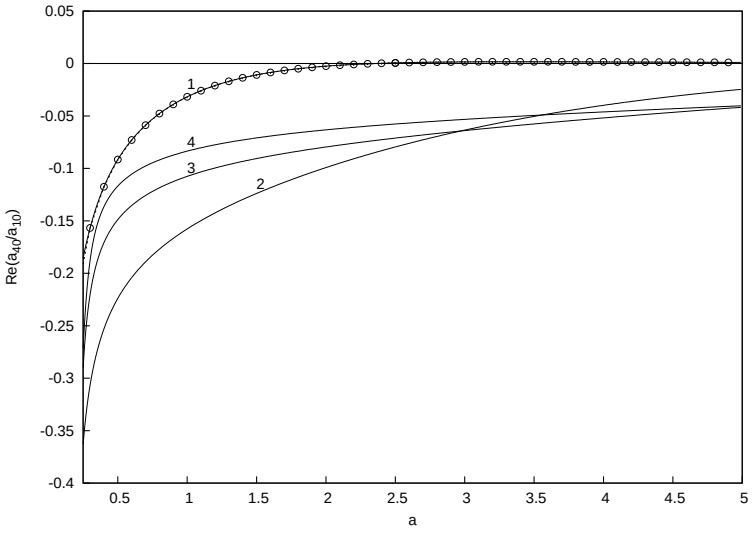

(b)

Figure 4.29: (a) Re(a_{20}/a_{10}); (b) Re(a_{40}/a_{10}) for the first four modes as a function of local cone radius a. Results are shown for solid wall with $n = 0$ and $a/r_s = 0.57$. Results for the first mode are indicated by $\circ$.

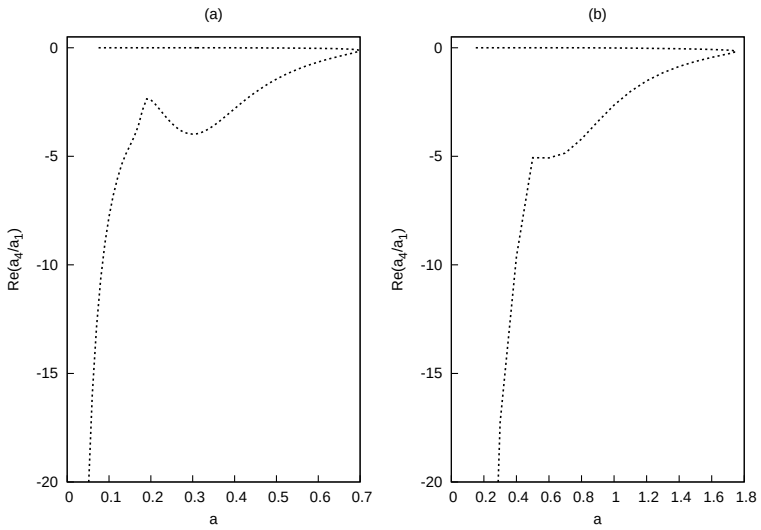

Figure 4.30: $\mathrm{Re}(a_4/a_1)$ as a function of local cone radius a in the absence of shock. Results are shown for solid wall with (a) $n = 1$ and (b) $n = 2$.

disturbances with these spanwise wavenumbers. By comparing the magnitudes of $\mathrm{Re}(a_3)$ and $\mathrm{Re}(a_4/a_1)$ (from figure 4.26 for example) we can infer that curvature has the effect of making the nonlinear effects stronger.

4.3.2 Effect of porous walls

We can now investigate the effect of porous coatings. We begin by considering the regular porous wall model of (2.3.4). The results using this model are compared to the results for a solid wall for non-axisymmetric modes.

We turn to figure 4.32 which compares $\mathrm{Re}(a_4/a_1)$ for $n = 1$ between the solid and regular porous walls for the first five modes ($m = 1 - 5$). We see that nonlinear effects are enhanced by the porous wall giving larger values of $\mathrm{Re}(a_4/a_1)$. In the presence of the porous wall nonlinear effects destabilise the lower modes (first and second) while stabilising the higher modes (three to five). We can see this from the fact that $\mathrm{Re}(a_4/a_1)$ for the porous wall has larger positive values for the first and second modes compared to

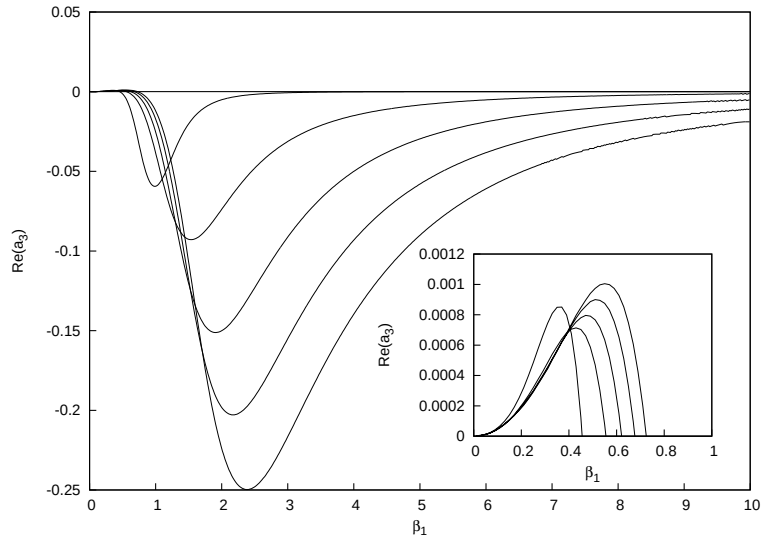

Figure 4.31: $\mathrm{Re}(a_3)$ for the first five modes as a function of spanwise wavenumber β_1 for $\overline{y}_s = 1.73$ (cf. equation 5.1 of Seddougui & Bassom 1994).

the solid wall and that $\mathrm{Re}(a_4/a_1)$ for the porous wall becomes positive at larger values of a compared with the solid wall for the higher modes. However once destabilised, the higher modes of the porous wall have larger values of $\mathrm{Re}(a_4/a_1)$ compared to the solid wall. For large enough values of a, we can expect the nonlinear effects to diminish just as in the solid wall case.

Figure 4.33 shows the corresponding results for $\mathrm{Re}(a_4/a_1)$ with $n = 2$. Here we see that nonlinearity destabilises the first, second, third and fourth modes in comparison to corresponding modes of the solid wall, while stabilising the fifth and possibly higher modes of the porous wall. Results obtained for $n = 3$ in figure 4.34 show that nonlinearity destabilizes all of the first five modes of the porous wall compared to the solid wall. We can thus infer that in presence of the porous wall, nonlinearity destabilizes lower modes with their mode number increasing with azimuthal wavenumber.

We now compare the effect of porosity on the nonlinear stability of axisymmetric disturbances. We look at figure 4.35 which shows $\mathrm{Re}(a_{40}/a_{10})$ as a function of a for the

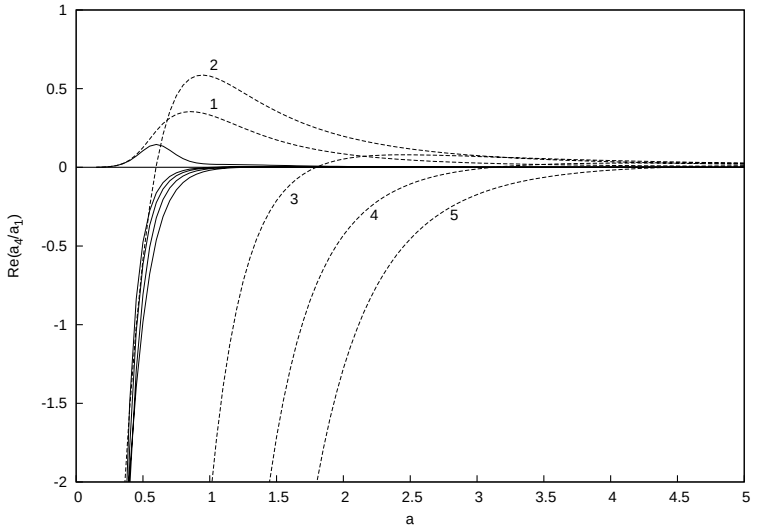

Figure 4.32: $\mathrm{Re}(a_4/a_1)$ for the first five modes as a function of local cone radius a for $n = 1$ and $a/r_s = 0.57$: —, solid wall; − − −, regular microstructure model (2.3.4).

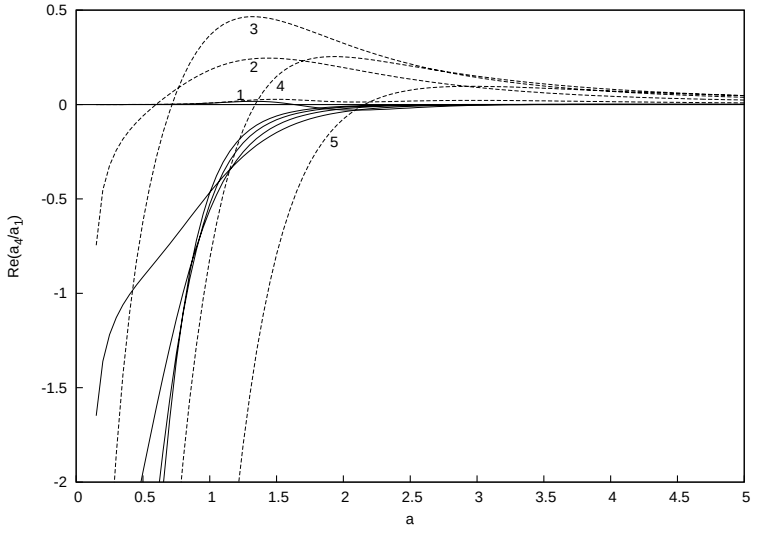

Figure 4.33: $\mathrm{Re}(a_4/a_1)$ for the first five modes as a function of local cone radius a for $n = 2$ and $a/r_s = 0.57$: —, solid wall; − − −, regular microstructure model (2.3.4).

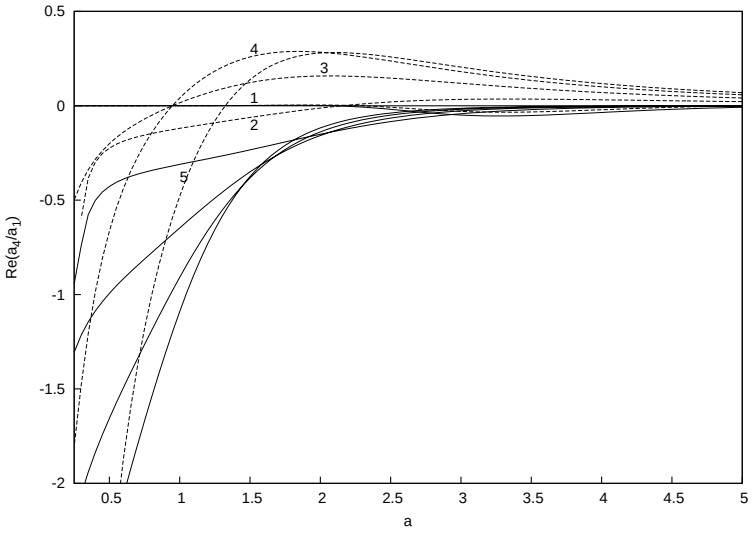

Figure 4.34: $\mathrm{Re}(a_4/a_1)$ for the first five modes as a function of local cone radius a for $n = 3$ and $a/r_s = 0.57$: —, solid wall; − − −, regular microstructure model (2.3.4).

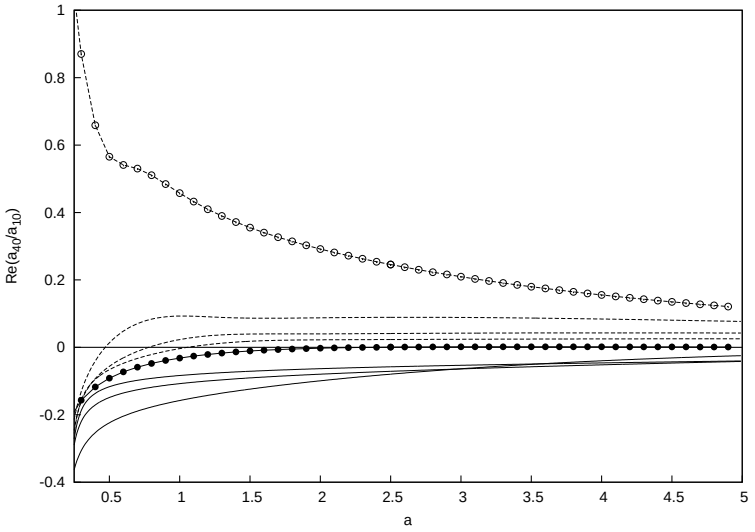

Figure 4.35: $\mathrm{Re}(a_{40}/a_{10})$ for the first four modes as a function of local cone radius a for $n = 0$ and $a/r_s = 0.57$: —, solid wall; − − −, regular microstructure model (2.3.4). Results for the first mode are indicated by • for solid wall and ∘ for porous wall.

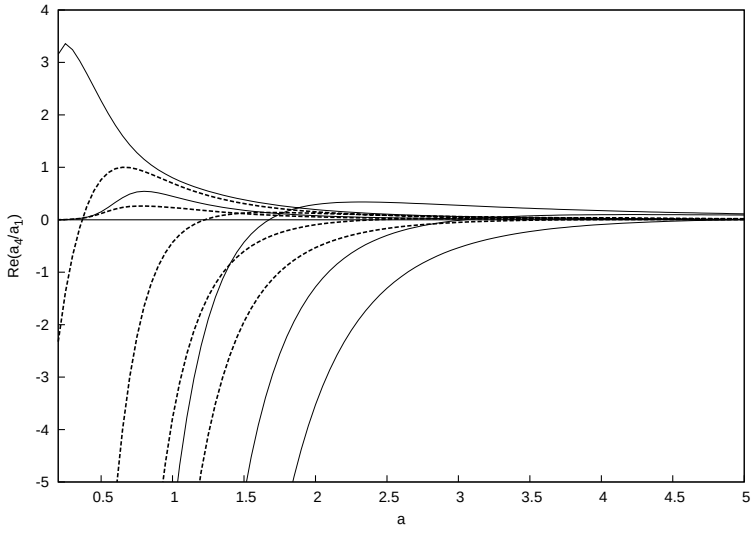

Figure 4.36: $\mathrm{Re}(a_4/a_1)$ for the first five modes as a function of local cone radius a for $n = 1$ and $a/r_s = 0.57$: —, random microstructure model (2.3.9); $---$, regular microstructure model (2.3.4).

porous wall and solid wall. Here we see that in the presence of porous wall all the modes are destabilised by nonlinearity with the most significant effect being felt by the first mode. This mode is destabilised for all values of a.

Next we consider the random microstructure model of (2.3.9). The results using this model are compared with those obtained using the regular microstructure model. Figure 4.36 shows $\mathrm{Re}(a_4/a_1)$ for $n = 1$ for both the models. We see that nonlinear effects destabilise the first two modes of the felt metal model when compared to the regular porous model. The effect on the higher modes is opposite as we see that $\mathrm{Re}(a_4/a_1)$ becomes positive at smaller values of a for the regular porous model as compared to the felt metal model. Once destabilized, values of $\mathrm{Re}(a_4/a_1)$ are more positive for the felt metal indicating that nonlinear amplification of disturbances will be stronger.

Finally we consider the mesh microstructure model of (2.3.6). Figure 4.37 shows $\mathrm{Re}(a_4/a_1)$ for $n = 1$ for both the models. The effect of the two models on the first

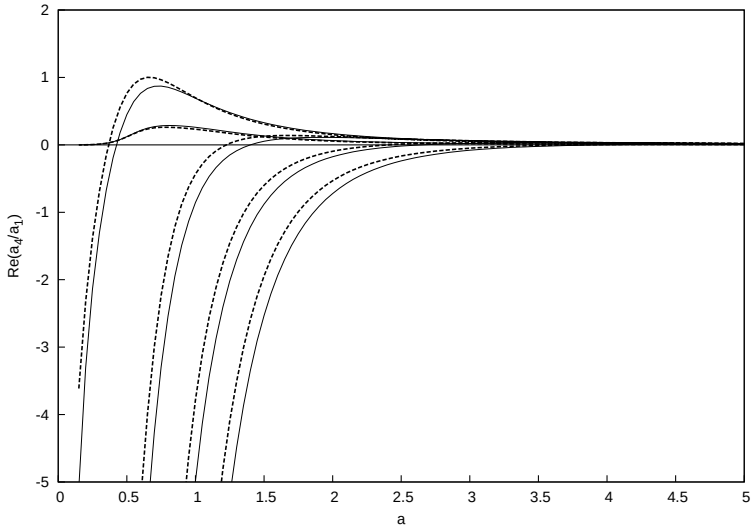

Figure 4.37: $\mathrm{Re}(a_4/a_1)$ for the first five modes as a function of local cone radius a for $n = 1$ and $a/r_s = 0.57$: —, mesh microstructure model (2.3.6); $- - -$, regular microstructure model (2.3.4).

mode is similar. For the higher modes nonlinear effects are slightly more destabilising for the regular model compared to the mesh model. This can again be seen by noting that $\mathrm{Re}(a_4/a_1)$ becomes positive at smaller values of a for the regular model compared to the mesh model. The effect of higher porosity is considered in more detail in the next section.

4.3.2.1 Parametric studies

In Section 4.2 the effects of wall cooling, porosity and pore-depth on the linear stability problem was investigated. In this section we examine their effects on the nonlinear stability.

We begin by examining the nonlinear stability results for the regular porous model with a higher porosity of $\phi_0 = \frac{\pi}{4}$. In figures 4.38a and 4.38b for $n = 0$ and $n = 1$, respectively, we see that higher porosity leads to nonlinearity having a stabilizing effect on mode numbers greater than one. This can be seen by noting the increase in the value of a where $\mathrm{Re}(a_4/a_1)$ becomes positive. However, for large values of a the destabilising

effect of nonlinearity is stronger with $\mathrm{Re}(a_4/a_1)$ being slightly larger for higher porosity. In figure 4.39a for $n = 2$ we see the stabilising effect of higher porosity for mode numbers greater than two and in figure 4.39b for $n = 3$ we see it for mode numbers greater than three.

In Section 4.2.1 we showed that moderate levels of wall cooling leads to a significant destabilisation of linearly unstable disturbances. The effect of nonlinearity on these disturbances is now considered. In figure 4.40 we show $\mathrm{Re}(a_4/a_1)$ against a for $n = 1$ for $T_w = T_{ad}$ and $T_w = 0.25T_{ad}$. The effect of wall cooling is to destabilise the first mode and stabilise the remaining modes. We can see this by noting that for the first mode $\mathrm{Re}(a_4/a_1)$ is larger for the colder wall and for the higher modes $\mathrm{Re}(a_4/a_1)$ becomes positive at larger values of a. Thus at smaller values of a, nonlinearity stabilises the modes that are most linearly amplified by wall cooling. At large enough a, these higher modes become destabilised by nonlinearity with $\mathrm{Re}(a_4/a_1)$ being more positive and thereby leading to greater nonlinear amplification in the presence of the colder wall.

Further discussion of the nonlinear stability results is presented in Section 5.3.

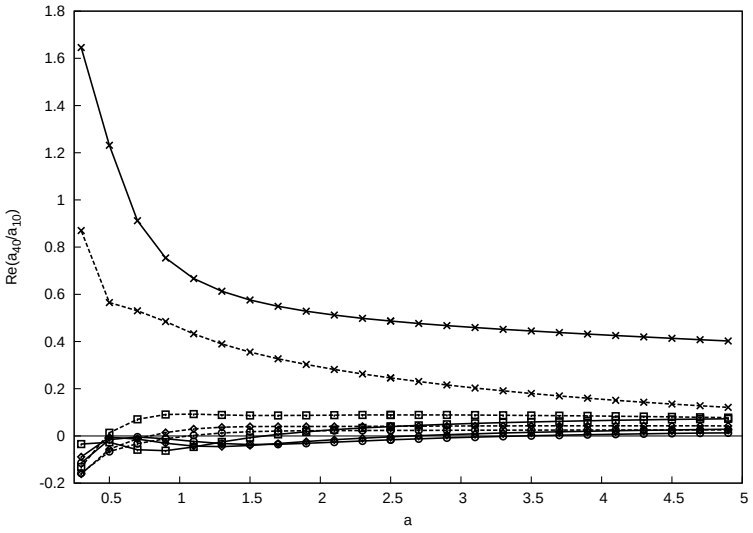

(a)

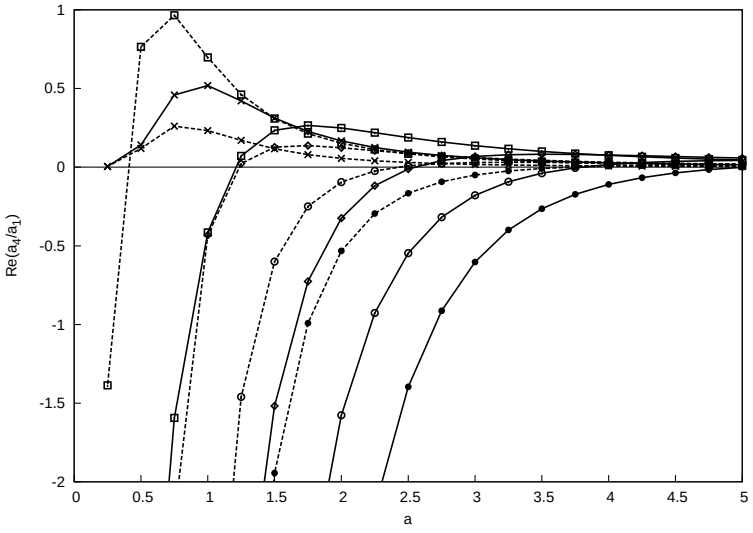

(b)

Figure 4.38: $\mathrm{Re}(a_4/a_1)$ as a function of local cone radius a for $a/r_s = 0.57$ and (a) $n = 0$; (b) $n = 1$. Results are shown using the regular microstructure model (2.3.4): —, $\phi_0 = \pi/4$; $- - -$,$\phi_0 = 0.2$. Symbols refer to mode number: $\times$, $m = 1$; $\square$, $m = 2$; $\diamond$, $m = 3$; $\circ$, $m = 4$; $\bullet$, $m = 5$.

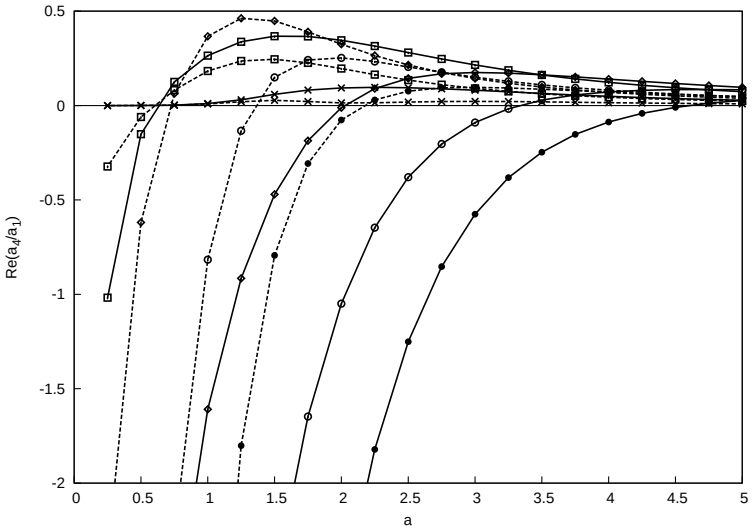

(a)

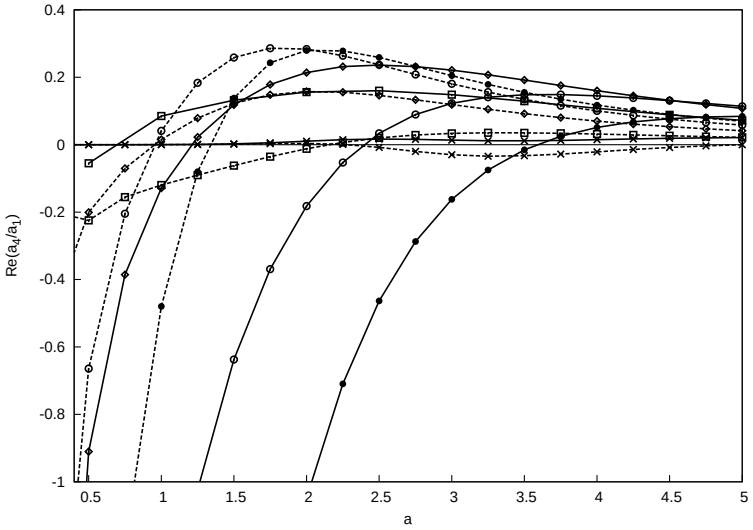

(b)

Figure 4.39: $\mathrm{Re}(a_4/a_1)$ as a function of local cone radius a for $a/r_s = 0.57$ and (a) $n = 2$; (b) $n = 3$. Results are shown using the regular microstructure model (2.3.4): —, $\phi_0 = \pi/4$; $- - -$,$\phi_0 = 0.2$. Symbols refer to mode number: $\times$, $m = 1$; $\square$, $m = 2$; $\diamond$, $m = 3$; $\circ$, $m = 4$; $\bullet$, $m = 5$.

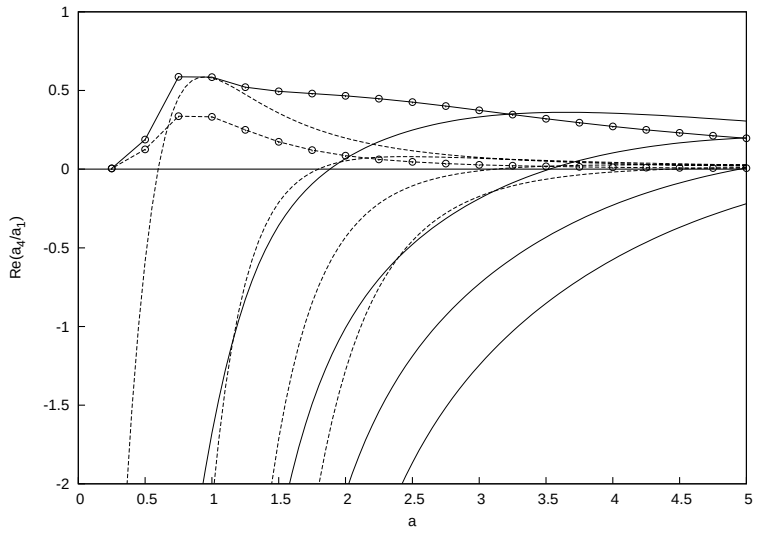

Figure 4.40: $\mathrm{Re}(a_4/a_1)$ for the first five modes as a function of local cone radius a for $n = 1$ and $a/r_s = 0.57$ using regular microstructure model (2.3.4): —, $T_w = 0.25T_{ad}$; $- - -$, $T_w = T_{ad}$. Results for the first mode are indicated by $\circ$.

Chapter 5

Discussion

In this study the weakly nonlinear stability of viscous modes in a hypersonic boundary layer on a slender cone was investigated. The problem was considered at increasing orders of the relative size of the disturbance amplitude of the viscous disturbances. After a lengthy analysis, an evolution equation that describes the streamwise development of the amplitude was derived at third order. The linear stability problem is obtained at first order and is governed by the solutions to the axisymmetric and non-axisymmetric eigenrelations. The effect of nonlinearity on disturbances that are linearly unstable is ascertained from the numerical evaluation of the coefficients of the evolution equation. We derive some asymptotic approximations to the eigenrelations and coefficients of the amplitude equation in Section 5.1. We summarise the results of the linear stability analysis in Section 5.2 and compare them with published studies on the second-mode instability in the presence of porous coatings. Finally in Section 5.3 we summarise the results of the nonlinear stability analysis and discuss the transition process for hypersonic boundary layers.

5.1 Asymptotic approximations - Solid wall case

In this section we will consider some asymptotic approximations to the non-axisymmetric linear eigenrelation and nonlinear coefficient $\mathrm{Re}(a_4/a_1)$ in the limit of large a and small a. We will consider the linear eigenrelation (3.1.7) in the following form

$$\frac{\mathrm{Ai}'(\xi_0)}{\int_{\xi_0}^{\infty}\mathrm{Ai}(\xi)d\xi} = \mathrm{i}^{1/3}\alpha^{4/3}\frac{n^2}{\alpha^2a^2}\frac{J_n(\alpha a)Y_n(\alpha r_s)-J_n(\alpha r_s)Y_n(\alpha a)}{J_n(\alpha r_s)Y_n'(\alpha a)-J_n'(\alpha a)Y_n(\alpha r_s)}, \tag{5.1.1}$$

where we have set $A_y = 0$ and written the modified Bessel functions I_n and K_n in terms of J_n and Y_n. For neutral solutions of (5.1.1), as in the classic planar incompressible stability problem it is found from the numerical results that $\xi_0 \approx -2.297\mathrm{i}^{1/3}$, and that the LHS may be approximated as $1.001\mathrm{i}^{1/3}$. This result is not valid for the porous wall case, due to the presence of the complex admittance term A_y in the equation. We can then seek to approximate the RHS of (5.1.1) depending on the size of the arguments of the Bessel functions. This will allow us to derive an approximate solution for α in the limit of large a or small a. This solution can then be substituted in the expressions for the nonlinear coefficients a_4 and a_1 to also obtain an approximate solution for $\mathrm{Re}(a_4/a_1)$. Thus we will be able to get an analytic confirmation of the behaviour of α and $\mathrm{Re}(a_4/a_1)$ illustrated by the numerical results.

5.1.1 Limit: $a >> 1$

We will begin by considering the limit of large a. Recall that we consider a/r_s to be some fixed quantity which implies that r_s is also large in this limit. From the numerical results (see figure 4.2 for example), we can see that in this limit α tends to some $O(1)$ quantity. This suggests that for large enough a we may consider $\alpha a >> 1$ and $\alpha r_s >> 1$. If we define $z = \alpha r_s$ and $\eta = \alpha(r_s - a)$, then we can write (5.1.1) as

$$\frac{\mathrm{Ai}'(\xi_0)}{\int_{\xi_0}^{\infty}\mathrm{Ai}(\xi)d\xi} = \mathrm{i}^{1/3}\alpha^{4/3}\frac{n^2}{\alpha^2 a^2}\frac{J_n(z-\eta)Y_n(z)-J_n(z)Y_n(z-\eta)}{J_n(z)Y_n'(z-\eta)-J_n'(z-\eta)Y_n(z)} \tag{5.1.2}$$

We then use the large argument expansions of the Bessel functions J_n and Y_n as given in Abramovitz & Stegun (1972). We have to $O(1/z^2)$

$$\begin{aligned}
J_n(z) \sim& \sqrt{\frac{2}{\pi z}}\left[\left(1-\frac{(\mu-1)(\mu-9)}{128z^2}\right)C_n(z)-\frac{\mu-1}{8z}S_n(z)\right],\\
J_n'(z) \sim& -\sqrt{\frac{2}{\pi z}}\left[\left(1-\frac{(\mu-1)(\mu+15)}{128z^2}\right)S_n(z)+\frac{\mu+3}{8z}C_n(z)\right],\\
Y_n(z) \sim& \sqrt{\frac{2}{\pi z}}\left[\left(1-\frac{(\mu-1)(\mu-9)}{128z^2}\right)S_n(z)+\frac{\mu-1}{8z}C_n(z)\right],\\
Y_n'(z) \sim& \sqrt{\frac{2}{\pi z}}\left[\left(1-\frac{(\mu-1)(\mu+15)}{128z^2}\right)C_n(z)+\frac{\mu+3}{8z}S_n(z)\right],
\end{aligned} \tag{5.1.3a}$$

where we define $\mu = 4n^2$ and

$$\begin{aligned}
C_n(z) =& \cos\left(z-\left(\frac{n}{2}+\frac{1}{4}\right)\right),\\
S_n(z) =& \sin\left(z-\left(\frac{n}{2}+\frac{1}{4}\right)\right).
\end{aligned} \tag{5.1.3b}$$

We can also make use of the fact that

$$\begin{aligned}
\cos\left(z-\eta-\left(\frac{n}{2}+\frac{1}{4}\right)\right) &= C_n(z)\cos(\eta)+S_n(z)\sin(\eta),\\
\sin\left(z-\eta-\left(\frac{n}{2}+\frac{1}{4}\right)\right) &= S_n(z)\cos(\eta)-C_n(z)\sin(\eta).
\end{aligned} \tag{5.1.3c}$$

Using (5.1.3) we can obtain

$$\begin{aligned}
&J_n(z-\eta)Y_n(z)-J_n(z)Y_n(z-\eta) \sim\\
&\frac{2}{\pi\sqrt{z(z-\eta)}}\left[\sin(\eta)+\frac{\mu-1}{8z}\cos(\eta)-\frac{\mu-1}{8(z-\eta)}\cos(\eta)\right.
\end{aligned}$$

$$- \frac{(\mu-1)(\mu-9)}{128z^2}\sin(\eta) - \frac{(\mu-1)(\mu-9)}{128(z-\eta)^2}\sin(\eta) + \frac{(\mu-1)^2}{64z(z-\eta)}\sin(\eta)\Bigg], \tag{5.1.4a}$$

$$J_n(z)Y_n'(z-\eta) - Y_n(z)J_n'(z-\eta) \sim$$
$$\frac{2}{\pi\sqrt{z(z-\eta)}}\Bigg[\cos(\eta) - \frac{\mu-1}{8z}\sin(\eta) + \frac{\mu+3}{8(z-\eta)}\sin(\eta)$$
$$- \frac{(\mu-1)(\mu-9)}{128z^2}\cos(\eta) - \frac{(\mu-1)(\mu+15)}{128(z-\eta)^2}\cos(\eta) + \frac{(\mu-1)^2}{64z(z-\eta)}\cos(\eta)\Bigg]. \tag{5.1.4b}$$

So to leading order (5.1.1) may be approximated as

$$1.001\mathrm{i}^{1/3} \approx \frac{\mathrm{i}^{1/3}n^2}{a^2\alpha^{2/3}}\frac{\sin(\eta)}{\cos(\eta)},$$

which requires

$$\tan(\eta) \approx \frac{a^2\alpha^{2/3}}{n^2} >> 1. \tag{5.1.4c}$$

So we let

$$\eta = (2m-1)\pi/2 - \delta, \qquad m = 1, 2, \ldots, \qquad \delta << 1. \tag{5.1.4d}$$

Then we can show that

$$\begin{aligned}\tan\left((2m-1)\pi/2 - \delta\right) &= \frac{\sin\left((2m-1)\pi/2+\delta\right)\cos(\delta) - \cos\left((2m-1)\pi/2+\delta\right)\sin(\delta)}{\cos\left((2m-1)\pi/2+\delta\right)\cos(\delta) - \sin\left((2m-1)\pi/2+\delta\right)\sin(\delta)} \\ &= \frac{\cos(\delta)}{\sin(\delta)} \approx \frac{1-\delta^2/2+\ldots}{\delta-\delta^3/6+\ldots},\end{aligned} \tag{5.1.4e}$$

where we obtain the last expression using Taylor expansions. Using (5.1.4e) in (5.1.4c), to leading order we get

$$\delta = \frac{n^2}{a^2\alpha^{2/3}}.$$

If we define $\varepsilon = r_s - a$, then

$$\alpha = \frac{\eta}{\varepsilon} \approx (2m-1)\pi/2\varepsilon^{-1},$$
$$a = r_s\left(1 - \frac{\varepsilon}{r_s}\right).$$

So

$$\delta \approx \frac{n^2\varepsilon^{2/3}}{r_s^2\left((2m-1)\pi/2\right)^{2/3}}, \tag{5.1.4f}$$

and using (5.1.4d) we can finally write

$$\alpha \sim (2m-1)\pi/2\varepsilon^{-1} - \frac{n^2\varepsilon^{2/3}}{r_s^2\left((2m-1)\pi/2\right)^{2/3}} + \ldots. \tag{5.1.4g}$$

We note here that this same equation was derived in Seddougui & Bassom (1997). In their paper $\varepsilon << 1$. We have shown that this solution is also valid if $\varepsilon \sim O(1)$ and $\eta \sim O(1)$. The prediction given by (5.1.4g) is shown in figure 5.1a for $n = 1$ and in figure 5.1b for $n = 2$. We can see very good agreement between this asymptotic solution and the computed values especially for the higher modes. The relatively poorer agreement for the first mode is due to z and $z - \eta$ not being large enough to make (5.1.4a) and (5.1.4b) sufficiently accurate.

We can now turn to the nonlinear coefficients a_4 and a_1 in (3.3.22d) and (3.3.22a) respectively. If we set $A_y = 0$ in these equations we can then write them in the form given in Stephen (2006), using the definitions from Seddougui & Bassom (1994). Thus

$$a_4 = \mathrm{i}^{-2/3}\alpha^{5/3}\frac{\alpha^{2/3}a^2L_5 - 2\mathrm{i}n^2g_{2n}L_6}{\alpha^{2/3}a^2L_7 - 2\mathrm{i}n^2g_{2n}L_8}, \tag{5.1.5a}$$
$$a_1 = -\mathrm{i}^{4/3}L_1 + 2L_4\mathrm{i}^{1/3}\alpha^{1/3}\frac{n^2}{a^2}\left[(b_nd_n + c_ne_n)\left(K_n(\mathrm{i}\alpha a) - \frac{K_n'(\mathrm{i}\alpha a)\alpha^{2/3}a^2}{\mathrm{i}n^2}\right)\right.$$

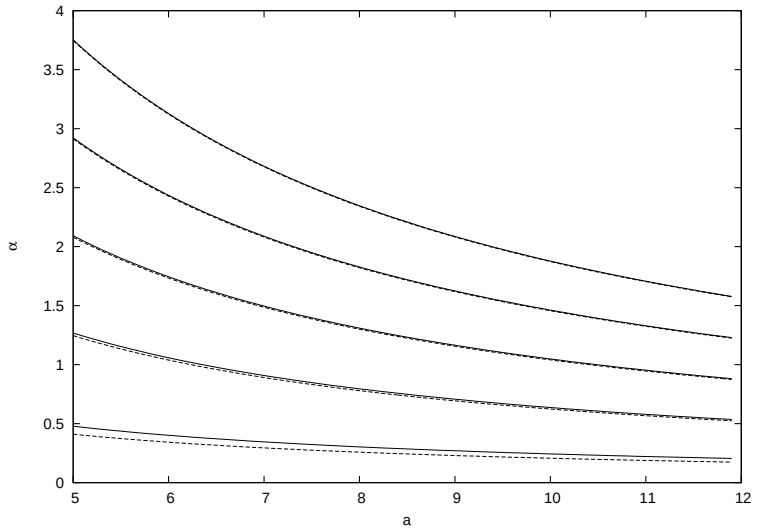

(a)

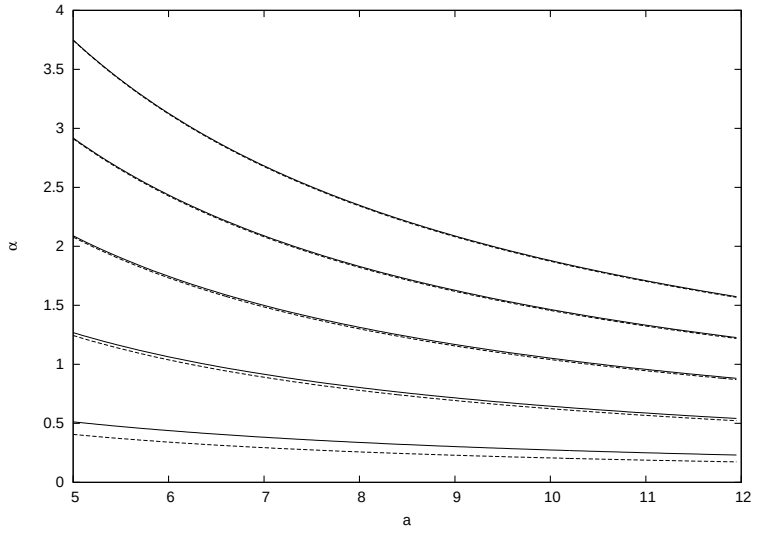

(b)

Figure 5.1: The first five neutral values of α for (a) $n = 1$; (b) $n = 2$: —, numerical solution of (5.1.1), − − −; the asymptotic approximation (5.1.4g).

$$- (b_n f_n + c_n d_n) \left(I_n(\mathrm{i}\alpha a) - \frac{I_n'(\mathrm{i}\alpha a)\alpha^{2/3}a^2}{\mathrm{i}n^2} \right) \Bigg], \tag{5.1.5b}$$

where $L_1 - L_8$, are $O(1)$ constants.

We will begin by looking at a_4. We consider the term g_{2n}. We can write this term as

$$g_{2n} = \mathrm{i}\frac{J_{2n}(2(z-\eta))Y_{2n}(2z) - J_{2n}(2z)Y_{2n}(2(z-\eta))}{J_{2n}(2z)Y_{2n}'(2(z-\eta)) - Y_{2n}(2z)J_{2n}'(2(z-\eta))}.$$

Substituting the appropriate expressions using (5.1.3) we can show that

$$\begin{aligned} g_{2n} \approx \mathrm{i} \Bigg[& \sin(2\eta) - \frac{16n^2-1}{16z}\cos(2\eta) - \frac{16n^2-1}{16(z-\eta)}\cos(2\eta) - \frac{(16n^2-1)(16n^2-9)}{512z^2}\sin(2\eta) \\ & + \frac{(16n^2-1)(16n^2-9)}{512(z-\eta)^2}\sin(2\eta) + \frac{(16n^2-1)^2}{256z(z-\eta)}\sin(2\eta) \Bigg] \times \\ & \Bigg[\cos(2\eta) - \frac{16n^2-1}{16z}\sin(2\eta) - \frac{16n^2+3}{16(z-\eta)}\sin(2\eta) - \frac{(16n^2-1)(16n^2-9)}{512z^2}\cos(2\eta) \\ & - \frac{(16n^2-1)(16n^2+15)}{512(z-\eta)^2}\cos(2\eta) + \frac{(16n^2-1)^2}{256z(z-\eta)}\cos(2\eta) \Bigg]^{-1}. \end{aligned} \tag{5.1.5c}$$

So to leading order, using (5.1.4d) we can write

$$\begin{aligned} g_{2n} &\approx \mathrm{i}\tan(2\eta) \\ &\approx \mathrm{i}\frac{\sin\left((2m-1)\pi + 2\delta\right)\cos(2\delta) - \cos\left((2m-1)\pi + 2\delta\right)\sin(2\delta)}{\cos\left((2m-1)\pi + 2\delta\right)\cos(2\delta) - \sin\left((2m-1)\pi + 2\delta\right)\sin(2\delta)} \\ &= -\mathrm{i}\frac{\sin(2\delta)}{\cos(2\delta)} \approx -2\mathrm{i}\frac{\delta - 4\delta^3/3 + \ldots}{1 - \delta^2 + \ldots} \approx -2\mathrm{i}\delta\left[1 + \frac{2\delta^2}{3} + \ldots\right]. \end{aligned} \tag{5.1.5d}$$

Thus $g_{2n} \sim O(\delta) << 1$. Using this result we can approximate (5.1.5a) as

$$a_4 \sim \mathrm{i}^{-2/3}\alpha^{5/3}\frac{L_5}{L_7}, \tag{5.1.5e}$$

where we have neglected the g_{2n} terms as they are much smaller than the $O(a^2)$ terms in the numerator and denominator of the fraction. Using (5.1.4g) we can write the approx-

imation for a_4 as

$$a_4 = \mathrm{i}^{-2/3}\frac{L_5}{L_7}\left((2m-1)\pi/2\right)^{5/3}\varepsilon^{-5/3} - \mathrm{i}^{-2/3}\frac{5n^2L_5}{3r_s^2L_7}\varepsilon^{-1} + \ldots. \tag{5.1.5f}$$

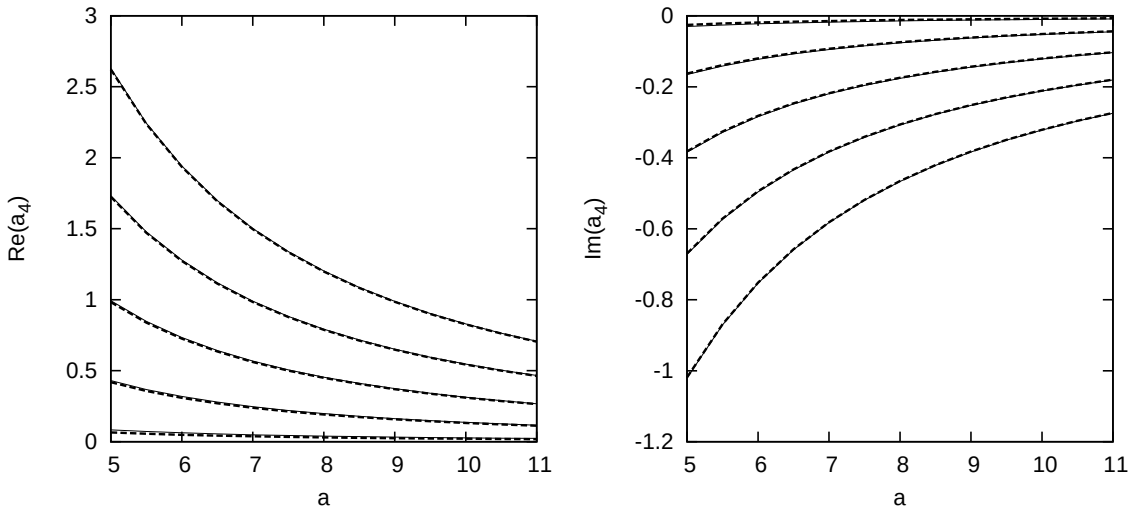

Figure 5.2: Real and Imaginary parts of a_4 for $n = 1$. Shown are —, the numerical evaluation of (5.1.5a), $- - -$; the asymptotic approximation (5.1.5f).

The solution given by (5.1.5f) is compared with the numerical evaluation of (5.1.5a) in figure 5.2 for $n = 1$ and in figure 5.3 for $n = 2$. We can see that there is very good agreement between the asymptotic solution and the computed values for all the modes.

We will now look at a_1. From (5.1.5b) we can see that our task is to expand the various terms containing the Bessel functions. We start with b_n and c_n. The definition of these functions are given (3.3.5). We will write these functions in terms of the Bessel functions J_n and Y_n. If we consider η/z to be small, we can simplify (5.1.4b) to obtain

$$J_n(z)Y_n'(z-\eta) - Y_n(z)J_n'(z-\eta) \sim \frac{2}{\pi\sqrt{z(z-\eta)}}\left[\cos(\eta) + \frac{\sin(\eta)}{2z} + \ldots\right], \tag{5.1.6a}$$

which is the denominator term of b_n and c_n. Using (5.1.4d) and Taylor expansions we can

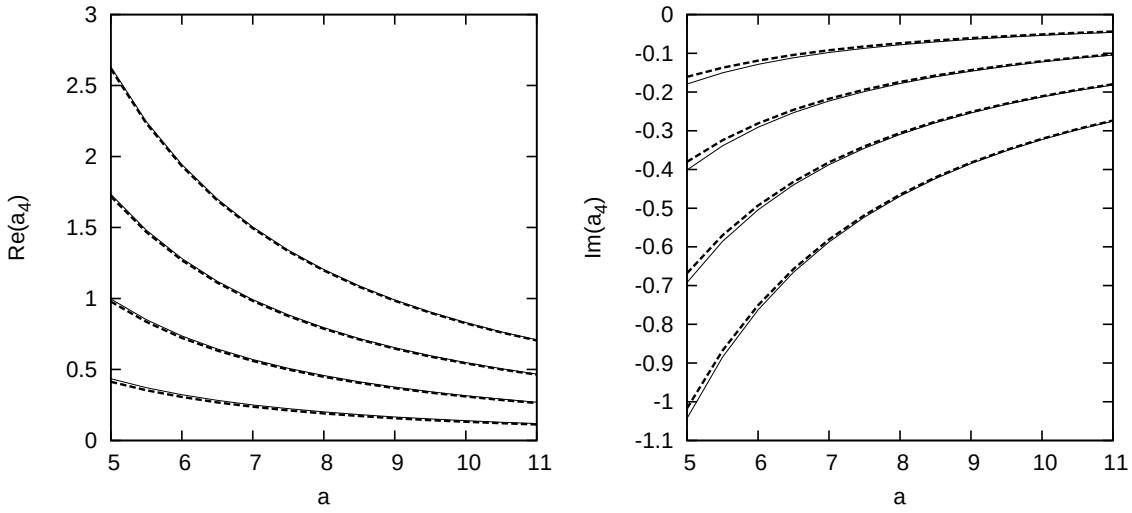

Figure 5.3: Real and Imaginary parts of a_4 for $n = 2$. Shown are —, the numerical evaluation of (5.1.5a), − − −; the asymptotic approximation (5.1.5f).

write

$$\begin{aligned}\sin(\eta) &= (-1)^{m+1}\left[1 - \frac{\delta^2}{2} + \ldots\right], \\ \cos(\eta) &= (-1)^{m+1}\left[\delta - \frac{\delta^3}{3} + \ldots\right].\end{aligned} \tag{5.1.6b}$$

Similarly using the above results alongwith (5.1.3c) we can write

$$\begin{aligned}C_n(z-\eta) =& (-1)^m\left(-S_n(z) + C_n(z)\delta + S_n(z)\delta^2/2 - C_n(z)\delta^3/6\right), \\ S_n(z-\eta) =& (-1)^m\left(C_n(z) + S_n(z)\delta - C_n(z)\delta^2/2 - S_n(z)\delta^3/6\right).\end{aligned} \tag{5.1.6c}$$

Substituting (5.1.6b) in (5.1.6a) we get

$$\begin{aligned}&\left[J_n(z)Y_n'(z-\eta) - Y_n(z)J_n'(z-\eta)\right]^{-1} \sim \\ &\qquad \mathrm{i}(-1)^m\sqrt{z(z-\eta)}\frac{1}{\delta}\left(1 + \frac{1}{2z\delta} + \ldots\right)\end{aligned} \tag{5.1.6d}$$

Using the above result and substituting (5.1.6b) in (5.1.3) we can write

$$b_n \approx \mathrm{i}(-1)^m e^{\frac{1}{2}n\pi\mathrm{i}}\sqrt{\frac{2(z-\eta)}{\pi}}\frac{1}{\delta}\left[C_n(z)-\frac{\mu-1}{8z}S_n(z)\right]\left(1+\frac{1}{2z\delta}+\ldots\right), \tag{5.1.6e}$$

$$c_n \approx \frac{1}{2}\pi\mathrm{i}e^{-\frac{1}{2}n\pi\mathrm{i}}\sqrt{\frac{\pi(z-\eta)}{2}}\frac{1}{\delta}\left(1+\frac{1}{2z\delta}+\ldots\right)\times \left[\left(C_n(z)-\mathrm{i}S_n(z)\right)-\mathrm{i}\left(C_n(z)-\mathrm{i}S_n(z)\right)\frac{\mu-1}{8z}\right]. \tag{5.1.6f}$$

Using the definitions of $C_n(z)$ and $S_n(z)$ from (5.1.3) we can obtain the following results

$$\begin{aligned} C_{n-1}(z) &= -S_n(z) \qquad S_{n-1}(z) = C_n(z), \\ C_{n+1}(z) &= S_n(z) \qquad S_{n+1}(z) = -C_n(z). \end{aligned}$$

Using the above in (5.1.6c) we also get

$$\begin{aligned} C_{n+1}(z-\eta) =&(-1)^m\left(-C_n(z)+S_n(z)\delta-C_n(z)\delta^2/2-S_n(z)\delta^3/6\right), \\ S_{n+1}(z-\eta) =&(-1)^m\left(S_n(z)-C_n(z)\delta-S_n(z)\delta^2/2+C_n(z)\delta^3/6\right), \\ C_{n-1}(z-\eta) =&(-1)^m\left(-C_n(z)-S_n(z)\delta+C_n(z)\delta^2/2+S_n(z)\delta^3/6\right), \\ S_{n-1}(z-\eta) =&(-1)^m\left(-S_n(z)+C_n(z)\delta+S_n(z)\delta^2/2-C_n(z)\delta^3/6\right). \end{aligned} \tag{5.1.6g}$$

We will now need to expand d_n, e_n and f_n (3.3.9d) for large arguments. We will write each of the functions in terms of J_n and Y_n. Substituting the asymptotic forms from (5.1.3) and using (5.1.6b) we will obtain after some simplification

$$\begin{aligned} I_n(\mathrm{i}z)K_n(\mathrm{i}z) &= \frac{-\pi\mathrm{i}}{2}J_n(z)\left(J_n(z)-\mathrm{i}Y_n(z)\right) \\ &= \frac{-1}{z}\left[\mathrm{i}C_n(z)\left(C_n(z)-\mathrm{i}S_n(z)\right)+\frac{1}{8z}\left(C_n(z)-\mathrm{i}S_n(z)\right)^2(\mu-1)\right], \\ I_{n-1}(\mathrm{i}z)K_{n+1}(\mathrm{i}z) &= \frac{\pi\mathrm{i}}{2}J_{n-1}(z)\left(J_{n+1}(z)-\mathrm{i}Y_{n+1}(z)\right) \end{aligned}$$

$$= \frac{1}{z}\left[S_n(z)\left(C_n(z) - \mathrm{i}S_n(z)\right) + \frac{1}{8z}\left(C_n(z) - \mathrm{i}S_n(z)\right)^2(\mu+3) - \frac{n}{z}\right].$$

Adding the above two expressions we get

$$I_n(\mathrm{i}z)K_n(\mathrm{i}z) + I_{n-1}(\mathrm{i}z)K_{n+1}(\mathrm{i}z) = \frac{1}{z}\left[-\mathrm{i} + \frac{1}{2z}\left(C_n(z) - \mathrm{i}S_n(z)\right)^2 - \frac{n}{z}\right].$$

Similarly using (5.1.6c) in the above result we can get

$$\begin{aligned} &I_n(\mathrm{i}(z-\eta))K_n(\mathrm{i}(z-\eta)) + I_{n-1}(\mathrm{i}(z-\eta))K_{n+1}(\mathrm{i}(z-\eta)) = \\ &= \frac{1}{z-\eta}\left[-\mathrm{i} - \frac{1}{2z}\left(C_n(z) - \mathrm{i}S_n(z)\right)^2 - \frac{n}{z} - \frac{\mathrm{i}\delta}{z}\left(C_n(z) - \mathrm{i}S_n(z)\right)^2\right]. \end{aligned}$$

Thus we can get an expression for d_n as

$$d_n \approx \frac{\mathrm{i}r_s}{2z}\left(C_n(z) - \mathrm{i}S_n(z)\right)^2 - \frac{\varepsilon}{2} + O(\varepsilon/z). \tag{5.1.6h}$$

Now we will consider e_n, and following the same procedure as before we will obtain the following terms

$$\begin{aligned} I_n^2(\mathrm{i}z) &= e^{n\pi\mathrm{i}}J_n^2(z) \\ &= \frac{2}{\pi z}\left(C_n^2(z) - \frac{S_n(z)C_n(z)}{4z}(\mu-1)\right), \\ I_{n-1}(\mathrm{i}z)I_{n+1}(\mathrm{i}z) &= e^{n\pi\mathrm{i}}J_{n-1}(z)J_{n+1}(z) \\ &= \frac{2}{\pi z}\left(-S_n^2(z) - \frac{S_n(z)C_n(z)}{4z}(\mu+3)\right). \end{aligned}$$

Subtracting the above expressions we get

$$I_n^2(\mathrm{i}z) - I_{n-1}(\mathrm{i}z)I_{n+1}(\mathrm{i}z) = e^{n\pi\mathrm{i}}\frac{2}{\pi z}\left[1 + \frac{S_n(z)C_n(z)}{z}\right].$$

Similarly using (5.1.6c) in the above result we can get

$$I_n^2(\mathrm{i}(z-\eta)) - I_{n-1}(\mathrm{i}(z-\eta))I_{n+1}(\mathrm{i}(z-\eta)) = e^{n\pi\mathrm{i}}\frac{2}{\pi(z-\eta)}\left[1 - \frac{S_n(z)C_n(z)}{z} + \frac{\delta}{z}\left(C_n^2(z) - S_n^2(z)\right)\right].$$

Thus we can get an expression for e_n as

$$e_n \approx \frac{-\mathrm{i}r_s e^{n\pi\mathrm{i}}}{\pi}\left(\frac{2S_n(z)C_n(z)}{z}\right) - \frac{\mathrm{i}\varepsilon}{\pi}e^{n\pi\mathrm{i}} + O(\varepsilon/z). \tag{5.1.6i}$$

Now we need to consider f_n and following the same procedure as before we will obtain the following terms

$$\begin{aligned}
K_n^2(\mathrm{i}z) &= -\frac{\pi^2}{4}e^{-n\pi\mathrm{i}}\left(J_(z) - \mathrm{i}Y_n(z)\right)^2 \\
&= -\frac{\pi}{2z}e^{-n\pi\mathrm{i}}\left(C_n(z) - \mathrm{i}S_n(z)\right)^2\left(1 - \frac{\mathrm{i}}{4z}(\mu-1)\right), \\
K_{n-1}(\mathrm{i}z)K_{n+1}(\mathrm{i}z) &= -\frac{\pi^2}{4}e^{-n\pi\mathrm{i}}\left(J_{n-1}(z) - \mathrm{i}Y_{n-1}(z)\right)\left(J_{n+1}(z) - \mathrm{i}Y_{n+1}(z)\right) \\
&= -\frac{\pi}{2z}e^{-n\pi\mathrm{i}}\left(C_n(z) - \mathrm{i}S_n(z)\right)^2\left[1 - \frac{\mathrm{i}}{4z}(\mu+3)\right].
\end{aligned}$$

Subtracting the above expressions we get

$$K_n^2(\mathrm{i}z) - K_{n-1}(\mathrm{i}z)K_{n+1}(\mathrm{i}z) = \frac{-\mathrm{i}\pi}{2z}e^{-n\pi\mathrm{i}}\left(C_n(z) - \mathrm{i}S_n(z)\right)^2\frac{1}{z}.$$

Similarly using (5.1.6c) in the above result we can get

$$K_n^2(\mathrm{i}(z-\eta)) - K_{n-1}(\mathrm{i}(z-\eta))K_{n+1}(\mathrm{i}(z-\eta)) = \frac{\mathrm{i}\pi}{2(z-\eta)}e^{-n\pi\mathrm{i}}\left(C_n(z) - \mathrm{i}S_n(z)\right)^2\left(1 + \frac{2\mathrm{i}\delta}{z}\right)\frac{1}{z}.$$

Thus we can get an expression for f_n as

$$f_n \approx -\frac{\pi}{2} r_s e^{-n\pi \mathrm{i}} \left(C_n(z) - \mathrm{i}S_n(z)\right)^2 \frac{1}{z} + O(\varepsilon/z). \tag{5.1.6j}$$

So now we can combine all these results and obtain to leading order

$$\begin{aligned} b_n d_n + c_n e_n &\approx (-1)^m e^{n\pi \mathrm{i}/2} \sqrt{\frac{z-\eta}{2\pi}} \frac{r_s}{2z\delta} \left(C_n(z) + S_n(z)\frac{\varepsilon z}{r_s}\right)\left(1 + \frac{1}{2z\delta}\right), \\ b_n f_n + c_n d_n &\approx (-1)^m e^{-n\pi \mathrm{i}/2} \sqrt{\frac{\pi(z-\eta)}{2}} \frac{1}{\delta}\left(1 + \frac{1}{2z\delta}\right)\left(C_n(z) - \mathrm{i}S_n(z)\right)\left[\frac{-\mathrm{i}r_s}{2z} + \frac{\varepsilon}{2}\right]. \end{aligned}$$

We now look at the expression for a_1 in (5.1.5b). We can expect $K_n(\mathrm{i}(z-\eta))$ and $K_n'(\mathrm{i}(z-\eta))$ to be of the same order. From (5.1.4c) and (5.1.4e) we can see that

$$\alpha^{2/3} a^2/n^2 \sim \tan(\eta) \sim O(1/\delta).$$

Thus $K_n'(\mathrm{i}(z-\eta))\delta^{-1} >> K_n(\mathrm{i}(z-\eta))$ and we can ignore the latter term when trying to obtain a leading order expansion for a_1. Using (5.1.3) and (5.1.6c) we can obtain the following expansions

$$\begin{aligned} K_n'(\mathrm{i}(z-\eta)) &= (-1)^m \frac{e^{-n\pi \mathrm{i}/2}}{4} \sqrt{\frac{2\pi}{z-\eta}} \left(C_n(z) - \mathrm{i}S_n(z)\right)\left[2 + 2\mathrm{i}\delta - \mathrm{i}\frac{\mu+3}{4z} + O(\delta/z)\right], \\ I_n'(\mathrm{i}(z-\eta)) &= (-1)^m \frac{-\mathrm{i}e^{-n\pi \mathrm{i}/2}}{2} \sqrt{\frac{2}{\pi(z-\eta)}} \times \\ &\qquad \left[-2C_n(z) - 2S_n(z)\delta + \frac{S_n(z)}{4z}(\mu+3) + O(\delta/z)\right]. \end{aligned} \tag{5.1.6k}$$

Thus, we can obtain after simplification

$$-(b_n d_n + c_n e_n) K_n'(\mathrm{i}(z-\eta)) \frac{\alpha^{2/3} a^2}{\mathrm{i}n^2} =$$

$$= \frac{-r_s a^2}{2z\delta n^2}\left(1+\frac{1}{2z\delta}\right)((2m-1)\pi/2)\,\varepsilon^{-2/3}\left(-\mathrm{i}C_n(z)-\mathrm{i}S_n(z)\frac{\varepsilon z}{r_s}\right)(C_n(z)-\mathrm{i}S_n(z)), \tag{5.1.6l}$$

where we have used $\alpha \sim ((2m-1)\pi/2)\,\varepsilon^{-1}$. Similarly,

$$-(b_n f_n + c_n d_n) I_n'(\mathrm{i}(z-\eta))\frac{\alpha^{2/3}a^2}{\mathrm{i}n^2} = \\ = \frac{-r_s a^2}{2z\delta n^2}\left(1+\frac{1}{2z\delta}\right)((2m-1)\pi/2)\,\varepsilon^{-2/3}(C_n(z)-\mathrm{i}S_n(z))(-2C_n(z)\left(\frac{-\mathrm{i}r_s}{2z}+\frac{\varepsilon}{2}\right). \tag{5.1.6m}$$

Substituting the above two expressions in (5.1.5b) and retaining only the largest terms will give us

$$a_1 \approx -L4\frac{\mathrm{i}^{1/3}r_s^2}{n^2}\left((2m-1)\pi/2\right)^{5/3}\varepsilon^{-2/3}\left(1+\frac{1}{2z\delta}\right).$$

Since $z=\alpha r_s$ and using (5.1.4f) for δ, we get

$$\frac{1}{2z\delta} = \frac{-\varepsilon^{1/3}r_s}{2n^2\left((2m-1)\pi/2\right)^{1/3}},$$

which allows us to express a_1 as

$$a_1 \approx -L_4\frac{\mathrm{i}^{1/3}r_s^2}{n^2}\left((2m-1)\pi/2\right)^{5/3}\varepsilon^{-2/3}\left(1-\frac{-\varepsilon^{1/3}r_s}{2n^2\left((2m-1)\pi/2\right)^{1/3}}\right). \tag{5.1.7}$$

Finally (5.1.5f)/(5.1.7) gives us

$$\mathrm{Re}(a_4/a_1) \approx \frac{\mathrm{i}L_5}{L_4L_7}\frac{n^2}{r_s^2}\left(\varepsilon^{-1}+\frac{\varepsilon^{-2/3}r_s}{n^2\left((2m-1)\pi/2\right)^{2/3}}-\frac{5n^2\varepsilon^{-1/3}}{r_s^2\left((2m-1)\pi/2\right)^{1/3}} \right. \\ \left. -\frac{5n^2}{r_s\left((2m-1)\pi/2\right)}+\ldots\right). \tag{5.1.8}$$

We note here that this equation is similar to that presented in Stephen (2006) for the limit $\varepsilon \to 0$. The solution given by (5.1.8) is compared with the numerical evaluation of

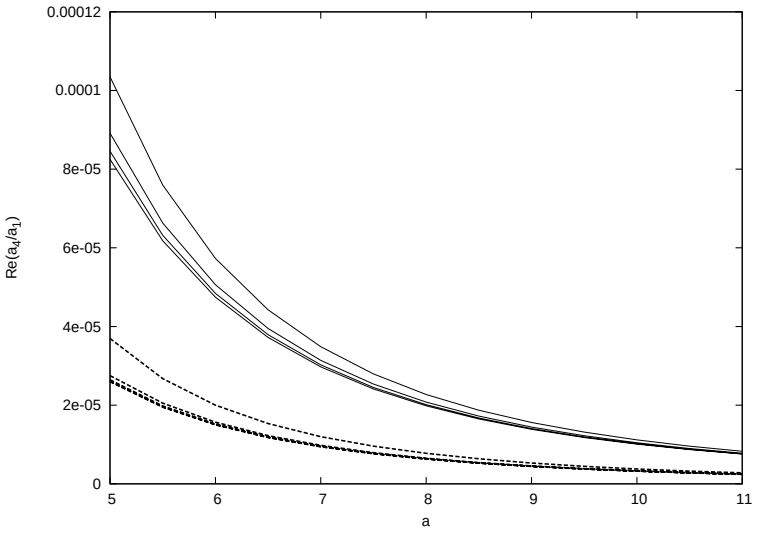

Figure 5.4: $\mathrm{Re}(a_4/a_1)$ for $n = 1$. Shown are —, the numerical evaluation of $\mathrm{Re}((5.1.5a)/(5.1.5b))$; $- - -$, the asymptotic approximation (5.1.8).

$\mathrm{Re}(a_4/a_1)$ using (5.1.5a) and (5.1.5b) in figure 5.4 for $n = 1$ and in figure 5.5 for $n = 2$. We see from these figures that the agreement between the asymptotic approximation and the numerical results is poor. The main limitation of the asymptotic series describing a_1 is that the expansions for the Bessel function terms d_n, e_n and f_n were truncated at $O(\varepsilon/z)$. For a fixed ratio $a/r_s = s$ say, $O(\varepsilon/z) \sim O(\alpha^{-1}(1-s))$, which is strictly not small. We can expect better agreement by retaining terms at this order and determining the next terms in the asymptotic series expansion (5.1.7), for a_1. This would however make the necessary algebraic simplification very cumbersome. The asymptotic approximation (5.1.8) however gives an analytic confirmation that $\mathrm{Re}(a_4/a_1) \to 0^+$ for $a >> 1$, and that the first mode ($m = 1$) will be the dominant mode in this limit.

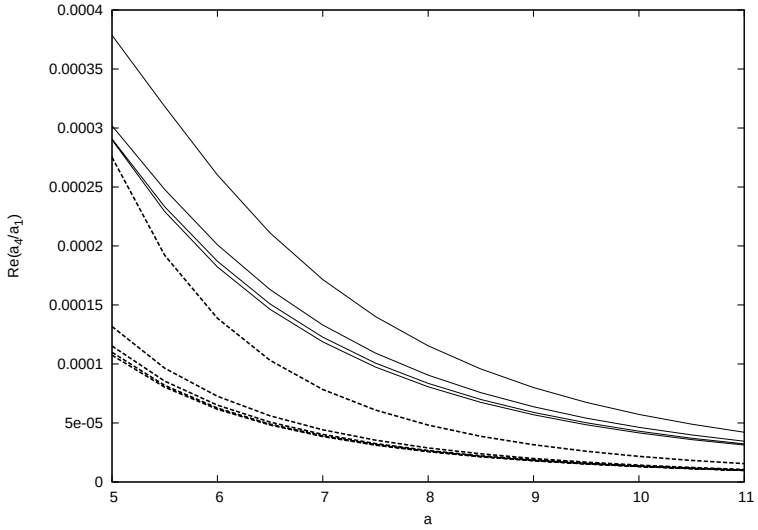

Figure 5.5: $\mathrm{Re}(a_4/a_1)$ for $n = 2$. Shown are —, the numerical evaluation of Re((5.1.5a)/(5.1.5b)); − − −, the asymptotic approximation (5.1.8).

5.1.2 Limit: $a << 1$

We can now consider the limit of small a. From the numerical results (see figure 4.2 for example), we can see two distinct behaviours for α as $a \to 0$. For the first mode ($m = 1$), we see that $\alpha \to 0$ as $a \to 0$. Thus in this limit we can take $\alpha r_s << 1$ and $\alpha a << 1$, and use the small argument expansions for the Bessel functions (Abramovitz & Stegun 1972)

in the linear eigenrelation (5.1.1). Thus we have

$$
\begin{aligned}
&J_n(\alpha a)Y_n(\alpha r_s) - J_n(\alpha r_s)Y_n(\alpha a) \approx \\
&\frac{1}{n!}\left(\frac{1}{2}\alpha a\right)^n\left[-\frac{(n-1)!}{\pi}\left(\frac{1}{2}\alpha r_s\right)^{-n}\right] + \left(\frac{1}{2}\alpha r_s\right)^n\frac{1}{n!}\left[\frac{(n-1)!}{\pi}\left(\frac{1}{2}\alpha a\right)^{-n}\right] \\
&= \frac{1}{n\pi}\left[\left(\frac{r_s}{a}\right)^n - \left(\frac{a}{r_s}\right)^n\right], \\
&\frac{1}{2}\left[J_n(\alpha r_s)Y_n'(\alpha a) - J_n'(\alpha a)Y_n(\alpha r s)\right] \approx \\
&\frac{1}{n\pi}\left(\frac{1}{2}\alpha r_s\right)^n\left[\frac{-(n-2)!}{\pi}\left(\frac{1}{2}\alpha a\right)^{-n+1} + \frac{n!}{\pi}\left(\frac{1}{2}\alpha a\right)^{-n-1}\right] \\
&= \frac{(n-1)!}{\pi}\left(\frac{1}{2}\alpha r_s\right)^{-n}\left[\frac{1}{(n-1)!}\left(\frac{1}{2}\alpha a\right)^{n-1} - \frac{1}{(n+1)!}\left(\frac{1}{2}\alpha a\right)^{n+1}\right] \\
&\approx \frac{2}{\pi\alpha a}\left[\left(\frac{r_s}{a}\right)^n + \left(\frac{a}{r_s}\right)^n\right].
\end{aligned}
\tag{5.1.9a}
$$

Substituting the above expansions in (5.1.1) we get

$$
1.001\mathrm{i}^{1/3} = \mathrm{i}^{1/3}\frac{n\alpha^{1/3}}{a}\left[\frac{\left(\frac{r_s}{a}\right)^n - \left(\frac{a}{r_s}\right)^n}{\left(\frac{r_s}{a}\right)^n + \left(\frac{a}{r_s}\right)^n}\right]^3,
$$

which allows us to obtain the leading order approximation for α as

$$
\alpha \approx \left(1.001\frac{a}{n}\right)^3\left[\frac{\left(\frac{r_s}{a}\right)^n - \left(\frac{a}{r_s}\right)^n}{\left(\frac{r_s}{a}\right)^n + \left(\frac{a}{r_s}\right)^n}\right]^3. \tag{5.1.9b}
$$

The prediction given by (5.1.9b) is shown in figure 5.6a for $n = 1$ and in figure 5.6b for $n = 2$. We can see very good agreement between the asymptotic approximation and the numerical solution of (5.1.1).

We now return to neutral results in figure 4.2 once again and see for the higher modes ($m > 1$), that $\alpha >> 1$ as $a \to 0$. This means that the arguments of the Bessel

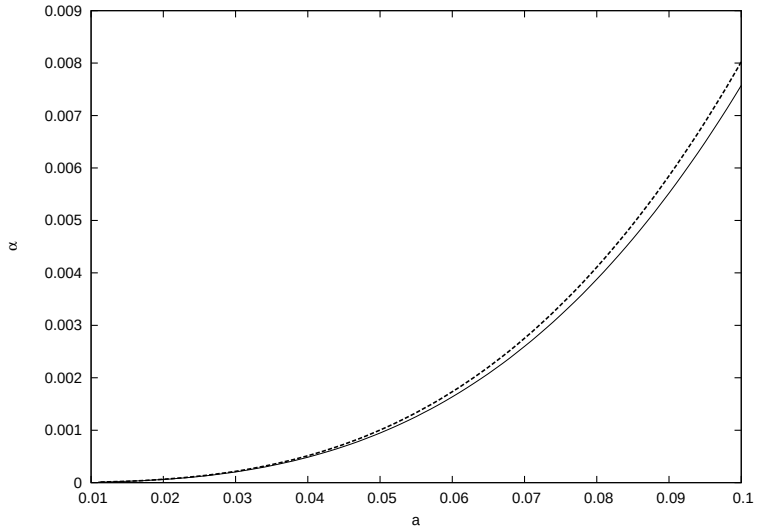

(a)

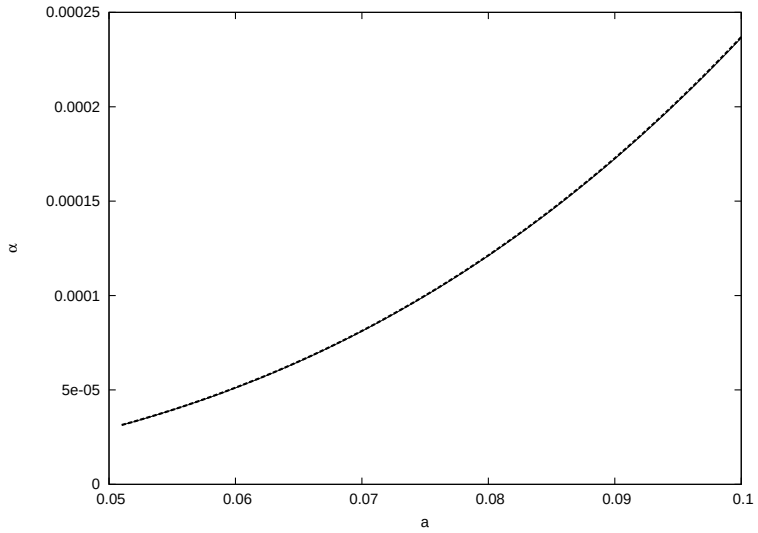

(b)

Figure 5.6: The first neutral values of α for (a) $n = 1$; (b) $n = 2$: —, numerical solution of (5.1.1); $- - -$, the asymptotic approximation (5.1.9b).

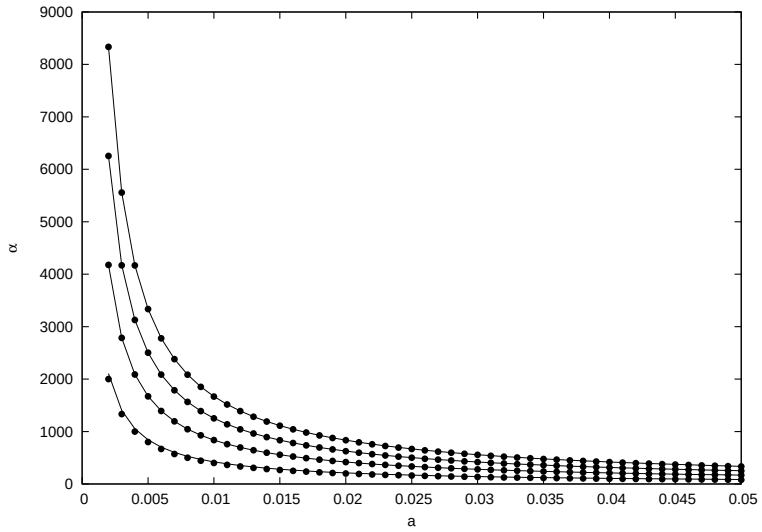

Figure 5.7: Neutral values of α for $n = 1$. Shown are the second to fifth modes with —, numerical solution of (5.1.1) and •, the leading order approximation (5.1.9f).

functions αr_s, αa tend towards some finite $O(1)$ quantity as $a \to 0$. Thus we are unable to approximate the Bessel functions in a similar fashion to what has been done thus far. We will instead try to approximate the behaviour of α using Taylor expansions. We let $z = \alpha r_s$, and thus $\alpha a = sz$, where $a/r_s = s$. Then we let $\alpha = \overline{\alpha}/r_s$, where $\overline{\alpha} = O(1)$. Then $\Omega = \overline{\Omega} r_s^{-2/3}$, where $\overline{\Omega} = O(1)$. Therefore $\overline{\xi_0} = -\mathrm{i}^{1/3}\overline{\Omega}\overline{\alpha}^{-2/3} = -2.297\mathrm{i}^{1/3}$. Thus the linear eigenrelation (5.1.1) can be approximated as

$$1.001 = \frac{n^2}{s^2}\overline{\alpha}^{-2/3} r_s^{-4/3} G(\overline{\alpha}), \tag{5.1.9c}$$

where $G(\overline{\alpha})$, is the ratio of the Bessel function terms. In (5.1.9c) we can see that $r_s^{-4/3} >> 1$, and thus in order for the LHS to balance the RHS we require $G(\overline{\alpha}) << 1$. So we let

$$\overline{\alpha} = \overline{\alpha_0} + r_s^{4/3}\overline{\alpha_1}, \tag{5.1.9d}$$

such that $\overline{\alpha_0}$ are the $m+1$ roots of $G(\overline{\alpha})=0$, for $m=1,2,\ldots$. This means that we require

$$J_n(s\overline{\alpha_0})Y_n(\overline{\alpha_0})-J_n(\overline{\alpha_0})Y_n(s\overline{\alpha_0})=0. \tag{5.1.9e}$$

We now let

$$F(\overline{\alpha})=\overline{\alpha}^{-2/3}r_s^{-4/3}G(\overline{\alpha})-1.001\frac{n^2}{s^2}=0.$$

Substituting in (5.1.9d) we can use Taylor expansion to write

$$F\left(\overline{\alpha_0}+r_s^{4/3}\overline{\alpha_1}\right)=F(\overline{\alpha_0})+r_s^{4/3}\overline{\alpha_1}F'(\overline{\alpha_0})+\ldots,$$

where

$$F(\overline{\alpha_0})=-1.001\frac{n^2}{s^2},$$
$$F'(\overline{\alpha_0})=\overline{\alpha_0}^{-2/3}r_s^{-4/3}G'\overline{\alpha_0}).$$

Thus we can express

$$\overline{\alpha}=\overline{\alpha_0}+r_s^{4/3}\left(1.001\frac{n^2}{s^2}\right)\frac{\overline{\alpha_0}^{2/3}}{G'(\overline{\alpha_0})}. \tag{5.1.9f}$$

Because we are unable to obtain an explicit analytic approximation for α we will be unable to proceed to utilise this expansion in the nonlinear coefficients. The value of this expansion lies in showing that in the limit of small a, to leading order the $m+1$ neutral modes of α behaves as the $m+1$ roots of (5.1.9e) . Once these roots have been numerically obtained, they can be used as initial guesses for the numerical solution of the full eigenrelation. In figure 5.7 we can see that this leading order approximation for α has

excellent agreement with the numerical solution of (5.1.1).

5.2 Discussion of linear stability results

5.2.1 Summary of neutral stability results

In Section 4.1.1 we presented the results of the neutral stability problem. The porous coatings were shown to have a significant effect only on the neutral values of frequency Ω. All three porous wall models produced a destabilising effect on the neutral curves. The felt-metal microstructure produced the most significant destabilisation. The mesh microstructure model despite having higher porosity produced comparable destabilisation to the regular circular pore microstructure model of lower porosity. The destabilising effect of porous coatings was more significant for non-axisymmetric neutral disturbances when compared to neutral axisymmetric disturbances. The difference between the neutral curves of the solid and porous walls was shown to decrease with increasing azimuthal wavenumber n.

5.2.2 Summary of spatial stability results

In Section 4.1.2 we presented results of the spatial stability problem. It was shown that the porous coatings will lead to larger amplification of unstable disturbances for both axisymmetric and non-axisymmetric disturbances. The largest unstable growth rates for axisymmetric disturbances occur for the first or second mode at small frequencies, while for non-axisymmetric modes it is always the highest mode that has the largest unstable growth rates (at higher frequencies). This is in contrast to the solid wall case, where it is always the lower modes that have the largest growth rates. It was seen that for increasing cone radii a, there is a marked decrease in the maximum unstable growth rates. This effect is more pronounced for the porous wall case. When comparing the effect of various porous wall models, it was seen that the felt-metal model produces significantly

larger unstable growth rates when compared to the regular porous model. The mesh microstructure model produced slightly larger unstable growth rates when compared to the regular porous model.

5.2.3 Discussion of parametric studies and comparison with second Mack mode studies

In Section 4.2 we examined the effect of some porous model parameters on the stability of the viscous modes. In Section 4.2.1 we showed that a moderate cooling of the porous cone surface leads to destabilisation of the neutral curves and significantly larger maximum unstable growth rates. Since the wall temperature T_w affects only the porous layer admittance quantity and is otherwise scaled out of the problem we are unable to consider the effect of wall cooling on the the solid wall case in this study. It must be noted that in this analysis we refer to moderate wall cooling in the sense that the wall temperature T_w is still large, and any decrease in its value does not alter the mean flow profiles of streamwise velocity and temperature. The studies of Fedorov *et al.* (2001) and Maslov (2003) investigate the effect of similar reductions in wall temperature on Mack's second mode instability. In these studies, the authors report a strong reduction of second mode growth rates on colder walls. Let us consider the porous wall model equations (2.3.1) and (2.3.4) in the asymptotic limit of deep pores ($\Lambda h >> 1$) and relatively small pore size ($|\zeta| << 1$). Using the small argument asymptotic forms of Bessel functions $J_0 \sim 1 - \frac{1}{4}\zeta^2$ and $J_1 \sim \frac{1}{2}\zeta$, we can then show that the wall admittance varies as $A_y \sim |\zeta| T_w^{1/2}$. Using the formula for ζ, we can then show that $A_y \sim O(T_w^{-11/16})$. Thus a decrease in T_w will lead to a corresponding increase in the porous wall admittance. This results in greater destabilisation of Mack's first-mode disturbances and greater stabilisation of Mack's second-mode disturbances, consistent with our observations and published results.

In Section 4.2.2 we examined the effect of Knudsen layers over the porous surface on the

instability of the first Mack mode disturbances and showed them to have a destabilising effect. From (2.3.4) we can deduce that finite Knudsen numbers increase the value of the porous layer admittance. Gas rarefaction effects are reported to be stabilising for Mack's second-mode disturbances as Knudsen layers allow deeper penetration of these disturbances into the pores (Maslov 2003, Fedorov *et al.* 2006).

In Section 4.2.3 we examined the effect of varying the pore radius, porosity and pore depth on the maximum unstable spatial growth rates. It was found that increasing pore radius or porosity had the effect of increasing the maximum growth rates. Theoretical investigation of the effect of increasing porosity and pore radius on Mack's second mode growth rates was reported in Fedorov *et al.* (2001). They show that increasing the pore radius and porosity leads to substantial reduction of the second-mode growth rates. Parametric studies of regular porous coatings and mesh coatings have been carried out with the focus on the stabilisation of Mack's second-mode instability (Fedorov *et al.* 2001, 2008, Lukashevich *et al.* 2010). These studies reveal that the porous layer performance can be optimised by controlling the porous layer thickness. These parametric studies indicate that optimal porous coatings have thickness $h \approx 3 - 3.5r_p$. Our results indicate that porous layer thickness in this range for regular porous coatings also provide optimal first mode stabilisation.

Parametric studies also show that high porosity provides maximum second-mode stabilisation. However numerical studies of Bres *et al.* (2009) reveal that porous coatings with too closely spaced pores trigger a new shorter wavelength instability whose growth rate can be larger than that of Mack's second mode. The authors have attempted to optimize the design of porous coatings based on the acoustic scattering properties of the porous layer. They propose a porous coating with fixed low porosity comprising of spanwise grooves. Each porous cavity has a depth H, half-width b and spacing s, all of which vary along the longitudinal length of the cone. Following Kozlov *et al.* (2005) the regular

porous model of (2.3.4) can be used to study this model by making the following changes:

$$\zeta = b\sqrt{\frac{\mathrm{i}\omega\rho_w}{\mu_w}R}, \quad F(B,\zeta) = \frac{\tan\zeta}{\zeta[1 - B\zeta\tan\zeta]}. \tag{5.2.1}$$

The effect of this new design on the first mode instability is examined. In figure 5.8

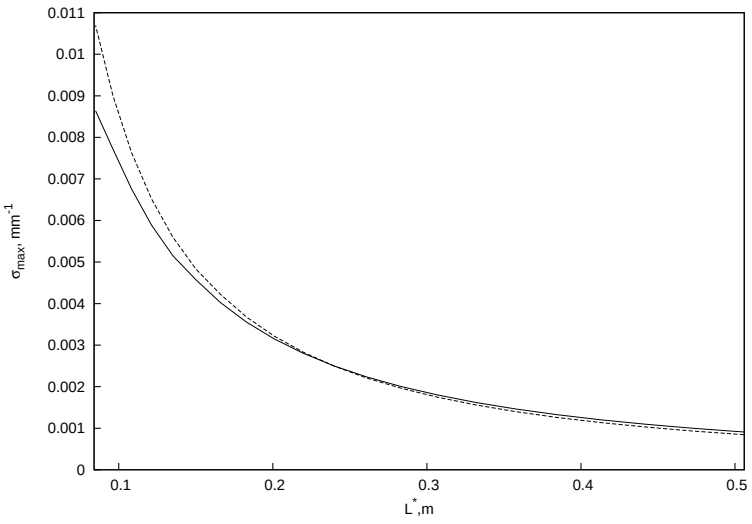

Figure 5.8: Variation of spatial growth rate parameter $\sigma_{\max} = \max(|-\alpha_i(\Omega)|)$ with longitudinal distance L^*: —, spanwise grooves with variable thickness (5.2.3); − − −, regular microstructure model (2.3.4) with infinite thickness. Results are shown for non-neutral non-axisymmetric mode $n = 1$.

maximum unstable growth rates of the first azimuthal mode $n = 1$ are compared using this porous model and the regular porous model both with porosity $\phi_0 = 0.2$. The regular porous model is assumed to be infinitely thick and the pore radius is fixed at 25μm. From figure 5.8 we see that at smaller streamwise distance the new design leads to lower amplification of unstable disturbances and with increasing streamwise distance the difference between the growth rates of the two models becomes very small. This novel design corresponds to porous coatings with low porosity and large cavity aspect

ratio ($2b/H$) i.e., thinner coatings with less pores. These type of coatings are easier to manufacture and incorporate into thermal protection systems in hypersonic vehicles (Bres *et al.* 2009).

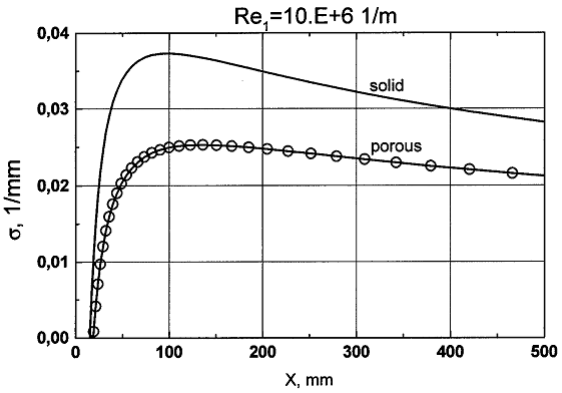

Figure 5.9: Spatial growth rate of the most unstable disturbance (second mode) on solid and porous surfaces (taken from Maslov 2003).

Numerical and experimental investigations of ultrasonic absorptive coatings have been reviewed in Section 1.2.1. The numerical studies investigated the effect of the porous coating on inviscid (Mack's second-mode) disturbances. These studies were concerned with the non-parallel linear stability problem for the planar case (no curvature effects). Nevertheless the results of the linear stability analysis conducted here can been compared with these results. Using figure 4.12 we can make a comparison of the dimensional growth rates for the first mode disturbances enhanced by the porous surface with those reported in Maslov (2003) for the second mode (figure 5.9). We see that the size of the maximum Mack's first-mode growth rates (figure 4.12) are smaller than those reported for the second-mode. In figure 5.10 we show the frequencies at which these maximum growth rates occur for Mack's first-mode. In figure 5.10 we can see that the frequency of the most unstable disturbances decrease in the downstream direction. We know that maximum unstable growth rates can be expected at small values of the streamwise distance. The experimental observed range for first-mode frequencies (Kendall 1967, Stetson *et al.* 1983,

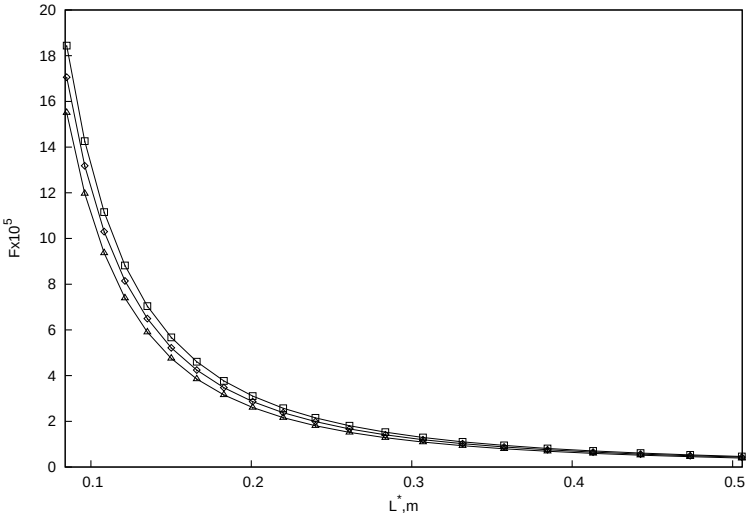

Figure 5.10: Variation of frequency parameter $F = \Omega^*/Re$ with longitudinal distance L^* using the regular microstructure model (2.3.4). Symbols refer to azimuthal wavenumbers: $\triangle$, $n = 1$; $\diamond$, $n = 2$; $\square$, $n = 3$.

Maslov 2003) is reported to be around $F = 4 - 5 \times 10^{-5}$. In figure 5.10 we see that the maximum growth rates occur at frequencies higher than this range. In the experimentally observed frequency range we can expect first-mode growth rates enhanced by the porous wall to be an order of magnitude smaller than those of the second-mode.

5.3 Discussion of nonlinear stability results

Results of the weakly nonlinear analysis have been presented in Section 4.3. The effect of the attached shock is found to be significant. In the absence of a shock, unstable solutions are possible only for a finite range of cone radius a and nonlinearity stabilises linearly unstable disturbances for all admissible values of a. The presence of the shock leads to multiple unstable modes for all values of a. The influence of curvature is also important. Curvature was found to enhance nonlinear effects.

The effect of nonlinearity is dependent on the mode number and cone radius a. For

axisymmetric disturbances on a solid wall, nonlinear effects tend to stabilise all higher modes while the lowest mode is slightly destabilised when a becomes large enough. In the presence of the porous wall all the modes are destabilised when compared to the solid wall. Our linear stability results show that the lowest mode is the most unstable and has largest spatial growth rates for both solid and porous walls. This most dangerous mode is also the most destabilized by nonlinearity in the presence of the porous wall.

For non-axisymmetric disturbances on a solid wall, nonlinear effects destabilise the lowest mode, while the higher modes are stabilised until a certain value of a which increases with azimuthal wavenumber. All porous wall models destabilise the neutral modes. When considering the effect of nonlinearity on linearly unstable modes, we can state that lower modes are greatly destabilised by nonlinearity while it has a stabilising effect on the higher modes. We show that it is the higher modes that have the largest spatial growth rates in the presence of the porous wall. The effect of nonlinearity is to stabilize these most linearly amplified modes by pushing the point of subcritical instability to larger values of a.

The random microstructure felt metal model was compared with the regular porous model. The felt metal significantly destabilises the neutral modes and strongly amplifies the linearly unstable modes with the higher modes giving the largest growth rates. Nonlinear effects in the presence of the felt metal coating stabilise these more dangerous higher modes over a larger range of a while destabilising the more slowly growing lower modes. When comparing the difference between the mesh microstructure model and the regular porous model, we notice similar effects between both models on all the modes. The regular porous model slightly destabilises all modes when compared to the mesh model. Since the felt metal and mesh coating have higher porosity, to corroborate these findings, nonlinear stability results for the regular porous model with a higher porosity of $\phi_0 = \frac{\pi}{4}$ was obtained. We show that porous coatings with higher porosity allows nonlin-

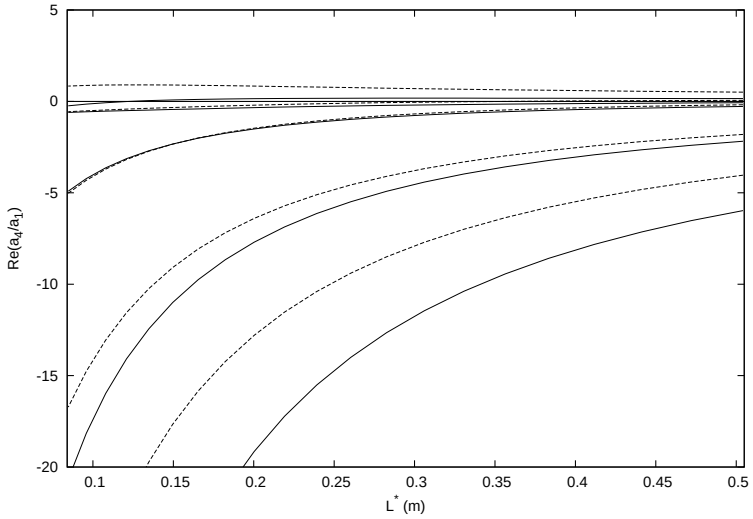

Figure 5.11: $\mathrm{Re}(a_4/a_1)$ for the first five modes as a function of local cone radius a for $n = 1$ and $a/r_s = 0.57$: —, spanwise grooves with variable thickness (5.2.3); $- - -$, regular microstructure model (2.3.4) with infinite thickness.

ear effects to stabilise higher mode number disturbances at a particular location with the mode number of the lowest mode that is stabilised increasing with increasing azimuthal wavenumber.

In Section 5.2.3 we discussed the limitations of porous coatings with very high porosities on the linear stability of the flow. A novel porous coating with low porosity and small thickness was considered and shown to produce smaller destabilisation of linearly unstable disturbances. The effect of nonlinearity in the presence of this coating is shown in figure 5.11. Here we can see $\mathrm{Re}(a_4/a_1)$ against streamwise distance L^* for the spanwise groove model with variable thickness and the regular porous model with infinite thickness. We see that in the presence of the novel porous coating model, nonlinearity has a stabilising effect on all the modes.

5.4 Relevance to the physics of laminar to turbulent transition

The weakly nonlinear stability of the first Mack mode (viscous) disturbances in the hypersonic boundary layer on a sharp slender cone with passive porous walls has been investigated. The analysis shows that small-amplitude linearly unstable disturbances can either evolve from the linear neutral point towards an equilibrium amplitude or there is a threshold amplitude.. The stability of this disturbance is dependent on the mode number and the local cone radius a where the viscous-inviscid interaction takes place. There are two situations depending on whether $\mathrm{Re}(a_4/a_1)$ is negative or positive for a particular value of a. If $\mathrm{Re}(a_4/a_1) < 0$ we have supercritical instability and an equilibrium amplitude so linearly unstable disturbances grow but saturate. If $\mathrm{Re}(a_4/a_1) > 0$ then we have subcritical instability and an initial threshold amplitude. Disturbances smaller than this amplitude grow but ultimately decay. For disturbances larger than this amplitude there will be unbounded growth. Thus, in the latter case nonlinear effects could lead a finite-amplitude mode towards breakdown and transition to turbulence. Thus, the size of the incoming disturbances is important in leading to transition to turbulence. The analysis here reveals the particular values of a for which the equilibrium state is subcritically unstable. Here nonlinearity enhances the amplification of a small-amplitude disturbance proportional to E that interacts with its harmonic, E^2 and mean flow disturbance, E^0. The effect of the attached shock is found to be significant. The presence of the shock leads to multiple unstable modes for all values of a. In the absence of shock, unstable solutions are possible only for a finite range of cone radius a and nonlinearity stabilises linearly unstable disturbances for all admissible values of a.

There have been some studies that investigate the nonlinear behaviour of viscous first-mode disturbances. Bicoherence diagrams from the experimental investigation of Bountin

et al. (2010) show that in the low-frequency range ($f_1, f_2 < 100$ kHz) nonlinear processes proceed more intensely on the porous surface compared to the solid. The authors suggest that this may be caused by the growth of the low-frequency disturbance amplitudes due to surface roughness. Bicoherence measurements of Chokani *et al.* (2005) have also identified a nonlinear interaction that is associated with the destabilised Mack's first mode. Simulations by De Tullio & Sandham (2010) of transition over a flat plate in the presence of oblique Mack's first mode show that the first mode grows faster than Mack's second mode and drives the flow directly to a turbulent state by nonlinear interactions. De Tullio & Sandham (2010) state that the first mode regains importance in the transition process at high Mach numbers for porous surfaces. Our results show that for sufficiently large a, nonlinear effects destabilise all linearly unstable viscous modes on a solid cone surface. At small values of a, corresponding to typical lengths of models tested in wind tunnels, it is the unstable mode with the lowest frequency that is destabilised by nonlinearity. Spatial instability results demonstrate that these are the fastest growing disturbances but maximum growth rates are significantly smaller than the second Mack mode. This may explain why in experiments, transition has been observed due to the second Mack mode on solid cones. In the presence of porous walls, lower-frequency first Mack modes are also destabilised by nonlinearity while higher-frequency first Mack modes that are destabilised on the solid wall at a particular location now become stabilised for a range of a. This effect is enhanced by models with higher porosity. Thus over porous surfaces we can expect interaction of first Mack modes in the low-frequency spectrum to lead to nonlinear amplification of disturbance amplitudes beyond the critical value.

Chapter 6

Conclusions

6.1 Limitations and further work

A comprehensive set of experiments exploring the effects of the porous coating have been published in Maslov (2003) and Rasheed (2001). Rasheed's results indicate that the porous coating is effective in damping the dominant inviscid modes and delaying transition compared to the solid case. Stability experiments of Maslov (2003) conclude that weak amplification of first-mode disturbances, and strong damping of second-mode disturbances occur in the presence of porous coatings. A direct comparison of our linear stability results with their experimental results was not done. They present their results in the form of disturbance amplitude spectra. In theory, the growth rate parameter (α_i) can be calculated by differentiating a polynomial curve-fit of the disturbance amplitude data. However as tabulated data was not available, this procedure was not done in this study.

As discussed by Seddougui & Bassom (1997) with reference to the study by Stuckert & Reed (1994), the inclusion of non-parallelism is an important factor when performing theoretical investigations that can be compared with experiments. Smith (1979b) showed that non-parallel effects emerge at higher orders of the asymptotic solution. His analysis

considered the flow stability of Blasius boundary layers and the analysis involved was laborious. The inclusion of non-parallel effects is yet to be done for the hypersonic viscous stability problems. The stability analysis performed here is based on the assumption of a weak hypersonic interaction ($\chi << 1$) as discussed in Section 2.4. As the Mach number increases, viscous interaction with the inviscid flowfield will become important. Chang *et al.* (1990) state that accounting for the viscous/inviscid interaction of the mean flow in their numerical studies on the linear stability of hypersonic boundary layers led to better agreement with the sharp cone experiment of Stetson *et al.* (1983) performed at Mach 8.

The stability analysis considered here (based on Stephen 2006) and that of Seddougui & Bassom (1994) does not consider any nonlinearities that can occur in the vicinity of the shock position r_s. Referring to the bounds on the shock inclination angle, (2.4.14), Seddougui & Bassom (1994) state that once σ reaches a value of $O(Re^{-1/37})$, the shock-layer problem becomes nonlinear. In such a situation, the velocity normal to the shock from the inviscid (outer flow) solution becomes comparable with the vertical velocity perturbation in the upper deck. Now, viscous effects in entropy and shear waves which are produced when the acoustic wave meets the shock and then convected with the flow cannot be ignored.

The porous wall models (derived from the analytical solution of Kozlov *et al.* 2005) and boundary condition (Malmuth *et al.* 1998) employed in this analysis is only an approximation as it ignores small scale effects that occur at the mouth and bottom of the porous cavity. These effects are mainly generated due to acoustic scattering occurring within each pore. Coupling between disturbances from neighbouring pore cavities is also not accounted for. Bres *et al.* (2009, 2010) and Sandham & Ludeke (2009) used DNS to resolve the flow within the pore cavities and study the acoustic properties of the porous layer. The results of the DNS investigations showed good agreement with those obtained using the theoretical model validating the robustness of the models used. A limiting

assumption of the theoretical model of the porous wall boundary condition is that the coating roughness is negligibly small (Fedorov *et al.* 2011). This ensures that the porous cavities do not trip the boundary layer i.e., there is no mean-flow distortion due to the presence of the porous coating. The theory used does not provide specific restrictions on the pore size.

Recently, parametric studies of porous wall models are underway with the focus on minimising the destabilising effect on the first Mack mode (Wang & Zhong 2010, 2011a,b). These authors have analysed the porous wall admittance and studied the effect of the admittance phase angle on Mack's first mode destabilisation. They investigated the variation of the phase angle of admittance with pore radius and thickness and show that there is a minimum phase angle indicating an optimal thickness or pore radius. Numerical simulations using the optimal pore radius indicate weaker destabilisation of the first mode (Wang & Zhong 2011b). Preliminary results are obtained by computing the variation of phase angle of the admittance A_y with pore radius r_p for a typical first Mack mode frequency of 100 kHz. These results are presented in figure 6.1. These results are not in quantitative agreement with Wang & Zhong (2011b). Moreover, we expect the smallest first-mode growth rates to occur in the limit of zero pore radius (solid wall). Further investigation in this area is required to resolve this issue and determine whether controlling the phase angle of admittance is a viable technique for designing optimum porous coatings.

In realistic flight situations, the surfaces of hypersonic flying vehicles will have temperatures much below adiabatic values. In these type of situations, reductions in surface temperature can be expected to alter the basic boundary layer flow at the surface leading to greatly increased surface heat transfer and shear stress. Studies that investigate the effect of such levels of surface cooling on the instability of viscous disturbances include those by Seddougui *et al.* (1991) for compressible flow over a flat plate, Gaponov & Terekhova (2010) for supersonic and hypersonic flow over porous surfaces, and the widely

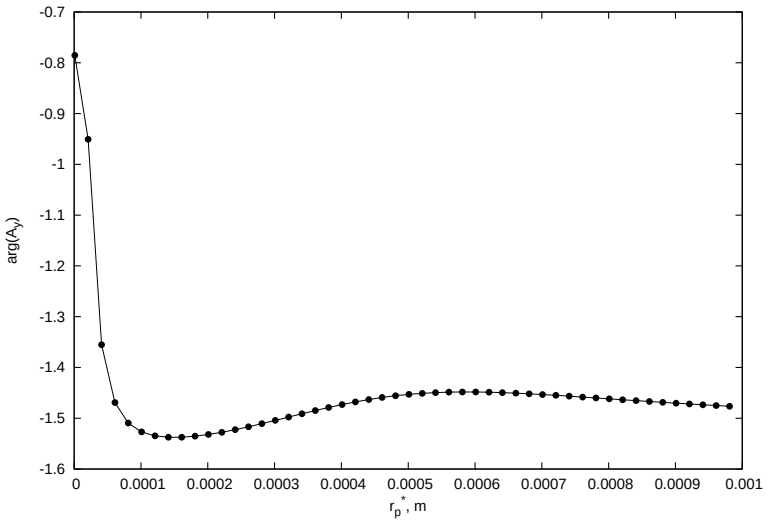

Figure 6.1: Variation of the phase angle of admittance A_y using the regular porous model (2.3.4) with pore radius r_p^*.

cited experimental investigations of Lysenko & Maslov (1984) for supersonic flow over a flat plate. Seddougui *et al.* (1991) show that even moderate levels of wall cooling, alters the triple-deck structure that exists in the uncooled case, provoking a new structure that includes an $O(Re^{-3/4})$ viscous lower tier and an $O(Re^{-2/3})$ buffer tier. The findings of Lysenko & Maslov (1984) conclude that wall cooling destabilises the first mode-disturbances, while Seddougui *et al.* (1991) report increase in the growth rate of first-mode disturbances. They however also report that wavenumbers and frequencies associated with the first-mode instability increase with surface cooling, at a given Reynolds number. The investigations of Gaponov & Terekhova (2011) accounting for both linear growth and nonlinear resonance interactions (three-wave systems) makes a distinction between the effect of wall cooling on supersonic ($M = 2$) and hypersonic ($M = 5$) flows. They expect wall cooling on porous surfaces to delay transition to turbulence for supersonic flow and accelerate transition for the hypersonic flow. A extension of the weakly nonlinear stability analysis conducted here into different wall cooling regimes that properly accounts for any

altered flow structure is important. Such an analysis will be invaluable in clarifying the effect of wall cooling on the viscous instability modes. The effects of porous walls can then be systematically included into such analysis as done in this study.

From the discussion in Section 5.3 with regards to the weakly nonlinear stability results it is evident that further research is required to establish whether Mack's first-mode instability can cause transition to turbulence in the presence of porous walls. The results of this study show that for a certain range of local cone radius a, nonlinearity can cause an unbounded amplification of linearly unstable small-amplitude disturbances. Once these disturbances reach finite amplitudes, they can drive secondary instabilities that lead to the breakdown of the flow. Various routes of transition have been observed numerically and experimentally in hypersonic boundary layers (discussed in the literature review). Among these, the two main routes through which the first Mack mode instability can lead to the breakdown of laminar flow are fundamental and subharmonic breakdown. The application of triple-deck asymptotic theory to describe the three-dimensional nonlinear development of Tollmien-Schlichting (TS) waves towards breakdown in planar boundary layers has been reviewed in Bowles (2000a,b). These studies are able to describe the features observed in experiments on the fundamental breakdown scenario in terms of a sequence of singularities in a hierarchy of governing equations. In this scenario 2-D TS waves develop into aligned rows of lambda (Λ)-shaped structures, called lambda vortices. This is then followed by a rapid breakdown to short-scaled structures called spikes. This process is characterised by the roll-up of vorticity in strong shear-layers associated with the lambda vortex into spanwise vortices, which subsequently develop into hairpin or omega (Ω)-vortices, and travel downstream as coherent stuctures in the flow (Bowles 2000a,b, Kachanov 1994). A weakly nonlinear analysis of the triple-deck equations is carried out using the method of multiple scales accounting for relatively slow spanwise variation (Smith & Walton 1989) and high frequencies (Stewart & Smith 1992, Smith &

Bowles 1992) in addition to the relatively slow streamwise variation. This type of analysis leads to coupled nonlinear partial differential equations that describe TS-wave/vortex interactions. These interactions terminate in a singularity finite distance downstream manifested as a blow-up of the vortex and wave amplitudes and spanwise focussing of the vortices (Stewart & Smith 1992). A fully nonlinear analysis of the triple-deck equations is then required. The singularity is resolved on a shorter streamwise lengthscale allowing normal pressure gradients to enter (Bowles 2000b, Smith 1988). Such analyses (Li *et al.* 1998, Smith *et al.* 2000) have been able to provide theoretical descriptions consistent with experiments. The subharmonic breakdown scenario is visualised as the appearance of alternating rows of staggered lambda vortices in the flow. This results from a resonant triad interaction between a pair of oblique subharmonic modes with a fundamental 2-D mode. The 2-D travelling waves scale on the 'upper-branch' of the TS neutral curve in contrast to the asymptotic analysis carried out in this study which scales on the 'lower-branch'. Nonlinear effects come into play in thin critical layers (where the phase speed of the disturbance is equal to the undisturbed fluid velocity). Resonant triad interactions and the role of nonlinear critical layers in subharmonic resonance in boundary layers have been studied by Mankbadi (1991), Mankbadi *et al.* (1993) and Goldstein (1995).

6.2 Conclusions

In this thesis an analysis of the weakly nonlinear stability of viscous (Mack's first mode) disturbances in the hypersonic boundary layer on a sharp slender cone with passive porous walls has been presented. A hierarchy of problems at increasing orders of the size of the relative amplitude of disturbances is considered. As a result of the analysis, an amplitude equation that describes the streamwise evolution of the disturbance amplitude has been derived. The linear stability of the disturbances is governed by the problem at first order. The linear stability problem was described by two eigenrelations depending on the nature

of the disturbances. The resulting transcendental equations were solved numerically for neutral solutions and spatially varying solutions. The results obtained demonstrated the destabilizing effect of porous coatings on the first-mode instability.

The coefficients of the nonlinear amplitude equation were numerically evaluated. The stability of the flow is governed by the signs of the real part of the coefficients. Numerical evaluation of the coefficients in this equation reveals that the stabilising or destabilising effect of nonlinearity on linearly unstable disturbances is dependent on the cone radius. The presence of porous walls significantly influences the effect of nonlinearity.

Appendix A
Abbreviations

Expressions involving integrals of Airy functions arise from terms containing the adjoint function and solutions for the flow perturbations. Such expressions also arise in other weakly nonlinear stability problems. Bassom (1989) first defined and evaluated these constants in his study of the nonlinear stability of free-surface flows. They were also used in the nonlinear stability problem of a cone with solid wall by Stephen (2006) and for that of a wedge by Seddougui & Bassom (1994). The definitions for all constants T_{ij} used here reduce to those defined in Bassom (1989) and Seddougui & Bassom (1994) by setting $A_y = 0$ where appropriate. The definitions of a_1 to a_4 and their axisymmetric counterparts can also be shown to reduce to those defined in Stephen (2006) by setting $A_y = 0$.

$$
\begin{aligned}
T_1 &= \mathrm{i}^{-1/3} \int_{\xi_o}^{\infty} \Big[K(\xi) + K'(\xi)(\xi - \xi_o)\Big] \Big(\int_{\xi_o}^{\xi} \mathrm{Ai}(s) ds \Big) d\xi, \\
T_3 &= -\mathrm{i}^{-1/3} \mathrm{Ai}(\xi_o) \mathrm{Ai}'(\xi_o), \\
T_6 &= -\mathrm{i}^{1/3} \int_{\xi_o}^{\infty} K'(\xi) \Big(\int_{\xi_o}^{\xi} \mathrm{Ai}(s) ds \Big) \left(\int_{\xi_o}^{\xi} \left(\int_{\infty}^{\xi_1} f^{**}(t) dt \right) d\xi_1 \right) d\xi, \\
T_7 &= \mathrm{i}^{1/3} \left[\frac{dH(\xi)}{d\xi} \right]_{\xi=\xi_0}, \\
T_8 &= -\mathrm{i}^{4/3} \int_{\xi_o}^{\infty} K'(\xi) \Big(\int_{\xi_o}^{\xi} H(t) dt \Big) \Big(\int_{\xi_o}^{\xi} \mathrm{Ai}(s) ds \Big)^c d\xi,
\end{aligned}
$$

$$T_{10} = \mathrm{i}^{2/3} \int_{\xi_o}^{\infty} K'(\xi) \left(\int_{\xi_o}^{\xi} \left(\int_{\xi_o}^{t} H(s) ds \right) dt \right) \Big(\mathrm{Ai}'(\xi) \Big)^c d\xi,$$

$$T_{11} = \mathrm{i}^{1/3} \int_{\xi_o}^{\infty} K'(\xi) \left(\int_{\xi_o}^{\xi} \left(\int_{\xi_o}^{t} \mathrm{Ai}(2^{1/3} s) ds \right) dt \right) \Big(\mathrm{Ai}(\xi) \Big)^c d\xi,$$

$$T_{12} = 2\mathrm{i}^{2/3} \int_{\xi_o}^{\infty} \overline{H}(t) dt,$$

$$T_{13} = 2^{2/3} \mathrm{i}^{1/3} \int_{\widehat{\xi_0}}^{\infty} \mathrm{Ai}(s) ds,$$

$$T_{14} = -2^{1/3} \frac{d}{d\widehat{\xi}} [\mathrm{Ai}(\widehat{\xi})]_{\widehat{\xi}=\widehat{\xi}_o},$$

$$T_{15} = \mathrm{i}^{1/3} \int_{\xi_o}^{\infty} K'(\xi) \left(\mathrm{Ai}'(\xi) - \mathrm{Ai}'(\xi_o) - \xi \Big(\int_{\xi_o}^{\xi} \mathrm{Ai}(s) ds \Big) \right) \left(\int_{\infty}^{\xi_1} f^{**}(t) dt \right) d\xi,$$

$$T_{16} = \int_{\xi_o}^{\infty} K'(\xi) \left(\mathrm{Ai}'(\xi) - \mathrm{Ai}'(\xi_o) - \xi \Big(\int_{\xi_o}^{\xi} \mathrm{Ai}(s) ds \Big) \right)^c H(\xi) d\xi,$$

$$T_{17} = \mathrm{i}^{-1/3} \int_{\xi_o}^{\infty} K'(\xi) \left(\mathrm{Ai}'(\xi) - \mathrm{Ai}'(\xi_o) - \xi \Big(\int_{\xi_o}^{\xi} \mathrm{Ai}(s) ds \Big) \right)^c \mathrm{Ai}(2^{1/3} \xi) d\xi,$$

$$T_{18} = \int_{\xi_o}^{\infty} K'(\xi) \Big(\int_{\xi_o}^{\xi} \mathrm{Ai}(s) ds \Big) d\xi,$$

$$T_{20} = T_6 + T_8 + 2T_{10} - T_{15} - T_{16},$$

$$T_{21} = T_9 + 2T_{11} - T_{17},$$

$$T_{22} = \mathrm{i} \int_{\xi_o}^{\infty} K'(\xi) \Big(\int_{\infty}^{\xi_1} f^{**}(t) dt \Big) \mathrm{Ai}'(\xi_0) d\xi,$$

$$T_{23} = \int_{\xi_o}^{\infty} K'(\xi) \overline{H}(\xi) \mathrm{Ai}'(\xi_0)^c d\xi,$$

$$T_{24} = \mathrm{i}^{-1/3} \int_{\xi_o}^{\infty} K'(\xi) \mathrm{Ai}(2^{1/3} \xi) \mathrm{Ai}'(\xi_0)^c d\xi,$$

$$T_{25} = \mathrm{i} \int_{\xi_o}^{\infty} K'(\xi) \mathrm{Ai}(\xi)^c d\xi,$$

$$L_2 = -\mathrm{i} T_1 \kappa^{-1} - 2\mathrm{i}^{2/3} \mathrm{Ai}(\xi_0) \mathrm{Ai}'(\xi_0) \kappa^{-1},$$

$$L_9 = \left\{ 2 \frac{\mathrm{i} n^2}{\alpha^{2/3} a^2} g_{2n} T_{13} - T_{14} + \left\{ \alpha^{1/3} g_{2n} T_{13} \right\} A_y \right\}^{-1},$$

$$L_{10} = \left\{ T_7 + 2 \frac{\mathrm{i} n^2}{\alpha^{2/3} a^2} g_{2n} T_{12} + \left[\alpha^{1/3} g_{2n} T_{12} + T_2 \frac{g_n}{2} \right] A_y \right\},$$

$$L_{11} = T_{20} - T_{21} L_9 L_{10},$$

$$L_{12} = \alpha^{-4/3} T_{14} L_9 L_{10} + \alpha^{-4/3} T_7 - A_y \mathbb{P}_1 T_{13},$$

$$
\begin{aligned}
L_{13} &= T_{23} - T_{24}L_9L_{10},\\
L_9^0 &= \left\{2\mathrm{i}\alpha^{4/3}g_{2n}^0T_{13} - T_{14} + \left\{\alpha^{1/3}g_{2n}^0T_{13}\right\}A_y\right\}^{-1},\\
L_{10}^0 &= \left\{T_7 + 2\mathrm{i}\alpha^{4/3}g_{2n}^0T_{12} + \left[\alpha^{1/3}g_{2n}^0T_{12} + T_2\frac{g_n^0}{2}\right]A_y\right\},\\
L_{11}^0 &= T_{20} - T_{21}L_9^0L_{10}^0,\\
L_{12}^0 &= \alpha^{-4/3}T_{14}L_9^0L_{10}^0 + \alpha^{-4/3}T_7 - A_y\mathbb{P}_{10}T_{13},\\
L_{13}^0 &= T_{23} - T_{24}L_9^0L_{10}^0,\\
\mathbb{P}_{10} &= \left(A_y + \mathrm{i}\alpha\right)^{-1},\\
\mathbb{P}_{20} &= \left(A_y + 2\mathrm{i}\alpha\right)^{-1}
\end{aligned}
$$

List of References

[1] M. Abramovitz and I. Stegun. *Handbook of Mathematical Functions with Formulas, Graphs, and Mathematical Tables.* Dover, 1972.

[2] J. F. Allard and Y. Champoux. New empirical equations for sound propagation in rigid frame fibrous materials. *J. Acoust. Soc. Am.*, 91:3346, 1992.

[3] K. Attenborough. Acoustical characteristics of porous materials. *Phys. Rep.*, 82(3):179–227, 1982.

[4] A. P. Bassom. Weakly nonlinear lower-branch stability of fully developed and developing free-surface flows. *IMA J. Appl. Math.*, 42(3):269–301, 1989.

[5] H. Bestek and W. Eissler. Direct Numerical Simulation of transition in Mach 4.8 boundary layers at flight conditions. In Rodi and Bergeles, editors, *Engineering Turbulence Modelling and Experiments*, volume 3. Elsevier Science, 1996.

[6] D. Bountin, A. A. Maslov, C. Chimytov, and A. Shiplyuk. Bispectral analysis of nonlinear processes in the hypersonic boundary layer on a porous cone surface. *Fluid Dyn.*, 45:415–421, 2010.

[7] D. Bountin, A. Shiplyuk, and A. A. Maslov. Evolution of nonlinear processes in a hypersonic boundary layer on a sharp cone. *J. Fluid Mech.*, 611:427–442, 2008.

[8] D. Bountin, A. Shiplyuk, and A. Sidorenko. Experimental investigations of disturbance development in the hypersonic boundary layer on conical models. In H. F. Fasel and W. S. Saric, editors, *Fifth IUTAM Symposium on Laminar-Turbulent Transition*. Springer, 2000.

[9] R. I. Bowles. On vortex interaction in the latter stages of boundary-layer transition. In H. F. Fasel and W. S. Saric, editors, *Fifth IUTAM Symposium on Laminar-Turbulent Transition*. Springer, 2000a.

[10] R. I. Bowles. Transition to turbulent flow in aerodynamics. *Phil. Trans. Roy. Soc. London*, 358:245–260, 2000b.

[11] G. A. Bres, T. Colonius, and A. V. Fedorov. Acoustic properties of porous coatings for hypersonic boundary-layer control. *AIAA J.*, 48:267–274, 2010.

[12] G. A. Bres, M. Inkman, T. Colonius, and A. V. Fedorov. Alternate designs of ultrasonic absorptive coatings for hypersonic boundary layer control. *AIAA Paper 2009-4217*, 2009.

[13] S. N. Brown, A. M. Khorrami, and A. Neish. On hypersonic boundary-layer interactions and transition. *Phil. Trans. Roy. Soc. London*, 335:139–152, 1991.

[14] C.-L. Chang and M. R. Malik. Oblique-mode breakdown and secondary instability in supersonic boundary layers. *J. Fluid. Mech.*, 273:323–360, 1994.

[15] C.-L. Chang, M. R. Malik, and M. Y. Hussaini. Effects of shock on the stability of hypersonic boundary layers. *AIAA Paper 90-1448*, 1990.

[16] N. Chokani. Nonlinear spectral dynamics of hypersonic laminar boundary layer flow. *Phys. Fluids*, 11(12):3846–3851, 1999.

[17] N. Chokani. Nonlinear evolution of Mack modes in a hypersonic boundary layer. *Phys. Fluids*, 17:014102, 2005.

[18] N. Chokani, D. A. Bountin, A. N. Shiplyuk, and A. A. Maslov. Nonlinear aspects of hypersonic boundary-layer stability on a porous surface. *AIAA J.*, 43:149–155, 2005.

[19] S. J. Cowley and P. Hall. On the instability of hypersonic flow past a wedge. *J. Fluid Mech.*, 214:17–42, 1990.

[20] N. De Tullio and N. D. Sandham. Direct Numerical Simulation of breakdown to turbulence in a Mach 6 boundary layer over a porous surface. *Phys. Fluids*, 22:094105–15, 2010.

[21] P. W. Duck. The inviscid axisymmetric stability of the supersonic flow along a circular cylinder. *J. Fluid Mech.*, 214:611–637, 1990.

[22] P. W. Duck and P. Hall. On the interaction of Tollmien-Schlichting waves in axisymmetric supersonic flows. *Q. J. Mech. App. Maths*, 42:115–130, 1989.

[23] P. W. Duck and P. Hall. Non-axisymmetric viscous lower-branch modes in axisymmetric supersonic flows. *J. Fluid Mech.*, 213:191–201, 1990.

[24] I. V. Egorov, A. V. Fedorov, and V. G. Soudakov. Receptivity of a hypersonic boundary layer over a flat plate with a porous coating. *J. Fluid Mech.*, 601:165–187, 2008.

[25] H. F. Fasel. Numerical investigation of transition in supersonic boundary layers using DNS and LES. Technical Report FA9550-05-1-0170, University of Arizona, 2008.

[26] A. V. Fedorov. Transition and stability of high-speed boundary layers. *Ann. Rev. Fluid. Mech.*, 43:79–95, 2011.

[27] A. V. Fedorov, G. A. Bres, M. Inkman, and T. Colonius. Instability of hypersonic boundary layer on a wall with resonating micro-cavities. *AIAA Paper 2011-373*, 2011.

[28] A. V. Fedorov, V. Kozlov, A. Shiplyuk, A. A. Maslov, and N. D. Malmuth. Stability of hypersonic boundary layer on porous wall with regular microstructure. *AIAA Journal*, 44(8):1866–1871, 2006.

[29] A. V. Fedorov and N. D. Malmuth. Hypersonic flow stabilization by ultrasonically transparent wall. Technical Report SCNM96-1, Rockwell Science Centre, 1996.

[30] A. V. Fedorov and N. D. Malmuth. Parametric studies of hypersonic laminar flow control using a porous coating of regular microstructure. *AIAA Paper 2008-588*, 2008.

[31] A. V. Fedorov, N. D. Malmuth, A. Rasheed, and H. G. Hornung. Stabilization of hypersonic boundary layers by porous coatings. *AIAA J.*, 39(4):605–610, 2001.

[32] A. V. Fedorov, A. Shiplyuk, A. A. Maslov, E. Burov, and N. D. Malmuth. Stabilization of high speed boundary layer using a porous coating. *AIAA Paper 2003-1970*, 2003a.

[33] A. V. Fedorov, A. Shiplyuk, A. A. Maslov, E. Burov, and N. D. Malmuth. Stabilization of a hypersonic boundary layer using an ultrasonically absorptive coating. *J. Fluid Mech.*, 479:99–124, 2003b.

[34] S. Gaponov, Yu. Ermolaev, A. Kosinov, V. Lysenko, N. Semenov, and B. Smorodsky. The influence of surface porosity on the stability and transition of supersonic boundary layer on a flat plate. *Thermophys. Aeromech+*, 17:259–268, 2010.

[35] S. A. Gaponov. Effect of the behaviour of a porous covering on boundary layer stability. *Izv. SO AN SSSR, Ser. Tech. Nauk*, 1(3):21–23, 1971. in Russian.

[36] S. A. Gaponov. Effect of gas compressibility on the stability of a boundary layer above a permeable surface at subsonic velocities. *J. Appl. Mech. Tech. Phy.*, 16(1):95–99, 1975.

[37] S. A. Gaponov. Stability of a supersonic boundary layer on a permeable surface with heat transfer. *Fluid Dyn.*, 12(1):33–37, 1977.

[38] S. A. Gaponov and N. M. Terekhova. Three-wave interactions between disturbances in the hypersonic boundary layer on impermeable and porous surfaces. *Fluid Dyn.*, 44:362–371, 2009.

[39] S. A. Gaponov and N. M. Terekhova. Linear evolution and interaction of disturbances in the boundary layers on impermeable and porous surfaces in the presence of heat transfer. *Fluid Dyn.*, 46:399–411, 2011.

[40] P. D. Germain and H. G. Hornung. Transition on a slender cone in hypervelocity flow. *Exp. Fluids*, 22(3):183–190, 1997.

[41] M. E. Goldstein. The role of nonlinear critical layers in boundary layer transition. *Phil. Trans. Roy. Soc. London*, 352:425–442, 1995.

[42] M. E. Goldstein and D. W. Wundrow. Spatial evolution of nonlinear acoustic mode-instabilities on hypersonic boundary-layers. *J. Fluid Mech.*, 219:585–607, 1990.

[43] P. Hall and F. T. Smith. A suggested mechanism for nonlinear wall roughness effects on high Reynolds number flow stability. *Stud. Appl. Math.*, 66:241–265, 1982.

[44] P. Hall and F. T. Smith. On the effects of nonparallelism, three-dimensionality, and mode interaction in nonlinear boundary-layer stability. *Stud. Appl. Math.*, 70:91–120, 1984.

[45] W. D. Hayes and R. Probstein. *Hypersonic Inviscid Flows*. Dover, 2004.

[46] W. D. Hayes and R. F. Probstein. *Hypersonic Flow Theory*, volume 1. Academic Press, second edition, 1966.

[47] F. Husmeier and H. F. Fasel. Numerical investigations of hypersonic boundary layer transition for circular cones. *AIAA Paper 2007-3843*, 2007.

[48] Y. S. Kachanov. Physical mechanisms of laminar-boundary-layer transition. *Ann. Rev. Fluid. Mech.*, 26:411–482, 1994.

[49] R. L. Kimmel. Aspects of hypersonic boundary layer transition control. *AIAA Paper 2003-0772*, 6-9 January 2003.

[50] R. L. Kimmel, A. Demetriades, and J. C. Donaldson. Space-time correlation measurements in a hypersonic transitional boundary layer. *AIAA J.*, 34(12):2484–2489, 1996.

[51] R. L. Kimmel and J. M. Kendall. Nonlinear disturbance in a hypersonic boundary layer. *AIAA Paper 91-0320*, 1991.

[52] P. S. Klebanoff, K. D. Tidstrom, and L. M. Sargent. The three-dimensional nature of boundary layer instability. *J. Fluid. Mech.*, 12:1–34, 1962.

[53] C. Koevary, A. Laible, C. Mayer, and H. F. Fasel. Numerical simulations of controlled transition for a sharp circular cone at Mach 8. *AIAA Paper 2010-4598*, 2010.

[54] A. D. Kosinov, A. A. Maslov, and S. G. Shevelkov. Experiments on the stability of supersonic laminar boundary layers. *J. Fluid Mech.*, 219:621–633, 1990.

[55] A. D. Kosinov, N. V. Semionov, S. G. Shevelkov, and O. I. Zinin. Experiments on the nonlinear instability of supersonic boundary layers. In S. P. Lin and W. Phillips, editors, *IUTAM Symposium on Nonlinear Instability of Nonparallel Flows*, pages 196–206. Springer, 1994.

[56] V. F. Kozlov, A. V. Fedorov, and N. D. Malmuth. Acoustic properties of rarefied gases inside pores of simple geometries. *J. Acoust. Soc. Am.*, 117(6):3402–3412, 2005.

[57] J. T. Lachowicz, N. Chokani, and S. P. Wilkinson. Boundary-layer stability measurements in a hypersonic quiet tunnel. *AIAA J.*, 34(12):2496–2500, 1996.

[58] A. Laible and H. F. Fasel. Numerical investigation of hypersonic transition for a flared and a straight cone at Mach 6. *AIAA Paper 2011-3565*, 2011.

[59] K. K. Leung and G. Emanuel. Hypersonic inviscid and viscous flow over a wedge and cone. *J. Aircraft*, 32:385–391, 1995.

[60] L. Li, J. D. A. Walker, R. I. Bowles, and F. T. Smith. Short-scale break-up in unsteady interactive layers: local development of normal pressure gradients and vortex wind-up. *J. Fluid. Mech.*, 374:355–378, 1998.

[61] S. V. Lukashevich, A. A. Maslov, A. N. Shiplyuk, A. V. Fedorov, and V. G. Soudakov. Stabilization of high-speed boundary layer using porous coatings of various thicknesses. *AIAA Paper 2010-4720*, 2010.

[62] V. I. Lysenko and A. A. Maslov. Effect of cooling on supersonic boundary-layer stability. *J. Fluid Mech.*, 147:39–52, 1984.

[63] L. M. Mack. Linear stability theory and the problem of supersonic boundary layer transition. *AIAA J.*, 13(3):278–289, 1975.

[64] L. M. Mack. Boundary layer stability theory. In *Special course on stability and transition of laminar flow*, number 709 in AGARD Report, 1984.

[65] M. R. Malik. Numerical-methods for hypersonic boundary-layer stability. *J. Comput. Phys.*, 86(2):376–413, 1990.

[66] N. D. Malmuth, A. V. Fedorov, V. Shalaev, J. Cole, and A. Kokhlov. Problems in high-speed flow prediction relevant to control. *AIAA Paper 98-2292*, 1998.

[67] R. R. Mankbadi. Resonant triad in boundary-layer stability. Technical Report NASA TM 105208, NASA Lewis Research Center, 1991.

[68] R. R. Mankbadi, X. Wu, and S. S. Lee. A critical-layer analysis of the resonant triad in blasius boundary layer: nonlinear interactions. *J. Fluid. Mech.*, 256:85–106, 1993.

[69] A. A. Maslov. Experimental and theoretical studies of hypersonic laminar flow control using ultrasonically absorptive coatings (UAC). Technical Report ISTC 2172-2001, International Science and Technology Centre, 2003.

[70] A. A. Maslov, T. Poplavskaya, and D. A. Bountin. Hypersonic boundary layer transition and control. In P. Schlatter and D. Henningson, editors, *Seventh IUTAM Symposium on Laminar-Turbulent Transition*, pages 19–26. Springer, 2010.

[71] C. D. Pruett and C.-L. Chang. Spatial direct numerical simulation of high speed boundary-layer flows. part II: Transition on a cone in Mach 8 flow. *Theoret. Comput. Fluid Dyn*, 7:397–424, 1995.

[72] A. Rasheed. *Passive hypervelocity boundary layer control using an ultrasonically absorptive surface*. PhD thesis, California Institute of Technology, 2001.

[73] M. Rasmussen. *Hypersonic flow*. Wiley Interscience, 1994.

[74] H. L. Reed, R. Kimmel, S. Schneider, D. Arnal, and W. S. Saric. Drag prediction and transition in hypersonic flow. *AIAA Paper 97-1818*, 1997.

[75] S. P. Schneider. Flight data for boundary-layer transition at hypersonic and supersonic speeds. *J. Spacecraft Rockets*, 36(1):8–20, 1999.

[76] S. P. Schneider. Hypersonic laminar-turbulent transition on circular cones and scramjet forebodies. *Prog. Aerosp. Sci.*, 40(1-2):1–50, 2004.

[77] S. O. Seddougui. Stability of hypersonic flow over a cone. In M. Y. Hussaini, T. B. Gatski, and T. L. Jackson, editors, *Transition, Turbulence and Combustion*, pages 50–59. Kluwer, 1994a.

[78] S. O. Seddougui and A. P. Bassom. Nonlinear instability of viscous modes in hypersonic flow past a wedge. *Q. J. Mech. App. Maths*, 47:557–582, 1994b.

[79] S. O. Seddougui and A. P. Bassom. Instability of hypersonic flow over a cone. *J. Fluid Mech.*, 345:383–411, 1997.

[80] S. O. Seddougui, R. I. Bowles, and F. T. Smith. Surface-cooling effects on compressible boundary-layer instability, and on upstream influence. *Eur. J. Mech. B/Fluids*, 10:117–145, 1991.

[81] A. N. Shiplyuk, D. A. Bountin, A. A. Maslov, and N. Chokani. Nonlinear mechanisms of the initial stage of the laminar–turbulent transition at hypersonic velocities. *J. Appl. Mech. Tech. Phy.*, 44:654–659, 2003.

[82] A. N. Shiplyuk, E. V. Burov, A. A. Maslov, and V. M. Fomin. Effect of porous coatings on stability of hypersonic boundary layers. *J. Appl. Mech. Tech. Phy.*, 45(2):286–291, 2004.

[83] F. T. Smith. Nonlinear stability of boundary layers for disturbances of various sizes. *Proc. R. Soc. A*, 368:573–589, 1979a. See also A 371 (1980) 439-440.

[84] F. T. Smith. On the non-parallel flow stability of the blasius boundary layer. *Phil. Trans. Roy. Soc. London*, 366:91–109, 1979b.

[85] F. T. Smith. Finite-time break-up can occur in any unsteady interacting boundary layer. *Mathematika*, 25:356–373, 1988.

[86] F. T. Smith. On the first-mode instability in subsonic, supersonic or hypersonic boundary-layers. *J. Fluid Mech.*, 198:127–153, 1989.

[87] F. T. Smith and R. I. Bowles. Transition theory and experimental comparisons on (a) amplification into streets and (b) a strongly nonlinear break-up criterion. *Proc. R. Soc. A*, 439:163–175, 1992.

[88] F. T. Smith, R. I. Bowles, and J. D. A. Walker. Wind-up of a spanwise vortex in deepening transition and stall. *Theoret. Comput. Fluid Dyn*, 14:135–165, 2000.

[89] F. T. Smith and S. N. Brown. The inviscid instability of a Blasius boundary-layer at large values of the Mach number. *J. Fluid Mech.*, 219:499–518, 1990.

[90] F. T. Smith and A. G. Walton. Nonlinear interaction of near-planar TS waves and longitudinal vortices in boundary-layer transition. *Mathematika*, 36:262–289, 1989.

[91] S. O. Stephen. Nonlinear instability of hypersonic flow over a cone. *Q. J. Mech. App. Maths*, 59:301–319, 2006.

[92] S. O. Stephen and V. Michael. Effects of porous walls on hypersonic boundary layer over a sharp cone. *AIAA Paper 2010-4286*, 2010a.

[93] S. O. Stephen and V. Michael. Effect of passive porous walls on hypersonic boundary layer. In P. Schlatter and D. Henningson, editors, *Seventh IUTAM Symposium on Laminar-Turbulent Transition*, pages 581–584. Springer, 2010b.

[94] S. O. Stephen and V. Michael. Effects of porous walls on hypersonic boundary layers over a sharp cone. *AIAA J*, 2012. Submitted.

[95] K. F. Stetson. On nonlinear aspects of hypersonic boundary-layer stability. *AIAA J.*, 26(7):883–885, 1988.

[96] K. F. Stetson and R. L. Kimmel. On hypersonic boundary-layer stability. *AIAA Paper 92-0737*, 1992.

[97] K. F. Stetson, R. L. Kimmel, E. R. Thompson, J. C. Donaldson, and L. G. Siler. A comparison of planar and conical boundary layer stability and transition at a Mach number of 8. *AIAA Paper 91-1639*, June 24-26 1991.

[98] K. F. Stetson, E. R. Thompson, J. C. Donaldson, and L. G. Siler. Laminar boundary layer-stability experiments on a cone at Mach 8. Part 1: Sharp cone. *AIAA Paper 83-1761*, July 1983.

[99] P. A. Stewart and F. T. Smith. Three-dimensional nonlinear blow-up from a nearly planar initial disturbance in boundary layer transition; theory and experimental comparisons. *J. Fluid. Mech.*, 244:649–676, 1992.

[100] K. Stewartson. *The theory of laminar boundary layers in compressible fluids*. Oxford University Press, 1964.

[101] J. Stilla. Engineering transition prediction for a hypersonic axisymmetric boundary layer. *J. Aircraft*, 31:1358–1364, 1994.

[102] M. R. Stinson. The propagation of plane sound waves in narrow and wide circular tubes and generalization to uniform tubes of arbitrary cross-sectional shape. *J. Acoust. Soc. Am.*, 89(2):550–559, 1991.

[103] M. R. Stinson and Y. Champoux. Propagation of sound and the assignment of shape factors in model porous materials having simple pore geometries. *J. Acoust. Soc. Am.*, 91(2):685–695, 1992.

[104] J. T. Stuart. On the non-linear mechanics of wave disturbances in stable and unstable parallel flows. *J. Fluid Mech.*, 9:353–370, 1960.

[105] G. Stuckert and H. L. Reed. Linear disturbances in hypersonic, chemically reacting shock layers. *AIAA J.*, 32:1384–1393, 1994.

[106] A. Thumm, W. Wolz, and H. F. Fasel. Numerical simulation of spatially growing three-dimensional disturbance waves in compressible boundary layers. In R. Michel and D. Arnal, editors, *Third IUTAM Symposium on Laminar-Turbulent Transition*. Springer, 1990.

[107] X. Wang and X. Zhong. Numerical simulation and theoretical analysis on boundary-layer instability affected by porous coating. *AIAA Paper 2009-3679*, 2009.

[108] X. Wang and X. Zhong. Effect of porous coating on boundary-layer instability. *AIAA Paper 2010-1243*, 2010.

[109] X. Wang and X. Zhong. Numerical simulations on mode S growth over feltmetal and regular porous coatings of a Mach 5.92 flow. *AIAA Paper 2011-375*, 2011a.

[110] X. Wang and X. Zhong. Phase angle of porous coating admittance and its effect on boundary-layer stabilization. *AIAA Paper 2011-3080*, 2011b.

[111] V. Wendt, M. Simen, and A. Hanifi. An experimental and theoretical investigation of instabilities in hypersonic flat-plate boundary-layer flow. *Phys. Fluids*, 7(4):877–887, 1995.

[112] A. Whitehead Jr. NASP aerodynamics. *AIAA Paper 89-5013*, 1989.

[113] X. Zhong and X. Wang. Direct numerical simulation on the receptivity, instability, and transition of hypersonic boundary layers. *Ann. Rev. Fluid. Mech.*, 45:527–561, 2012.